RHEINISCH-WESTFÄLISCHE TECHNISCHE HOCHSCHULE AACHEN

Investigation of Systematic Effects and Uncertainties involved in the Determination of the Invariant Spin Axis in a storage ring for an EDM Measurement

Von der Fakultät für Mathematik, Informatik und Naturwissenschaften der RWTH Aachen University zur Erlangung des akademischen Grades eines Doktors der Naturwissenschaften genehmigte Dissertation

vorgelegt von

Maximilian Vitz, M.Sc.

aus

Mönchengladbach

Berichter: Univ.-Prof. Dr. rer. nat. Jörg Pretz
Univ.-Prof. Dr. rer. nat. Achim Stahl

Tag der mündlichen Prüfung: 25. November 2024

Diese Dissertation ist auf den Internetseiten der Universitätsbibliothek verfügbar.

Abstract

The excess of matter over antimatter in the known part of the Universe cannot be explained by the Standard Model of particle physics. Mechanisms that violate $\mathcal{CP}$ symmetry exist in the Standard Model and can be used to explain the excess of matter over antimatter. However, they are too weak to account for the observed asymmetry. Therefore, additional sources of $\mathcal{CP}$ violation are being investigated. A promising candidate for further $\mathcal{CP}$ violation beyond those established in the Standard Model is the permanent electric dipole moment of elementary particles. Using storage rings as particle traps, the EDM of charged particles can be studied, since the orientation of the polarization rotation axis also called the invariant spin axis is determined by the EDM.

Therefore, the JEDI collaboration at Jülich has carried out the first direct EDM measurement of deuterons with the Precursor Runs at the storage ring COSY. Using solenoids and an RF Wien filter, the invariant spin axis tilt angle was determined. In addition to the influence of the EDM, the ISA tilt angle is also influenced by the storage ring systematics. Therefore, particle and spin tracking simulations in an accurate simulation model of the COSY storage ring are required to disentangle a potential EDM signal from the storage ring systematics.

This thesis presents the development of such a simulation model of the COSY storage ring, based on the BMAD software library, in order to investigate the systematic effects, present during the Precursor Run 2 in 2021. Correction factors depending on the measurement method are shown and the uncertainties of the systematic effects and the COSY orbit measurements are discussed. Finally, it is shown that the measured ISA tilt angles at the RF Wien filter obtained during Precursor Run 2 are too large to originate from storage ring systematics in COSY or a potential EDM.

Zusammenfassung

Der Überschuss an Materie gegenüber Antimaterie im bekannten Teil des Universums lässt sich nicht mit dem Standardmodell der Teilchenphysik erklären. Allerdings existieren Mechanismen, die die $\mathcal{CP}$-Symmetrie verletzen, im Standardmodell und können zur Erklärung des Überschusses von Materie gegenüber Antimaterie herangezogen werden. Diese sind jedoch zu schwach, um die beobachtete Asymmetrie zu erklären. Daher werden zusätzliche Quellen der $\mathcal{CP}$-Verletzung untersucht. Ein vielversprechender Kandidat für $\mathcal{CP}$-Verletzungen, die über die im Standardmodell etablierten hinausgehen, ist das permanente elektrische Dipolmoment von Elementarteilchen. Mit Hilfe von Speicherringen als Teilchenfallen kann das EDM geladener Teilchen untersucht werden, da die Orientierung der Polarisationsdrehachse, auch invariante Spinachse genannt, durch das EDM bestimmt wird.

Aus diesem Grund hat die JEDI-Kollaboration in Jülich eine erste direkte EDM-Messung von Deuteronen mit den Precursor Runs am Speicherring COSY durchgeführt. Mit Hilfe von Solenoiden und dem RF Wien Filter wurde der Neigungswinkel der invariante Spinachsen bestimmt. Neben dem Einfluss des EDM wird der Neigungswinkel der ISA auch durch die Systematik des Speicherrings beeinflusst. Daher sind Teilchen- und Spin-Tracking-Simulationen in einem präzisen Simulationsmodell des COSY-Speicherrings erforderlich, um ein potenzielles EDM Signal von der Systematik des Speicherrings zu entkoppeln.

In dieser Arbeit wird die Entwicklung eines solchen Simulationsmodells des COSY Speicherrings, basierend auf der BMAD-Softwarebibliothek, vorgestellt um die systematischen Effekte während des Precursor Runs 2 im Jahr 2021 zu untersuchen. Es werden Korrekturfaktoren in Abhängigkeit von der Messmethode aufgezeigt und die Unsicherheiten der systematischen Effekte und der COSY Orbitmessungen diskutiert. Abschließend wird gezeigt, dass die gemessenen ISA-Neigungswinkel am RF Wien Filter, die während des Precursor Run 2 ermittelt wurden, zu groß sind, um von Speicherringsystematiken in COSY oder einem möglichen EDM herrühren zu können.

Acknowledgments

I would like to begin this thesis by thanking everyone who has contributed to it over the years and without whom this work would never have been possible.

First of all, I would like to thank my supervisor Prof. Dr. Jörg Pretz for his advice, patience and guidance. Through him I was able to gain many valuable experiences as a PhD student. Many thanks to Prof. Dr. Andreas Lehrach for his support during all this time and for introducing me to the topic of accelerator physics. I would also like to thank Dr Ralf Gebel, who gave me the opportunity to attend conferences all over the world as a young scientist and to gain such excellent experience. I really appreciate your support.

I would also like to thank the members of the JEDI collaboration and the staff of the IKP in Jülich. Thank you for all the constructive discussions and for the help from all sides when needed. It has always been a great pleasure for me to work in such an international, friendly and professional environment and I will definitely miss these times. I wish everyone continued success and enjoyment in their work. My special thanks go to Dr. Volker Hejny, Dr. Alexander Nass, Dr. Frank Rathmann, Dr. Hans Joachim Stein, Dr. Jan Hetzel, Dr. Michael Hartmann and Dr. Achim Andres.

Last but not least, I would like to thank my parents, Korinna and Roland Vitz, who have supported me throughout the years, as well as my wife, Pia Vitz, for her patience and unconditional support.

Contents

CHAPTER 1

Introduction

The purpose of physics is to explain the nature of things in terms of equations and mathematical models. One of the most famous and well-established models is the SM (**S**tandard **M**odel) of particle physics. This generally accepted model describes elementary particles and their interactions, and has been confirmed by many experimental observations, while also making predictions that have led to many new discoveries in the past. Despite its success, there are areas of modern physics where the SM cannot provide an explanation. One such area is the dominance of matter over antimatter in the known part of the Universe. Although the SM predicts this asymmetry, the observed asymmetry is orders of magnitude larger than the SM prediction. One possible explanation for this observation is the disappearance of antimatter during the baryogenesis of the Universe. However, this would require more violation of the $\mathcal{CP}$ symmetry than the SM considers. The permanent EDM (**E**lectric **D**ipole **M**oment) of elementary particles is predicted by the SM and contributes to the violation of the $\mathcal{CP}$ symmetry. So far, only upper bounds on the EDM magnitude have been derived from measurements. The measurement of a finite EDM can therefore be seen as a probe for models that try to explain physics beyond the SM, and improves the understanding of the fundamentals of physics.

One of those measurements is being carried out by the JEDI (**J**ülich **E**lectric **D**ipole Moment **I**nvestigation), which wants to measure the EDM of protons and deuterons directly. This is currently done at the COSY (**CO**oler **SY**nchrotron) storage ring, located at Forschungszentrum Jülich in Germany, although there are future plans for direct measurements of protons and deuterons proposed in dedicated storage rings, which are utilizing pure electric fields or a combination of electric and magnetic fields. So far, two direct measurements of the deuteron EDM have been performed in 2019 and 2021 by the JEDI collaboration in the so-called Precursor Runs 1 and 2, which should demonstrate that the

principles and tools necessary for an EDM measurement in a storage ring are applicable and operational. The aim of this thesis is to simulate the COSY storage ring and the conditions during Precursor Run 2 in order to understand and interpret the measured data and to disentangle a potential EDM signal from systematic effects that naturally occur in any storage ring.

Therefore the thesis is structured, so that Chapter (2) gives an overview over the matter-antimatter asymmetry in the modern Universe and motivates the theoretical background of the topic by discussing fundamental symmetries and introducing the EDM.

In Chapter (3) and Chapter (4) the basic knowledge necessary to understand particle and spin physics in storage rings is presented. The influence of an EDM on the spin motion is also discussed. The focus is on the equations of motion describing particle trajectories, the evolution of spin and polarization in electromagnetic fields, and the derivation of particle and spin transfer matrices for the magnetic elements present in a storage ring.

The chapters (5) and (6) present the main features of the storage ring COSY used and needed for an EDM experiment and describe how these features are implemented in the simulation model used for this thesis. In addition, the simulation program BMAD (**B**aby **M**ethodical **A**ccelerator **D**esign) is presented, which was used for the simulations performed in this thesis.

Chapter (7) will discuss the measurement method for the EDM using the RF Wien filter and static solenoids in COSY. The determination of the correction factors, which have to be considered in view of a disturbed beam path, will also be presented.

In Chapter (8) the systematic effects and the beam orbit in COSY present during Precursor Run 2 are discussed. To reproduce the measured beam orbit, an optimization algorithm is presented and applied in the BMAD simulation. On this basis, the expected measurement results of the RF Wien filter and the solenoids are compared with the simulation results.

Finally this thesis will conclude with Chapter (9), where a conclusion and a short summary of the result presented in this thesis is given. In addition, on outlook on the future of the project is presented.

CHAPTER 2

Scientific Motivation

This thesis was written as part of the JARA-FAME program within the JEDI project. The JARA program (**J**ülich **A**achen **R**esearch **A**lliance) [1] is a cooperation between the Forschungszentrum Jülich [2] and the RWTH (**R**heinisch-**W**estfälische **T**echnische **H**ochschule) Aachen University [3], which combines disciplinary research at the RWTH Aachen University with programme-oriented research at Forschungszentrum Jülich. The FAME (**F**orces and **MA**tter **E**xperiments) [1] section of the JARA program deals with particle physics and tries to explain the currently visible dominance of matter over antimatter. Therefore, the JEDI project [4] is collaborating to search for a permanent electric dipole moment in protons and light nuclei, as this would represent a difference between matter and antimatter and thus contribute to the visible asymmetry between both. Details about the matter-antimatter asymmetry, the necessary violation of fundamental discrete symmetries in physics as well as details about the EDM are discussed in the following chapter to give a scientific background for this research.

2.1 Matter-Antimatter Asymmetry

The SM of particle physics, which describes elementary particles and their interactions, is very successful in explaining many experimental observations. Unfortunately, it fails to explain the observed dominance of matter over antimatter in the known part of the Universe, which is one of the great unsolved puzzles of cosmology [5]. In the early stages of its history, the Universe was hot and antimatter was present when pair production and annihilation reactions were in thermal equilibrium. As the Universe expanded and cooled down, the energy available for pair production became too small. For this reason, almost all particles and antiparticles were annihilated, with a small amount of matter surviving. The amount of remaining matter over antimatter is defined as the BAU (**B**aryon **A**symmetry

of the **U**niverse), the difference between the number of baryons N_{B} and the number of antibaryons $N_{\bar{\mathrm{B}}}$ divided by their sum. Assuming that there are no antibaryons left in the modern universe and that the products of the annihilation processes are mostly photons, the ratio of baryons to anti-baryons can be redefined by a baryon-to-photon density ratio η_{BAU} [6]:

$$\eta_{\mathrm{BAU}} = \frac{N_{\mathrm{B}}}{N_\gamma} = \frac{N_{\mathrm{B}} - N_{\bar{B}}}{N_\gamma} \approx \frac{N_{\mathrm{B}} - N_{\bar{\mathrm{B}}}}{N_{\mathrm{B}} + N_{\bar{\mathrm{B}}}}. \tag{2.1}$$

The study of the abundance of light elements in the BBN (**B**ig-**B**ang-**N**ucleosynthesis) provides one source of estimation of the baryon-to-photon density ratio η_{BAU} [7]. Another source is the observation of the temperature fluctuations in the CMB (**C**osmic **M**icrowave **B**ackground) [8]. Both methods show consistent results, giving values of $\eta_{\mathrm{BAU}} \approx 6 \cdot 10^{-10}$. However, estimates based on the SM give a smaller density ratio of $\eta_{\mathrm{BAU}} \approx 1 \cdot 10^{-18}$ [9, 10]. There are two different theories to explain this discrepancy:

- During the evolution of the Universe, regions of matter and antimatter were formed and separated. As a result, antimatter exists in larger quantities in the modern Universe. However, regions dominated by antimatter have yet to be discovered.
- During the evolution of the Universe, an asymmetric annihilation process of matter and antimatter resulted in the dominance of one over the other.

This work is based on the assumption that the asymmetry between matter and antimatter is caused by the asymmetric annihilation process. The conditions that form the basis for such a process were formulated by A. D. Sakharov and are therefore called *Sakharov criteria* [11]:

- **Violation of baryon conservation law:** The annihilation process must violate the baryon conservation law, where each baryon carries the quantity $n_{\mathrm{B}} = +1$ and each antibaryon carries the quantity $n_{\mathrm{B}} = -1$. The process of violating this law played an important role in the early universe, but has a negligible role under laboratory conditions [11].
- **Violation of $\mathcal{C}$ and $\mathcal{CP}$ symmetries:** Without a violation of $\mathcal{C}$ and $\mathcal{CP}$ symmetries, the production rate of baryons and antibaryons is equally likely. Therefore, this violation of fundamental symmetries is necessary to obtain an excess of baryons over antibaryons [11].
- **Phase of non thermal equilibrium:** The generation of the assymetry had to take place during a phase of non thermal equilibrium in Universe. The reason is that $\mathcal{CP}$ invariance would assure that the baryon conservation law would hold on average [10].

In the SM there is the violation of fundamental symmetries, such as $\mathcal{C}$ and $\mathcal{CP}$ violation, included and explainable [10]. These symmetries are discussed in the following section.

2.2 Discrete Symmetries and Their Violation

Since a symmetry is defined as a transformation under which a system remains invariant, it is naturally related to conservation laws. Besides *continuous symmetries*, there are also *discrete symmetries* in nature, which played an important role in the development of quantum mechanics [12]. This section discusses the three fundamental discrete symmetry transformations and their violation.

$\mathcal{P}$-Symmetry

The $\mathcal{P}$ symmetry defines a parity transformation that reverses the sign of all spatial coordinates of a process while leaving the time coordinates unchanged. Polar vectors such as position are affected by the transformation, while axial vectors such as angular momentum are not. When considering electromagnetic fields, an electric field represented by a polar vector is inverted by the $\mathcal{P}$ transformation, whereas a magnetic field retains its orientation since it is represented by an axial vector [12]. One process that violates P-symmetry is the beta decay of polarized ^{60}Co [13], described by Equation (2.2). In this decay, the direction in which the electron is emitted is favoured to be opposite to the direction of the nuclear spin, regardless of its orientation. Since the velocity inverts its sign under parity transformation, this indicates a parity-violating process.

$$^{60}_{28}\mathrm{Co} \rightarrow ^{60}_{27}\mathrm{Ni} + \mathrm{e}^- + \bar{\nu}_\mathrm{e} + 2\gamma \tag{2.2}$$

$\mathcal{C}$-Symmetry

The charge conjugation $\mathcal{C}$ defines a symmetry transformation of a particle into its antiparticle. Applying this symmetry transformation therefore inverts all additive quantum numbers such as charge, baryon and lepton number or strangeness, while preserving other quantities such as spin, position or momentum [12]. Evidence for a $\mathcal{C}$ violating process can be found by considering the $\mathcal{C}$ transformation of a left-handed neutrino into a left-handed anti-neutrino, which is not observed [13]:

$$\pi^+ \rightarrow \mu^+_\mathrm{L} + \nu_{\mu,\mathrm{L}} \quad \overset{\mathcal{C}-\text{Transformation}}{\Rightarrow} \quad \pi^- \rightarrow \mu^-_\mathrm{L} + \bar{\nu}_{\mu,\mathrm{L}}. \tag{2.3}$$

$\mathcal{T}$-Symmetry

A transformation where only the time coordinate is inverted is called a time reversal transformation $\mathcal{T}$. This implies a reversible physical process with equal rates in both

directions. Tests of this symmetry in the strong and electromagnetic interactions showed no evidence for a violation of this symmetry. A first observation of a $\mathcal{T}$ violating process in the weak sector was measured in the decay of neutral kaons, where the probability P of the transformation K^0 into $\bar{K}^0$ and vice versa showed an asymmetry [14]:

$$\frac{P(\bar{K}^0 \to K^0) - P(K^0 \to \bar{K}^0)}{P(\bar{K}^0 \to K^0) + P(K^0 \to \bar{K}^0)} \neq 0. \tag{2.4}$$

Violation of $\mathcal{CP}$-Symmetry in the SM

As mentioned above, a violation of $\mathcal{CP}$ symmetry is required for the mechanism that creates the asymmetry between baryons and antibaryons. A first indication of a $\mathcal{CP}$ violation in nature was found in the measurement of the decay of the K^0 [15]. The decay into two pions implies that the K^0 is not a pure eigenstate of $\mathcal{CP}$, since decay into a two-pion final state would not be allowed in this case. This process was included in the SM via a complex phase proportional to the CP violation in the CKM matrix (**C**abibbo-**K**obayashi-**M**askawa) [16]. Unfortunately, the $\mathcal{CP}$ violation in the CKM matrix of the SM is not sufficient to explain the matter-antimatter asymmetry. Therefore, additional sources of $\mathcal{CP}$ violation are important to investigate. The EDM is a possible candidate for an additional symmetry breaking process and will be discussed in the following section.

Since the symmetries already discussed seem to be violated individually, it is practical to combine them to find a combined symmetry that is not broken. The $\mathcal{CPT}$-Theorem is such a combined symmetry [17]. It requires that the local quantum field theory is Lorentz invariant, which leads to the conservation of the combination of $\mathcal{C}$, $\mathcal{P}$ and $\mathcal{T}$ transformations to arbitrary order.

2.3 Electric Dipole Moment

An EDM $\vec{d}$ is defined as a permanent separation of charges within a particle. Similar to the MDM (**M**agnetic **D**ipole **M**oment) $\vec{\mu}$, it is a fundamental property. Its orientation parallel or anti-parallel to the particle spin $\vec{s}$ and is the only distinguishable quantization axis:

$$\vec{d} = \frac{\eta_{\mathrm{EDM}}}{2} \frac{q}{mc} \vec{s}, \tag{2.5}$$

$$\vec{\mu} = \frac{g_{\mathrm{MDM}}}{2} \frac{q}{mc} \vec{s}. \tag{2.6}$$

MDM and EDM are scaled by the charge q and the mass m of the particles. They also include a dimensionless scaling factor g_{MDM} and η_{EDM} for the different dipole moments.

The Hamiltonian **H** in Equation (2.7) shows the interaction of the dipole moments for a particle at rest with an external electric $\vec{E}$ and magnetic $\vec{B}$ field [5]. Performing symmetry transformations on this Hamiltonian demonstrates the symmetry breaking due to an existing EDM:

$$\begin{aligned} \mathbf{H} = &\quad -\vec{\mu}\cdot\vec{B} - \vec{d}\cdot\vec{E}, \\ \mathcal{P}:\mathbf{H} = &\quad -\vec{\mu}\cdot\vec{B} + \vec{d}\cdot\vec{E}, \\ \mathcal{T}:\mathbf{H} = &\quad -\vec{\mu}\cdot\vec{B} + \vec{d}\cdot\vec{E}. \end{aligned} \tag{2.7}$$

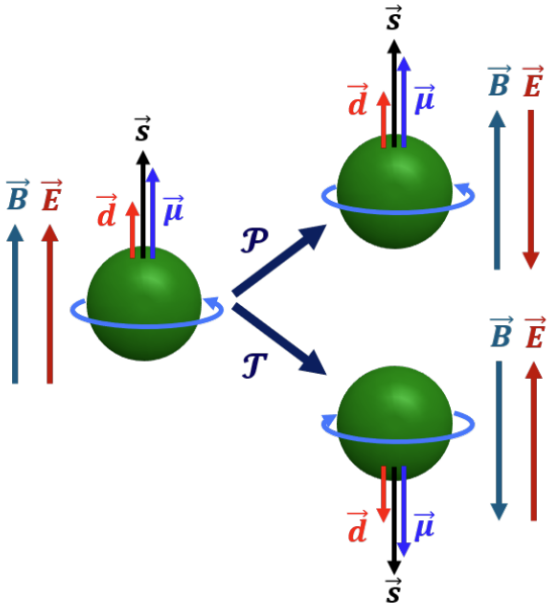

Figure 2.1: Schematic of the effect of an external magnetic field $\vec{B}$ and electric field $\vec{E}$ on the particle's spin axis $\vec{s}$, assuming an EDM $\vec{d}$ and MDM $\vec{\mu}$ contribution. Symmetry transformations such as the parity transformation $\mathcal{P}$ and the time reversal transformation $\mathcal{T}$ reverse the design of the electric field while leaving the magnetic field contribution unchanged. Taken from [18].

The consequence of the symmetry breaking of $\mathcal{P}$ and $\mathcal{T}$ is equivalent to a $\mathcal{CP}$ violation, provided that the $\mathcal{CPT}$ theorem holds. In the SM an EDM cannot arise in the first order. It just appears as a higher order loop effect. Therefore the SM prediction for the weak sector for an EDM is for example very small for the neutron [5]:

$$d_{\text{Neu}} \approx \quad 10^{-32}\,\text{e}\cdot\text{cm}. \tag{2.8}$$

In the strong sector of the SM an EDM also arises as an higher order loop effect and is coupled to the θ_{QCD} term. Unfortunately this quantity is also expected to be very small, with an upper limit derived from a neutron measurement [19, 20]:

$$d_{\mathrm{Neu}} \approx \quad (-2.9 \pm 0.9) \cdot 10^{-16}\,\mathrm{e} \cdot \mathrm{cm} \cdot \theta_{\mathrm{QCD}}, \quad \text{with} \quad \theta_{\mathrm{QCD}} < 10^{-10}. \tag{2.9}$$

Measuring an EDM at a higher limit than the SM prediction increases the CP violation and helps to explain the measured asymmetry between matter and antimatter. So far, upper bounds for an EDM have been found, but not an EDM signal itself. It is not sufficient to measure only the EDM of one particle, e.g. the neutron, because the source of the EDM cannot be found in this way. The results for upper limits of different particles are summarized in the Table (2.1) [21]:

Particle	Neutron	Proton	Electron
|d|	$1.8 \cdot 10^{-26}$ e · cm (90% C. L.) [22]	$7.9 \cdot 10^{-25}$ e · cm (95% C. L.) [23]	$4.1 \cdot 10^{-30}$ e · cm (90% C. L.) [24]

Table 2.1: Upper EDM limits for different particle species.

The JEDI collaboration aims to determine the EDM in protons and deuterons using a storage ring. A first direct measurement of the deuteron EDM was therefore carried out in the so-called Precursor Runs 1 and 2 at the COSY storage ring in Jülich [25]. Since a storage ring EDM experiment requires high precision, it is essential to have a thorough understanding of the behaviour of a particle beam circulating in a storage ring. Therefore, the next chapter discusses the fundamental forces induced by the magnetic and electric fields and on the stored particle beam as well as its transverse and longitudinal motion.

CHAPTER 3

Beam Dynamics in a Synchrotron

3.1 Lorentz Force

The forces that deflect, focus and accelerate charged particles in a storage ring result from the interaction of these particles with electric and magnetic fields. This interaction is described by the *Lorentz force* [26]:

$$\vec{F}_{\mathrm{L}} = q(\vec{E} + \vec{v} \times \vec{B}). \tag{3.1}$$

The Lorentz force indicates the direction and magnitude of the force on a particle with charge q and velocity $\vec{v}$ in face of an electric field with strength $\vec{E}$, and a magnetic field with flux density $\vec{B}$ in the lab system at the particle's current position. For singly charged particles such as protons and deuterons, the charge q is equal to the elementary charge e. Forces perpendicular to the current velocity $\vec{v}$ result in a circular deflection of the particles, keeping the kinetic energy constant as the magnitude $|v|$ remains unchanged. Forces parallel to the current velocity $\vec{v}$ lead to a change in velocity and hence a change in kinetic energy [27].

In a storage ring, the forces induced by the magnetic field are mainly perpendicular to the particle's velocity $\vec{v}$. As a result, they can only deflect and focus the particles. Acceleration, which is defined as a change in kinetic energy, requires a longitudinal electric field. By understanding the location and strength of electric and magnetic fields inside a storage ring, one is able to forecast the trajectory of charged particles. The process of guiding particles through the electric and magnetic fields of a storage ring is called *beam optics* or *beam dynamics* [26, 27]. The general physical principles of beam dynamics in a strong focusing synchrotron were developed by E. B. Courant and H. S. Snyder [27, 28].

3.2 Coordinate System

To be able to perform calculations to guide the charged particles on dedicated trajectories through the ring, one has to define suitable coordinate system. Given that the dimensions of a beam are significantly smaller than the entire storage ring, particle coordinates are defined relative to their ideal trajectory around the storage ring. This ideal trajectory is also called *design orbit*. The individual particles are characterized within a co-moving coordinate system, originating from the design orbit. The horizontal discrepancy between the reference particle on the design orbit and the described particle is denoted as x, the vertical as y, and the longitudinal as z. Figure (3.1) provides a visual representation of the co-moving coordinate system [27].

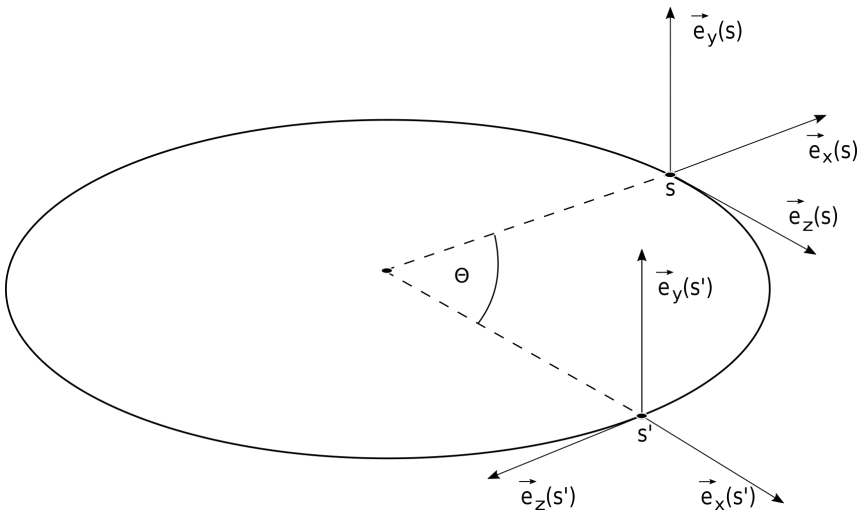

Figure 3.1: Sketch of the co-moving coordinate system with the Cartesian coordinates $\vec{e}_{\mathrm{x}}(s/s')$, $\vec{e}_{\mathrm{y}}(s/s')$ and $\vec{e}_{\mathrm{z}}(s/s')$ at two different location s and s' inside the storage ring. The coordinate system at s' is rotated by an angle Θ in relation to s. The origin of co-moving coordinate system is always the design orbit. Adapted from [27].

A special feature of the co-moving coordinate system is a rotation of the whole coordinate system when the reference particle is deflected by a magnet due to the Lorentz force. In most cases this deflection takes place in the xz plane of the storage ring. Therefore, the transformation of the basis vectors from one location, denoted s, to another, denoted s', is defined by the following equations [27, 29]:

$$\begin{aligned} \vec{e}_{\mathrm{x}}(s') &= +\cos(\theta) \cdot \vec{e}_{\mathrm{x}}(s) + \sin(\theta) \cdot \vec{e}_{\mathrm{z}}(s), \\ \vec{e}_{\mathrm{y}}(s') &= \vec{e}_{\mathrm{y}}(s), \\ \vec{e}_{\mathrm{z}}(s') &= -\sin(\theta) \cdot \vec{e}_{\mathrm{x}}(s) + \cos(\theta) \cdot \vec{e}_{\mathrm{z}}(s). \end{aligned} \tag{3.2}$$

3.3 Transverse Beam Dynamics

3.3.1 Magnetic Multipole Fields

In order to keep the reference particle with momentum p_0 on its circular trajectory through the storage ring an equilibrium between Lorentz force and centrifugal force is necessary. Therefore a static transversal magnetic field B_y is needed, which is indicated in Equation (3.3). The magnetic field can be expanded in a Taylor series for small deviations from the ideal trajectory, as shown below [27]:

$$\frac{1}{R(x,y,z)} = \frac{q}{p_0} B_\mathrm{y}(x,y,z) \tag{3.3}$$

$$\begin{aligned} \Rightarrow \frac{q}{p_0} B_\mathrm{y}(x) &= \frac{q}{p_0} B_{\mathrm{y},0} + \frac{q}{p_0}\frac{dB_\mathrm{y}}{dx}\cdot x + \frac{1}{2!}\frac{q}{p_0}\frac{d^2 B_\mathrm{y}}{dx^2}\cdot x^2 + \ldots \\ &= \frac{1}{R} + k_1 \cdot x + \frac{1}{2!} k_2 \cdot x^2 + \ldots \\ &\quad \text{Dipole} \qquad \text{Quadrupole} \qquad \text{Sextupole} \end{aligned} \tag{3.4}$$

This way, one receives a description that shows the effect of different magnetic multipole contributions such as the dipole, the quadrupole and the sextupole. Higher order configurations can also be considered in this way. The quantities k_1 and k_2 represent the strengths of the quadrupole and sextupole. While dipole fields are used for beam deflection and guidance, quadrupole fields contribute to beam focusing. The next higher order is the sextupole, which are used for chromaticity correction. In cases where only the two lowest multipoles are used to guide the beam in a storage ring, this is referred to as *linear beam optics* [27].

3.3.2 Hill's Differential Equation

The effect of linear beam optics on the beam path will be discussed in the next sections. As a consequence of the chosen approaches for the co-moving coordinate system, taking into account the Taylor series of the magnetic field, *Hill's differential equations* for the horizontal and vertical motion follow. The complete differential equation is given in the Equation (3.5). Hill's differential equations are the fundamental basis for describing linear particle motion in transverse phase space. They assume magnetic multipoles up to linear order and decoupling of horizontal and vertical motion [27, 29].

$$\begin{aligned} x''(s) + \left(\frac{1}{R^2(s)} - k_1(s)\right) x(s) &= \frac{1}{R(s)}\frac{\Delta p}{p_0}, \\ y''(s) + k_1(s) y(s) &= 0. \end{aligned} \tag{3.5}$$

The quantities used in the differential equations are the second derivatives with respect to the parameter s of the local horizontal displacement $x''(s)$ and the local vertical displacement $y''(s)$. The dependence on s of the bending radius $R(s)$ indicates that it contributes only at locations along the particle's path s where dipole fields are present. Similarly, $k_1(s)$ denotes the strength of a quadrupole and is therefore associated with quadrupole fields. Since a quadrupole focuses in one direction but defocuses in the other, a convention must be chosen for a positive $k_1(s)$. In this context, a positive $k_1(s)$ value describes a horizontally defocusing quadrupole. A momentum deviation of a particle with respect to the reference particle is given by $\Delta p/p_0$. Its presence in the horizontal motion is related to the deflection by dipoles of the plane of the storage ring, which is momentum dependent [27].

3.3.3 General Trajectories - Homogenous Solution

Assuming that there is no coupling between the horizontal and vertical planes of particle motion, the differential equation can be solved independently for each plane. Another simplifying assumption is that the fields of the dipoles and quadrupoles start at full strength immediately at the start of the magnets and drop abruptly to zero at the end. The fields are also constant along the beam axis inside the magnets. This magnet model is called the *hard edge model* and is a very good approximation for calculating the beam optics of complex magnet structures. It is also postulated that all particles have nominal energy, giving $\Delta p/p_0 = 0$. This leaves a simplified version of the differential equation, which represents the horizontal motion of the particles in a quadrupole, given by [26, 27]:

$$x''(s) - k_1 \cdot x(s) = 0, \quad \text{with} \quad k_1 = \text{const.} \tag{3.6}$$

In the same way, the vertical motion is defined. These linear and homogeneous second order differential equations can be solved directly analytically. The integration constants are determined by the initial conditions. Therefore, it is postulated that at the beginning of the magnet the particle position is given by $x_0 = x(0)$ and the angular velocity by $x'_0 = x'(0)$. In the case of a horizontally defocusing magnet with $k_1 > 0$ the solution is given by [27]:

$$\begin{aligned} x(s) &= x_0 \cosh(\sqrt{k_1}s) + \frac{x'_0}{\sqrt{k_1}} \sinh(\sqrt{k_1}s), \\ x'(s) &= \sqrt{k_1} x_0 \sinh(\sqrt{k_1}s) + x'_0 \cosh(\sqrt{k_1}s). \end{aligned} \tag{3.7}$$

An elegant notation for the transformation of the phase space from the beginning of a magnet to the point s[1] is the matrix form. Equation (3.7) can be rewritten as a matrix $\mathbf{M}_{\mathrm{Q},k_1>0}$ which transforms the initial conditions to their final position:

$$\begin{pmatrix} x(s) \\ x'(s) \end{pmatrix} = \begin{pmatrix} \cosh(\sqrt{k_1}s) & \frac{1}{\sqrt{k_1}}\sinh(\sqrt{k_1}s) \\ \sqrt{k_1}\sinh(\sqrt{k_1}s) & \cosh(\sqrt{k_1}s) \end{pmatrix} \begin{pmatrix} x_0 \\ x'_0 \end{pmatrix} = \mathbf{M}_{\mathrm{Q},k_1>0} \begin{pmatrix} x_0 \\ x'_0 \end{pmatrix}. \tag{3.8}$$

Similarly, the matrix $\mathbf{M}_{\mathrm{Q},k_1<0}$ for a horizontally focusing quadrupole with $k_1 < 0$ can be constructed:

$$\begin{pmatrix} x(s) \\ x'(s) \end{pmatrix} = \begin{pmatrix} \cosh(\sqrt{|k_1|}s) & \frac{1}{\sqrt{|k_1|}}\sinh(\sqrt{|k_1|}s) \\ -\sqrt{|k_1|}\sinh(\sqrt{|k|}s) & \cosh(\sqrt{|k_1|}s) \end{pmatrix} \begin{pmatrix} x_0 \\ x'_0 \end{pmatrix} = \mathbf{M}_{\mathrm{Q},k_1<0} \begin{pmatrix} x_0 \\ x'_0 \end{pmatrix}. \tag{3.9}$$

So far only the horizontal space has been discussed. Since the quadrupole has a focusing effect in one phase space direction and a defocusing effect in the other, the vertical phase space is just a matrix with inverted focusing and the insertion of $x = y$.

A simplified version of Hill's differential equations can also be constructed for a dipole. Assuming particles with nominal energy $\Delta p/p_0 = 0$ and a dipole field with no gradient $k_1 = 0$, a differential equation given by

$$x''(s) - \frac{1}{R^2} \cdot x(s) = 0, \quad \text{with} \quad R = \text{const}, \tag{3.10}$$

follows. Since a dipole only acts in horizontal phase space, the effect in vertical phase space is only a translation by the dipole length. The solution of the differential equation for a dipole, is the sector dipole matrix $\mathbf{M}_{\mathrm{SD}}$ [27]:

$$\begin{pmatrix} x(s) \\ x'(s) \end{pmatrix} = \begin{pmatrix} \cos(\frac{s}{R}) & R\sin(\frac{s}{R}) \\ -\frac{1}{R}\sin(\frac{s}{R}) & \cos(\frac{s}{R}) \end{pmatrix} \begin{pmatrix} x_0 \\ x'_0 \end{pmatrix} = \mathbf{M}_{\mathrm{SD}} \begin{pmatrix} x_0 \\ x'_0 \end{pmatrix}. \tag{3.11}$$

In storage rings, *rectangular dipole magnets* are often used because they are easier to manufacture. Unlike *sector dipole magnets*, these magnets have their face angles rotated relative to the beam path by an angle ψ. While this rotation of the face angles does not change the total deflection angle in the dipole, it introduces another effect called *edge*

[1] This can also mean the end and thus the length of the magnet.

focusing. Therefore, horizontally, the rectangular dipole matrix $\mathbf{M}_{\mathrm{RD}}$ must be corrected for each face angle by the edge focusing matrix $\mathbf{M}_{\mathrm{Edge}}$, shown in Equation (3.12) in contrast to the sector dipole matrix [27].

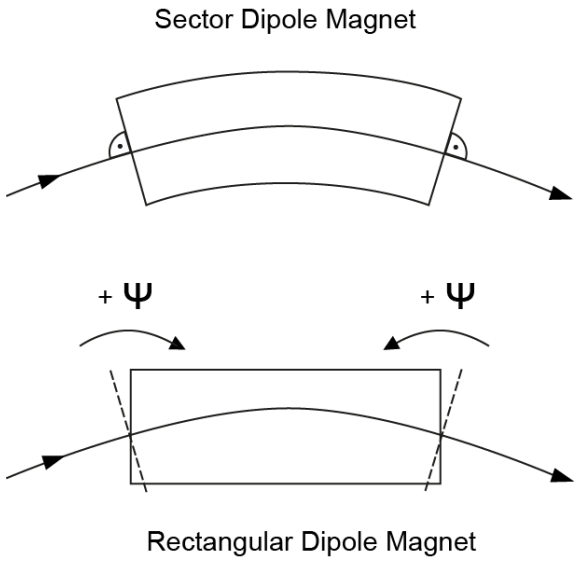

Figure 3.2: Sketch of the edge focusing effect caused by rotating the face angles of a sector dipole magnet relative to the beam path. The result is a rectangular shaped dipole magnet. Adapted from [27].

$$\begin{aligned} \mathbf{M}_{\mathrm{Edge}} &= \begin{pmatrix} 1 & 0 \\ \frac{\tan(\psi)}{R} & 1 \end{pmatrix} \\ \Rightarrow \mathbf{M}_{\mathrm{RD}} &= \mathbf{M}_{\mathrm{Edge}}\mathbf{M}_{\mathrm{SD}}\mathbf{M}_{\mathrm{Edge}} \end{aligned} \tag{3.12}$$

Edge focusing also occurs in the vertical direction. It is identical to the horizontal edge focusing effect, but the sign is reversed. This means that edge focusing has a defocusing effect in the horizontal plane and a focusing effect in the vertical plane [27].

The particle trajectories can thus be calculated as a system of transformation matrices from one particular location in the storage ring to another. The composition of the transformation matrices depends on the magnetic elements through which the trajectory vector passes. This will be explained in more detail in Section (3.3.5).

3.3.4 Dispersive Trajectories - Inhomogeneous Solution

The dipole magnet also has another effect on the particle trajectory. Since the deflection angle is momentum dependent, the assumption $\Delta p/p_0 \neq 0$ leads to a special trajectory called *dispersive trajectory* or *dispersion* $D_{\mathrm{x}}(s)$. The modified differential equation under the condition $\Delta p/p_0 = 1$ for a dipole therefore is [27]:

$$\begin{aligned} x''(s) + & \quad \frac{1}{R^2(s)} x(s) = & \frac{1}{R(s)} \frac{\Delta p}{p_0} \\ \Rightarrow D_{\mathrm{x}}''(s) + & \quad \frac{1}{R^2(s)} D_{\mathrm{x}}(s) = & \frac{1}{R(s)} \end{aligned} \tag{3.13}$$

The solution of this inhomogeneous differential equation is a combination of the homogeneous part already presented and the inhomogeneous part due to the momentum offset. The result of the inhomogeneous part thus extends the homogeneous part with the initial conditions $D_{\mathrm{x},0}$ and $D'_{\mathrm{x},0}$ [27]:

$$\begin{aligned} D_{\mathrm{x}}(s) = & \quad D_{\mathrm{x},0} \cos\left(\frac{s}{R}\right) + \quad D'_{\mathrm{x},0} R \sin\left(\frac{s}{R}\right) + \quad R\left(1 - \cos\left(\frac{s}{R}\right)\right), \\ D'_{\mathrm{x}}(s) = & -\frac{D_{\mathrm{x},0}}{R} \sin\left(\frac{s}{R}\right) + \quad D'_{\mathrm{x},0} \cos\left(\frac{s}{R}\right) + \quad \sin\left(\frac{s}{R}\right). \end{aligned} \tag{3.14}$$

Due to the inhomogeneous solution, the system of equations can no longer be represented by a 2x2 matrix. One has to switch to a 3x3 matrix, given by [27]:

$$\begin{pmatrix} D_{\mathrm{x}}(s) \\ D'_{\mathrm{x}}(s) \\ 1 \end{pmatrix} = \begin{pmatrix} \cos\left(\frac{s}{R}\right) & R\sin\left(\frac{s}{R}\right) & R\left(1 - \cos\left(\frac{s}{R}\right)\right) \\ -\frac{1}{R}\sin\left(\frac{s}{R}\right) & \cos\left(\frac{s}{R}\right) & \sin\left(\frac{s}{R}\right) \\ 0 & 0 & 1 \end{pmatrix} \begin{pmatrix} D_{\mathrm{x},0} \\ D'_{\mathrm{x},0} \\ 1 \end{pmatrix} = \mathbf{M}_{\mathrm{SB}} \begin{pmatrix} D_{\mathrm{x},0} \\ D'_{\mathrm{x},0} \\ 1 \end{pmatrix} \tag{3.15}$$

In this way, dispersion shifts the total horizontal particle path x_{Tot} at positions inside the storage ring where it does not vanish [27]:

$$x_{\mathrm{Tot}}(s) = x(s) + x_{\mathrm{D}}(s) = x(s) + D_{\mathrm{x}}(s)\frac{\Delta p}{p_0}. \tag{3.16}$$

3.3.5 Particle Transfer Matrix Formalism

As outlined above, the change in path caused by a magnetic element[2] can be represented using a matrix. So far it has only been shown for the horizontal and vertical space separately. To describe the full motion of the particles, a 6x6-dimensional matrix is required. This is why one also speaks of a *six-dimensional phase space*. A passage of several elements is obtained by multiplying the corresponding matrices. For example, the transport of a particle from position $s = 0$ with phase space coordinates $\vec{V}(s = 0)$ through a dipole M_{SD} and a quadrupole $M_{\mathrm{Q},k_1<0}$ to position s' can be represented as [29]:

[2] The same works for an electrical element.

$$\begin{aligned} \vec{V}(s') = &\quad \mathbf{M}_{\mathrm{SD}}\mathbf{M}_{\mathrm{Drift}}\mathbf{M}_{\mathrm{Q},k_1<0} \cdot \vec{V}(s=0) \\ \Rightarrow \vec{V}(s') = &\quad \mathbf{M}_{\mathrm{Transport}} \cdot \vec{V}(s=0). \end{aligned} \tag{3.17}$$

In this equation the matrix $\mathbf{M}_{\mathrm{Drift}}$ denotes the empty space, also called *drift space*, between the magnets. This is a simple translation matrix defined by the length L_{Drift} of the drift space. Assuming decoupled horizontal and vertical motion, the basic structure of a 6×6-dimensional transport matrix can be represented as sketched by [29]:

$$\begin{aligned} \mathbf{M}_{\mathrm{Transport}} &= \begin{pmatrix} M_{11} & M_{11} & 0 & 0 & 0 & M_{16} \\ M_{21} & M_{22} & 0 & 0 & 0 & M_{26} \\ 0 & 0 & M_{33} & M_{34} & 0 & 0 \\ 0 & 0 & M_{43} & M_{44} & 0 & 0 \\ M_{51} & M_{52} & 0 & 0 & 1 & M_{56} \\ 0 & 0 & 0 & 0 & 0 & 1 \end{pmatrix} \\ &= \begin{pmatrix} \langle x|x\rangle & \langle x|x'\rangle & 0 & 0 & 0 & \langle x|\delta\rangle \\ \langle x'|x\rangle & \langle x'|x'\rangle & 0 & 0 & 0 & \langle x'|\delta\rangle \\ 0 & 0 & \langle y|y\rangle & \langle y|y'\rangle & 0 & 0 \\ 0 & 0 & \langle y'|y\rangle & \langle y'|y'\rangle & 0 & 0 \\ \langle z|x\rangle & \langle z|x'\rangle & 0 & 0 & \langle z|z\rangle & \langle z|\delta\rangle \\ 0 & 0 & 0 & 0 & 0 & \langle \delta|\delta\rangle \end{pmatrix}. \end{aligned} \tag{3.18}$$

The corresponding phase space vector $\vec{V}$ must then be defined by [29]:

$$\vec{V} = \begin{pmatrix} x \\ x' \\ y \\ y' \\ z \\ \delta \end{pmatrix} = \begin{pmatrix} \text{local horizontal displacement} \\ \text{angular horizontal displacement} \\ \text{local vertical displacement} \\ \text{angular vertical displacement} \\ \text{local longitudinal displacement} \\ \text{relative momentum deviation} \end{pmatrix}. \tag{3.19}$$

In the 6x6-dimensional transport matrix the elements M_{16} and M_{26} show the dispersive component due to a momentum offset in a dipole. On the other hand, M_{11}, M_{12}, M_{21} and M_{22} represent the homogeneous solution of the horizontal phase space, while M_{33}, M_{34}, M_{43} and M_{44} denote the homogeneous solution of the vertical phase space. The other aspects of this matrix will be discussed in the context of the longitudinal phase space in Section (3.4) [29].

3.3.6 Betafunction und Betatron Oscillation

Although the matrix formalism developed so far allows the calculation of individual particle trajectories through any magnetic structure, it does not yet provide any information about the properties of the beam as a collective of particles. Therefore, the calculation method needs to be extended to treat the entire beam. A similar approach can be used to solve the differential equation for a quadrupole, now assuming that k_1 is a property of the particle position s. The resulting differential equation and its solution for the horizontal phase space are sketched in the following equations [27]:

$$x''(s) - k_1(s)x(s) = 0 \tag{3.20}$$

$$\Rightarrow x_\beta(s) = \sqrt{\epsilon_\mathrm{x}\beta_\mathrm{x}(s)}\cos(\psi_\mathrm{x}(s) + \phi_\mathrm{x}). \tag{3.21}$$

The solution $x_\beta(s)$ shows an oscillation of the particles around the orbit. The combination of $\sqrt{\epsilon_\mathrm{x}\beta_\mathrm{x}(s)}$ forms the location dependent amplitude of the oscillation, where the parameter ϵ_x is called *emittance* or *Courant-Snyder invariant*. This property depends on the initial conditions of the particle and is therefore constant[3]. The so-called β function is the optical parameter that varies with the beam focusing $k_1(s)$ and therefore depends on the position s. Together with the phase advance $\psi_\mathrm{x}(s)$ and the phase ϕ_x, these quantities describe the motion of a single particle induced by the quadrupole magnets. The phase advance is directly related to the β function as shown in Equation (3.22). An identical solution is obtained for the vertical phase space with the sign reversed [27].

$$\psi_\mathrm{x}(s) = \int_0^s \frac{1}{\beta_\mathrm{x}(s')} ds'. \tag{3.22}$$

3.3.7 Phase Space Ellipse and Liouville's theorem

To describe the motion of particles in the each transverse plane i, two additional parameters $\alpha_\mathrm{i}(s)$ and $\gamma_\mathrm{i}(s)$ are introduced, which directly depend on the β-function as shown in Equation (3.23). In combination with $\beta(s)$ they are called *optical functions* as they define the optics of the storage ring [27].

$$\alpha_\mathrm{i}(s) = -\frac{1}{2}\frac{\mathrm{d}\beta_\mathrm{i}(s)}{ds} \quad \text{and} \quad \gamma_\mathrm{i}(s) = \frac{1+\alpha_\mathrm{i}^2(s)}{\beta_\mathrm{i}(s)}. \tag{3.23}$$

[3] This simple assumption holds if a linear, energy conserving system is considered for the storage ring. In general, the emittance of a particle is subject to change over the storage time due to numerous effects such as cooling, intrabeam scattering, etc.

An ellipse equation can be constructed from the equations of motion and the optical functions. This *phase space ellipse* puts the previously introduced emittance into a physical context. The emittance now defines the area $A = \pi\epsilon$ of the phase space ellipse. This is described for the horizontal phase space in Equation (3.24) and illustrated in Figure (3.3). The vertical phase space behaves in the same way. The shape and orientation of the ellipse depends on the β-function and therefore changes with the position s in the storage ring. The area of the ellipse is independent of the position s and therefore constant over the circumference of the ring. This is also manifested in the *Liouville theorem*, which states that the volume element of a phase space is constant in time if the particles obey the canonical equations of motion [27].

$$\gamma_{\mathrm{x}}(s)x^2(s) + 2 \cdot \alpha_{\mathrm{x}}(s)x(s)x'(s) + \beta_{\mathrm{x}}(s)x'^2(s) = \epsilon_{\mathrm{x}} \tag{3.24}$$

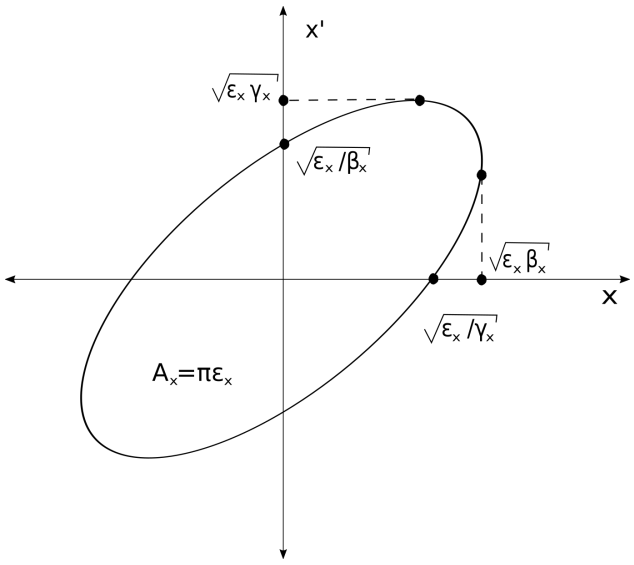

Figure 3.3: Horizontal phase space ellipse at a position s inside a storage ring. The horizontal axis shows the local horizontal displacement x of a particle relative to the design trajectory, and the vertical axis shows the angular horizontal displacement x'. The optical functions $\alpha_{\mathrm{x}}(s)$, $\beta_{\mathrm{x}}(s)$ and $\gamma_{\mathrm{x}}(s)$ define the orientation and shape of the ellipse, while the area A_{x} is defined by the Courant-Snyder invariant ϵ_{x}. Adapted from [27].

As the phase space ellipse has been derived under the assumption of vanishing $\Delta p/p_0$ and $1/R(s) = 0$, for a complete description one has to consider dispersive trajectories in the horizontal phase space due to dipole magnets. Dispersive trajectories move the horizontal phase space ellipse sideways around a reference point, but do not change its area. The reference point around which the phase space ellipse is constructed and around which the dispersive motion will take place is called the *closed orbit*. Figure (3.3) sketches a scenario in which the closed orbit is chosen to be on the design trajectory of the storage. In reality, this is not necessarily the case.

3.3.8 Periodic Solution and Closed Orbit

Since the particles are to be kept in a storage ring, both the calculated orbit and the optical functions must merge into themselves after a full revolution and thus represent a *periodic solution* of Hill's differential equation. For this purpose, the magnetic structure is arranged according to certain symmetries in order to simplify the calculation of the beam optics and to reduce the number of different magnetic circuits. By varying the quadrupole strengths k of the individual symmetry groups, the β function can be varied until a closed solution is found. This closed solution of the β-function represents the so-called *working point* of the storage ring. More on this topic will be presented in the next section [27].

In an idealized storage ring, particle motion due to betatron oscillations and dispersive trajectories would fully describe the behavior of the individual particles in a particle beam. In reality, the reference path inside the storage ring is also perturbed by magnetic misalignments, dipole errors, etc. These perturbations are called *systematics*. A perturbed orbit that still gives a closed solution is called *closed orbit*. In general, the motion of particles in the case of an uncoupled system can be described as a combination of betatron oscillations $x_\beta(s)$, dispersive trajectories $x_\mathrm{D}(s)$ and the closed orbit $x_\mathrm{Clo}(s)$ via [26]:

$$x(s) = x_\mathrm{Clo}(s) + x_\beta(s) + x_\mathrm{D}(s). \tag{3.25}$$

These perturbations due to various effects cannot be avoided. One way to get some control over the closed orbit is to use short dipole magnets at different positions inside the storage ring, which are therefore called *corrector magnets* or *steerer magnets*. This topic is discussed in more detail in Section (3.3.11).

3.3.9 Working Point and Betatron Tune

Since the magnetic structure repeats itself after each full revolution, the magnetic forces acting on the beam are also periodically repeated. As the particles in the beam also oscillate due to the transverse focusing forces, they can become resonant. In the case of resonance, the oscillation amplitude increases, which can lead to beam loss. As these resonances only occur at a certain number of betatron oscillations per revolution and are therefore related to the optics of the storage ring they are called *optical resonances*. The number of betatron oscillations per revolution is called the *betatron tune*. It must be calculated separately for the horizontal and vertical phase space, assuming an uncoupled motion, and is given by the Equation (3.26), where i denotes the horizontal and vertical phase space respectively [27].

$$Q_\mathrm{i} = \frac{1}{2\pi} \oint \frac{ds}{\beta_\mathrm{i}(s)} \qquad \text{with} \qquad i = x, y \tag{3.26}$$

The combination of horizontal Q_x and vertical Q_y betatron tune defines the *working point* of a storage ring. This working point can now be associated with an optical resonance. The resonance condition criteria for an optical resonance is described by [27]:

$$m \cdot Q_x + n \cdot Q_y = p \qquad \text{with} \qquad m, n, p \, \epsilon \, \mathbb{Z}. \tag{3.27}$$

The reason that the beam amplitude increases as a result of resonance lies in the field errors of the magnets and their *fringe fields*, which deviate from the previously very simple hard edge model. As a result, when a resonance condition is met, these errors add up over several revolutions and drive the beam further and further away from its closed orbit. The class of magnet causing this effect determines the order of the resonance. This is represented by the integer parameters m and n, which together define the order of the resonance over $|m| + |n|$. An integer resonance is generated by a dipole, a half integer resonance by a quadrupole, and so on. The lower the order of the resonance, the stronger it is. To avoid losing particles due to optical resonances, the working point must be chosen far away from any low order resonance. Typically a *tune diagram* like the one shown in the Figure (3.4) is used to show the position of the working point with respect to the main resonances [27].

3.3.10 Chromaticity

Due to a momentum deviation $\Delta p/p_0$ from the reference particle, other particles move on a different trajectory than the design particle. For this reason, they also experience a change in the optics of the storage ring. The quantity that describes the relationship between the change in optics in the form of a change in the working point ΔQ_i as a function of the momentum deviation is called the *chromaticity* and is defined individually for both transverse planes i by [27]:

$$\xi_i := \frac{\Delta Q_i}{\Delta p/p_0} \qquad \text{with} \qquad i = x, y. \tag{3.28}$$

A momentum deviation can also be interpreted as a quadrupole error. Since a particle permanently retains a momentum deviation, all quadrupoles in a storage ring have a quadrupole error proportional to $\Delta p/p_0$. In a large, strongly focused storage ring, the contribution of the quadrupole strength $k_1(s)$ to the chromaticity becomes dominant in combination with the local β-function $\beta_i(s)$. Therefore, to determine the total shift of the working point, the chromaticity has to be calculated by integration over all quadrupoles [27, 30]:

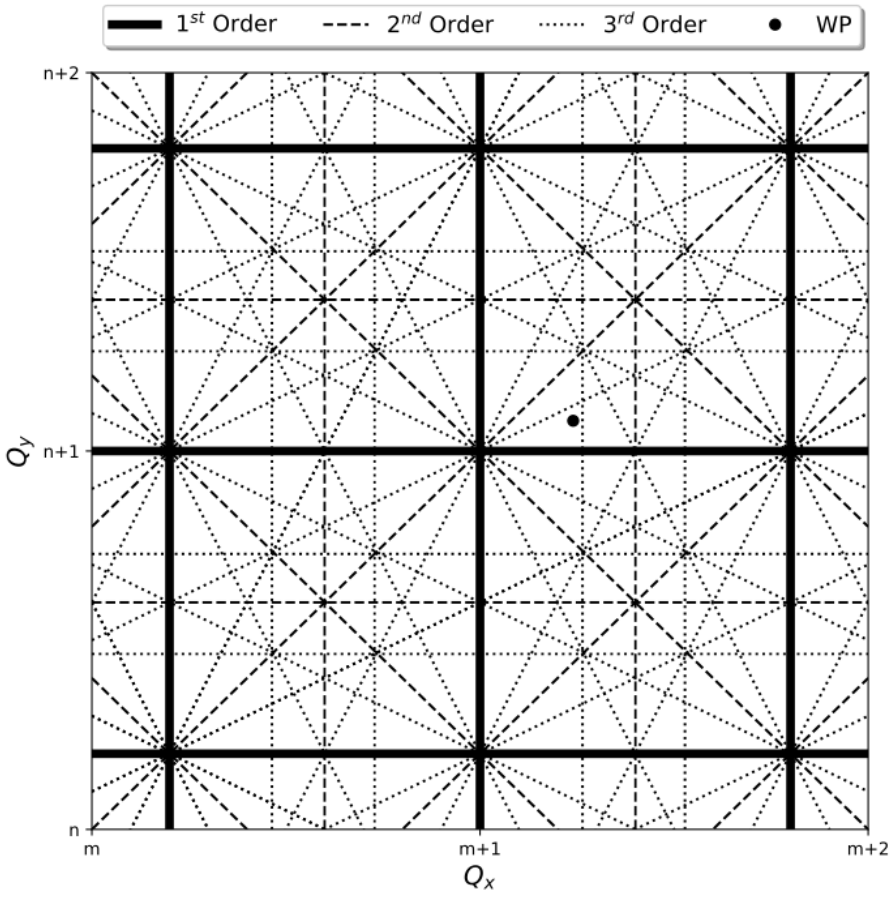

Figure 3.4: Tune diagram with arbitrary working point and optical resonances up to third order. The horizontal axis shows the horizontal betatron tune Q_x and the vertical axis the vertical betatron tune Q_y. The integers m and n define the order of the resonance over $|m| + |n|$. Inspired by [27].

$$\Delta Q_\mathrm{i}^\mathrm{Nat} = \frac{1}{4\pi} \oint \frac{\Delta p}{p_0} k_1(s) \beta_\mathrm{i}(s) ds \qquad \text{with} \qquad i = x, y. \tag{3.29}$$

Sextupoles distributed in the ring, placed on regions of non-vanishing dispersion, are used to adjust chromaticity. They generate local quadrupole components depending on the transverse position of the particle as it passes through the sextupole, as shown in figure (3.5). Their effect on the chromaticity depends on their strength $k_2(s)$ and the local dispersion $D_\mathrm{x}(s)$. The so-called *natural chromaticity* is therefore defined as the chromaticity of the ring arising from the focusing fields of quadrupoles and dipoles [29, 30]. The total chromaticity of a storage ring is a combination of the natural chromaticity and the chromaticity correction by the sextupoles, which is defined by [27]:

$$\Delta Q_\mathrm{i}^\mathrm{Sex} = \frac{1}{4\pi} \oint \frac{\Delta p}{p_0} k_2(s) D_\mathrm{x}(s) ds \qquad \text{with} \qquad i = x, y. \tag{3.30}$$

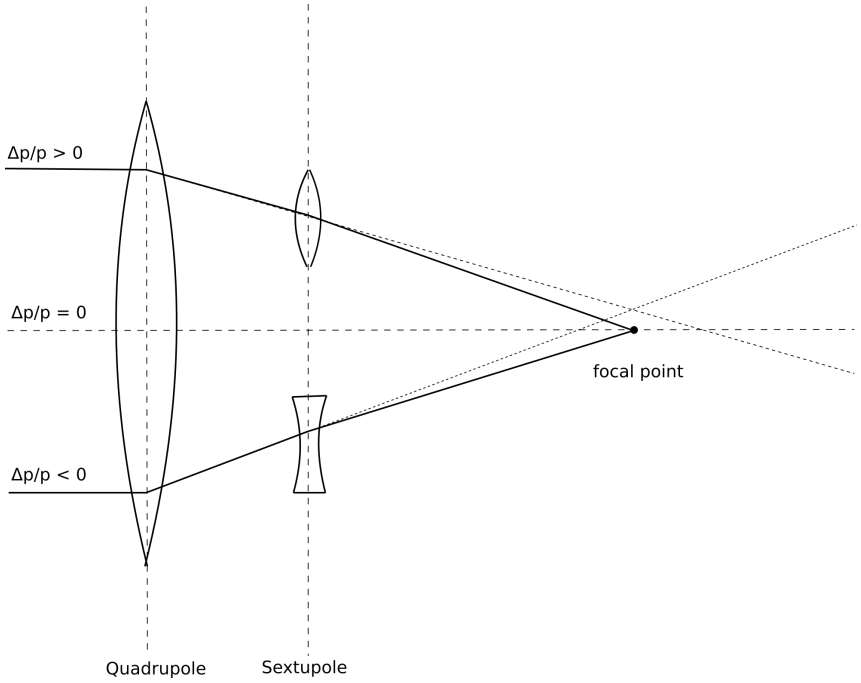

Figure 3.5: Sketch of the principle of chromaticity correction by a sextupole. Sextupoles produce a local quadrupole component depending on the transverse position of the particle. Adapted from [29].

3.3.11 Orbit Correction and Orbit Response Matrix

As discussed in Section (3.3.8), control of the closed orbit is required so that the storage ring *systematics*[4] that cause orbit perturbations can be compensated. This requires two devices. The first is called a corrector magnet, which is a short dipole magnet used to give the beam a controlled kick in the vertical or horizontal direction. The second one is called BPM (**B**eam **P**osition **M**onitor) and is used to measure the orbit with respect to its centre. For more information on how the BPM works, please refer to Section (5.1.3). Using both devices, the orbit can be corrected using the ORM (**O**rbit **R**esponse **M**atrix) method. The ORM $\mathbf{M}_{\mathrm{ORM}}$ is a matrix that defines how the beam responds to the dipole corrector magnets. It relates the beam offsets at the BPM positions in horizontal $\Delta\vec{x}$ and vertical $\Delta\vec{y}$ phase space to the dipole corrector kicks $\Delta\vec{\theta}_{\mathrm{x}}$ and $\Delta\vec{\theta}_{\mathrm{y}}$ at their respective positions inside the ring via [31, 32] :

$$\begin{pmatrix} \Delta\vec{x} \\ \Delta\vec{y} \end{pmatrix} = \mathbf{M}_{\mathrm{ORM}} \begin{pmatrix} \Delta\vec{\theta}_x \\ \Delta\vec{\theta}_y \end{pmatrix}. \tag{3.31}$$

A single element M_{ij} of the ORM is therefore defined by the shift in orbit at BPM i caused

[4] This includes misalignments of magnetic elements, field errors, etc.

by the change in magnetic strength in the corrector magnet j [31, 32]:

$$M_{\mathrm{ij,x}} = \frac{\Delta x_{\mathrm{i}}}{\Delta \theta_{\mathrm{x,j}}} \quad \text{or} \quad M_{\mathrm{ij,y}} = \frac{\Delta y_{\mathrm{i}}}{\Delta \theta_{\mathrm{y,j}}}. \tag{3.32}$$

A theoretical derivation of the ORM is possible based on the optical function β, the phase advance ϕ and the dispersion D_{x} at the position of the BPMs i and the corrector magnets j. Also to be considered are betatron tunes Q, the momentum compaction factor α_{p}[5], the Lorentz factor γ_0 of the reference particle and the ring circumference C_0. Assuming vanishing coupling of the horizontal and vertical beam dynamics, the matrix elements given in Equation (3.32) can be calculated theoretically using [31, 33]:

$$\begin{aligned} M_{\mathrm{ij,x}} &= \frac{\sqrt{\beta_{\mathrm{x,i}}\beta_{\mathrm{x,j}}}}{2\sin(\pi Q_{\mathrm{x}})}\cos(\phi_{\mathrm{x,i}} - \phi_{\mathrm{x,j}} - \pi Q_{\mathrm{x}}) - \frac{D_{\mathrm{x,i}}D_{\mathrm{x,j}}}{\left(\alpha_{\mathrm{p}} - \frac{1}{\gamma_0^2}\right)C_0}, \\ M_{\mathrm{ij,y}} &= \frac{\sqrt{\beta_{\mathrm{y,i}}\beta_{\mathrm{y,j}}}}{2\sin(\pi Q_{\mathrm{y}})}\cos(\phi_{\mathrm{y,i}} - \phi_{\mathrm{y,j}} - \pi Q_{\mathrm{y}}). \end{aligned} \tag{3.33}$$

To find the appropriate set of steerer kicks to flatten the orbit, a pseudoinverse of the ORM matrix must be computed. This is typically done using SVD (**S**ingular **V**alue **D**ecomposition) [31, 33].

3.4 Longitudinal Beam Dynamics

3.4.1 Momentum Compaction Factor

Due to the dipole contributions, particles with momentum deviation follow dispersive orbits. Usually, the dispersive orbits have a different length compared to the design orbit. The change in orbit length can be specified as a function of the momentum deviation. For circular accelerators this also leads to a dependence of the revolution period on the particle momentum. This plays an important role in the longitudinal phase focusing of the individual particles of a beam. The ratio of the relative change in path length $\Delta C/C_0$ to the relative change in momentum $\Delta p/p_0$ is called the *momentum compaction factor* α_0 and is defined as [27]:

$$\frac{\Delta C}{C_0} = \alpha_0 \frac{\Delta p}{p_0}. \tag{3.34}$$

Since the main contribution to the momentum compaction factor comes from the curvature $R(s)$ of the dipoles, the path lengthening effects of the quadrupoles can be neglected,

[5] This property will be discussed in Section (3.4).

as they only occur as higher order effects. The relationship between curvature and dispersion $D_{\mathrm{x}}(s)$ at the dipoles leads to another more theoretical description of the momentum compaction factor [27]:

$$\alpha_0 = \frac{1}{C_0} \oint \frac{D_{\mathrm{x}}(s)}{R(s)} ds. \tag{3.35}$$

A consequence of the different path length of particles with a momentum difference is a change in their revolution time ΔT with respect to the revolution time T_0 of the reference particle. The difference in revolution time depends on particle's energy, represented by the relativistic γ-factor γ_0, and the momentum compaction factor [27]:

$$\frac{\Delta T}{T_0} = \left(\alpha_0 - \frac{1}{\gamma_0^2} \right) \frac{\Delta p}{p_0}. \tag{3.36}$$

3.4.2 Phase Focusing and Synchrotron Frequency

Electric fields are used to accelerate, decelerate or bunch a particle beam. In a storage ring, this is done by using so-called *cavities*. The circulating particles must maintain a well-defined fixed phase ψ_{s} with respect to the high-frequency voltage U_0 of the cavity. In this way a focusing effect in the longitudinal phase space is achieved. The focusing effect in the longitudinal phase space is called *phase focusing*. While the fixed phase ψ_{s} defines whether energy is gained or lost through the cavity, the property W_0 describes the energy loss of a particle per revolution, e.g. by synchrotron radiation. In this way one can formulate an equation describing the energy change for one revolution [27]:

$$E_0 = eU_0 \sin \psi_{\mathrm{s}} - W_0. \tag{3.37}$$

Since not all particles pass through the cavity with the ideal phase, but with a small phase difference $\psi_\Delta = \psi_{\mathrm{s}} + \Delta\psi$, they receive an additional amount of energy ΔE. From this fact one can derive a second order differential equation,

$$\Delta \ddot{E} + \omega_s^2 \Delta E = 0, \tag{3.38}$$

which describes the motion in the longitudinal phase space of a particle entering the cavity with a phase difference from the reference phase. What enters the description is the second derivative of the energy change after the time Δt and the so-called *synchrotron frequency*

ω_s, given by [27]:

$$\omega_s = \omega_0 \sqrt{-\frac{eU_0 h \cos\psi_s}{2\pi\beta_0^2 E}\left(\alpha_0 - \frac{1}{\gamma_0^2}\right)}. \tag{3.39}$$

The synchrotron frequency describes the oscillation of the particles around the reference particle in longitudinal phase space. It is intuitively related to the momentum compaction factor, since this property describes the difference in revolution time and thus the time and phase of arrival at the cavity. Other important quantities are the cavity's maximum voltage U_0, the harmonic h at which it operates with respect to the rotational frequency ω_0, the relativistic γ_0 and the velocity β_0 and the energy of the particle E [27].

CHAPTER 4

Spin Dynamics in a Storage Ring

In addition to the description of the particle motion, the description of the spin motion is necessary for a storage ring EDM experiment. The spin motion is strongly coupled to the particle motion, which is referred to as *spin-orbit-coupling*. This chapter discusses the properties related to the particle spin, the general spin motion in a storage ring, and the effect of different spin manipulation devices on the spin.

4.1 Polarization Formalism

Polarization is the beam property that provides access to the particle spin. It is defined as the average spin orientation of a particle ensemble:

$$\vec{P} = \frac{1}{N} \sum_{i=1}^{N} \vec{S}_{\mathrm{i}}. \tag{4.1}$$

The formalism is very different for spin-$\frac{1}{2}$ particles such as protons and spin-1 particles such as deuterons. Therefore, the formalism for both types of particles will be discussed below [34].

4.1.1 Spin-$\frac{1}{2}$ Particles

The spin state of a single spin-$\frac{1}{2}$ particle can be expressed by the Pauli spinor ψ, where the two possible spin states of spin-$\frac{1}{2}$ particles correspond to the spinor components ψ_{i} [36]:

$$\psi = \begin{pmatrix} \psi_1 \\ \psi_2 \end{pmatrix}. \tag{4.2}$$

Each observable spin is associated with a Hermitian operator, which is also the case for spin-$\frac{1}{2}$ particles. A useful tool for describing this operator are the Pauli spin operators extended by the identity matrix σ_0. They form a complete basis of the Hermitian 2x2 matrices [36]:

$$\hat{\vec{S}} = \frac{\hbar}{2}\vec{\sigma}, \tag{4.3}$$

$$\vec{\sigma} = \begin{pmatrix} \sigma_1 \\ \sigma_2 \\ \sigma_3 \end{pmatrix} \quad \text{with} \quad \sigma_1 = \begin{pmatrix} 0 & 1 \\ 1 & 0 \end{pmatrix}, \quad \sigma_2 = \begin{pmatrix} 0 & -i \\ i & 0 \end{pmatrix}, \quad \sigma_3 = \begin{pmatrix} 1 & 0 \\ 0 & -1 \end{pmatrix}. \tag{4.4}$$

An observable is defined as the expectation value $\langle A \rangle$ of the associated operator $\hat{A}$. This leads to a dependence on the density matrix ρ as shown below [36]:

$$\langle A \rangle = \langle \psi^\dagger | \hat{A} | \psi \rangle = \mathrm{Tr} \rho \hat{A}, \tag{4.5}$$

$$\text{with} \quad \rho = |\psi\rangle\langle\psi| = \begin{pmatrix} |\psi_1|^2 & \psi_1 \psi_2^* \\ \psi_1^* \psi_2 & |\psi_2|^2 \end{pmatrix}. \tag{4.6}$$

In the case of a single spin $\frac{1}{2}$ particle, the density function based on Equation (4.3) is in terms of the Pauli spin operators [36]:

$$\langle \hat{\vec{S}} \rangle = \frac{\hbar}{2} \mathrm{Tr} \rho \vec{\sigma}, \tag{4.7}$$

$$\rho = \frac{1}{N} \begin{pmatrix} \sum_{i=1}^N |\psi_1^{(i)}|^2 & \sum_{i=1}^N \psi_1^{(i)} \psi_2^{(i)*} \\ \sum_{i=1}^N \psi_1^{(i)*} \psi_2^{(i)} & \sum_{i=1}^N |\psi_2^{(i)}|^2 \end{pmatrix} = \frac{1}{2}(\sigma_0 + \vec{P}\vec{\sigma}). \tag{4.8}$$

An ensemble of N particles with a quantization state $m = +\frac{1}{2}$ and N with a quantization state $m = -\frac{1}{2}$ in a beam will have a vector polarization according to Equation (4.9). One speaks of a fully polarized beam if $P_\mathrm{V} = \pm 1$ and of a fully unpolarized beam if $P_\mathrm{V} = 0$ [34].

$$P_\mathrm{V} = \frac{N^{m=+\frac{1}{2}} - N^{m=-\frac{1}{2}}}{N^{m=+\frac{1}{2}} + N^{m=-\frac{1}{2}}} \tag{4.9}$$

4.1.2 Spin-1 Particles

Similar to a spin-$\frac{1}{2}$ particle the spin state of a single spin-1 particle can be expressed by the Pauli spinor [36]:

$$\psi = \begin{pmatrix} \psi_1 \\ \psi_2 \\ \psi_3 \end{pmatrix}. \tag{4.10}$$

The three different spin states along the quantization axis correspond to the three spinor components ψ_i. To characterize a spin-1 system, a minimum set of nine independent Hermitian matrices is required. Taking into account the 3x3 identity matrix $\widehat{S}_0$ and the basic spin-1 operators, defined by:

$$\widehat{S}_1 = \frac{\hbar}{\sqrt{2}} \begin{pmatrix} 0 & +1 & 0 \\ +1 & 0 & +1 \\ 0 & +1 & 0 \end{pmatrix}, \quad \widehat{S}_2 = \frac{\hbar}{\sqrt{2}} \begin{pmatrix} 0 & -i & 0 \\ +i & 0 & -i \\ 0 & +i & 0 \end{pmatrix}, \quad \widehat{S}_3 = \hbar \begin{pmatrix} +1 & 0 & 0 \\ 0 & 0 & 0 \\ 0 & 0 & -1 \end{pmatrix}, \tag{4.11}$$

at least five more matrices are needed to complete the set. In principle, the nine second order tensors constructed by the outer product can be used as a basis for the 3x3 Hermitian operators. For simplicity, however, the commonly used operators $\widehat{S}_0, \widehat{S}_1, \widehat{S}_2, \widehat{S}_3$ should be retained. The standard Cartesian notation is based on the ten operators shown below [36]:

$$\widehat{S}_0, \widehat{S}_1, \widehat{S}_2, \widehat{S}_3, \widehat{S}_\mathrm{ij} = \frac{3}{2}(\widehat{S}_\mathrm{i}\widehat{S}_\mathrm{j} + \widehat{S}_\mathrm{j}\widehat{S}_\mathrm{i}) - 2\widehat{S}_0\delta_\mathrm{ij}, \quad i,j \in 1,2,3 \tag{4.12}$$

Analogous to Equation (4.7) the expectation value $\langle\widehat{\vec{S}}\rangle$ depends on the density function ρ. In case of a spin-1 particle the density function does look as follows [36]:

$$\rho = \frac{1}{3}\left[\widehat{S}_0 + \frac{3}{2}\sum_{i=1}^{3} P_\mathrm{i}S_\mathrm{i} + \frac{1}{3}\sum_{i=1}^{3}\sum_{i=j}^{3} P_\mathrm{ij}S_\mathrm{ij}\right], \quad \text{with} \quad P_\mathrm{ij} = P_\mathrm{ji}. \tag{4.13}$$

Considering the three particular quantization states of spin-1 particles, a vector polarization P_V and a tensor polarization P_T along the quantization axis can therefore be defined via [34]:

$$P_{\mathrm{V}} = \frac{N^{m=+1} - N^{m=-1}}{N^{m=1} + N^{m=0} + N^{m=-1}}, \tag{4.14}$$

$$P_{\mathrm{T}} = \frac{N^{m=+1} + N^{m=-1} - 2N^{m=0}}{N^{m=+1} + N^{m=0} + N^{m=-1}}. \tag{4.15}$$

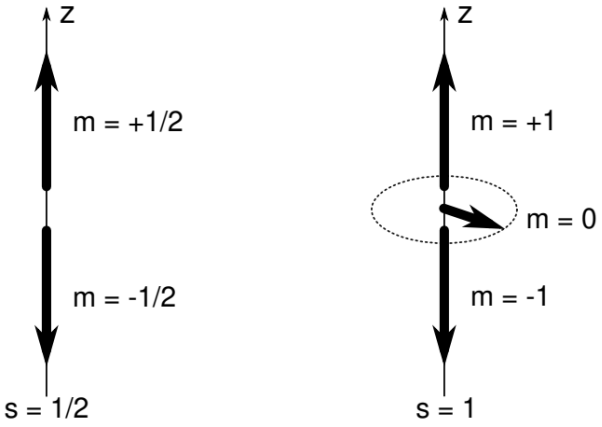

Figure 4.1: Sketch of the possible spin states for a spin-$\frac{1}{2}$ particle like the proton and a spin-1 particle like the deuteron. The spin-$\frac{1}{2}$ particle with $s = \frac{1}{2}$ shown on the left has two different spin states, while the spin-1 particle shown on the right has three. The quantization axis is chosen to be the z-axis. Taken from [35].

4.2 Generalized Thomas-BMT Equation

After the general definition of spin and polarization it is necessary to describe the effect of electric $\vec{E}$ and magnetic $\vec{B}$ fields on these properties. Since these fields are also the ones experienced by the spin inside the storage ring, the evolution of the spin in the center of mass system of the particle depends on their interaction with the EDM $\vec{d}$ and MDM[1] $\vec{\mu}$. This is summarized by [37]:

$$\frac{d\vec{S}}{dt} = \vec{\Omega} \times \vec{S} = \vec{\mu} \times \vec{B} + \vec{d} \times \vec{E}. \tag{4.16}$$

Transforming both electromagnetic fields into the curvilinear laboratory reference system of a storage ring, leads to the so called Thomas-BMT (**B**argmann-**M**ichel-**T**elegdi) equation [38, 39]:

$$\frac{d\vec{S}}{dt} = \vec{\Omega} \times \vec{S} = \vec{\Omega}_{\mathrm{MDM}} \times \vec{S} + \vec{\Omega}_{\mathrm{EDM}} \times \vec{S}, \tag{4.17}$$

[1] See also Equation (2.5) and Equation (2.6)

$$\text{with} \quad \vec{\Omega}_{\text{MDM}} = -\frac{q}{m}\left[\left(G+\frac{1}{\gamma_0}\right)\vec{B} - \frac{G\gamma_0}{\gamma_0+1}(\vec{\beta}\cdot\vec{B})\vec{\beta} - \left(G+\frac{1}{\gamma_0+1}\right)\vec{\beta}\times\frac{\vec{E}}{c}\right], \tag{4.18}$$

$$\text{and} \quad \vec{\Omega}_{\text{EDM}} = -\frac{q}{mc}\frac{\eta_{\text{EDM}}}{2}\left[\vec{E} - \frac{\gamma_0}{\gamma_0+1}(\vec{\beta}\cdot\vec{E})\vec{\beta} + c\vec{\beta}\times\vec{B}\right]. \tag{4.19}$$

It is important to note that the spin vector is defined in the rest frame of the particle, unlike the electric and magnetic fields which are evaluated in the curvilinear laboratory reference frame. In the following, the spin motion is discussed under the assumption of a vanishing EDM, since the MDM contribution to the spin motion is dominant. Section (5.2.4) will illustrate how the EDM contribution to the spin motion can be investigated. In terms of particle motion, the electromagnetic fields can be decomposed into parallel and perpendicular contributions with respect to the design orbit [39]:

$$\vec{\Omega}_{\text{MDM}} = \quad \vec{\Omega}_{\text{B}_\perp} + \vec{\Omega}_{\text{B}_\parallel} + \vec{\Omega}_{\text{E}_\perp} \tag{4.20}$$

$$= \quad -\frac{q}{\gamma_0 m}\left[(1+\gamma_0 G)\vec{B}_\perp + (1+G)\vec{B}_\parallel - \left(G\gamma_0 + \frac{\gamma_0}{\gamma_0+1}\right)\vec{\beta}\times\frac{\vec{E}}{c}\right]. \tag{4.21}$$

The momentum of a particle $\vec{p}$ itself precesses under the influence of electromagnetic fields in a storage ring. Therefore, the relative orientation of spin to the particles momentum has to be identified by using the *cyclotron frequency* Ω_{Cyc}, given by [39]:

$$\frac{d\vec{p}}{dt} = \vec{\Omega}_{\text{Cyc}} \times \vec{p}, \tag{4.22}$$

$$\vec{\Omega}_{\text{Cyc}} = -\frac{q}{\gamma_0 m}\left(\vec{B}_\perp - \frac{1}{\beta_0^2}\vec{\beta}\times\frac{\vec{E}}{c}\right). \tag{4.23}$$

The relative spin precession $\vec{\Omega}_{\text{MDM,Rel}}$ is then derived from the difference between the spin rotation due to MDM and the spin rotation due to the total particle momentum rotation [39, 40]:

$$\vec{\Omega}_{\mathrm{MDM,Rel}} = \vec{\Omega}_{\mathrm{MDM}} - \vec{\Omega}_{\mathrm{Cyc}} \tag{4.24}$$

$$= -\frac{q}{\gamma_0 m}\left[G\gamma_0\vec{B}_\perp + (1+G)\vec{B}_\parallel - \left(G\gamma_0 - \frac{\gamma_0}{\gamma_0^2-1}\right)\vec{\beta}\times\frac{\vec{E}}{c}\right]. \tag{4.25}$$

In principle, one can easily observe the effect of an EDM on the spin motion by suppressing any contribution of the MDM to the spin rotation with $\vec{\Omega}_{\mathrm{MDM,Rel}} \stackrel{!}{=} 0$ This is commonly referred to as the *Frozen Spin Method*. Unfortunately, in a classical pure magnetic storage ring, it is not possible to achieve a configuration that satisfies this criterion, although it is mathematically possible. The reason is that a vertical magnetic field from the dipoles $\vec{B}_\perp$ is needed to keep a particle inside the storage ring [41, 42]:

$$G\gamma_0\vec{B}_\perp \stackrel{!}{=} 0. \tag{4.26}$$

However, in a storage ring with purely electrical bending elements, the criteria for frozen spin can be satisfied by [41, 42]:

$$\left(G\gamma_0 - \frac{\gamma_0}{\gamma_0^2-1}\right) = 0 \quad \Rightarrow \quad p_{\mathrm{Mag}} = \frac{mc}{\sqrt{G}}. \tag{4.27}$$

This is possible when the stored particle reaches its so-called *magic momentum* p_{Mag}, which depends on the properties of the particle itself. This limits the set of elementary particles where frozen spin can be achieved, since only a positive G can lead to frozen spin. Another way to achieve frozen spin in a storage ring is to use combined fields in the bending elements. Using combined fields it does no longer matter whether particles with positive or negative G are stored, as long as the required field magnitudes can be achieved [41, 42]:

$$\vec{E}_{\mathrm{x}} = \frac{\gamma_0 m\beta_0^2}{qR}\frac{1}{\left(\frac{1}{\gamma_0^2-1} - G\right)\frac{\beta_0^2}{G}+1}, \tag{4.28}$$

$$\vec{B}_{\mathrm{y}} = \frac{\gamma_0 m\beta_0^2}{qR}\frac{\left(\frac{1}{\gamma_0^2-1} - G\right)}{\left(\frac{1}{\gamma_0^2-1} - G\right)\frac{\beta^2}{G}+1}\frac{\beta_0}{G}. \tag{4.29}$$

Since no frozen spin can be achieved in a classical storage ring, another property is needed to study the EDM. Since, $\vec{\Omega}_{\mathrm{MDM}}$ is perpendicular $\vec{\Omega}_{\mathrm{EDM}}$ a non-vanishing EDM tilts the spin rotation axis in the radial direction. This is indicated by Figure (4.2). The tilt angle

is described by the ratio of the EDM and MDM contributions:

$$\phi_{\mathrm{EDM}} = \arctan\left(\frac{\eta_{\mathrm{EDM}}\beta_0}{2G}\right). \tag{4.30}$$

In addition to the EDM other ring properties also tilt the spin precession axis. To show their impact on the spin precession axis the spin transfer matrix formalism has to be introduced.

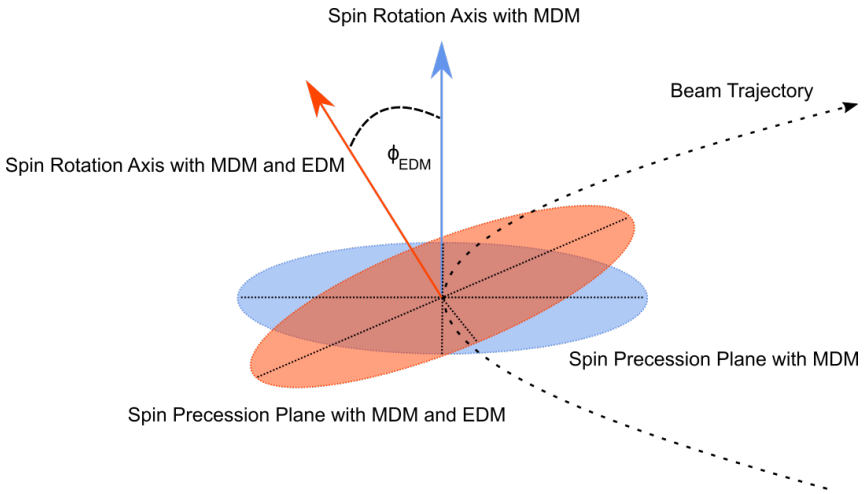

Figure 4.2: Sketch of the radial tilt of the spin precession axis by an existing EDM signal. The blue plane and arrow indicate the spin precession plane and axis with MDM contribution, while the orange plane and arrow assumes the existance of an EDM in parallel, giving the spin rotation axis a constant radial tilt angle ϕ_{EDM}.

4.3 Spin Transfer Matrix Formalism

Similar to the particle transfer matrix formalism in Section (3.3.5) a spin transfer matrix formalism can be defined. It utilizes the matrix $\mathbf{T}$ to describe the change of the spin vector $\vec{S}$ in between two positions θ_{i} and θ_{j} inside a storage ring caused by one element:

$$\vec{S}(\theta_{\mathrm{j}}) = \mathbf{T}(\theta_{\mathrm{j}}, \theta_{\mathrm{i}}) \cdot \vec{S}(\theta_{\mathrm{i}}). \tag{4.31}$$

Since the Pauli Matrices σ_i supplemented by the identity matrix σ_0 form a complete basis of the Hermitian 2x2-matrices, a spin transfer matrix can be parametrized as follows:

$$\begin{aligned}\mathbf{T} &= \sigma_0 t_0 + i\sigma_1 t_1 + i\sigma_2 t_2 + i\sigma_3 t_3 \\ &= \begin{pmatrix} t_0^2 + t_1^2 - t_2^2 - t_3^2 & 2(t_1 t_2 - t_0 t_3) & 2(t_1 t_3 + t_0 t_2) \\ 2(t_1 t_2 + t_0 t_3) & t_0^2 - t_1^2 + t_2^2 - t_3^2 & 2(t_2 t_3 - t_0 t_1) \\ 2(t_1 t_3 - t_0 t_2) & 2(t_2 t_3 + t_0 t_1) & t_0^2 - t_1^2 - t_2^2 + t_3^2 \end{pmatrix}. \end{aligned} \tag{4.32}$$

Based on the Thomas-BMT equation and depending on the orbit, the values t_i can be determined for each element. Passing through more than one element is realized by multiplying the matrices of the elements passed. Since the forces in a storage ring act periodically on a closed orbit, a *one turn matrix* $\mathbf{T}_\mathrm{OT} = \mathbf{T}(\theta_{\mathrm{i}+2\pi}, \theta_\mathrm{i})$ can be defined. At each position inside the ring an eigenvector of this matrix can be constructed. This eigenvector $\vec{n}$ is called the *invariant spin axis*, while the rotation around this eigenvector is named *spin tune* ν_s [43, 44]:

$$\vec{n} = \frac{1}{\sqrt{1 - T(\theta_{\mathrm{i}+2\pi}, \theta_\mathrm{i})^2}} \begin{pmatrix} \pm T_\mathrm{x}(\theta_{\mathrm{i}+2\pi}, \theta_\mathrm{i}) \\ \pm T_\mathrm{y}(\theta_{\mathrm{i}+2\pi}, \theta_\mathrm{i}) \\ \pm T_\mathrm{z}(\theta_{\mathrm{i}+2\pi}, \theta_\mathrm{i}) \end{pmatrix}. \tag{4.33}$$

4.3.1 Dipole influence on the Invariant Spin Axis

In the following, the invariant spin axis and the spin tune are briefly discussed in some special cases. Assuming that the only field a particle experiences during a revolution in the storage ring is the dipole field, Equation (4.25) can be used to set up a one-turn matrix:

$$\mathbf{T}_\mathrm{OT} = \mathbf{T}_\mathrm{Dip} = \begin{pmatrix} \cos(2\pi\gamma_0 G) & 0 & \sin(2\pi\gamma_0 G) \\ 0 & 1 & 0 \\ -\sin(2\pi\gamma_0 G) & 0 & \cos(2\pi\gamma_0 G) \end{pmatrix} \tag{4.34}$$

This one-turn matrix results from the fact that a dipole rotates the ISA on the design orbit only around its vertical axis. If the particle spin has an orientation in the accelerator plane, each individual dipole magnet rotates the spin vector by an amount $\gamma G \cdot \alpha$, which correlates with the rotation angle α of the dipole magnet. The spin tune can now be determined over a full revolution as follows:

$$\mathrm{Tr}(\mathbf{T}_\mathrm{OT}) = 2\cos(2\pi\gamma_0 G) + 1 \tag{4.35}$$

$$\Rightarrow \nu_\mathrm{s} = \gamma_0 G = \nu_{\mathrm{s},0}. \tag{4.36}$$

As the rotation of the dipoles on the spin tune is dominant over all other rotations, which will now be discussed, and also necessary, to keep a particle in the storage, Equation (4.36) defines the reference spin tune $\nu_{s,0}$. As mentioned above, the position dependent eigenvector can be determined from the transfer matrix for the spin over the whole ring. Under the assumption that only dipole magnets influence the beam, this is constant and points purely in the vertical direction, indicated by:

$$\text{Eigenvector: } \vec{n} = \begin{pmatrix} 0 \\ 1 \\ 0 \end{pmatrix} = \vec{n}_0 \tag{4.37}$$

A purely vertically aligned invariant spin rotation axis therefore reflects the idealized invariant spin axis orientation $\vec{n}_0$. If the closed orbit is perturbed and thus deviates from the design orbit, the invariant spin axis will be tilted. The effects of this will be discussed later in this thesis. The remainder of this chapter deals with so-called spin manipulators on a perfect design orbit in order to neglect the effects of a perturbed orbit.

4.3.2 Solenoid Influence on the Invariant Spin Axis

A solenoid is such a spin manipulator. It has a longitudinal magnetic field $\vec{B}_{\parallel} = B_z$ and therefore does not perturb the orbit if its magnetic field is completely parallel to the particle beam. In contrast to a dipole magnet, a solenoid causes a rotation χ_{Sol} around the horizontal spin axis as shown by:

$$\mathbf{T}_{\text{Sol}} = \begin{pmatrix} +\cos(\chi_{\text{Sol}}) & +\sin(\chi_{\text{Sol}}) & 0 \\ -\sin(\chi_{\text{Sol}}) & +\cos(\chi_{\text{Sol}}) & 0 \\ 0 & 0 & 1 \end{pmatrix}, \tag{4.38}$$

$$\text{with } \chi_{\text{Sol}} = \frac{q(1+G)}{\gamma_0 m} \int B_z dl. \tag{4.39}$$

In order to construct the one turn matrix for a solenoid, the influence of the dipole magnets must be taken into account. However, since a solenoid only acts at one point in the storage ring, the new one-turn matrix for the solenoid can be calculated directly by multiplying the solenoid spin transfer matrix and the one-turn matrix for the dipoles:

$$\mathbf{T}_{\mathrm{OT}} = \mathbf{T}_{\mathrm{Sol}} \cdot \mathbf{T}_{\mathrm{Dip}} = \begin{pmatrix} +\cos(\chi_{\mathrm{Sol}})\cos(2\pi\gamma_0 G) & +\sin(\chi_{\mathrm{Sol}}) & +\cos(\chi_{\mathrm{Sol}})\sin(2\pi\gamma_0 G) \\ -\sin(\chi_{\mathrm{Sol}})\cos(2\pi\gamma_0 G) & +\cos(\chi_{\mathrm{Sol}}) & +\sin(\chi_{\mathrm{Sol}})\sin(2\pi\gamma_0 G) \\ -\sin(2\pi\gamma_0 G) & 0 & +\cos(2\pi\gamma_0 G) \end{pmatrix}. \tag{4.40}$$

The presence of the solenoid changes both the spin tune, given by Equation (4.42), and the invariant spin axis, given by Equation (4.43). Due to the rotation of the invariant spin axis at the position of the solenoid, it now depends on the position θ in the ring, so that both the solenoid and the dipoles affect its tilt from the vertical axis.

$$\mathrm{Tr}(\mathbf{T}_{\mathrm{OT}}) = \cos(\chi_{\mathrm{Sol}})\cos(2\pi\gamma_0 G) + \cos(\chi_{\mathrm{Sol}}) + \cos(2\pi\gamma_0 G) \tag{4.41}$$

$$\Rightarrow \nu_{\mathrm{s}} = \arccos\left(\cos\left(\frac{\chi_{\mathrm{Sol}}}{2}\right)\cos(\pi\gamma_0 G)\right) \tag{4.42}$$

$$\text{Eigenvector: } \vec{n}(\theta) = \frac{1}{\sqrt{1-\cos^2(\pi\gamma_0 G)\cos^2\left(\frac{\chi_{\mathrm{Sol}}}{2}\right)}} \begin{pmatrix} \sin(\chi_{\mathrm{Sol}}/2)\sin((\pi-\theta)\gamma_0 G) \\ \cos(\chi_{\mathrm{Sol}}/2)\sin(\pi\gamma_0 G) \\ \sin(\chi_{\mathrm{Sol}}/2)\cos((\pi-\theta)\gamma_0 G) \end{pmatrix} \tag{4.43}$$

4.3.3 RF Wien Filter Influence on the Invariant Spin Axis

Finally, the so-called RF (**R**adio **F**requency) Wien filter will be discussed at this point. The concept of this spin manipulator for measuring the tilt of the invariant spin axis will be neglected for the time being and moved to Section (5.2.4). Only its direct influence on ISA and Spin Tune will be discussed here. As the name suggests, the RF Wien filter is a device that periodically changes its electromagnetic fields. This is a vertically oriented magnetic field $B_{\perp} = B_{\mathrm{y}}$ and a radially oriented electric field $E_{\perp} = E_{\mathrm{x}}$. The strength of the fields is set so that there is no perturbation of the particle beam[2] is caused by this device. Similar to a dipole, the RF Wien filter thus causes the spin to rotate around the vertical axis:

$$\mathbf{T}_{\mathrm{WF}} = \begin{pmatrix} \cos(\chi_{\mathrm{WF}}) & 0 & \sin(\chi_{\mathrm{WF}}) \\ 0 & 1 & 0 \\ -\sin(\chi_{\mathrm{WF}}) & 0 & \cos(\chi_{\mathrm{WF}}) \end{pmatrix}, \tag{4.44}$$

[2] See Lorentz force in Equation (3.1). This also reflects an idealized assumption, as will be shown later.

$$\text{with} \quad \chi_{\mathrm{WF}} = \frac{q}{\gamma_0 m}\left(\gamma_0 G \int B_{\mathrm{y}} dl - \left(\gamma_0 G - \frac{\gamma_0}{\gamma_0^2 - 1}\right)\frac{\beta_0}{c}\int E_{\mathrm{x}} dl\right). \tag{4.45}$$

In addition, the dipoles must also be taken into account for the RF Wien filter to construct the one-turn matrix, which is defined by:

$$\mathbf{T}_{\mathrm{OT}} = \mathbf{T}_{\mathrm{WF}} \cdot \mathbf{T}_{\mathrm{Dip}} = \begin{pmatrix} +\cos(2\pi\gamma_0 G + \chi_{\mathrm{WF}}) & 0 & +\sin(2\pi\gamma_0 G + \chi_{\mathrm{WF}}) \\ 0 & 1 & 0 \\ -\sin(2\pi\gamma_0 G + \chi_{\mathrm{WF}}) & 0 & +\cos(2\pi\gamma_0 G + \chi_{\mathrm{WF}}) \end{pmatrix}. \tag{4.46}$$

Since both the dipoles and the RF Wien filter represent a spin rotation around the vertical axis, the spin tune also results from the sum of both effects, as can be seen in Equation (4.48). The eigenvector thus remains vertically aligned, as given by Equation (4.49), which means that an RF Wien filter does not affect the invariant spin axis itself but the spin tune.

$$\mathrm{Tr}(\mathbf{T}_{\mathrm{OT}}) = 2\cos(2\pi\gamma_0 G + \chi_{\mathrm{WF}}) + 1 \tag{4.47}$$

$$\Rightarrow \nu_{\mathrm{s}} = \gamma_0 G + \frac{\chi_{\mathrm{WF}}}{2\pi} \tag{4.48}$$

$$\text{Eigenvector: } \vec{n} = \vec{n}_0 = \begin{pmatrix} 0 \\ 1 \\ 0 \end{pmatrix} \tag{4.49}$$

CHAPTER 5

Experimental Setup at COSY

The JEDI collaboration aims to determine the EDM in protons and deuterons using a storage ring. A first direct measurement of the deuteron EDM was therefore carried out in the so-called Precursor Runs 1 and 2 at the COSY storage ring in Jülich. This chapter provides an overview of the accelerator complex around COSY (**CO**oler **SY**nchrotron) at the Forschungszentrum Jülich. In addition, a detailed description of the experimental setup utilized for the polarization measurements of the ISA (**I**nvariant **S**pin **A**xis) will be provided.

5.1 The Accelerator Facility COSY

The COSY accelerator facility, located at Forschungszentrum Jülich in Germany, is a large scientific infrastructure, designed to accelerate and store polarized and unpolarized ions. This facility is composed of three essential sections, each playing a distinctive role in the overall particle acceleration process. The first component is the ion source, responsible for generating polarized and unpolarized hydrogen H^-- or deuterium D^--ions. Those ions receive an initial acceleration in the following section, a cyclotron known as JULIC (**JU**elich **L**ight **I**on **C**yclotron). Connected to JULIC via an injection beam line is the storage ring COSY. Marking the last section of the acceleration process, the ions are further accelerated in COSY until reaching their targeted energy. From here, the ion beams will be guided to internal and external experiments. A schematic overview of accelerator facility is provided in Figure (5.1). For a better understanding of the three sections of the COSY accelerator facility, they will be discussed in more detail in the following chapters [45, 46].

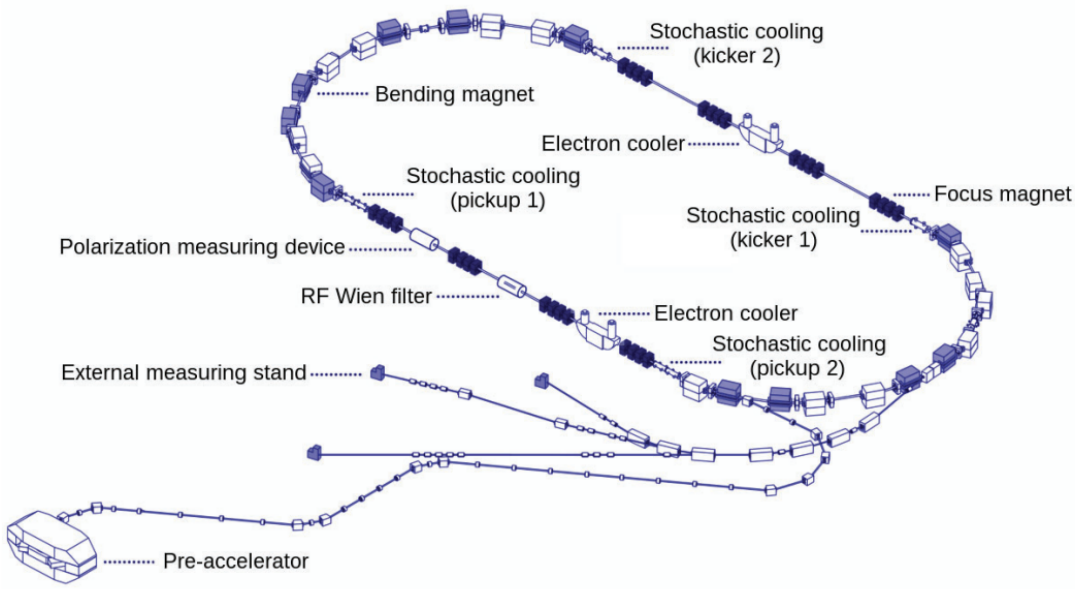

Figure 5.1: Schematic view of the COSY storage ring and the JULIC pre-accelerator. Highlighted are the main magnets, the cooling sections, the radio frequency Wien filter device and a polarimeter. Adapted from [47].

5.1.1 Polarized Beam Source

The ions, which are required for the accelerator experiments, are generated by a CBS (**C**olliding **B**eam **S**ource). It takes advantage of the charge exchange reaction of neutral hydrogen H^0 or deuterium D^0 beams with neutral cesium Cs^0 beams in a collision region [48].

$$H^0/D^0 + Cs^0 \Rightarrow H^-/D^- + Cs^+ \tag{5.1}$$

The neutral hydrogen and deuterium beams are produced in ground state by a dissociator and a cooled nozzle. To receive polarization, the neutral hydrogen/deuterium beams have to pass through two sextupole magnets. Using the inhomogeneous field of the first sextupole magnet, the beam is split by the spin states of the shell electrons. The second sextupole magnet serves as an achromatic lens, focusing the atoms into the collision region. Prior to reaching the ionization region, the electron polarization is converted to nuclear polarization via two RF (**R**adio **F**requency) transition units switching between the hyperfine substates of the atoms. Two available RF transition units allow the selection of desired spin states. After the collision, a Wien filter is utilized to separate the ions from electrons and background, while also aligning the beam polarization with the cyclotron's main magnetic field. This alignment preserves the polarization during the subsequent pre-acceleration process within the cyclotron [49].

5.1.2 The Cyclotron JULIC

Ions originating from the CBS undergo pre-acceleration as they are injected into the cyclotron JULIC. Beam pulses are initiated by a chopper positioned in the beamline between the ion source and the axial injection into the cyclotron. The ion beams from the source are adjusted to align with the RF-phase acceptance of the cyclotron using a combination of a double-gap buncher and a sawtooth buncher. For the injection onto a constant orbit, a Hyperbolic Inflector located near the cyclotron center is utilized. At the end of the acceleration process, the beam is extracted through a septum deflector in the pole gap area, redirecting it into the injection beam line leading to COSY. This extraction process is achieved through multi-turn extraction. Typically, polarized H^--ions are delivered at a kinetic energy of 45 MeV/c for injection into COSY, while polarized D^--ions are delivered at a kinetic energy of 75 MeV/c [46, 50].

5.1.3 The Cooler Synchrotron COSY

Connected to JULIC via a roughly 100 m long transfer beam line is the main synchrotron and storage ring COSY. After traversing the transfer beam line, a stripping injection method is used to shoot the particles into the COSY storage ring. In this process, negatively charged ions pass through a thin foil, resulting in the removal of two electrons. This way, polarized and unpolarized protons or deuterons are stored in COSY. Another feature of this process is the option to stack new injections on top of particles already stored.

Design

The storage ring and synchrotron COSY is designed in a racetrack configuration, comprising two 180° arcs measuring 52 m each and two straight sections with a length of 39.7 m. Consequently, the entire structure has a circumference of approximately 183.4 m. The ion beams within COSY can achieve momenta of up to 3.7 GeV/c. The acceleration occurs within an RF cavity situated in the middle of one of the straight sections. Following the synchrotron principle of COSY, a continuous adjustment of the magnetic bending fields, corresponding to the beam momentum, is necessary. This adjustment is carried out by the dipole magnets in the arcs of COSY. In total, there are 24 normal-conducting dipoles, each generating magnetic fields of up to 1.67 T. Upon reaching the desired energy, the ion beams become available for deployment in internal experiments located at various target positions within the straight sections. Over time, a multitude of experiments, such as ANKE [51], EDDA [52] and the WASA [53] experiments, have been conducted at these internal target locations. Additionally, the beam can also be extracted from the storage ring. Directed along a transfer beam line, the ion beams can be shot on three external measurement stands.

Beam Cooling

The acronym COSY derives from the use of cooling systems based on two different principles. Since 1993, a 100 keV electron cooler has been used to reduce the phase space distribution immediately after injection. The maximum electron energy of 100 keV/c limits the cooling range of the facility to beam energies of about 600 MeV/c for protons and 1200 MeV/c for deuterons. The primary objective of the electron cooler is to increase the intensity of polarized protons by cooling during the stacking process [54]. In addition, a second 2 MeV electron cooler was installed at COSY in 2013, allowing cooling over the entire energy range of COSY [55].

In addition to electron cooling, stochastic cooling is available for both protons and deuterons. The stochastic cooling system for COSY is designed for proton momenta in the range of 1500 MeV/c to 3400 MeV/c. Within COSY, stochastic cooling is regularly used for internal target experiments to achieve equilibrium conditions between target heating and stochastic cooling. The cooling system consists of a 4 m pick-up tank and a 2 m kicker for the horizontal and vertical planes respectively [54].

Ion Optics

To achieve beam focusing, 56 magnetic quadrupoles were installed. They are organized into a total of 14 families, each consisting of four quadrupoles. Within a given family, the magnets share the same dimensions and are connected to a common power supply.

Among these families, eight quadrupole families (MQT1-MQT8) are situated in the straight sections. These families collectively form four triplets (either FDDF or DFFD[1]) within each of the straights. Such a triplet acts an optical lens, as it focuses in the two transverse dimensions. By adjusting the quadrupole strengths to achieve a betatron phase advance of either π or 2π per straight section a telescope configuration is established[2]. Hence, the straight sections are also referred to as the 'Target Telescope' and the 'Cooler Telescope'. When there is a phase advance of 2π, the linear transfer matrix of transverse phase space coordinates within each straight section transforms into a unity matrix [43]. Consequently, in terms of linear optics, the straight sections are ion-optically transparent and do not affect the optical functions in the arc sections. The remaining six quadrupole families (MQU1-MQU6) are located in the arcs, forming six identical mirror-symmetrical unit cells (configuration FODO-OFOD[3]). This arrangement allows for tuning the ion optics in various configurations, as both arcs show mirror symmetry with respect to the center of the straight sections. Therefore, a sixfold symmetry (P = 6) can be established by equally powering each cell. During the polarization experiments described in this thesis, a

[1] F = horizontally focusing quadrupole, D = horizontally defocusing quadrupole
[2] See Equation (3.21) and Equation (3.22) for more information.
[3] O = space (optical elements) in between the quadrupoles

configuration with minimized dispersion in the straights was utilized, to minimize the momentum dependency at the interaction point. The MQU4 family was employed to reduce the dispersion in the straights, while the MQU1/MQU5 and MQU2/MQU6 families were used to preserve both betatron tunes. This adjustment results in a twofold symmetry (P = 2). Both optical settings are illustrated in Figure (5.2) [43].

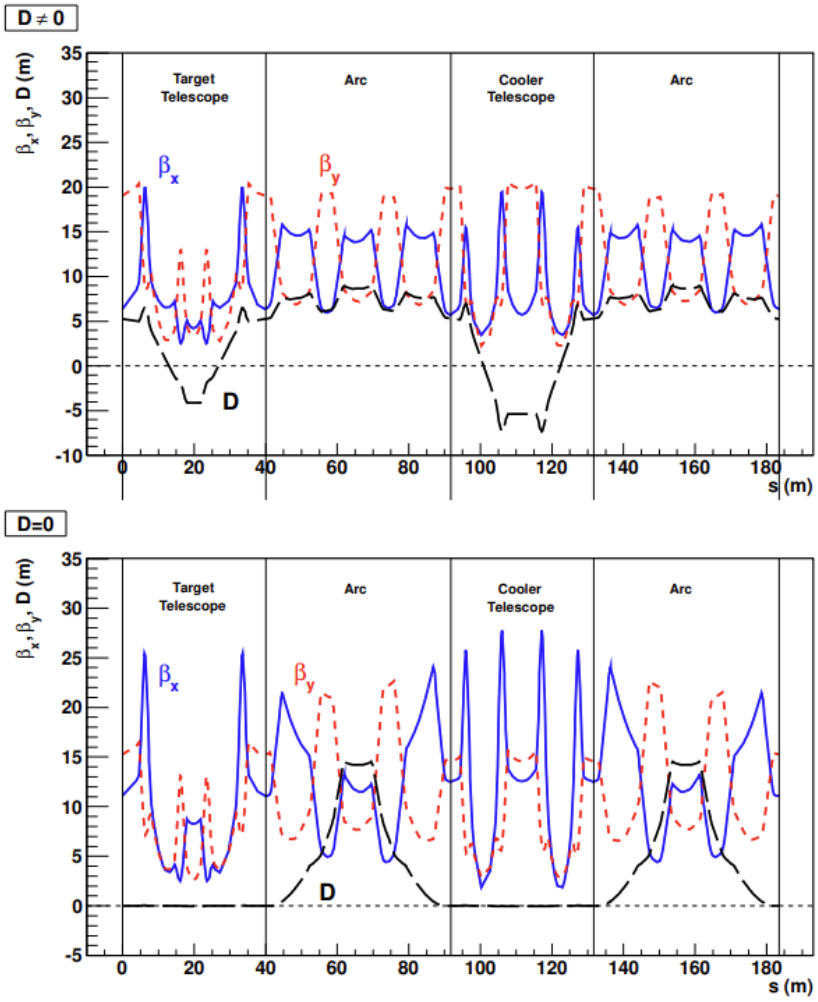

Figure 5.2: Optical functions (β_x, β_y) and dispersion D for two different configurations of COSY. **Top:** Sixfold symmetry, typical used for injection with the arc unit cells behaving symmetrically. **Bottom:** Twofold symmetry with minimized dispersion in the straights. The position of 0 marks the beginning of the straight right after the injection. Taken from [56].

The sextupole magnets represent the highest multipole order implemented at COSY, with a current total of 17 sextupoles installed. Among these, seven sextupole magnets are placed in the straight sections, each powered by an individual power supply. The remaining ten sextupole magnets in the arcs are organized into three families (MXS, MXL, MXG), each sharing a common power supply. While the MXS and MXG sextupole families comprise four magnets each, the MXG sextupole family consists out of two magnets positioned at

the center of the arcs. The sextupoles in the arcs play a crucial role in the chromaticity correction. Their impact on the chromaticity does strongly depend on the optical functions at the sextupole locations. The seven reside in the telescopes are responsible to form the separatrix for the outgoing particles [43, 45]. A sketch of all optical elements forming a family and their position within COSY can be found in Figure (9.1).

Magnet Type	**Groups**	**Location**	**Quantity**
Dipole	no	Arc	24
Quadrupole	MQT1-MQT8	Telescope	32
	MQU1-MQU6	Arc	24
Sextupole	no	Telescope	7
	MXS	Arc	4
	MXL	Arc	4
	MXG	Arc	2

Table 5.1: Overview of optical magnetic elements installed in COSY.

Beam Position Monitors

In order to accurately control the particle beam, it is essential to know the exact position of the beam in relation to the design orbit. Consequently, a total of 30 BPMs (**B**eam **P**osition **M**onitors) are used to track the beam trajectory in both horizontal and vertical planes. The choice of BPM shapes is dictated by the different configurations of the beam pipes in telescopes and arcs. For arcs, a rectangular shape with dimensions of 150 mm $\times$ 60 mm is chosen, while for telescopes a cylindrical shape with a diameter of 150 mm is used [57]. A typical BPM consists of pairs of electrodes, each 130 mm long [45, 58].

With each revolution, the ion beam generates signals at the electrodes. These signals from opposite electrodes are then combined to produce a difference and a sum signal. The ratio of the difference and sum signals is used to determine the position of the beam relative to the center of the BPM. A linear correlation between this ratio and the beam position is established by a diagonal cut in the structure of both rectangular and cylindrical tubes. Figure (5.3) and Figure (5.4) provide visual representations of the cylindrical and rectangular BPM designs [58].

Each BPM contains four plates to measure the amplified and digitized signal in the upper V_{Up}, lower V_{Down}, right V_{Right} and left V_{Left} plates. This configuration allows simultaneous determination of the horizontal x_{BPM} and vertical y_{BPM} beam positions. It is crucial to take into account the geometric factors K_{x} and K_{y} related to the sensor sensitivity, as well as the relative position of the BPMs to the designed beam path x_{Off} and y_{Off}. Equation (5.2) summarizes the measurement principle of the BPMs [59, 60, 61].

$$
\begin{aligned}
x_{\mathrm{BPM}} &= K_{\mathrm{x}} \cdot \frac{V_{\mathrm{Left}} - V_{\mathrm{Right}}}{V_{\mathrm{Left}} + V_{\mathrm{Right}}} + x_{\mathrm{Off}} \\
y_{\mathrm{BPM}} &= K_{\mathrm{y}} \cdot \frac{V_{\mathrm{Up}} - V_{\mathrm{Down}}}{V_{\mathrm{Up}} + V_{\mathrm{Down}}} + y_{\mathrm{Off}}
\end{aligned}
\tag{5.2}
$$

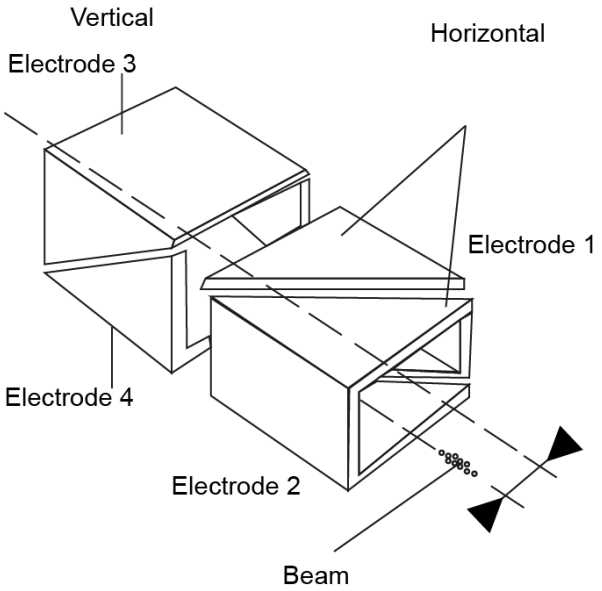

Figure 5.3: Illustration of a conventional rectangular BPM, cut diagonally to separate it into electrodes for position detection in each direction. The signal at electrodes 1 and 2 can be used to determine the horizontal beam position, while the signal at electrodes 3 and 4 can be used to determine the vertical beam position. Adapted from [58].

In addition to the BPMs mentioned above, there are also BPMs with a special geometry inside the beamline. These are in particular the two associated with the 2 MeV electron cooler [55] and the two thin Rogowski coil BPMs near the so-called RF Wien filter [62].

A quantity that usually occurs together with BPMs is the so-called orbit RMS (**R**ooth **M**ean **S**quare). The orbit RMS is defined by the difference between the design orbit and the closed orbit in the horizontal x_{i} and vertical y_{i} phase space at the position of the BPMs in a storage ring as sketched by Equation (5.3).

$$
x_{\mathrm{RMS}} = \sqrt{\frac{1}{N}\sum_{i=1}^{N} x_{\mathrm{i}}^2} \quad \text{and} \quad y_{\mathrm{RMS}} = \sqrt{\frac{1}{N}\sum_{i=1}^{N} y_{\mathrm{i}}^2} \tag{5.3}
$$

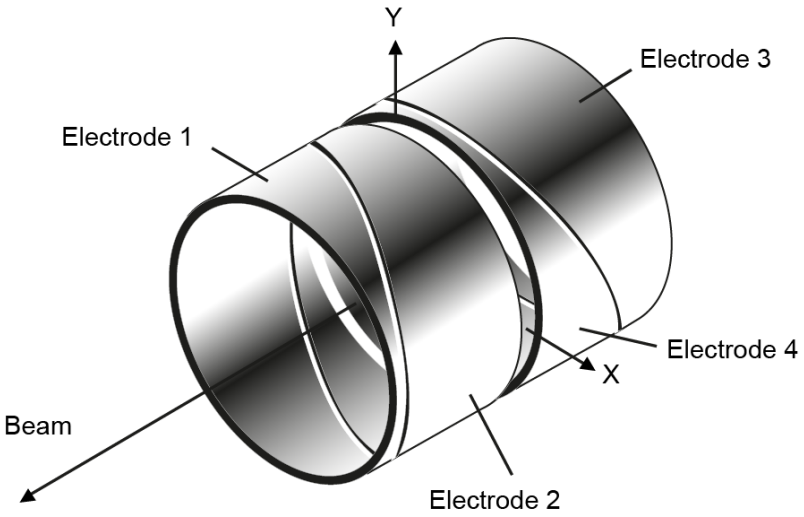

Figure 5.4: Illustration of a conventional split-cylindrical BPM, which is cut diagonally to separate it into two electrodes for position detection in each direction. With the electrodes 1 and 2, also called right and left, one is able to determine the horizontal position of the beam while with electrodes 3 and 4, typically called up and down, work the same way for the vertical direction. Adapted from [63].

Steerer Magnets for Orbit Control

After the BPMs measure the beam's position, it is essential to make corrections. This involves utilizing orbit control software, which uses the measured orbit data and computes the necessary adjustments for the correcting magnets, known as steerers, using the Orbit Response Matrix. For closed orbit corrections 40 steerers are installed. The objective is to achieve the desired orbit by implementing these adjustments in those steerers [45, 64].

There are two approaches for obtaining an Orbit Response Matrix for orbit correction. The simpler method involves calculating the Orbit Response Matrix from the accelerator model. However, for better optimization that reflects the current machine state, a measured Orbit Response Matrix is preferred. In the earlier stages of orbit control software usage, the Orbit Response Matrix was derived from the model due to the absence of a fast automated procedure for measurement. Presently, automated measurement procedures for the Orbit Response Matrix are available, making a measured Orbit Response Matrix the predominant choice for orbit optimization [59].

Once the optimal steerer settings for the desired orbit are determined by the Orbit Response Matrix, they are applied to the machine. Determining these optimal settings involves utilizing SVD (**S**ingular **V**alue **D**ecomposition) to pseudo-invert the Orbit Response Matrix, with the exclusion of small singular values. The cut-off threshold, typically a fixed value, may be selected by the user. The desired orbit change is then multiplied by the inverted Orbit Response Matrix to calculate the necessary steerer adjustments. To avoid beam loss, only a fraction of the calculated change is applied in each step, and the process

is repeated until the orbit is as close as possible to the desired state [31, 59].

5.2 Spin Manipulators in COSY

In addition, several devices are installed in COSY to manipulate and detect the polarization of the bunched ion beam. These devices will be presented in the following sections.

5.2.1 Radiofrequency Solenoid

The COSY injection system provides only vertically polarized protons and deuterons [65]. The RF Solenoid provides a time-dependent longitudinal field to switch from vertical polarization to in-storage plane polarization, where the polarization vector starts to precess around the invariant spin axis [66, 67].

5.2.2 Snake Solenoid

Siberian snakes provide a static longitudinal field and can be used to avoid crossing depolarizing resonances in circular accelerators during the acceleration process. It is also possible to use a Siberian Snake as a spin rotator. In this case, a vertically polarized beam has already been accelerated to the desired energy. The Siberian Snake is switched on after the acceleration process to transfer the vertical polarization to the horizontal plane and to provide longitudinal polarization at the position of the Siberian Snake [65, 68]. Such a Snake Solenoid is implemented in COSY and used to measure the invariant spin axis in two independent ways.

5.2.3 2 MeV Solenoid

Apart from the solenoids deliberately installed in COSY to manipulate the spin and thus the polarization, there are also solenoids with longitudinal fields that mainly serve a different purpose. These include the compensation solenoids of the two electron coolers [54, 55]. In the context of this work, only the compensation solenoid of the 2 MEV cooler plays a role. Its main function is to compensate for the longitudinal magnetic field generated by the electron cooler at both ends of the cooler [55, 69, 70]. Similar to the Snake Solenoid its static longitudinal magnetic field can be used to determine the Invariant Spin Axis.

5.2.4 RF Wien Filter

The so-called RF Wien filter is, as the name suggests, an RF device. It is installed in COSY so that its electric field is radial and the magnetic field is vertical. Both fields are designed so that the Lorentz force on the nominal beam is always zero, despite permanent changes in field strength. This is to avoid perturbation of the closed orbit by the RF Wien filter. The RF Wien filter is thus a pure spin manipulator with the purpose of measuring the radial component of the ISA, which carries information about the magnitude of the

EDM. Since a non-vanishing EDM causes a tilt of the radial ISA and an oscillation of the vertical polarization, one can try to determine these quantities. Unfortunately, the ISA cannot be measured directly. The frequency of the oscillation of the vertical polarization comes from the spin rotation in COSY plane due to the MDM and is therefore given by $f_s = \nu_s f_{Rev} = \gamma G f_{Rev}$. This fast oscillation of the vertical polarization in combination with the amplitude of the oscillation, which becomes very small for protons and deuterons, cause the vertical polarization to average out over time. The RF Wien filter is able to introduce an artificial spin resonance that causes an additional rotation of the spin around the vertical axis, preventing the signal from averaging out. Due to the additional spin kick, a fraction of the vertical polarization is preserved each revolution, resulting in an accumulation of vertical polarization over time. This principle of operation is illustrated in the Figure (5.5) [71, 72].

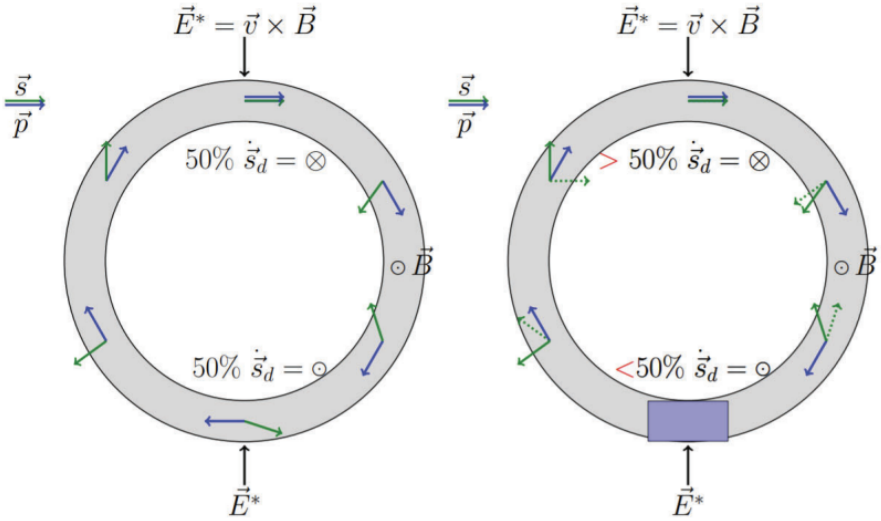

Figure 5.5: Schematic representation of the working principle of the RF Wien filter. While in the left figure the spin $\vec{s}$ (green) precesses freely in the COSY plane and is on average 50% parallel to the direction of motion $\vec{p}$ (blue) and 50% antiparallel to it, the situation changes with the introduction of the RF Wien filter, represented by the blue box in the right figure. The additional spin kick at the RF Wien filter position breaks the symmetry so that the spin vector is no longer 50% parallel and 50% antiparallel to the direction of motion. As a result, some of the vertical polarization remains and accumulates over time.

In order to accumulate the vertical polarization, the RF Wien filter must run at one of the harmonics k_{WF} of the spin precession frequency. Assuming a beam momentum of $p_0 = 970\,\mathrm{MeV/c}$, the revolution frequency of deuterons f_{Rev} in COSY is about 750 kHz. If the $k_{WF} = -1$ harmonic of the precession frequency is chosen, the WF frequency at which the fields must change is $f_{WF} \approx 871\,\mathrm{kHz}$, as shown in Equation (5.4). The values given here correspond to those used during the Precursor Runs, which are further discussed in Section (5.3) [73].

$$f_{\mathrm{WF}} = (1 + k_{\mathrm{WF}}) f_{\mathrm{s}} = (1 + k_{\mathrm{WF}}) \gamma G f_{\mathrm{Rev}} \approx 871\,\mathrm{kHz} \tag{5.4}$$

With the RF Wien filter induced build-up of vertical polarization one measures the relative orientation of the magnetic field axis of the RF Wien filter $\vec{n}_{\mathrm{WF}}$ and the ISA $\vec{n}_{\mathrm{ISA}}$. This can be roughly described by:

$$\begin{aligned} |\vec{n}_{\mathrm{WF}} \times \vec{n}_{\mathrm{ISA}}|^2 &= \left| \begin{pmatrix} \phi_{\mathrm{WF}} \\ 1 \\ 0 \end{pmatrix} \times \begin{pmatrix} \phi_{\mathrm{EDM}} + \phi_{\mathrm{Ring}} \\ 1 \\ \xi_{\mathrm{Sol}} + \xi_{\mathrm{Ring}} \end{pmatrix} \right|^2 \\ &= (\phi_{\mathrm{EDM}} + \phi_{\mathrm{Ring}} - \phi_{\mathrm{WF}})^2 + (\xi_{\mathrm{Sol}} + \xi_{\mathrm{Ring}})^2. \end{aligned} \tag{5.5}$$

As the RF Wien filter can be rotated around the beam by an angle ϕ_{WF} it is used to compensate the radial tilt of the ISA due to ring systematics ϕ_{Ring} and the EDM signal ϕ_{EDM} in parallel. A static solenoid in the opposite straight of the RF Wien filter tilts the longitudinal ISA by ξ_{Sol} and can be used to compensate for the existing ISA tilt due to ring systematics ξ_{Ring}. If both ISA and RF Wien filter are parallel to each other, the build-up of vertical polarization is zero despite the RF Wien filter being switched on. This state must therefore be found. The goal of this thesis is to evaluate ϕ_{Ring} and ξ_{Ring} using simulations and to compare the simulation results to measurement results.

Experimental results have been obtained by the JEDI collaboration, which is carrying out a long-term project to measure the permanent EDM of protons and deuterons in a storage ring. In order to develop the final high-precision experiment, a multi-stage strategy is proposed. The goal of the first step of the strategy is to demonstrate the feasibility of critical technologies for EDM measurement at an already existing facility. For this reason, the so-called *Precursor Runs* 1 and 2 have been carried out at the COSY facility in 2019 and 2021 [25].

5.3 The Precursor Runs

During the Precursor Runs, vertically polarized deuterons with momenta of $p_0 = 970\,\mathrm{MeV/c}$ were stored in the COSY storage ring. By using the RF Solenoid, the vertical polarization was transferred in the storage ring plane. By observing the build-up of vertical polarization induced by the RF Wien filter on a polarimeter, the tilt angle of the ISA was determined. Since, besides the EDM, several systematic effects in the COSY storage ring affect the vertical build-up, a simulation of the experiment is necessary to separate the actual EDM signal from these systematic effects. This was the starting point for the work carried out in this thesis. Since several improvements have been made between Precursor

Run 1 and 2, such as alignment campaigns of the COSY magnet system, the installation of the new JEPO polarimeter or an improved tuning of the RF Wien filter, this work will mainly compare its results with those obtained during Precursor Run 2 [25].

CHAPTER 6

Simulation Model of COSY

In order to fully investigate particle and spin motion, it is crucial to construct a simulation model that accurately represents the real machine and experimental setup during Precursor Run 2. This chapter presents the model created for this thesis and for this purpose.

6.1 BMAD and TAO

The simulations carried out in this thesis use BMAD, a subroutine library used to track charged particles in storage rings. The nomenclature BMAD is derived from the MAD simulation program (now known as MAD-X [74]). Developed at the Laboratory for Elementary Particle Physics at Cornell University, this library of subroutines takes an object-oriented approach and is coded in Fortran (**FOR**mula **TRAN**slation) 90. BMAD has a modular structure to increase flexibility. Its design aims to empower programmers by providing pre-built functions for common tasks such as lattice file parsing and particle tracking, reducing the need to code such functions from scratch. Using the BMAD subroutine library streamlines program development, saving time and minimizing programming errors. BMAD enables the study of single and multiple particle beam and spin dynamics. It provides tracking algorithms, including Runge-Kutta [76], PTC (**P**olymorphic **T**racking **C**ode) [75] and symplectic integration. It also provides various routines for calculating transfer matrices, emittances, Twiss parameters, dispersion and more. BMAD is equipped to handle elements such as quadrupoles, RF cavities, solenoids, dipole bends, etc. In addition, elements can be defined to control the attributes of other elements [77].

During the development of BMAD it became apparent that many simulation programs have common requirements such as data plotting and machine parameter display. As mentioned above, the advantage of BMAD over a stand-alone simulation program is the

streamlined development process. However, a disadvantage of BMAD is that, as a toolkit, it is not possible to perform calculations without first developing a program. To overcome this limitation, the program TAO (**T**ool for **A**ccelerator **O**ptics) was developed using the BMAD software library. TAO provides functions such as viewing lattices, performing Twiss and orbit calculations, and non-linear optimization on these lattices and their parameter. In addition, TAO's object-oriented design makes it relatively easy to extend its functionality. In the course of this thesis, TAO was frequently used for these tasks [78].

BMAD offers several calculation methods for tracking a particle through a lattice element. These methods are able to determine the phase space or spin coordinates at the exit end of the element based on the coordinates at the start. In addition, they define how the linear transfer map through an element is calculated [79]. For consistency, only one calculation method is used for all these tasks. Nevertheless, a selection of calculation methods will be shown in the next section, as they will be discussed later in this thesis in more detail.

6.1.1 Particle Tracking Algorithms

A 'tracking_method' attribute can be set for each element in a BMAD lattice file. This attribute defines the algorithm used to calculate the phase space coordinates at the exit end of an element, based on the coordinates at the start of the same element. Three routines are examined in more detail:

- **Bmad_Standard**: This calculation method uses typical tracking formulas based on a paraxial approximation, with an emphasis on computational speed. Although the tracking is non-symplectic, the non-symplectic errors generally fall within a small regime, allowing the use of Bmad_Standard in the vast majority of cases [79].
- **Runge_Kutta**: Runge_Kutta tracking in BMAD uses the fourth-order Runge-Kutta integration algorithm with adaptive step-size control. Although this method is slower and non-symplectic compared to non-Runge-Kutta methods, it is typically accurate [76, 79].
- **Symp_Lie_PTC**: This approach involves symplectic tracking by using a Hamiltonian with Lie operator techniques. While this method preserves symplecticity, it can have a very slow computational speed [75, 79].

6.1.2 Spin Tracking Algorithms

In addition to specifying the 'tracking_method' attribute, it is necessary to define the 'spin_tracking_method' attribute. Similar to the previous attribute, this parameter determines the algorithm used to calculate the spin orientation at the exit end of an element, based on the spin orientation at the beginning of the same element. Three routines, the same as those discussed before, are examined in more detail:

- **Bmad_Standard**: Regarding spin tracking, the Bmad_Standard method uses Romberg integration of spin rotation matrices for spin tracking [80, 79].
- **Runge_Kutta**: Spin tracking in the Runge_Kutta method uses the same fourth-order integrator used for orbital coordinates to track the spin rotation vector [79, 76].
- **Symp_Lie_PTC**: Similar to particle tracking, the Symp_Lie_PTC tracking method applies symplectic integration using Hamiltonian and Lie operators [75, 79].

6.2 Lattice Model

Originally, a BMAD simulation model of COSY created by V. Poncza [18] and Y. Dutheil [81] served as the initial basis for the BMAD simulation model created for this thesis. However, it became clear that certain modifications were needed for this work, as magnetic elements had been replaced or moved along the storage ring. At that time, the most accurate model with shifted elements already incorporated was the MAD-X simulation model of COSY developed by I. Bekman and J. Hetzel [82, 74]. Using the MAD-X model as a reference, a new BMAD simulation model was created with shifted elements, while retaining most of the characteristics of the old BMAD simulation model. This refined BMAD simulation model subsequently served as the structural framework for the thesis, with ongoing updates and incorporation of new features. The following sections provide a comprehensive overview of the old and new features embedded in the BMAD simulation model of COSY.

6.2.1 Dipole Design

When describing dipole magnets in COSY, one has to distinguish between the physical length of the magnet and the effective field length. While the physical length of the magnet is $L^{\mathrm{Dip}}_{\mathrm{Phy}} = 1.755\,\mathrm{m}$ [83], its effective field length is $L^{\mathrm{Dip}}_{\mathrm{Eff}} = 1.833\,\mathrm{m}$. The C-type dipole magnets are arranged alternately in the ring, with a pattern of alternating joke inside and joke outside the ring. When viewed from above, these dipoles have a rectangular box shape and can also be described as such [84]. Since the MAD-X model and other COSY simulation programs use a sector bend as a starting point for the design of the bending magnets, this behavior was adapted in the design process for the BMAD simulation model. Therefore, a series of 24 sector bends is implemented with a field that produces a bend angle of $\alpha^{\mathrm{Dip}}_0 = 15°$. The entry and exit angles are modified by $\beta^{\mathrm{Dip}}_1 = \beta^{\mathrm{Dip}}_2 = 7.5°$ to give the sector bend the shape of a rectangular bending magnet. The length of the implemented dipole magnet is chosen to be the effective field length of the dipole, as BMAD does not work with the physical elements, but with the field of the elements. If, as in the Precursor Run 2, deuterons with a momentum of $p^{\mathrm{Deu}}_0 = 970\,\mathrm{MeV/c}$ are to be stored in the COSY simulation model, the application of these quantities leads to a dipole field strength of $B^{\mathrm{Dip}}_{\mathrm{y},0} = 0.472\,\mathrm{T}$ and a bending radius of $\rho^{\mathrm{Dip}}_0 = 7\,\mathrm{m}$. By default, the dipole field in BMAD is described by a box field via a hard edge model.

Dipole Fringe Fields

As fringe fields of dipoles can have a significant influence on orbit and optics, the implementation of fringe fields for the dipole magnets is a critical issue in the BMAD simulation model [85]. In contrast to the hard edge model, a fringe field describes a more realistic field profile with an increase in field strength at the entrance region, a constant peak value $B_{\mathrm{y},0}^{\mathrm{Dip}}$ in the center and a decrease in field strength at the exit region of the dipole [86, 87, 88]. In BMAD an implementation of fringe fields can be achieved by adjusting two parameters describing the total fringe field integral F_{Int} and the half pole gap of the dipole H_{Gap} as shown in Equation (6.1). These parameters are directly related to the Enge function $B_{\mathrm{y}}^{\mathrm{Enge}}$ with its coefficients C_i as described in Equation (6.2) [79, 89].

$$F_{\mathrm{Int}} \cdot H_{\mathrm{Gap}} = \int_{\mathrm{Pole}} B_{\mathrm{y}}^{\mathrm{Enge}}(s) \cdot \frac{B_{\mathrm{y},0}^{\mathrm{Dip}} - B_{\mathrm{y}}^{\mathrm{Enge}}(s)}{2 \cdot (B_{\mathrm{y},0}^{\mathrm{Dip}})^2} \tag{6.1}$$

$$B_{\mathrm{y}}^{\mathrm{Enge}}(s) = \frac{B_{\mathrm{y},0}^{\mathrm{Dip}}}{1 + \exp(P(s))}, \qquad \text{with} \qquad P(s) = C_0 + C_1 \cdot s + C_2 \cdot s^2 + \mathcal{O}(s^3) \tag{6.2}$$

This naturally leads to the question of the appropriate values for the parameters F_{Int} and H_{Gap} when characterizing the dipole magnets of COSY. The determination of the half pole gap is straightforward, as the geometric aperture of the dipole is easily quantifiable and has already been documented in design reviews [83, 84]. It is found to be $H_{\mathrm{Gap}} = 0.045\,\mathrm{m}$.

Determining the fringe field integral F_{Int} is a bit more complicated. If the evolution of the dipole field strength and the size of the half-pole gap are known, the fringe field integral can be calculated. This is done by a simulation based on the geometric properties of the COSY dipoles, performed by J. Böker in 2019 [90, 91]. This simulation considers the dipoles BE21 and BE22, as well as the vertical steerer magnet, quadrupole and sextupole between them. The results of the simulation show that the field integral F_{Int} is in the expected range of 0.510 to 0.530, depending on the nearby material. If a dipole is free standing, the magnitude is about 0.530, whereas in the presence of a nearby vertical steerer magnet, the dipole field is shortened, resulting in a reduced fringe field integral of about 0.510. For simplicity, a fringe field integral of a free standing dipole of $F_{\mathrm{Int}} = 0.530$ is assumed for each dipole in the BMAD simulation model of COSY.

Dipole Shortening Effect

Another detail shown by J. Böker's simulation is the reduction of the effective field length of the dipoles due to nearby magnetic material. While the effective field length of a single detached dipole is determined to be $L_{\mathrm{Eff}}^{\mathrm{Dip}} = 1.833\,\mathrm{m}$, the situation changes when the dipole is installed in COSY. The same effect is also discussed by L. Leunissen based on a simulation and measurement in 1997 [92]. In his work he observes that the iron of nearby

steering magnets interacts with the fringe fields of the dipoles and thus shortens the effective length. Using a dipole field strength of $B_{y,0}^{Dip} = 1\,T$, he estimates the shortening to be about 0.26% to 0.34% of the effective length of a dipole, depending on the distance, the type of steering magnet[1] and the direction of steering. He also investigated the effect of a quadrupole on the dipole field. It turns out that this dipole shortening effect due to quadrupoles is negligibly small due to the large distance between quadrupoles and dipoles in the COSY lattice.

In contrast, J. Böcker's simulation assumes a dipole field strength of $B_{y,0}^{Dip} = 0.462\,T$. In his simulation it can be seen that a neighboring sextupole also causes a reduction in the effective field length of a dipole. J. Stein [91] uses J. Böcker's simulation to estimate the shortening of the effective field length of the dipoles due to the sextupoles and steerer magnets in the COSY ring. He finds a much larger reduction in the effective field length of the dipole magnets from 1.07% to 2.60%. This is most likely due to the lower field strength of the dipole magnets. Assuming that only dipoles with sextupoles and steerers in their vicinity are affected by a shortening of their effective fields, a total of 15 dipoles in COSY are affected by a shortening effect. The Table (6.1) shows the 15 dipoles with steerers and sextupoles in their vicinity, including the expected shortening. The shortening effect itself can be summarized as a property of the distance, field shape and geometry of the iron. This effect is also directly related to the reduction of the fringe field integral F_{Int} due to nearby material.

Dipole	**Perturbation Source**	**Expected Shortening**
BE02	MSV10	1.07 %
BE03	MSH11	2.60 %
BE04	MX05	1.07 %
BE05	MSH13	2.60 %
BE06	MSV14 & MX07	1.60 %
BE09	MX09	1.07 %
BE10	MSV18	1.07 %
BE11	MSH19	2.29 %
BE14	MSV30	1.07 %
BE16	MX14	1.07 %
BE18	MSV34 & MX16	1.95 %
BE19	MSH35	2.29 %
BE21	MX18	1.07 %
BE22	MSV38 & MSH39	2.37 %
BE24	MSH41	2.60 %

[1] A distinction is made between the different construction types of steering magnets, namely H-type and C-type .

Table 6.1: Dipoles with steerer magnets (MSV/MSH) and sextupoles (MX) in the vicinity, including the expected shortening calculated by J. Stein based on the simulation by J. Bökers.

There are several ways to model a dipole shortening effect in the BMAD simulation model of COSY. On the one hand, the shortening can be produced by a horizontal steerer of zero length in the dipole center. The passing particle receives a horizontal kick angle $\Delta x'$ from this steerer, which pushes the particle to an outer trajectory, mimicking a shortening of the effective dipole length. On the other hand, BMAD offers the possibility to apply attributes to a dipole, such as an additional horizontal kick[2], or the insertion of a magnetic field error. In terms of particle tracking, all these options are equivalent, as shown by the Equation (6.3), with negligible small deviations. For the BMAD simulation model of COSY, the method of applying a magnetic field error is used [27].

$$\Delta x' = \frac{L_{\mathrm{Eff}}^{\mathrm{Dip}}}{\rho_0^{\mathrm{Dip}} B_{\mathrm{y,0}}^{\mathrm{Dip}}} \cdot B_{\mathrm{Err}}^{\mathrm{Dip}} \tag{6.3}$$

In addition to the shortening effects estimated by J. Stein, M. Hartmann [93] is currently investigating the dipole shortening effect, based on the results of a beam time at the COSY storage ring in 2023. He claims that it is not possible to distinguish the dipole shortening effect from the effects caused by magnet misalignment and the estimated adjustment accuracy of the dipole magnetic fields, which is about 0.5 % of their absolute field. By assuming a shortening in all dipole magnets, he is able to produce a good match between simulated and measured orbits. The shortenings determined by this method are in the same order of magnitude as those determined by J. Stein.

As these systematics strongly influence the horizontal closed orbit, they have to be implemented in the BMAD model of COSY. Initially, the shortenings estimated by J. Stein in Table (6.1) are used for the model. Later in this work they will be redefined as fitting parameters, since it is not possible to distinguish them from other systematic effects. The Table (6.2) provides a overview of the attributes of a dipole magnet, which are introduced in this section and utilized to simulate the Precursor Run 2 in the COSY storage ring via BMAD.

[2] In contrast to the steerer magnet of zero length in the dipole center, this kick is applied along the whole length of the dipole, not just at its center.

Attribute	Magnitude
Effective Length $L_{\mathrm{Eff}}^{\mathrm{Dip}}$	1.833 m
Bending Angle α_0^{Dip}	15°
Entry Angle β_1^{Dip}	7.5°
Exit Angle β_2^{Dip}	7.5°
Magnetic Field $B_{\mathrm{y},0}^{\mathrm{Dip}}$	0.462 T
Bending Radius ρ_0^{Dip}	7 m
Fringe Field Integral F_{Int}	0.530
Half Pole Gap H_{Gap}	0.045 m
Field Error $B_{\mathrm{Err}}^{\mathrm{Dip}}$	individual

Table 6.2: Datasheet of the sector dipole magnet implemented in the BMAD simulation of the COSY lattice for the simulation of the Precursor Run 2.

6.2.2 Quadrupole Design

The design of the quadrupoles in COSY's BMAD simulation model is also not straightforward. There are two main reasons for this. The first reason is that the quadrupole magnets have to be implemented with magnet misalignments to account for systematic effects. These misalignments are given for a specific reference position of the quadrupole. In BMAD this reference position is always the center of the magnet. Unfortunately, the physical reference marks are at the beginning of the quadrupole, as will be shown in Section (6.2.6). In order to implement measured misalignments without additional effort, all quadrupoles are divided into two halves. The reference positions are marked by adding two marker elements, one in front of the first half and one in front of the second half. The two markers and the two dipole halves are supported by a girder structure to transfer misalignments. The reference point of the girder structure is chosen as the marker at the beginning of the quadrupole. This allows the misalignments to be applied to the girder structure, which transfers the misalignments from the marker at the start of the first quadrupole to the individual dipole halves. The mathematical background for this is given in Section (6.2.6). An example of a split quadrupole supported by a girder structure is shown below:

$$\text{Quadrupole: QU01} \Rightarrow \text{QU01: line} =$$
$$\underbrace{(\ \text{QU01\_Marker\_1, QU01\_Half\_1}\ ,\ \text{QU01\_Marker\_2}\ ,\ \text{QU01\_Half\_2}\ )}_{\text{Supported by the girder structure QU01\_Support.}}$$

Another problem is that some of the quadrupoles in the straight sections have corrector windings fitted, which act as steerer magnets when powered. To account for this, steerer magnets are added in the center of the previously explained girder structure where necessary. This is sketched below.

Quadrupole: QT01 ⇒ QT01: line =

(QT01_Marker_1, QT01_Half_1 , QT01_Marker_2, HKicker_01 , QT01_Half_2)

Supported by the girder structure QT01_Support.

As with dipole magnets, a distinction must be made between the physical length and the effective length of quadrupole magnets. There are also two different types of quadrupoles. One is the quadrupole in the straight section QT and the other is the quadrupole in the arc QU. In total there are 32 quadrupoles in the straight section and 24 in the arcs, with four quadrupoles forming a family. Table (6.3) therefore summarizes the main characteristics of all the quadrupoles, while Table (6.4) shows the strengths applied to each quadrupole family to simulate Precursor Run 2 [83].

Attribute	**Magnitude**
QU Physical Length $L^{\mathrm{QU}}_{\mathrm{Phy}}$	0.300 m
QU Effective Length $L^{\mathrm{QU}}_{\mathrm{Eff}}$	0.380 m
QU Families	QU1-QU6
QT Physical Length $L^{\mathrm{QT}}_{\mathrm{Phy}}$	0.570 m
QT Effective Length $L^{\mathrm{QT}}_{\mathrm{Eff}}$	0.650 m
QT Families	QT1-QT8

Table 6.3: Attributes implemented in the BMAD simulation model of COSY for the quadrupole families in the straight section QT and in the arc QU.

Quadrupole Family	**Quadrupole Strength**
QU1	$-0.291997\,\frac{1}{\mathrm{m}}$
QU2	$+0.363592\,\frac{1}{\mathrm{m}}$
QU3	$-0.291997\,\frac{1}{\mathrm{m}}$
QU4	$+0.446509\,\frac{1}{\mathrm{m}}$
QU5	$-0.291997\,\frac{1}{\mathrm{m}}$
QU6	$+0.363592\,\frac{1}{\mathrm{m}}$
QT1	$-0.537464\,\frac{1}{\mathrm{m}}$
QT2	$+0.498917\,\frac{1}{\mathrm{m}}$
QT3	$+0.711981\,\frac{1}{\mathrm{m}}$
QT4	$-0.658880\,\frac{1}{\mathrm{m}}$
QT5	$-0.603644\,\frac{1}{\mathrm{m}}$
QT6	$+0.558404\,\frac{1}{\mathrm{m}}$
QT7	$-0.601440\,\frac{1}{\mathrm{m}}$
QT8	$+0.548490\,\frac{1}{\mathrm{m}}$

Table 6.4: Quadrupole settings of the BMAD simulation model of COSY used to produce sixfold symmetry with minimized dispersion in the straight sections at a deuteron momentum of $p_0^{\mathrm{Deu}} = 970\,\mathrm{MeV/c}$. These settings are used to simulate Precursor Run 2.

A shortening of the effective quadrupole field length has so far not been considered in the BMAD simulation model of COSY. The reason for this is that its effect on the orbit and optic of COSY is expected to be very small and even more difficult to estimate than the shortening effect in the dipoles. The same applies to the fringe field of the quadrupoles. Therefore, a quadrupole fringe field is not implemented in the current model.

6.2.3 Sextupole Design

There are a total of 17 sextupole magnets in the COSY storage ring. These are divided into 10 sextupoles in the arc regions of COSY and 7 sextupoles in the straight sections of COSY. The 10 sextupoles in the arcs together form 3 families, each family having sextupoles of different construction. The four sextupoles of the MXS family are symmetrically located in the outer sections of the arcs, while the four sextuplets of the MXL family are symmetrically distributed further inside the arc. The two sextuplets of the MXG family are located in the center at the apexes of the arcs. The 7 sextupoles in the straights are all identical in construction and are the same as the MXL sextupoles in the arcs. While the sextupoles in the arcs are used to control the chromaticity in COSY, the sextupoles in the straights are used to compensate for the multipole components of the dipoles and quadrupoles. As the sextupoles in the straights were not used during Precursor Run 2 they will be not further discussed. A distinction must also be made between the physical length and the effective field length of the sextupoles. The Table (6.5) shows both lengths, as well as a summary of the sextupole families in the arcs and their settings during Precursor Run 2. By specifying the effective field length and the sextupole field, the sextupoles can be easily implemented in the BMAD simulation of COSY. No systematic effects were deliberately assumed for the sextupole magnets, as these are currently neither known nor considered to have a significant influence on the orbit and optics.

Attribute	Magnitude
MXS Physical Length $L_{\text{Phy}}^{\text{MXS}}$	0.090 m
MXS Effective Length $L_{\text{Eff}}^{\text{MXS}}$	0.140 m
MXS Family Members	4
MXS Position	Outer Arc
MXL Physical Length $L_{\text{Phy}}^{\text{MXL}}$	0.200 m
MXL Effective Length $L_{\text{Eff}}^{\text{MXL}}$	0.243 m
MXL Family Members	4
MXL Position	Inner Arc
MXG Physical Length $L_{\text{Phy}}^{\text{MXG}}$	0.300 m
MXG Effective Length $L_{\text{Eff}}^{\text{MXG}}$	0.328 m
MXG Family Members	2
MXG Position	Center Arc
MXS Sextupole Strength k_2^{MXS}	$+2.48768\,\frac{1}{m^3}$
MXL Sextupole Strength k_2^{MXL}	$-0.38585\,\frac{1}{m^3}$
MXG Sextupole Strength k_2^{MXG}	$+1.14209\,\frac{1}{m^3}$

Table 6.5: Sextupole families in the COSY arcs and settings of the BMAD simulation model of COSY for the simulation of Precursor Run 2.

6.2.4 Steerer Magnets and Calibration

The BMAD simulation model of COSY uses the 'Hkicker' and 'Vkicker' elements to perform orbit corrections analogue to those in the real COSY storage ring. In the real COSY storage ring there are a total of 23 steerer magnets for horizontal orbit control and a total of 20 steerer magnets for vertical orbit control. In the simulation, these are implemented by 23 HKickers and 20 VKickers, which are positioned at identical locations to their real counterparts, but without physical length. The effect of a steerer magnet on the orbit is a change in momentum based on its direction of action and the magnitude of its angle θ_{Kick}. To determine this kick angle from the real COSY storage ring for the simulation, the steerer magnets have to be calibrated.

The aim of calibrating the steerers is to find a coefficient C_{Kick} for each steerer that relates the steerer current $I\%$, given as a percentage of its maximum current, to the angle θ_{Kick}. As this angle depends on the momentum of the particle beam, the calibration coefficients are normalized by the rigidity $B_{\text{y,0}}^{\text{Dip}}\rho_0^{\text{Dip}}$. This is described by Equation (6.4). The calibration coefficients were recalibrated at COSY in the summer of 2020 using the 4-bump method and the ORM method [94]. The results of the campaign are shown in Figure (6.1) and Figure (9.2).

$$C_{\text{Kick}} = \frac{I\%}{\theta_{\text{Kick}} B_{\text{y,0}}^{\text{Dip}} \rho_0^{\text{Dip}}} \tag{6.4}$$

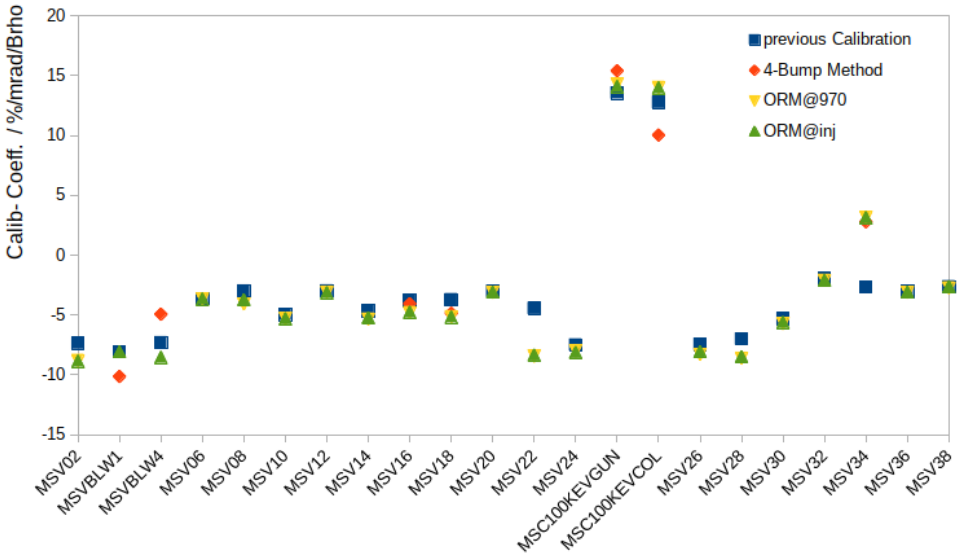

Figure 6.1: Calibration factors for the vertical steerers magnets determined by the 4-bump and ORM method at two different beam energies. The recalibration campaign from summer 2020 is compared with the previously determined calibration factors. Taken from [94].

Based on the calibration factors, the kick angles θ_{Kick} can be determined for the Precursor Run 2 in spring 2021. Their values are listed individually for each steerer in the Table (6.6). Here, a positive kick for a horizontal steerer pushes a particle to an outer trajectory, while a negative kick pushes it to an inner trajectory. Similarly, a positive kick for a vertical steerer pushes a particle upwards, while a negative kick pushes the particle beam downwards.

HKicker	Steerer Kick θ_{Kick}	VKicker	Steerer Kick θ_{Kick}
MSH01	+0.222 mrad	MSV02	−0.089 mrad
MSHBLW2	+0.057 mrad	MSVBLW1	+0.043 mrad
MSHBLW3	+0.114 mrad	MSVBLW4	−0.058 mrad
MSH05	+0.050 mrad	MSV06	−0.123 mrad
MSH07	−0.239 mrad	MSV08	−0.035 mrad
MSH09	+0.184 mrad	MSV10	+0.023 mrad
MSH11	−0.244 mrad	MSV12	+0.058 mrad
MSH13	−0.394 mrad	MSV14	−0.054 mrad
MSH17	+0.890 mrad	MSV16	−0.111 mrad
MSH19	−0.332 mrad	MSV18	+0.053 mrad
MSH21	+0.060 mrad	MSV20	+0.063 mrad
MSH23	+0.267 mrad	MSV22	−0.016 mrad
MSHBLWD1	−1.722 mrad	MSV24	−0.056 mrad
MSHBLWD3	+0.704 mrad	MSV26	−0.068 mrad
MSH27	+0.626 mrad	MSV28	−0.012 mrad
MSH29	+0.030 mrad	MSV30	+0.035 mrad
MSH31	−0.233 mrad	MSV32	+0.093 mrad
MSH33	+0.905 mrad	MSV34	−0.158 mrad
MSH35	−0.410 mrad	MSV36	+0.272 mrad
MSH37	+0.050 mrad	MSV38	−0.164 mrad
MSH39	−0.201 mrad	/	/
MSH41	−0.509 mrad	/	/
MSH43	−0.346 mrad	/	/
MSC100KEVGUN	−1.239 mrad	MSC100KEVGUN	+0.204 mrad
MSC100KEVCOL	+2.278 mrad	MSC100KEVCOL	+0.195 mrad

Table 6.6: Horizontal and vertical steerer magnets including their kick angle θ_{Kick} from the Precursor Run 2.

6.2.5 Beam Position Monitors

The BPMs implemented in the simulation also have a physical length of zero and are installed in the same position as their counterparts in the real COSY storage ring. The COSY simulation model comprises a total of 30 horizontal BPMs and 29 vertical BPMs. These elements can be used in the simulation for orbit control, as they have an attribute that specifies the beam position relative to their center, the so-called *BPM orbit*. Ideally, this simulated BPM orbit should correspond to the orbit measured by the BPMs in the real COSY storage ring. Therefore the alignment of the BPMs in the simulation plays a crucial role, which will be further discussed later in this thesis.

6.2.6 Implementation of Magnet Misalignments

As mentioned above, it is important to know the position of the magnets design orbit in order to estimate their influence on the particle beam. One way to determine the orientation of the magnets relative to the design orbit is to make a laser-based measurement between their reference marks and then correct their orientation. The company Stollenwerk&Burghof [95] carried out such a measurement and correction of the COSY magnets in April 2019 and January 2020. Only the alignment of the dipoles and quadrupoles, which have reference marks, can be determined, as shown in the Figure (6.2).

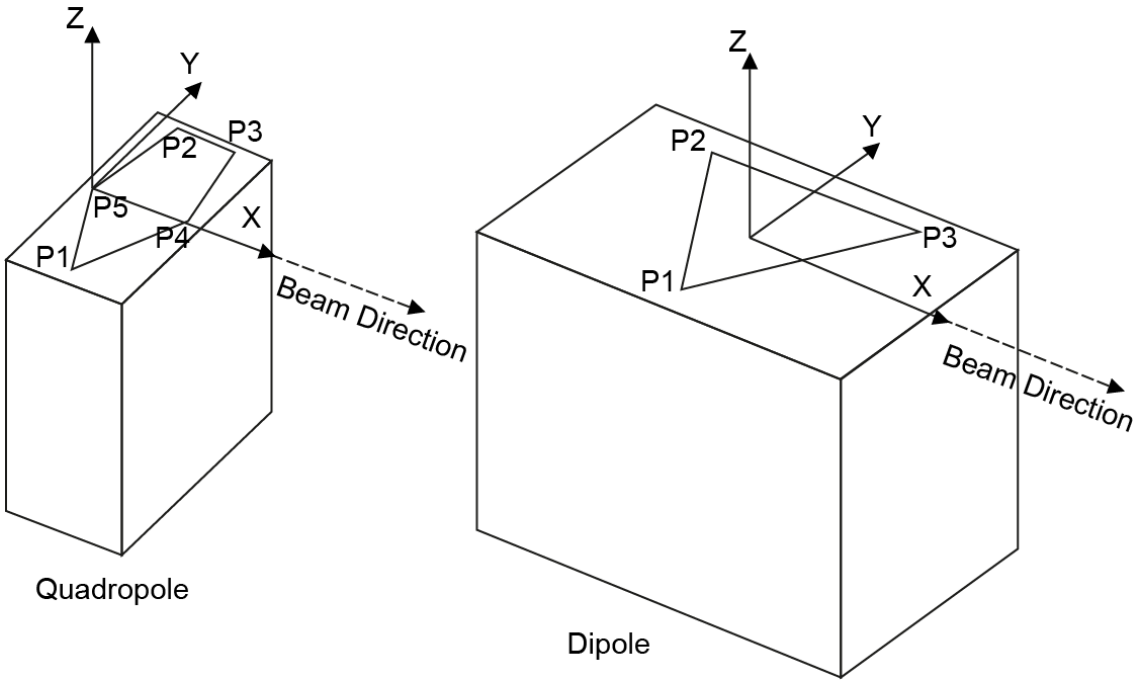

Figure 6.2: Reference marks P1-P5 of the quadrupole and dipole magnets used by the company Stollenwerk&Burghof to determine the orientation of the COSY magnets.

This allows the horizontal x_{Off}, vertical y_{Off} and longitudinal z_{Off} offsets of a magnet to be determined. It also gives the horizontal θ_{Off} and vertical ϕ_{Off} orientation and its roll angle around the design axis ψ_{Off}. As sketched in Figure (6.2), the measurement for the dipoles is performed at their center, while the measurement for the quadrupole is performed at its beginning. The offsets measured at the quadrupole start, given by the vector $V_{\mathrm{Off}}^{\mathrm{Beg}}$, have to be transformed to its center, given by $V_{\mathrm{Off}}^{\mathrm{Cen}}$. In BMAD, for this purpose, an internal coordinate transformation is applied to a quadrupole of length L_{Qua}, described by Equation (6.5).

$$V_{\mathrm{Off}}^{\mathrm{Cen}} = R \cdot L_{\mathrm{Half}} + V_{\mathrm{Off}}^{\mathrm{Beg}} \tag{6.5}$$

$$\text{with} \quad R = R_y(\theta_{\text{Off}})R_{-x}(\phi_{\text{Off}})R_z(\psi_{\text{Off}}), \quad L_{\text{Half}} = \begin{pmatrix} 0 \\ 0 \\ L/2 \end{pmatrix} \quad \text{and} \quad V_{\text{Off}}^{\text{Beg}} = \begin{pmatrix} x_{\text{Off}} \\ y_{\text{Off}} \\ z_{\text{Off}} \end{pmatrix} \tag{6.6}$$

$$R_y(\theta_{\text{Off}}) = \begin{pmatrix} +\cos(\theta_{\text{Off}}) & 0 & +\sin(\theta_{\text{Off}}) \\ 0 & 1 & 0 \\ -\sin(\theta_{\text{Off}}) & 0 & +\cos(\theta_{\text{Off}}) \end{pmatrix} \tag{6.7}$$

$$R_{-x}(\phi_{\text{Off}}) = \begin{pmatrix} 1 & 0 & 0 \\ 0 & +\cos(\phi_{\text{Off}}) & +\sin(\phi_{\text{Off}}) \\ 0 & -\sin(\phi_{\text{Off}}) & +\cos(\phi_{\text{Off}}) \end{pmatrix} \tag{6.8}$$

$$R_z(\psi_{\text{Off}}) = \begin{pmatrix} +\cos(\psi_{\text{Off}}) & +\sin(\psi_{\text{Off}}) & 0 \\ -\sin(\psi_{\text{Off}}) & +\cos(\psi_{\text{Off}}) & 0 \\ 0 & 0 & 1 \end{pmatrix} \tag{6.9}$$

In general, misalignments of sextupoles and steerers magnets cannot be measured, since they have no reference mark. As some steerers are mounted on top of quadrupoles in form of windings they share the same misalignments as the corresponding quadrupole. The misalignments of all other steerer magnets and sextupoles are assumed to be zero. The measurement results of the company Stollenwerk&Burghof regarding the offsets of the quadrupole magnets in the straight sections of COSY and in the arcs can be found as an example in the Figure (6.3) and (6.4). All other results can be found in the appendix in the figures (9.3), (9.4), (9.5), (9.6). A detailed discussion of these offsets will be postponed to a later chapter.

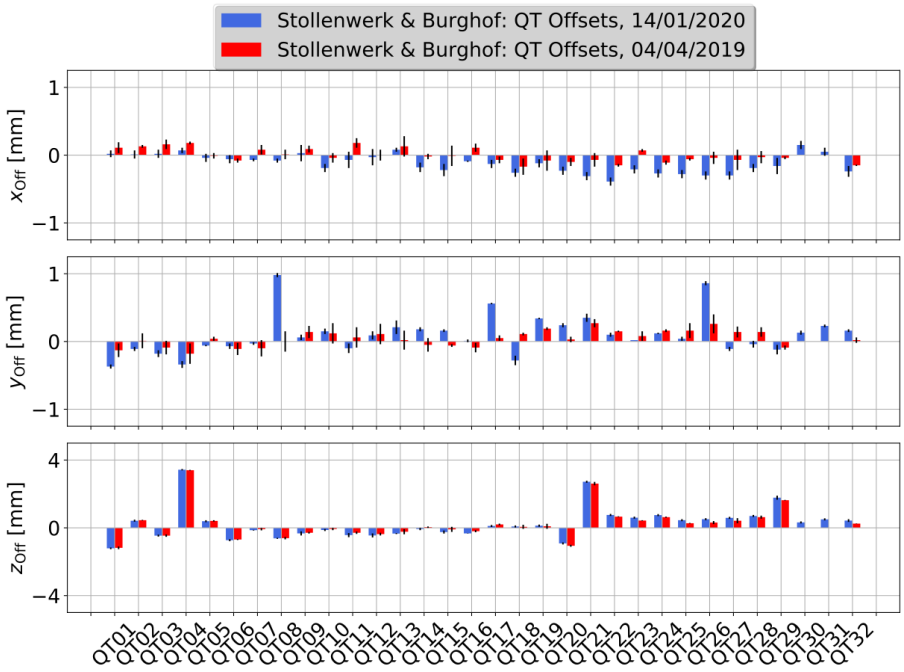

Figure 6.3: Measured offset of the quadrupole magnets in COSY in its **straight** sections by the company Stollenwerk&Burghof in April 2019 and January 2020. The blue and red colored bars show the measured magnitude of the offset, while a measurement error given by the company is shown as a black error bar.

6.2.7 RF Wien Filter

In the simulation, the RF Wien filter is represented in two different ways. On the one hand, it is possible to implement a idealized RF Wien filter. For this, its radial electric field E_x and its vertical magnetic field B_y are defined as box fields. Thus, a passing particle beam experiences both Rf Wien filter fields at full strength as soon as it enters the RF Wien filter. This idealized model of a RF Wien filter has a length of $L_{WF} = 1100\,\text{mm}$ and has its center at the target position *TP1* in COSY. The magnetic field has a strength of $0.03\,\text{mT}$, while the electric field is defined so that the Lorentz force is zero in the RF Wien filter.

Alternatively, the BMAD simulation program can read in the field map of an electromagnetic field to use for particle and spin tracking. A simulated electromagnetic field map by Jamal Slim [47] is available for the RF Wien filter, which describes the full length of the RF Wien filter $L_{WF} = 1100\,\text{m}$, as well as $\pm 5\,\text{mm}$ from its center in transverse phase space. The field map consists of 10^6 simulated data points. Each phase space direction, horizontal x, vertical y and longitudinal z, is described by 10^2 data points. Interpolation between the points is done in BMAD to describe the intermediate spaces. Figure (6.5) and Figure (6.6) show the radial electric field E_x and the vertical magnetic field B_y of the simulated RF Wien filter in the plane $y = 0\,\text{mm}$. In addition, figures (9.7), (9.8), (9.9) and (9.10) show the electromagnetic fields of the simulated RF Wien filter field in all other directions.

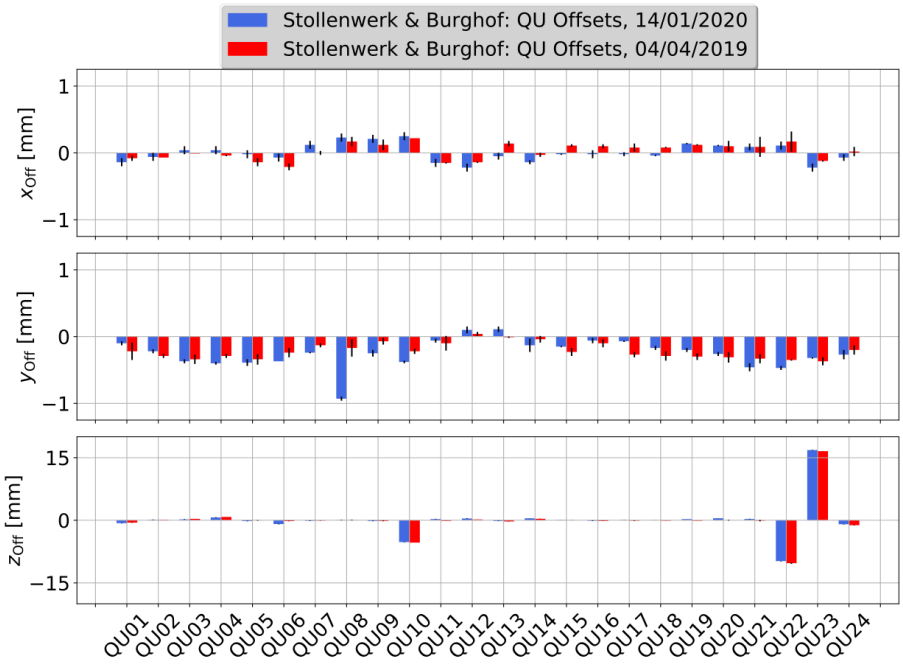

Figure 6.4: Measured offset of the quadrupole magnets in COSY in its **arc** sections by the company Stollenwerk&Burghof in April 2019 and January 2020. The blue and red colored bars show the measured magnitude of the offset, while a measurement error given by the company is shown as a black error bar.

In Figure (6.5) and Figure (6.6) it can be seen that, unlike the idealized RF Wien filter, this simulated model of a *realistic RF Wien filter* has a fringe region that describes the rise and fall of the electric and magnetic fields. Within this fringe region the Lorentz force is not zero because the electric and magnetic fields rise at different rates. Therefore, there is a kick in the horizontal phase space. In order to minimize the disturbance to the particle beam caused by the RF Wien filter, one of the filter's fields must be scaled. To describe the orbit along the storage ring globally, the horizontal orbit RMS (**R**ooth **M**ean **S**quare) x_{RMS} is defined. This is shown in Equation (6.10) and results from the relative horizontal deviations x_{i} from the nominal orbit at each element i.

$$x_{\mathrm{RMS}} = \sqrt{\frac{1}{N}\sum_{i=1}^{N} x_{\mathrm{i}}^2} \tag{6.10}$$

Figure (6.7) shows the dependence of the horizontal orbit RMS on the scaling of the simulated magnetic field of the RF Wien filter by the factor B_{Sca}. Since a scaling factor is required at which the horizontal orbit RMS is minimal, it can be roughly determined to be $B_{\mathrm{Sca}} = 1.00045$. This scaling factor will be used in the rest of this paper. As the figures (9.7), (9.8), (9.9) and (9.10) show, the influence of all other field components of the RF

Wien filter is negligible compared to the main fields E_x and B_y. This is also the reason why the realistic RF Wien filter has no influence on the vertical orbit and its RMS value. By default, these RF Wien filter fields are all statically defined in the COSY simulation model. During tracking, however, these can be varied so that the RF Wien filter acts like an RF device from the perspective of the particle beam.

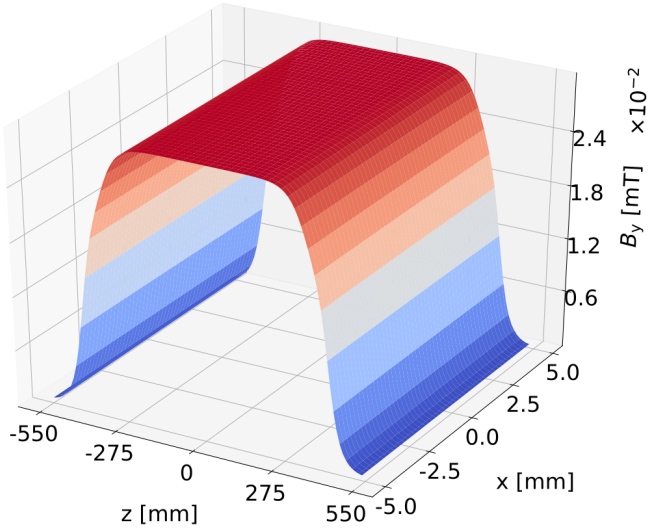

Figure 6.5: Simulated field map of the vertical magnetic field component of a realistic RF Wien filter in the plane $y = 0\,\text{mm}$. The field map consists of a total of 10^4, with 10^2 points in each direction. A position of $x = 0\,\text{mm}$ and $z = 0\,\text{mm}$ indicates the target position *TP1* and the center of the RF Wien filter [47].

6.2.8 Solenoids

A total of three static solenoids are implemented in the COSY simulation model. These are the previously mentioned Snake Solenoid and the two compensation solenoids of the electron coolers, the 2 MeV Solenoid and the 100 keV Solenoid [55, 65]. These are represented in simplified form by a purely longitudinal field. They are also assigned the same length of $L_{\text{Sol}} = 676.667\,\text{mm}$. This length was chosen for the Snake Solenoid in J. Hetzel's MAD-X model and is adopted for all static solenoids in COSY's BMAD model. Thus, the effect of each solenoid on orbit and spin at the same field strength depends only on the position of the solenoid in the lattice. The RF Solenoid is currently not represented in either the MAD-X COSY lattice or the BMAD COSY lattice [66, 67]. Its mode of action, the transfer of the vertical polarization into the COSY plane, can be reproduced differently in a simulation. For tracking, the initial spin components must be defined differently depending on the orientation of the polarization direction. As the RF Solenoid is switched off after this transfer, it does not affect the beam or the ISA and does not need to be considered further in a simulation.

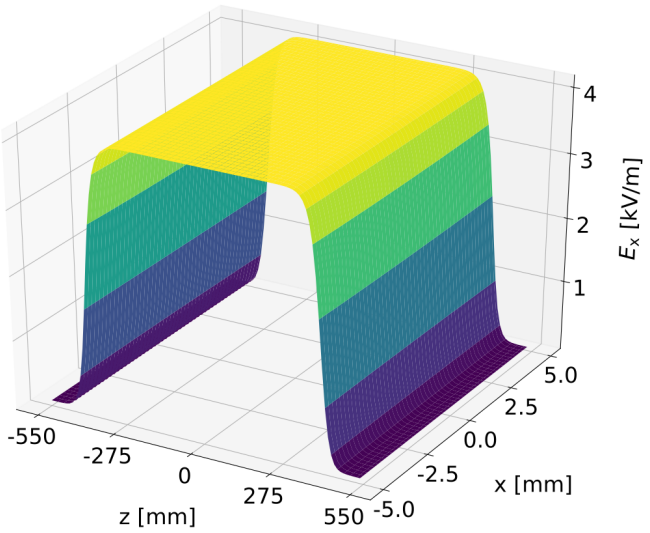

Figure 6.6: Simulated field map of the radial electric field component of a realistic RF Wien filter in the plane $y = 0\,\text{mm}$. The field map consists of a total of 10^4, with 10^2 points in each direction. A position of $x = 0\,\text{mm}$ and $z = 0\,\text{mm}$ indicates the target position *TP1* and the center of the RF Wien filter [47].

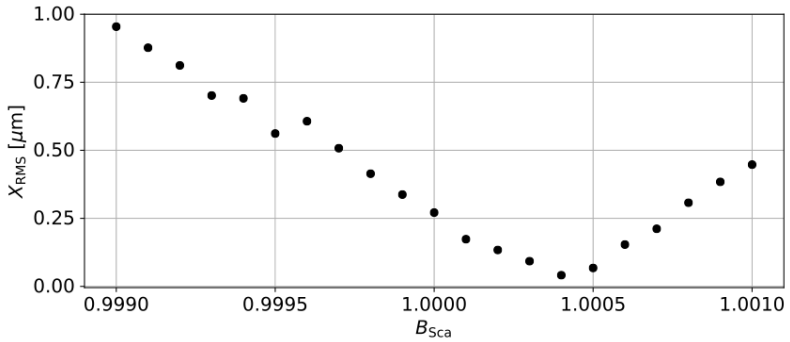

Figure 6.7: Dependence of the horizontal orbit RMS on the scaling parameter B_{Sca} of the simulated magnetic RF Wien filter field. The minimal horizontal orbit perturbation occurs at a scaling of approximately $B_{\text{Sca}} = 1.00045$.

CHAPTER 7

Determination of the Invariant Spin Axis

Having discussed Precursor Run 2 to determine the ISA and presented the BMAD simulation model to replicate the experiment, it is necessary to look at the determination mechanism of the ISA tilt angle in the BMAD simulation model. As part of this, it is necessary to analyze several factors that influence the calculation of the ISA. A starting point for the discussion will be the effect of the spin tracking algorithm on the ISA tilt angle.

7.1 Benchmarking of Spin Tracking Algorithm

To better understand the impact of the BMAD tracking algorithms on the ISA tilt angle, it is necessary to compare the results of the algorithms when calculating the particle's passage through an existing element in the storage ring. The algorithms studied for this purpose have already been presented in the previous chapter. In the later context they will be referred to as BS (**B**mad_**S**tandard), RK (**R**unge_**K**utta) and PTC (Symp_Lie_**PTC**).

In this study, deuterons with a momentum of $p_0 = 970\,\mathrm{MeV/c}$ are stored in the BMAD COSY lattice and the dipole, quadrupole and sextupole magnets are operated with the values from the tables (6.2), (6.4) and (6.5). The effects of a potential EDM signal, the shortened acting dipoles, those due to magnet displacements and contributions from steerer magnets have initially been neglected. As a result, the closed beam orbit in COSY should be exactly on the design orbit and the orientation of the ISA should be purely vertical. The TAO program is then used to calculate the closed orbit and the ISA tilt angle on the closed orbit for various tracking algorithms, resulting in all tracking algorithms being able to describe this initial setup in terms of orbit and ISA tilt angle.

Incorporating an EDM signal or a longitudinal field that mimics a solenoid into the simulation will shift the ISA tilt angle as shown in the previous chapters. However, the orbit does not change. Again, the result of all tracking algorithms is identical and perfectly described by theory. A first differences in the outcome of the tracking algorithm occur when an orbit kick is introduced by either a ramping up a steerer magnet or misaligning an arbitrary quadrupole magnet. As the ISA tilt angle is mainly influenced by the vertical phase space, as it will be demonstrated further below, the kick or misalignment has to be in the vertical direction so that any difference in the ISA tilt angle becomes visible. For this reason, the performance of all tracking algorithms is tested for the scenario of one vertically misaligned quadrupole. Since the quadrupole can be arbitrarily chosen, the quadrupole *QT02* is misaligned by $y_{\text{Off}}^{\text{QT02}} = 1\,\text{mm}$ during the investigation. Figure (7.1) summarizes the results of the computed vertical closed orbits y^{Clo} for the tracking algorithms used and also compares their differences.

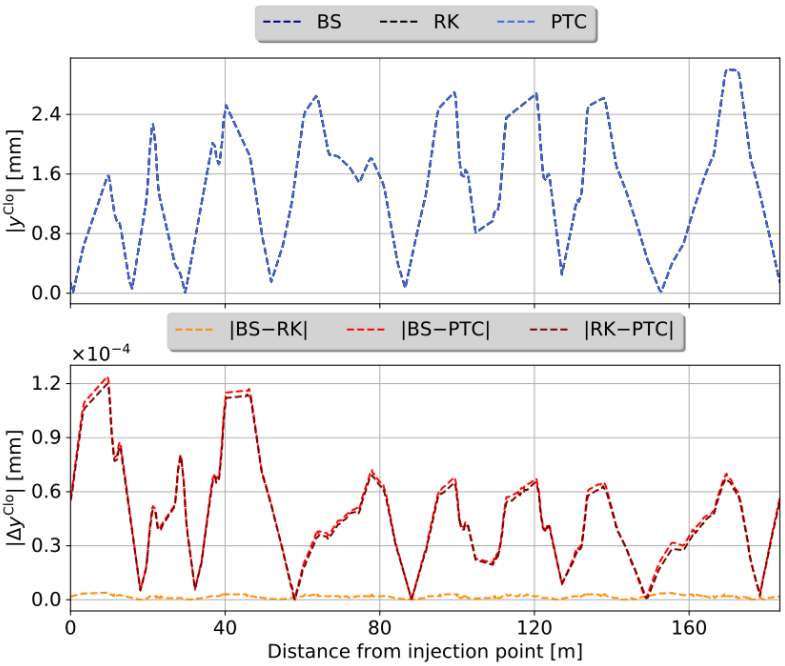

Figure 7.1: Comparison of the tracking results of three different tracking algorithms for the vertical closed orbit in COSY after vertical displacement of the quadrupole *QT02* by $y_{\text{Off}}^{\text{QT02}} = 1\,\text{mm}$. As the graphs in the top panel, which show the absolute vertical orbit, overlap, the differences between the tracking algorithms are shown in the bottom panel.

In the top panel of Figure (7.1) the y-axis describes the position of a particle on the vertical closed orbit with respect to the design orbit. The reason why the horizontal orbit is not shown is that the particle moves completely in horizontal phase space on the design orbit. This is not the case for the vertical phase space, where the closed orbit deviates from the design orbit by a few millimeter due to the vertical misalignment of the quadrupole *QT02*.

The graphs in different colors represent the results of the different tracking algorithms. As in the upper panel there is hardly any difference between the different tracking algorithms visible, the lower panel shows the calculated differences in between the tracking algorithms. As the differences in orbit tracking are four orders of magnitude less than the absolute orbit, it can be concluded that these differences are negligible. However, it should be noted that the largest differences occur when PTC tracking is included.

Identical simulations with similar results were performed for other quadrupoles to account for different β functions at their dedicated position in COSY. The vertical orbits always ended in a range of a few mm, while the difference between the tracking algorithms is calculated to be well below μm. It will be shown later that a closed orbit of a few millimeter or a quadrupole misalignment of up to 1 mm is also the order of magnitude to be expected in a realistic COSY setup. Therefore, it is not necessary to check for larger magnet displacements or closed orbits. Similar results are also obtained when the quadrupole is misaligned in horizontal direction. Unfortunately, one aspect that cannot be illuminated by the horizontal displacement of a quadrupole is the tilt angle of the ISA for different tracking algorithms. This tilt angle is therefore analyzed in more detail for the vertical quadrupole *QT02*. Here, Figure (7.2) summarizes the results of the absolute radial $|n_x|$ and longitudinal $|n_z|$ ISA tilt angles for the different tracking algorithms, while Figure (7.3) shows these differences explicitly.

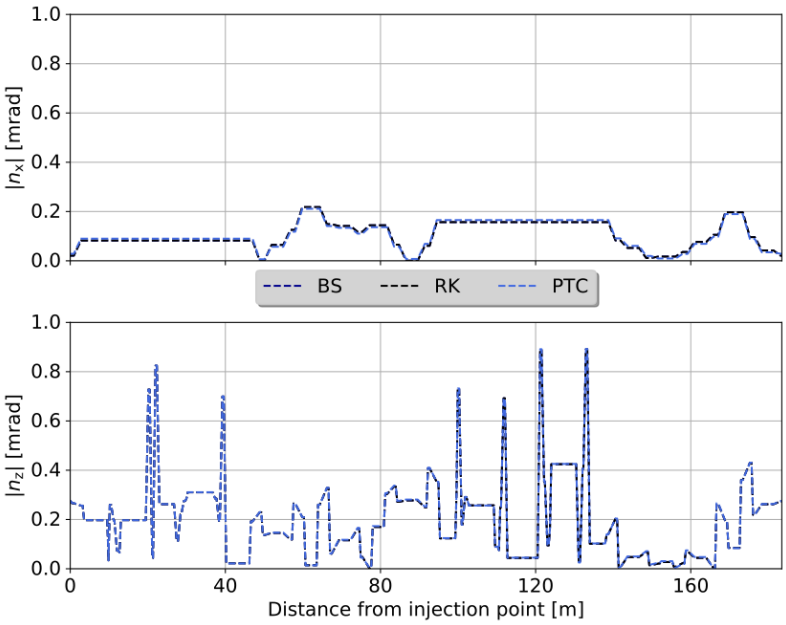

Figure 7.2: Absolute radial (top image) and longitudinal (bottom image) ISA tilt angle for the particle on the closed orbit in COSY after displacement of the quadrupole *QT02* by $y_{\mathrm{Off}}^{\mathrm{QT02}} = 1\,\mathrm{mm}$ in the vertical direction. The results of three different tracking algorithms are compared. In this scope, no discernible difference is visible, as the corresponding graphs overlap.

As illustrated in Figure (7.2), both panels demonstrate that a vertical closed orbit, situated a few millimeters from the design orbit, results in an ISA tilt angle of less than one milliradian in both the radial and longitudinal directions. At this scale, the differences between the chosen tracking programs are not discernible, and it is therefore worthwhile to plot their differences instead. This is done in Figure (7.3). It shows that the differences between the tracking algorithms studied are less than 10^{-2} mrad. Similar to the orbit case, the largest differences between the tracking algorithms occur when PTC tracking is considered.

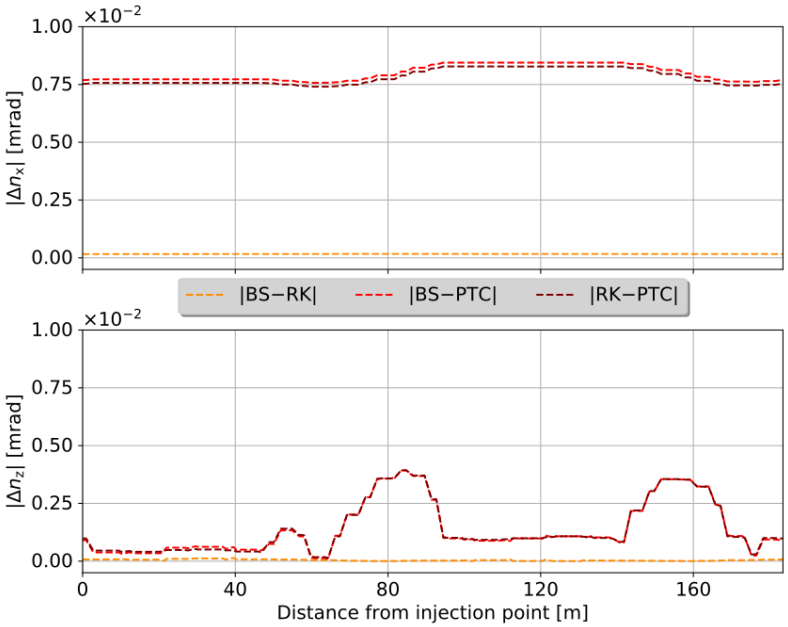

Figure 7.3: Differences in the absolute radial (top image) and longitudinal (bottom image) ISA tilt angle for the particle on the closed orbit in COSY after displacement of the quadrupole *QT02* by $y_{\text{Off}}^{\text{QT02}} = 1\,\text{mm}$ in the vertical direction. The results of three different tracking algorithms are compared.

In addition to the scenario of a misaligned quadrupole, the scenario of a steerer kick on the orbit can be analyzed. In this case, the misalignment of the quadrupole is removed while an arbitrary steerer magnet is used to kick the vertical orbit. Steerer magnet *MSV02* is chosen with a kick magnitude of $\theta_{\text{Kick}} = 1\,\text{mrad}$, as this represents the magnitude of the largest steerer kicks during Precursor Run 2. Figure (7.4) shows the resulting vertical closed orbit as well as the differences in between the analyzed tracking algorithms. As the steerer kick is only applied in vertical phase space, the horizontal closed orbit is identical to the design orbit and is therefore not shown. Due to the large steerer kick, the vertical closed orbit is now at a distance of up to 10 mm from the design orbit and is about four times larger than the vertical closed orbit due to the quadrupole misalignment. When comparing the differences in the closed orbit between the tracking algorithms, there are deviations in the order of some μm. However, the difference of a some μm is still about

four orders of magnitude smaller than the absolute vertical closed orbit. The differences become more impactful when comparing ISA tilt of the particle on the closed orbit, illustrated by Figure (7.5) and Figure (7.6).

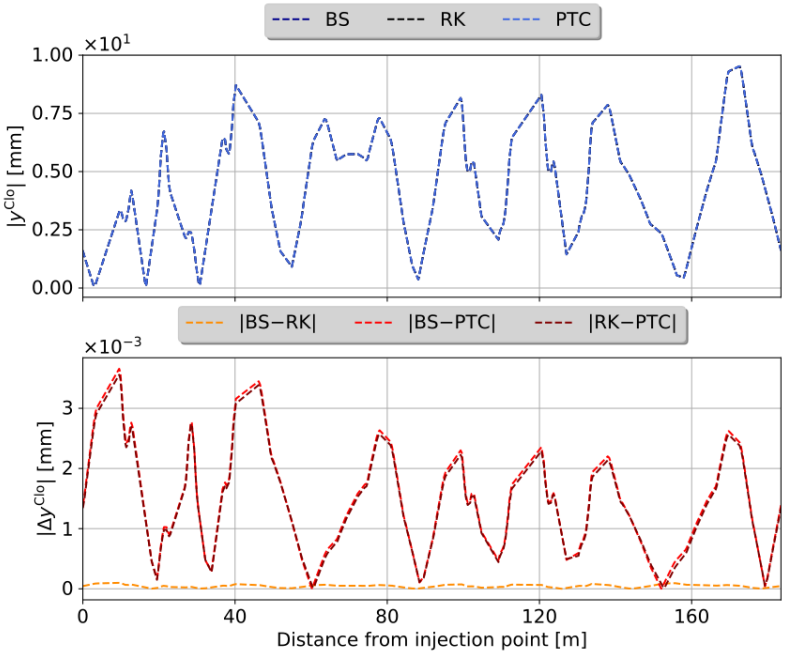

Figure 7.4: Comparison of the tracking results of three different tracking algorithms for the vertical closed orbit in COSY after giving the vertical orbit a kick of $\theta_{\text{Kick}} = 1\,\text{mrad}$ at the position of steerer magnet *MSV02*. The top panel shows the absolute vertical orbit, while the bottom panel displays the difference in between the different tracking algorithms.

The RK tracking algorithm has, as Figure (7.5) and Figure (7.6) indicate, a problem to properly track the ISA orientation in comparison to the other two tracking algorithms. The reason for this problem is the slicing approach that RK uses when tracking through an element. As the steerer magnet in the BMAD simulation model has a length of zero, the RK tracking algorithm is unable to handle the steerer magnet properly. One solution out of this problem is therefore the assignment of length to the steerer magnet. However, for the sake of simplicity, this is not done. Therefore, RK tracking algorithm is excluded as a possible tracking algorithm for this thesis. Having ruled out RK, the question remains as to whether the BS or PTC tracking algorithm should be used as the preferred tracking algorithm. While PTC takes advantage of symplectic tracking by using a Hamiltonian with Lie operator techniques, it should be more accurate than the BS tracking algorithm. However, PTC has a very slow computation time and is therefore unsuitable for many of the computationally intensive algorithms involved in ISA determination. For this reason, BS is selected as the preferred tracking algorithm. Based on the differences between of BS and PTC in orbit and spin tracking, the uncertainties $\sigma_{\text{Tracking,Orbit}}$ and $\sigma_{\text{Tracking,ISA}}$ are defined when using the BS algorithm instead of PTC algorithm. Since this uncertainty is

dominated by the size of the closed orbit, it can be shown that it cannot be larger than:

$$\sigma_{\text{Tracking,Orbit}} \leq 5\mu\text{m} \quad \text{and} \quad \sigma_{\text{Tracking,ISA}} \leq 5\mu\text{rad} \tag{7.1}$$

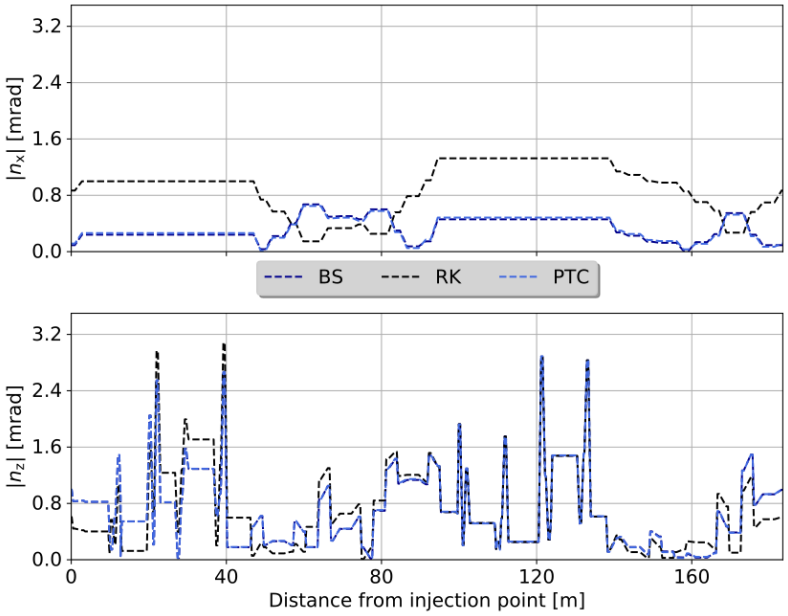

Figure 7.5: Absolute radial (top image) and longitudinal (bottom image) ISA tilt angle for the particle on the closed orbit in COSY after giving the vertical orbit a kick of $\theta_{\text{Kick}} = 1\,\text{mrad}$ at the position of steerer magnet *MSV02*. The results of three different tracking algorithms are compared.

7.2 Determination of Stable Spin Axis with Solenoids

Unlike the direct calculation of the ISA in a simulation using TAO or BMAD, the ISA tilt cannot be measured directly in a real experiment. As explained before, radial and longitudinal ISA tilt angle can be measured simultaneously at the RF Wien filter position using a static solenoid and the RF Wien filter. Alternatively, each static solenoid in the COSY storage ring also provides access to the longitudinal ISA tilt angle at its position. The so-called *spin tune mapping* method can be used for this purpose [96]. This method can also be used in a simulation to determine the ISA tilt angle.

7.2.1 Spin Tune Map and Solenoid Calibration

As the name of the method suggests, spin tune mapping analyzes the change in spin tune in the form of a map. In an idealized storage ring with purely magnetic guiding elements, as in COSY, the spin tune is given by $\nu_{\text{s},0} = \gamma_0 G$, as explained in Section (4.3.1). Misaligned magnets and other systematics in COSY perturb the idealized closed orbit and thus also the idealized spin tune $\nu_{\text{s,Clo}}$. The perturbed spin tune can additionally be manipulated by static solenoids $\Delta\nu_{\text{s}}$ as described in Section (4.3.2). In COSY the Snake Solenoid and the

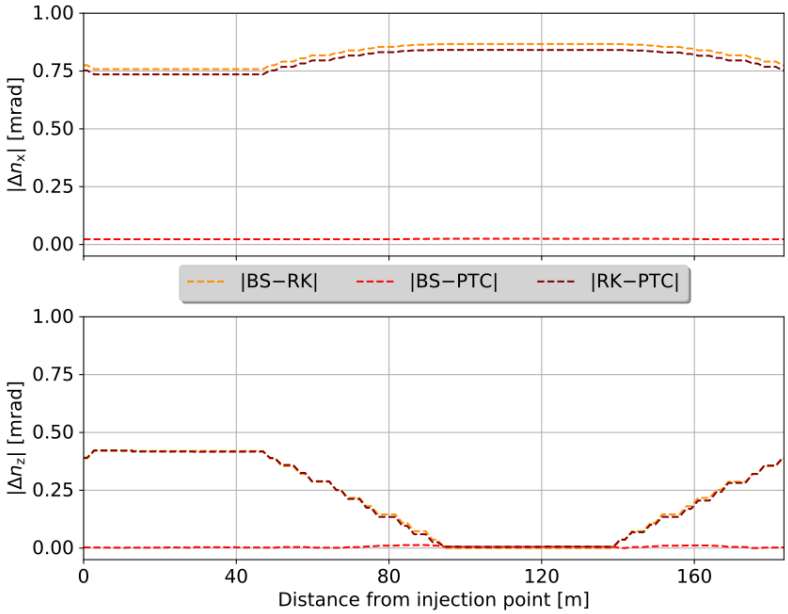

Figure 7.6: Differences in the absolute radial (top image) and longitudinal (bottom image) ISA tilt angle for the particle on the closed orbit in COSY after giving the vertical orbit a kick of $\theta_{\mathrm{Kick}} = 1\,\mathrm{mrad}$ at the position of steerer magnet *MSV02*. The results of three different tracking algorithms are compared.

2 MeV Solenoid are static and are therefore used to generate a spin tune map described by the Equation (7.2). This map depends on the longitudinal magnetic field of the solenoid magnets B_{Sol} and B_{Sna}.

$$\begin{aligned}\pi \sin(\pi\nu_{\mathrm{s,Clo}}) \cdot \Delta\nu_{\mathrm{s}} = &- \cos(\pi\nu_{\mathrm{s,Clo}}) \left(\cos\frac{k_{\mathrm{Sna}}B_{\mathrm{Sna}}}{2} \cos\frac{k_{\mathrm{Sol}}B_{\mathrm{Sol}}}{2} - 1 \right) \\ &- c_{\mathrm{Sol}} \sin(\pi\nu_{\mathrm{s,Clo}}) \sin\frac{k_{\mathrm{Sna}}B_{\mathrm{Sna}}}{2} \cos\frac{k_{\mathrm{Sol}}B_{\mathrm{Sol}}}{2} \\ &- c_{\mathrm{Sna}} \sin(\pi\nu_{\mathrm{s,Clo}}) \cos\frac{k_{\mathrm{Sna}}B_{\mathrm{Sna}}}{2} \sin\frac{k_{\mathrm{Sol}}B_{\mathrm{Sol}}}{2} \\ &- \sin\frac{k_{\mathrm{Sna}}B_{\mathrm{Sna}}}{2} \sin\frac{k_{\mathrm{Sol}}B_{\mathrm{Sol}}}{2}\end{aligned} \tag{7.2}$$

Two important variables that appear in Equation (7.2) are the calibration factors of the solenoids k_{Sol} and k_{Sna}. The calibration factor of the Snake Solenoid k_{Sna} is also needed in the next section to determine the longitudinal ISA tilt angle at the RF Wien filter location. Two other variables not explained so far are the projections of the ISA at the solenoid location c_{Sol} and c_{Sna}. These quantities give access to the longitudinal ISA at each solenoid location. These four variables must be determined by fitting the Equation (7.2) to a spin tune map. To illustrate this process and how a spin tune map is calculated in the BMAD simulation, an example is shown in Figure (7.7), where the measured steerer magnet kicks from Precursor Run 2 and the measured magnet misalignments in 2020 by

Stollenwerk&Burghof have been loaded into the BMAD simulation model, creating an arbitrary closed orbit.

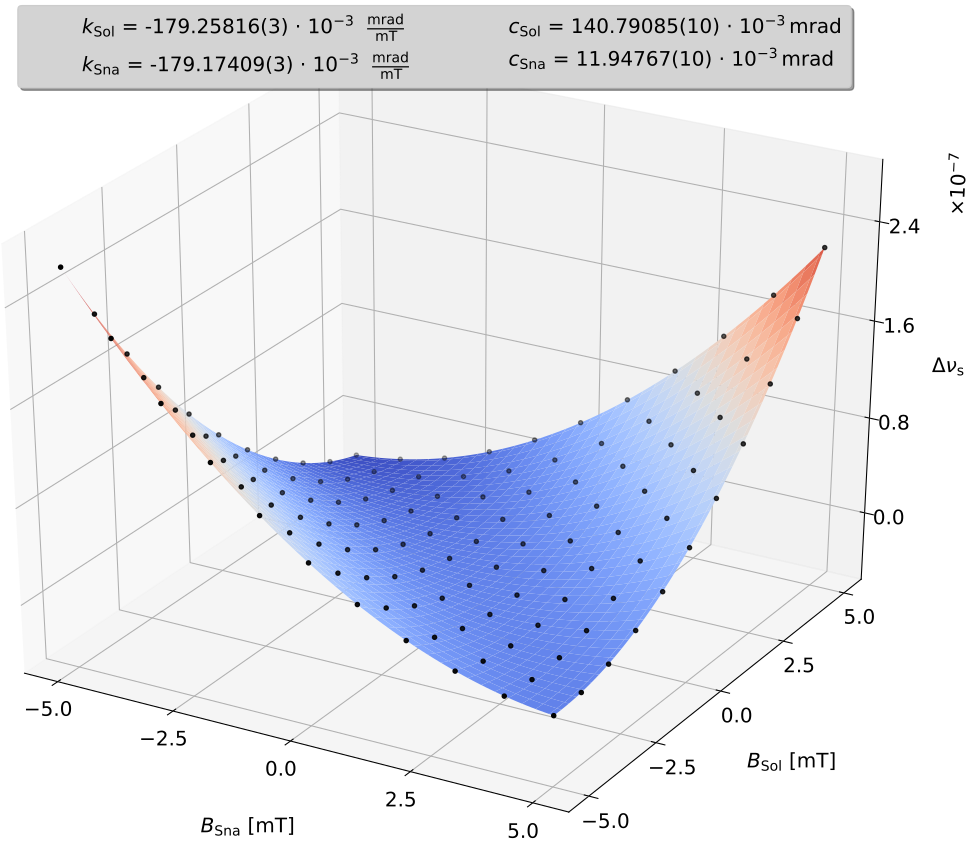

Figure 7.7: Spin tune map after applying measured steerer kicks and magnet misalignments to an idealized COSY lattice. The black dots indicate the simulated data points, while the continuous plane in blue and red shows the result of fitting the Equation (7.2) to the data points. The corresponding fit parameters are shown in the legend.

Figure (7.7) shows the effect of varying the field strength of the 2 MeV Solenoid B_{Sol} and the Snake Solenoid B_{Sna} on the spin tune. Field values in the range ± 5 mT are chosen as the spectrum of field variation. The resulting simulated changes in the spin tune $\Delta\nu_s$ are shown on the z-axis, indicated by black dots. An arbitrarily chosen grid of 11×11 points forms this spin tune map. The error on each of the simulated spin tune changes is determined to be 10^{-13}, which comes from the numerical precision of the BMAD simulation program. No residuals are shown because the numerical error is an order of magnitude larger than the residuals of the fit. The blue-red surface plot shows the result of fitting the Equation (7.2) to the simulated points. The resulting fit parameters are given in the legend to the plot. It is noticeable that the results of k_{Sol} and k_{Sna} differ. Since both magnets in the simulation model have a purely longitudinal field and do not differ in length, one would expect an identical calibration parameter. It can be shown that this is the case

if the closed orbit is identical to the design orbit, so it can be concluded that the difference is caused by the path difference in the individual solenoid.

On the other hand, it is not surprising that the projections of the longitudinal ISA c_{Sol} and c_{Sna} differ from each other, since they should indicate the longitudinal ISA tilt angle at different positions inside the COSY ring. To check the accuracy of the spin tune mapping method, these quantities have to be compared with the respective longitudinal ISA tilt angle at the position of the solenoids $n_{z,\mathrm{Sol}}$ and $n_{z,\mathrm{Sna}}$. This is done in Equation (7.3) and Equation (7.4).

$$n_{\mathrm{z,Sol}} = -393.95\,\mu\mathrm{rad} \quad \not\Leftrightarrow \quad c_{\mathrm{Sol}} \approx +140.79\,\mu\mathrm{rad} \tag{7.3}$$

$$n_{\mathrm{z,Sna}} = +79.04\,\mu\mathrm{rad} \quad \not\Leftrightarrow \quad c_{\mathrm{Sna}} \approx +11.95\,\mu\mathrm{rad} \tag{7.4}$$

Both equations show that the projection of the longitudinal ISA is not equivalent to the tilt of the longitudinal ISA at identical positions. This has not been the case and will be explained in Section (7.2.2) with the need for correction factors. Before that, the so-called *solenoid calibration* should be introduced. This is nothing more than the simplification of Equation (7.2), assuming that only one solenoid is turned on. The resulting equation

$$\Delta\nu_{\mathrm{s}} = -\frac{1}{\pi}\left(\cot(\pi\nu_{\mathrm{s,Clo}})\left(\cos\frac{k_{\mathrm{Sol}}B_{\mathrm{Sol}}}{2} - 1\right)\right) - c_{\mathrm{Sol}}\sin\frac{k_{\mathrm{Sol}}B_{\mathrm{Sol}}}{2}, \tag{7.5}$$

shows the case where the 2 MeV Solenoid is switched on. An analogous equation can also be formulated for the Snake Solenoid. Based on this simplified equation, the calibration factors and the projection of the longitudinal ISA at the solenoid position can be determined from simulated spin tune changes using only one solenoid. Figure (7.8) and Figure (9.11) show this determination method for the scenario already discussed for the spin tune map method. In these figures the simulated spin tune changes are shown in the top panel as a function of the solenoid field variations. The lower panels show the residuals of the fitting Equation (7.5) to the simulated data points. The simulated data points are shown in black, while the fit is shown in blue. As explained above, the errors in the simulated spin tune changes are due to the numerical precision of the BMAD simulation program. They are an order of magnitude larger than the residuals of the fit. The parameters of the fit are given in the legend. They differ by a small amount from the corresponding fit parameter of the spin tune map, which cannot be explained within their errors. The exact reason for this has not yet been identified.

The advantage of the solenoid calibration method is that only one solenoid is required to determine the projection of the longitudinal ISA at its position. The other solenoid can

be used to manipulate the tilt angle of the longitudinal ISA. In this way it can be shown that the projection of the longitudinal ISA is equal to the longitudinal ISA tilt angle when the closed orbit and the design orbit are identical, as shown by Equation (7.6).

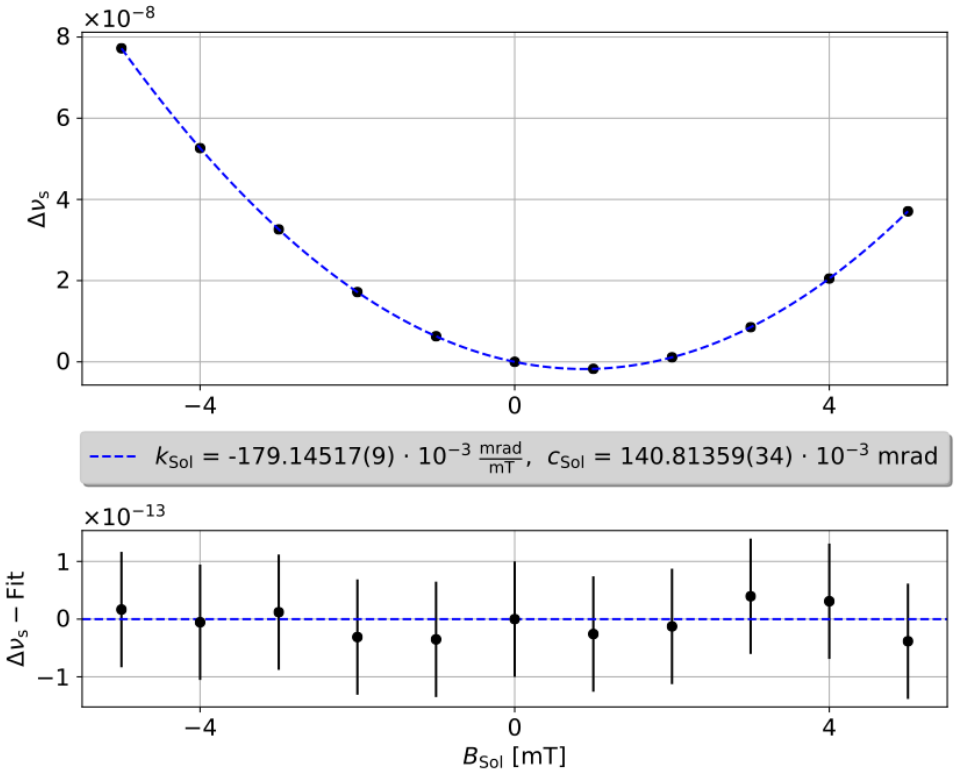

Figure 7.8: Calibration of the 2 MeV Solenoid after applying the measured steerer kicks and measured magnet displacements to an idealized COSY lattice. In the top panel, the black dots indicate the simulated data points, while the blue line shows the result of fitting the Equation (7.5) to the data points. The bottom panel shows the residuals from the top panel.

$$\text{Closed Orbit} = \text{Design Orbit} \quad \Rightarrow \quad n_{z,\text{Sol}} = c_{\text{Sol}} \quad \text{and} \quad n_{z,\text{Sna}} = c_{\text{Sna}} \tag{7.6}$$

This shows that the orientation of the beam trajectory and the magnetic field of the solenoid have an effect on the determination of the ISA longitudinal tilt angle and must therefore be taken into account. This fact will be investigated in more detail in the next section in the form of solenoid tilt angles and different beam trajectories at the solenoid position to determine correction factors for the spin tune map and solenoid calibration.

7.2.2 Correction Factors for Spin Tune Map and Solenoid Calibration

In order to determine a correction factor for the spin tune map method and the solenoid calibration method, it is necessary to generate various closed orbits that deviate from the

design orbit in transverse phase space. To generate these closed orbits, random kick values are generated for the horizontal and vertical steerer magnets of COSY and implemented in the BMAD simulation model. They are calculated using a normal distribution with an expectation value equal to no steerer kick. The standard deviation is set to produce kick values of $\sigma_{\mathrm{Gaus,Ste}} = 1\,\mathrm{mrad}$. It can be shown that this constraint only plays a role in avoiding particle loss, but has no effect on the result of this investigation. Using these closed orbits, the correlation between the orientation of the beam axis at solenoid magnet position, given by the relative horizontal $P_{\mathrm{x,i}} = \frac{p_{\mathrm{x,i}}}{p_0}$ and vertical $P_{\mathrm{y,\,i}} = \frac{p_{\mathrm{y,i}}}{p_0}$ momentum, and the difference between the longitudinal ISA projection and the longitudinal ISA tilt angle $c_{\mathrm{i}} - n_{\mathrm{z,i}}$ can be studied. The i denotes the individual solenoid position while p_0 represents the reference particle momentum. A clear dependence on the relative vertical momentum can be observed as shown in Figure (7.9) and Figure (9.12) for the single solenoid. A dependence on the relative horizontal momentum at the solenoid position cannot be observed.

In the upper panel, Figure (7.9) and Figure (9.12) show the aforementioned difference on their y-axis as a function of the relative vertical momentum at the position of the solenoids on the x-axis. The simulated data points are shown in black. Their error bars result from the fit error in the determination of c_{i} by the solenoid calibration method. A blue line indicates a linear fit to the simulated data points. The residuals of this linear fit are shown in the lower panel, while the fit parameters with error are shown in the legend. These plots confirm that there is no difference in the absence of relative vertical momentum. This can be seen from the non-existent offset in the linear fit function. When such an offset is considered as a fitting parameter, it is zero within the fitting error. Once the beam passes through the magnet with a relative vertical momentum, the projection of the longitudinal ISA must be corrected for this relative vertical momentum so that it again corresponds to the longitudinal ISA. This is indicated by the slope of the linear fit, which is close to $1\,\frac{\mathrm{mrad}}{\mathrm{mrad}}$ for both magnets. The small deviation from a slope of exactly $1\,\frac{\mathrm{mrad}}{\mathrm{mrad}}$ can be explained by the fact that a solenoid has a steering effect on the trajectory of the beam as soon as it does not pass through the center of the solenoid. The correction factor for passing the solenoid with a relative vertical momentum can be interpreted as a change from the particle reference system to the storage ring reference system.

In addition to the investigation of the beam axis orientation at solenoid position, also the orientation of the solenoid magnets has to be investigated. To do this, the random steerer kicks are set back to zero so that the closed orbit and the design orbit are identical. To measure a non-zero longitudinal ISA without disturbing the orbit, one solenoid magnet is operated statically[1] while the other magnet is varied for the solenoid calibration. The solenoid calibration is performed for different horizontal $\phi_{\mathrm{x,i}}$ and vertical $\phi_{\mathrm{y,i}}$ pitch angles of the solenoids as shown in figures (7.10), (9.13), (9.14) and (9.15). A pitch angle is a

[1] Without being rotated relative to the beam path.

horizontal or vertical rotation of the solenoid around its center.

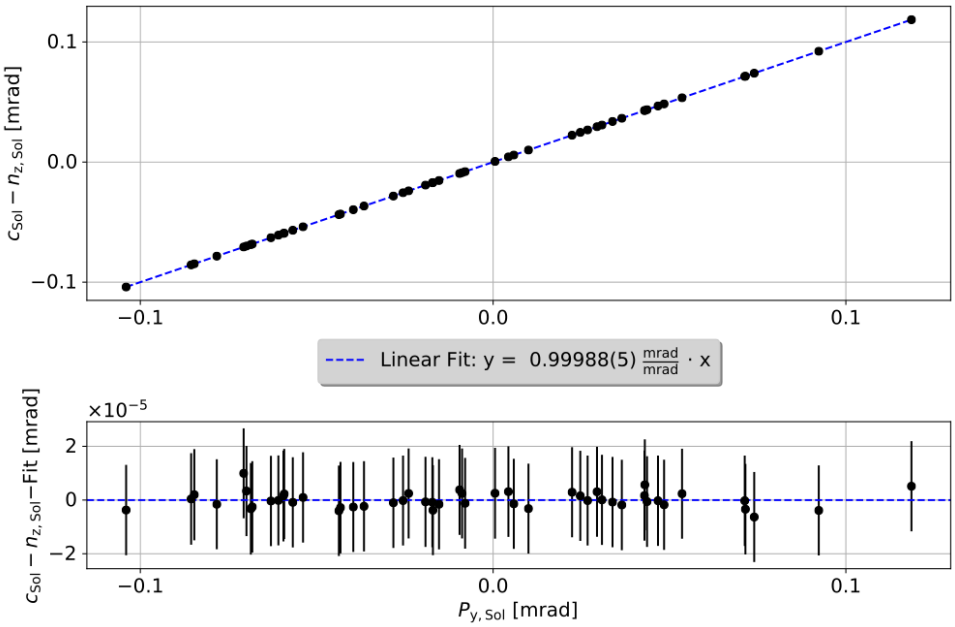

Figure 7.9: Determination of a correction factor for the 2 MeV Solenoid after perturbation of the closed orbit by random steerer kicks. The top panel shows the difference between the projection of the longitudinal ISA and the actual longitudinal ISA tilt at the solenoid position as a function of the relative vertical momentum of the beam at the solenoid position. The simulated differences are shown as black dots, while a linear fit with the fit parameter given in the legend is shown in blue. The bottom panel shows the residuals of the linear fit.

The dependence of the difference on the vertical pitch angle of the solenoid magnets can be seen in Figure (7.10) and Figure (9.13), while Figure (9.14) and Figure (9.15) show the dependence of the difference on the horizontal pitch angle of the magnets. In all these figures, the simulated differences are shown in black, while a cubic fit is shown in blue, with the fit parameters and errors given in the legend. The bottom panel shows the residuals of the fit. As before, the errors in the simulated data points come from the fit error on c_i by the solenoid calibration method.

In contrast to the previous investigation, a cubic rather than a linear fit is required to describe the simulated data points. In addition, significantly larger angles of rotation were analyzed due to the precise determination of the third order polynomial in the cubic fit. In general, it can be seen that there is a dependence on the pitch angle of the solenoid magnet. This dependence is vanishingly small in contrast to the dependence of the difference on the relative vertical momentum beam at the magnet position. This can be seen immediately by comparing the fit parameters of the slopes. Whereas previously this factor was of the order of $1\frac{\text{mrad}}{\text{mrad}}$, it is now of the order of $10^{-4}\ \frac{\text{mrad}}{\text{mrad}}$ and lower. Furthermore, this factor is now different for the Snake Solenoid and the 2 MeV Solenoid. This can be

explained by the steering effect of the solenoid when it is not aligned with the beam trajectory. Due to the difference in the β function at the position of the different magnets, a different orbit response is caused. The fit parameters for the offset and the second order polynomial were zero within their fit errors and are therefore not shown. Since the pitch angle of the solenoid magnets is thus assumed to be negligibly small for the determination of a correction factor between the projection of the longitudinal ISA and the longitudinal ISA tilt, Equation (7.7) can be formulated to determine the longitudinal ISA from the projection of the longitudinal ISA.

$$\begin{aligned} n_{\mathrm{z,Sol}} &= c_{\mathrm{Sol}} - P_{\mathrm{y,Sol}} \\ n_{\mathrm{z,Sna}} &= c_{\mathrm{Sna}} - P_{\mathrm{y,Sna}} \end{aligned} \tag{7.7}$$

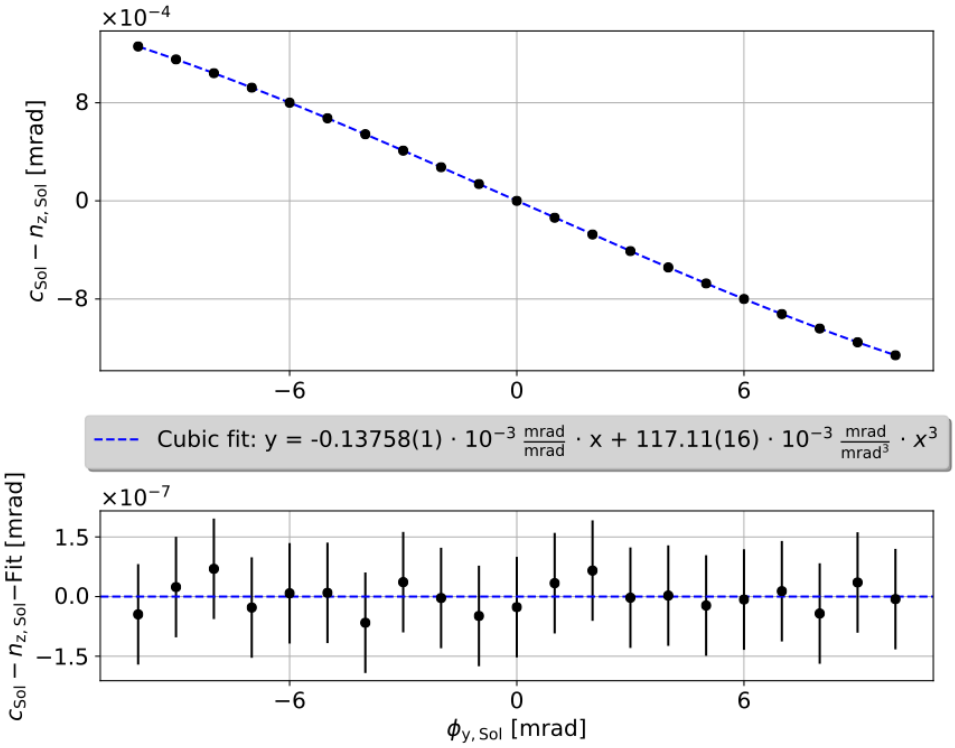

Figure 7.10: Determination of a correction factor for the 2 MeV Solenoid after pitching the solenoid by an angle $\phi_{\mathrm{y,Sol}}$ in the vertical direction. The top panel shows the difference between the projection of the longitudinal ISA and the actual longitudinal ISA at the solenoid position as a function of the vertical tilt angle of the solenoid. The simulated differences are shown as black dots, while a cubic fit with the fit parameter given in the legend is shown in blue. The bottom panel shows the residuals of the cubic fit.

7.3 Determination of the ISA with an idealized RF Wien Filter

The parallel determination of the radial and longitudinal ISA at one location in COSY requires more effort than the previously discussed method. The RF Wien filter was developed to make this possible. The background was that an existing EDM signal of a particle on the design orbit causes a very fast oscillation $\nu_{\mathrm{s,EDM}}$ of the vertical spin component with small amplitude $A_{\mathrm{ver,EDM}}$. This topic has already been discussed in Section (5.2.4). The amplitude and spin tune for an EDM of size $\eta_{\mathrm{EDM}} = 1 \cdot 10^{-4}$ and a deuteron momentum of $p_0 = 970\,\mathrm{MeV/c}$ are given by:

$$|A_{\mathrm{ver,EDM}}| = \left| \frac{\eta_{\mathrm{EDM}} \cdot \beta_0}{2G} \right| \approx 1.60633 \cdot 10^{-4}, \quad \text{and} \tag{7.8}$$

$$|\nu_{\mathrm{s,EDM}}| = \left| \gamma_0 G \sqrt{1 + \left(\frac{\eta_{\mathrm{EDM}} \beta_0}{2G} \right)^2} \right| \approx 0.1609772. \tag{7.9}$$

Figure (7.11) displays a BMAD simulation of a scenario, where a particle is moving in an idealized COSY lattice on the design orbit with spin components initially in the COSY plane. In addition, an EDM signal of the previous described magnitude is assumed. In the upper panel the horizontal spin component s_{x} at a fixed position in COSY is plotted against the simulated revolutions n in COSY, while in the lower panel the vertical spin component s_{y} at a same fixed position in COSY is also plotted against the revolutions in COSY. Simulated data points are indicated in black. A sinusoidal curve was fitted to the simulated data to determine amplitude and frequency and is shown in blue. The fitting parameters are given in the legends. The evaluation position for the simulated data points in COSY was chosen to be the RF Wien Filter location. However, the location does not matter so far, because the design orbit and the closed orbit are identical.

In Figure (7.11) the horizontal spin component s_{x} has been chosen as an example to show the full rotations around the mainly vertically oriented ISA. This can be observed from the amplitude of $|A_{\mathrm{hor,EDM}}| \approx 1$ and the fact that the longitudinal spin component s_{z} would show a π-shifted oscillation with the amplitude of $|A_{\mathrm{lon,EDM}}| \approx 1$. The frequency of the horizontal oscillation is given by the EDM and MDM contributions, as shown by Equation (7.9), and agrees with the theoretical prediction. The same applies to the vertical oscillation frequency. Similarly, the amplitude of the vertical oscillation $|A_{\mathrm{ver,EDM}}|$ agrees with the theoretical prediction from Equation (7.8). This small and fast oscillation is difficult to access experimentally. Therefore, the RF Wien filter has to be used.

The RF Wien filter running on one of the harmonics k_{har} of the spin precession frequency $\nu_{\mathrm{s,Clo}}$, as explained in Section (5.2.4), causes an additional rotation of the spin around the vertical axis, resulting in a macroscopic build-up of the vertical polarization. This spin

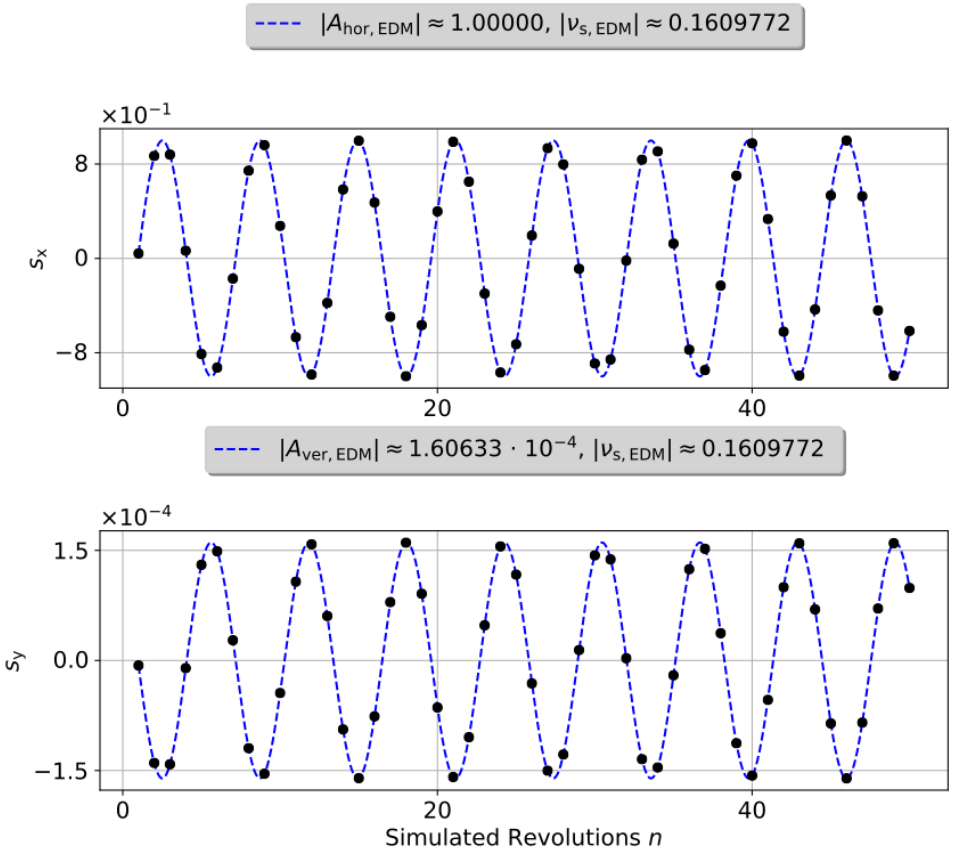

Figure 7.11: Evolution of the horizontal (top panel) and vertical (bottom panel) spin components for a few revolutions in COSY. The particle moves on the design orbit and an EDM of $\eta_{\text{EDM}} = 1 \cdot 10^{-4}$ is assumed. The simulated data points are marked in black, while a fitted sinusoidal curve is indicated by a blue line. The legends show the fitted amplitude and frequency of the oscillation. Errors in the simulated data points and fit parameters are at a numerical level of $1 \cdot 10^{-12}$.

precession frequency $\nu_{\text{s,Clo}}$ must be the one on the closed orbit and can therefore differ in general from a spin tune of $\nu_{\text{s,0}}$ or $\nu_{\text{s,EDM}}$. To adjust the RF Wien filter fields $E_{\text{x,WF}}$ and $B_{\text{y,WF}}$ in the BMAD simulation model, they are varied at the beginning of each revolution n in COSY. To increase the effect of the RF Wien filter and reduce the simulation time, a parameter A_{Amp} is introduced to scale the maximum RF Wien filter fields $E_{\text{max,WF}}$ and $B_{\text{max,WF}}$. The magnitude of A_{Amp} has to be carefully chosen for each COSY setup, as too large fields can lead to particle loss in the RF Wien filter during tracking due to imperfect Lorenz force cancellation. In addition, a relative phase φ_{rel} for the RF Wien Filter has to be chosen. Its purpose is explained later in this section. The complete adjustment of the RF Wien Filter fields in the simulation is shown by Equation (7.10).

$$
\begin{aligned}
E_{\mathrm{x,WF}} &= A_{\mathrm{Amp}} \cdot E_{\mathrm{max,WF}} \cdot \cos\left(2\pi \cdot n \cdot |k_{\mathrm{har}} + \nu_{\mathrm{s,Clo}}| + \varphi_{\mathrm{rel}}\right) \\
B_{\mathrm{y,WF}} &= A_{\mathrm{Amp}} \cdot B_{\mathrm{max,WF}} \cdot \cos\left(2\pi \cdot n \cdot |k_{\mathrm{har}} + \nu_{\mathrm{s,Clo}}| + \varphi_{\mathrm{rel}}\right)
\end{aligned}
\tag{7.10}
$$

Based on these periodic field changes of the RF Wien filter, it is now possible to observe a build-up of vertical polarization. The next section will explain how the tilt of the ISA can be determined from this build-up.

7.3.1 Direct Fit method

The build-up of vertical polarization P_{y} can also be defined as the angle α between vertical polarization and polarization in the COSY plane, given by P_{x} and P_{z}. This is shown in Equation (7.11). In a simulation, a beam does not necessarily have to be used to describe the build-up of vertical polarization by the RF Wien filter. In first order, this it can also be described by the spin components s_{x}, s_{y} and s_{z} of the particle on the closed orbit.

$$
\alpha = \arctan\left(\frac{P_{\mathrm{y}}}{\sqrt{P_{\mathrm{x}}^2 + P_{\mathrm{z}}^2}}\right) \approx \arctan\left(\frac{s_{\mathrm{y}}}{\sqrt{s_{\mathrm{x}}^2 + s_{\mathrm{z}}^2}}\right) \tag{7.11}
$$

In the following, the tilt of the ISA, for a particle on the design orbit, assuming an EDM corresponding to $\eta_{\mathrm{EDM}} = 10^{-4}$ is investigated. It is the identical scenario as in Section (7.3), except that this time the RF Wien filter and the Snake Solenoid are switched on. As described in Section (5.2.4), the fields of both elements are required to find a set-up in which the RF Wien filter field is parallel to the ISA.

To achieve this state, the RF Wien filter must be rotated by different angles $\phi_{\mathrm{WF}}^{\mathrm{set}}$ around the particle beam. The change in angle α per revolution n as a function of the rotation angle of the RF Wien filter provides information about the radial tilt of the ISA. Similarly, the dependence of the angle α per revolution n for different Snake Solenoid field strengths provides information about the longitudinal tilt of the ISA. Unfortunately, the 2 MeV solenoid cannot be used for this purpose because it is located in the same straight section of COSY as the RF Wien filter[2]. To convert the Snake solenoid field strength $B_{\mathrm{Sna}}^{\mathrm{set}}$ to a rotation angle of the longitudinal ISA $\xi_{\mathrm{Sna}}^{\mathrm{set}}$, the calibration factor k_{Sna}, which will be properly introduced in Section (7.2.1), must be used:

$$
\xi_{\mathrm{Sna}}^{\mathrm{set}} = k_{\mathrm{Sna}} \cdot B_{\mathrm{Sna}}^{\mathrm{set}} \tag{7.12}
$$

[2] Due to its location it will also affect the radial ISA tilt. This problem can also be understood by looking at Equation (4.43) and assuming a phase advance of $\theta = \pi$.

The RF Wien filter field and ISA are parallel to each other if there is no build-up of vertical polarization with different relative RF Wien filter phases $\varphi_{\mathrm{rel}}^{\mathrm{set}}$. The dependence of the build-up of the angle α per revolution n on the previously described variables $\phi_{\mathrm{WF}}^{\mathrm{set}}$, $\xi_{\mathrm{Sna}}^{\mathrm{set}}$ and $\varphi_{\mathrm{rel}}^{\mathrm{set}}$ can be summarized by:

$$\begin{aligned}\left(\frac{\mathrm{d}\alpha}{\mathrm{d}n}\right)_{\mathrm{Sim}} &= A_{\mathrm{sol}} \cdot \left(\sin\left(\frac{\xi_{\mathrm{Sna}}^{\mathrm{set}}}{2\sin\pi\cdot\nu_{\mathrm{s,Clo}}} - \xi_{\mathrm{Sna}}^{0}\right)\cdot\cos(\phi_{\mathrm{WF}}^{\mathrm{set}} - \phi_{\mathrm{WF}}^{0})\cdot\cos(\varphi_{\mathrm{rel}}^{\mathrm{set}} - \varphi_{\mathrm{rel}}^{0})\right) \\ &\quad - A_{\mathrm{WF}}\cdot\left(\sin(\phi_{\mathrm{WF}}^{\mathrm{set}} - \phi_{\mathrm{WF}}^{0})\cdot\sin(\varphi_{\mathrm{rel}}^{\mathrm{set}} - \varphi_{\mathrm{rel}}^{0})\right).\end{aligned} \tag{7.13}$$

The variables A_{Sna}, A_{WF}, ξ_{Sol}^{0}, ϕ_{WF}^{0} and $\varphi_{\mathrm{rel}}^{0}$ introduced in Equation (7.13) are fitting parameters. Here A_{Sna} and A_{WF} represent scaling depending on the RF Wien filter field $B_{\mathrm{y,WF}}$ and the path s of the particle beam through the RF Wien filter. Equation (7.14) displays the expected scaling parameters for a deuteron passing the RF Wien Filter at its maximum field of $B_{\mathrm{max,WF}} = 0.03\,\mathrm{mT}$ at a momentum $p_0 = 970\,\mathrm{MeV/c}$.

$$\begin{aligned}A_{\mathrm{Sna}} = A_{\mathrm{WF}} &= 4\pi\cdot\frac{1+G}{\gamma_0^2}\cdot\int_0^{L_{\mathrm{WF}}}\frac{B_{\mathrm{y,WF}}}{\beta_0}\mathrm{d}s \\ &\approx 4\pi\cdot\frac{1+G}{\gamma_0^2}\cdot\frac{B_{\mathrm{y,WF}}\cdot L_{\mathrm{WF}}}{\beta_0} \qquad \approx 3.865\cdot10^{-9}\,\frac{1}{\mathrm{mrad}}\end{aligned} \tag{7.14}$$

The quantities ξ_{Sna}^{0} and ϕ_{WF}^{0} in Equation (7.13) represent the tilt angles of RF Wien Filter and Snake Solenoid at which the vertical polarization build-up is zero. They thus show the tilt of the ISA at the RF Wien filter position and are to be computed in the simulation for an idealized RF Wien filter to determine the ISA tilt due to an EDM of $\eta_{\mathrm{EDM}} = 10^{-4}$.

To do this, the build-up of vertical polarization must first be determined in the BMAD simulation. To speed up the simulation, the RF Wien filter fields are first scaled up by a factor of $A_{\mathrm{Amp}} = 100$. The vertical build-up for a particle starting on the closed orbit with initial spin purely in COSY plane can then be accurately determined for $n = 100$ revolutions using the fitting function from Equation (7.15). Figure (7.12) shows this as an example for an arbitrary setup of RF Wien filter and Snake Solenoid.

$$\begin{aligned} \alpha(n) &= x_0 + x_1 \cdot n + x_2 \cdot \cos\left(2\pi \cdot x_3 \cdot n + x_4\right) \\ &= x_0 + \left(\frac{\mathrm{d}\alpha}{\mathrm{d}n}\right)_{\mathrm{Sim}} \cdot A_{\mathrm{Amp}} \cdot n + A_\alpha \cdot \cos\left(2\pi \cdot \nu_{\mathrm{s},\alpha} \cdot n + x_4\right) \end{aligned} \tag{7.15}$$

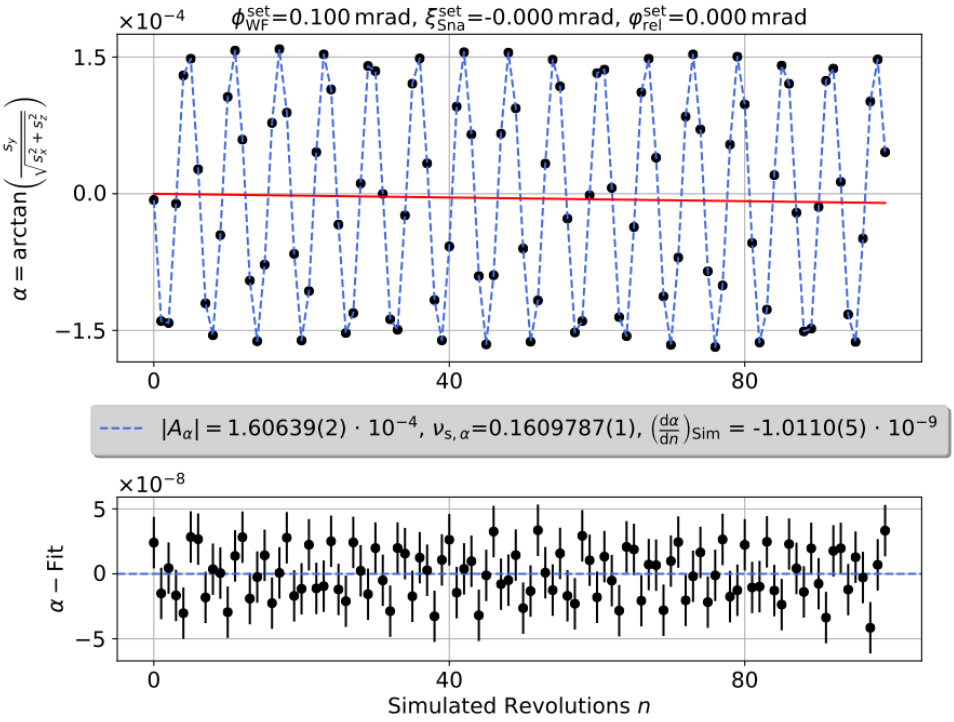

Figure 7.12: Example of the build-up of vertical polarization due to the RF Wien filter for a particle on the design orbit, assuming an EDM of $\eta_{\mathrm{EDM}} = 10^{-4}$. The top panel shows the build-up of the vertical polarization angle α at the position of the RF Wien filter as a function of the number of revolutions n in COSY. The simulated data points are marked in black, while the fit according to Equation (7.15) is shown in blue. The bottom panel shows the residuals of the fit. The main parameters of the fit are shown in the legend in the middle, while the title indicates the RF Wien filter and Snake Solenoid setup used to create this buildup. A red line shows the linear build-up of Equation (7.15).

The top panel of the Figure (7.12) shows the simulated data points of the vertical polarization angle α at the position of the RF Wien filter in black as a function of the number of revolutions n in COSY. The result of fitting Equation (7.15) to the simulated data points is shown in blue, while the most important fit parameters are shown in the center of the figure.

In contrast to the situation in Figure (7.11), where only a numerical error of 10^{-12} was assumed for the simulated data points, the situation regarding the errors becomes more complicated. The reason for this problem is that the RF Wien filter not only causes a net build-up of vertical polarization, which can be described in the fit formula by the fit parameter x_1, but it also causes a periodic change in the spin tune $\nu_{s,\alpha}$. This relationship can also be found in Equation (4.48) and is not described by the fit formular. A solution out of this problem is the proper scaling of the error on the simulated data points. This works, since the RF Wien filter field is on average zero, so that the average spin tune is the one predicted by theory, as shown in Equation (7.9). Thus, the assumption of a constant spin tune is still reasonable. To upscale the errors, Equation (7.15) was first fitted to the simulated data with a numerical error of 10^{-12}. The average residual of the first six simulated data points is determined, as these six data points describe an almost complete spin rotation to a good approximation, and adopted as the new error for all data points. The result of this approach can be observed in the residuals in the lower panel of the Figure (7.12). These residuals show that the fit was successful. The expected systematic scattering of the residuals can be observed, which moves cyclically around the fitting line due to the changing spin tune. In addition, it can be shown that χ^2/ndof moves between 0.5 and 2.0 for different setups of RF Wien filter and Snake Solenoid.

As discussed before, the fitting parameter $\nu_{s,\alpha}$ is expected to be the spin tune predicted by the theory from (7.9). This is the case within the error of the fitting parameter. The amplitude of the oscillation $|A_\alpha|$ also matches the expectation from Equation (7.8) within its error. This has been deliberately sketched for a solenoid switched off, as the Snake Solenoid shifts the amplitude and the spin tuning in addition as this spin manipulator is not vanishing average in contrast to the RF Wien filter field.

The red line shows a linear fit based on the offset and the slope from the fit of Equation (7.15) to the simulated data points. The slope can be found in the legend. It can be seen very clearly that the simulation of 100 cycles with a RF Wien filter field scaling factor of $A_{\text{Amp}} = 100$ is already sufficient to precisely determine the structure of vertical polarization. In order to determine the inclination of the ISA based on Equation (7.13), nine different relative phases $\varphi_{\text{rel}}^{\text{set}}$, equally distributed between 0 and 2π, are run through with fixed RF Wien filter rotation and fixed solenoid strength. In total, three different RF Wien filter rotations $\phi_{\text{WF}}^{\text{set}}$ and three different solenoid settings ξ_{Sna}^{0} are simulated. In combination with the relative RF Wien filter phases 81 different build ups of vertical polarization are simulated. The different simulated slopes are summarized in Figure (7.13).

When fitting the Equation (7.13) to the simulated slopes $\left(\frac{\mathrm{d}\alpha}{\mathrm{d}n}\right)_{\text{Sim}}$, the resulting fit parameters can be used to recalculate so-called fitted slopes $\left(\frac{\mathrm{d}\alpha}{\mathrm{d}n}\right)_{\text{Fit}}$. An ideal line is shown in blue for comparison. Both slopes agree quite well with each other and have a difference

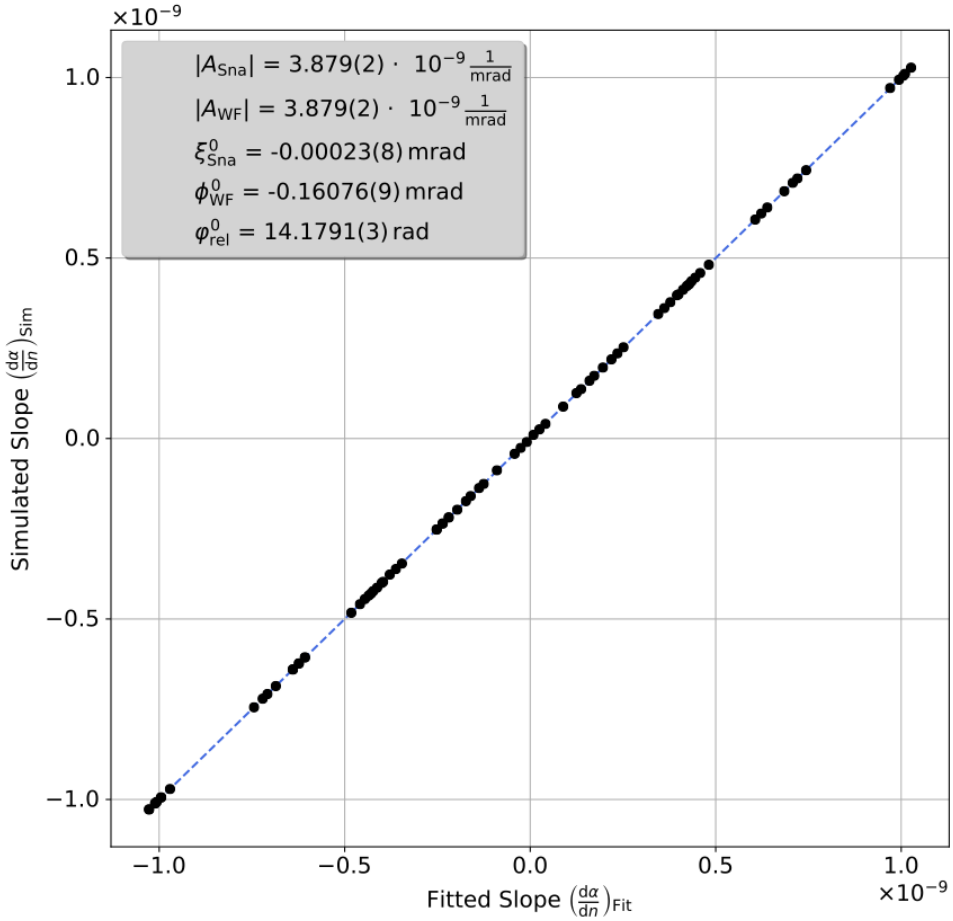

Figure 7.13: Vertical polarization build-up α per revolution n for different RF Wien filter settings and Snake Solenoid strengths. The black dots mark the simulated slopes on the y-axis, as shown in Figure (7.12). After fitting the Equation (7.13) to these simulated slopes, the resulting fit parameter, given in the legend of the figure, can be used to construct so-called fitted slopes. These fitted slopes mark the counterpart to the simulated slopes and are therefore plotted against each other. An ideal line, indicating that the simulated slope and the fitted slope are equal, is shown in blue.

just below the order of 10^{-12} where the fit errors are located. This form of presentation was chosen because it is not possible to show four individual parameters in dependence on each other in one plot. For a better form of presentation, slices can be made by fixing the Snake Solenoid to a particular strength and plotting the simulated build-ups as a function of $\phi_{\mathrm{WF}}^{\mathrm{set}}$ and $\varphi_{\mathrm{rel}}^{\mathrm{set}}$ as shown in Figure (7.14). Here the simulated slopes are marked in black, while the fit is shown as a blue surface plot.

Since the fits using the fit parameters from Figure (7.13) agree quite well with the simulated data, these fit parameters have to be discussed in terms of their agreement with the theoretical prediction. The scaling parameters A_{Sol} and A_{WF} differ by several σ from their theoretical prediction from Equation (7.14). An exact reason for this discrepancy has not

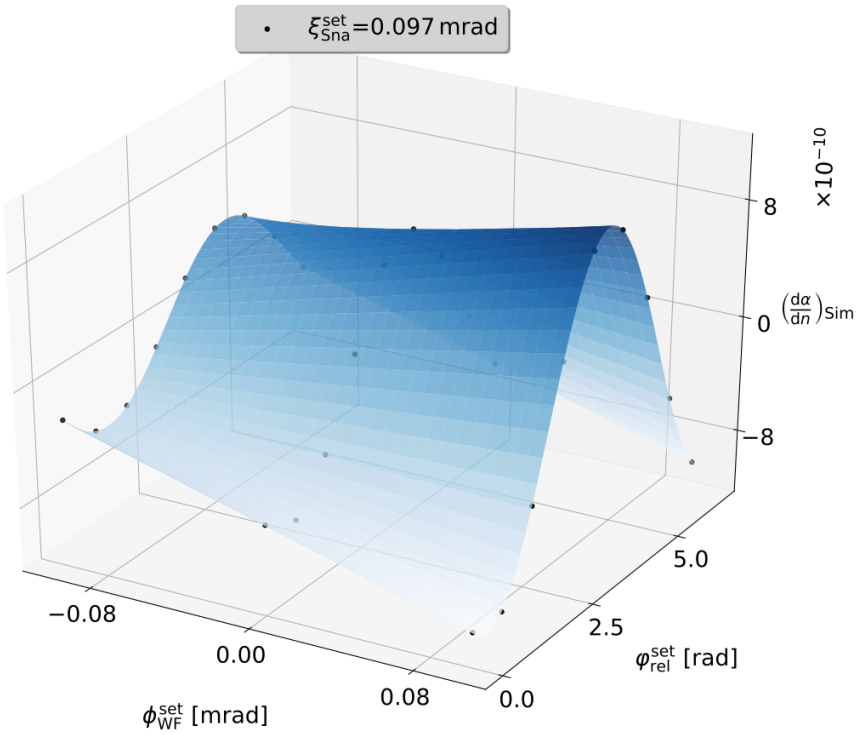

Figure 7.14: Three-dimensional slice of the simulated slopes of the vertical polarization build-up $\left(\frac{d\alpha}{dn}\right)_{Sim}$ as a function of the RF Wien filter rotation ϕ^{set}_{WF} and different RF Wien filter phases φ^{set}_{rel} at a fixed solenoid setting. The simulated slopes are marked in black, while a surface plot based on the Equation (7.13) and the fit parameter given in Figure (7.13) is shown in blue.

yet been found. Meanwhile, the tilt of the radial ISA, given by the fitting parameter ϕ^0_{WF}, agrees perfectly with the prediction from Equation (4.30). The tilt of the longitudinal ISA, given by ξ^0_{Sna}, is also zero within its fitting error, and is therefore as expected.

In summary, the simulation of the RF Wien filter and its use to determine the ISA tilt angle within the BMAD simulation is successful. The method used to determine the ISA tilt angle directly from the build-up of the vertical polarization should be called the direct fit method. Its disadvantage is the difficulty in visualizing the results. Therefore, an alternative method is shown below.

7.3.2 EDM Resonance Map Method

This method is the construction of the so-called *EDM resonance map*. This is a simplification of the direct fit method by reducing one parameter. Equation (7.13) is transformed into Equation (7.16) and Equation (7.17). In this way the determination of the maximum vertical polarization build-up $\left|\left(\frac{d\alpha}{dn}\right)_{max}\right|$ for different relative phases at the RF Wien filter with a fixed RF Wien filter tilt and Snake Solenoid setting using Equation (7.16). The individual simulated vertical polarization build-ups $\left(\frac{d\alpha}{dn}\right)_{Sim}$ are determined in the same way

as in the previous section. Figure (7.15) shows the dependence of $\left(\frac{\mathrm{d}\alpha}{\mathrm{d}n}\right)_{\mathrm{Sim}}$ on the relative RF Wien filter phase $\varphi_{\mathrm{rel}}^{\mathrm{set}}$ and the determination of the maximum vertical polarization $\left|\left(\frac{\mathrm{d}\alpha}{\mathrm{d}n}\right)_{\mathrm{max}}\right|$ for a fixed RF Wien filter rotation and Snake Solenoid field.

$$\begin{aligned}\left(\frac{\mathrm{d}\alpha}{\mathrm{d}n}\right)_{\mathrm{sim}}(\varphi_{\mathrm{rel}}^{\mathrm{set}}) &= \sqrt{\left(\frac{\mathrm{d}\alpha}{\mathrm{d}n}\right)_{\mathrm{max}}^{2}} \cdot \sin\left(\varphi_{\mathrm{rel}}^{\mathrm{set}} + x_1\right) \\ &= x_0 \cdot \sin\left(\varphi_{\mathrm{rel}}^{\mathrm{set}} + x_1\right)\end{aligned} \tag{7.16}$$

$$\left|\left(\frac{\mathrm{d}\alpha}{\mathrm{d}n}\right)_{\mathrm{max}}\right| = \sqrt{A_{\mathrm{Sna}}^2\left(\frac{\xi_{\mathrm{Sna}}^{\mathrm{set}}}{2\sin\pi\nu} - \xi_{\mathrm{Sna}}^{0}\right)^2 + A_{\mathrm{WF}}^2(\phi_{\mathrm{WF}}^{\mathrm{set}} - \phi_{\mathrm{WF}}^{0})^2} = \epsilon_{\mathrm{EDM}} \tag{7.17}$$

For this reason, Figure (7.15) shows the simulated build-up as a function of the relative phase of the RF Wien filter. While the simulated data points are shown as black dots, Equation (7.16) is fitted to them in blue to determine the amplitude of the oscillation and thus the maximum build-up for the applied RF Wien filter rotation and Snake Solenoid field. The residuals of the fit are shown in the bottom panel, while the determined amplitude is shown in the legend. The errors of the simulated data points are propagated errors from the fit parameter from the build-up of vertical polarization. If needed magnitude of the error bars can be reduced in the BMAD simulation by simulating more revolutions n. The fit parameter $\left|\left(\frac{\mathrm{d}\alpha}{\mathrm{d}n}\right)_{\mathrm{max}}\right|$ including the its fit error can be used to generate an EDM resonance map depending on $\xi_{\mathrm{Sna}}^{\mathrm{set}}$ and $\phi_{\mathrm{WF}}^{\mathrm{set}}$, which is described by Equation (7.17). In addition, the quantity $\left|\left(\frac{\mathrm{d}\alpha}{\mathrm{d}n}\right)_{\mathrm{max}}\right|$ can be interpreted as the so-called *EDM Resonance Strength* ϵ_{EDM}. Figure (7.16) shows the EDM resonance map corresponding to Figure (7.13). Comparing the fit parameters of the EDM resonance map with those of the direct fit method, no differences can be detected. Using the perfectly aligned 2 MeV Solenoid, which runs statically during the determination of a map minimum, the longitudinal ISA can also be manipulated without perturbing the closed orbit. This allows a relationship between map minimum and ISA to be derived for a small angle approximation, as shown by:

$$\text{Closed Orbit} = \text{Design Orbit} \quad \Rightarrow \quad n_{\mathrm{x,WF}} = -\phi_{\mathrm{WF}}^{0} \quad \text{and} \quad n_{\mathrm{z,WF}} = -\xi_{\mathrm{Sna}}^{0}. \tag{7.18}$$

7.3.3 EDM Resonance Map Correction Factors

As shown in the determination of the longitudinal ISA using the solenoid calibration method, correction factors are required whenever there is a relative angle between the beam path and the device. This is also the case for the RF Wien filter using the direct fit method and the EDM resonance map method. This aspect will be addressed in this section. Firstly, a pitch angle of the Wien filter is discussed.

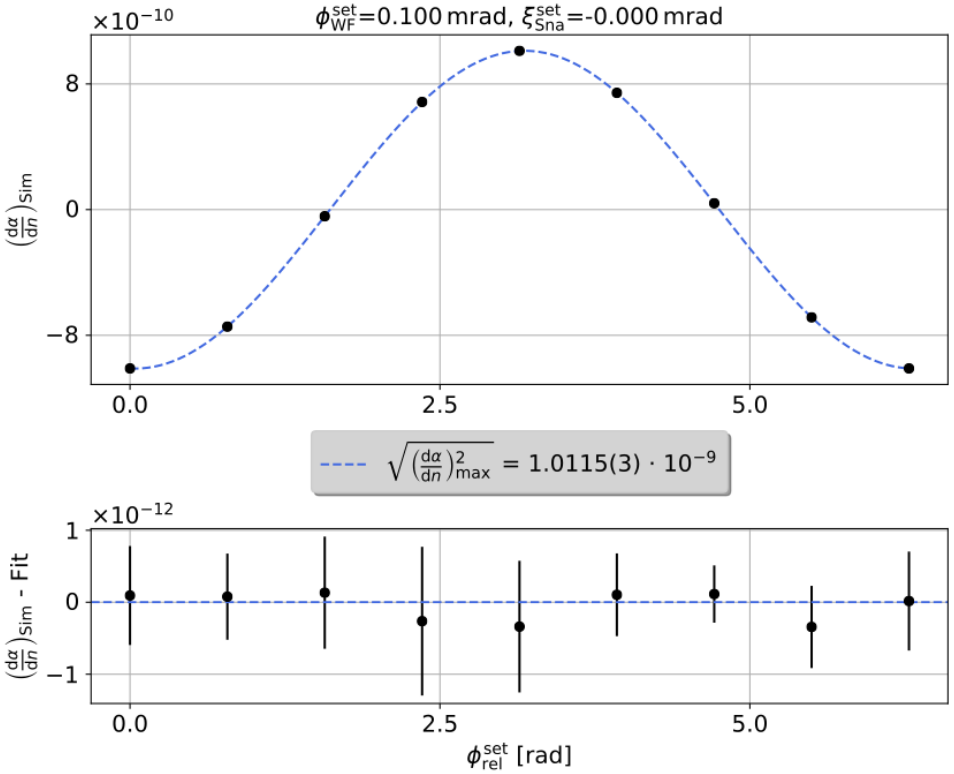

Figure 7.15: Dependence of the vertical polarization build-up on the relative RF Wien filter phase with fixed RF Wien filter tilt and Snake Solenoid setting. The top panel shows the simulated vertical polarization as black points, while the fit of Equation (7.16) to these points is shown in blue. The important fit parameter for the amplitude of the oscillation is shown in the legend. The residuals of the fit are shown in the bottom panel.

A pitch of the RF Wien filter is a horizontal or vertical rotation of the RF Wien filter around its center. This means that the electric and magnetic fields of the RF Wien filter are no longer perpendicular to the beam direction, but at an angle $\theta_{x,WF}$ or $\theta_{y,WF}$. The result is that the Lorentz force on the beam no longer adds up to zero, so that the pitch of the RF Wien filter perturbs the particle beam. This effect occurs mainly in the horizontal phase space and therefore has no effect on the tilt of the ISA. For pitch angles up to 1 mrad, oscillations with an amplitude of a few nm occur in the horizontal phase space and below 1 nm in the vertical phase space. These periodic oscillations move at the synchrotron frequency around the closed orbit. To a good approximation, the closed orbit can therefore be assumed to be stable for small tilt angles of the RF Wien filter.

In a BMAD simulation, the pitch angle of the RF Wien filter can be specified directly in its definition. An EDM resonance map can then be calculated as explained in the previous section. The sum of the minima ϕ^0_{WF} and ξ^0_{Sna} determined in this way and the ISA tilt at the RF Wien filter $n_{x,WF}$ and $n_{z,WF}$ determined using the TAO program can then

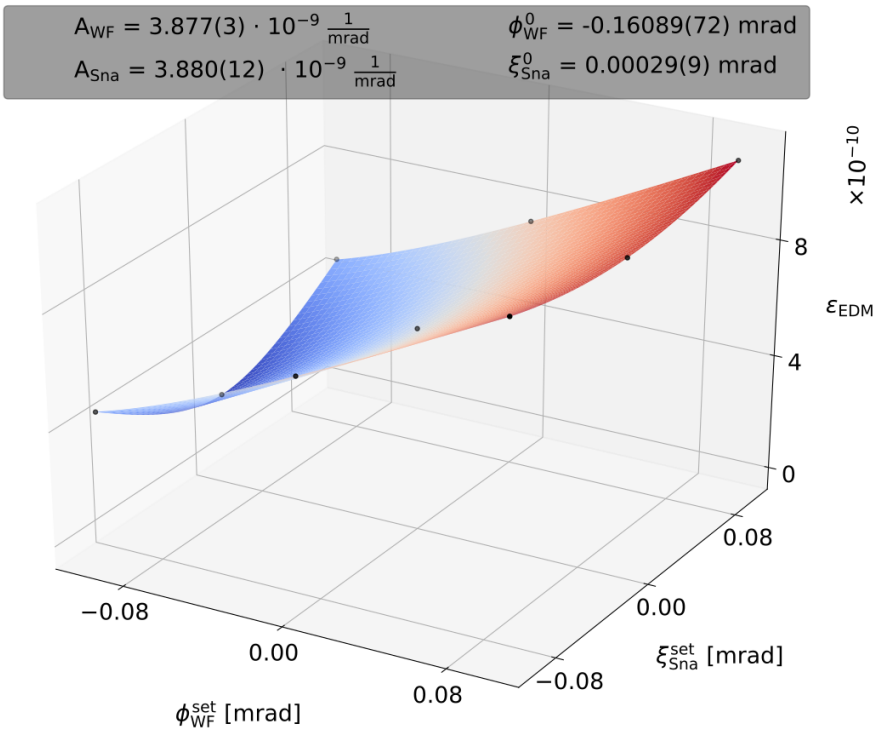

Figure 7.16: EDM resonance map for a deuteron moving on the design orbit with an EDM signal of $\eta_{EDM} = 10^{-4}$. The black dots show the EDM resonance strengths determined by Equation (7.16) as a function of RF Wien filter rotation and Snake Solenoid field. The fitting of Equation (7.17) is shown as a blue-red plane, with the fitting parameters given in the legend.

be plotted against the pitch angle of the RF Wien filter. The results of this procedure using an idealized COSY lattice and an idealized RF Wien filter with an EDM signal of $\eta_{EDM} = 10^{-4}$ are shown in the figures (7.17), (9.16), (9.17) and (9.18). The top panel shows the aforementioned difference between the horizontal and vertical slopes of the RF Wien filter. A linear fit, shown in blue, was applied to the simulated data points, shown in black. The errors on the simulated data points come directly from fitting the map minima. The lower panel shows the results of the linear fit, with the slope of the fit given in the legend. As the offset of the fit is zero within its errors for all different figures, it is not shown here.

The most interesting dependency is shown in Figure (7.17). In all other figures, the slope indicates that there is no dependence of the difference on the RF Wien filter pitch angle. The situation changes when comparing the longitudinal ISA slope and the longitudinal map minimum as a function of vertical pitch angle. A slope can be determined which is comparable to the relativistic γ_0 of the reference particle within one standard deviation. Varying the reference momentum p_0 of the particle beam shows that this fit parameter is indeed correlated with the γ_0. It is also possible to derive this scaling factor directly from the Thomas-BMT equation. It can also be seen how the errors on the

simulated data points increase with larger vertical pitch angles. This is due to the fact that the resonance map only covers the range of ±0.1 mrad in the longitudinal direction. If the fitting points are outside the resonance map, the error on these points also increases.

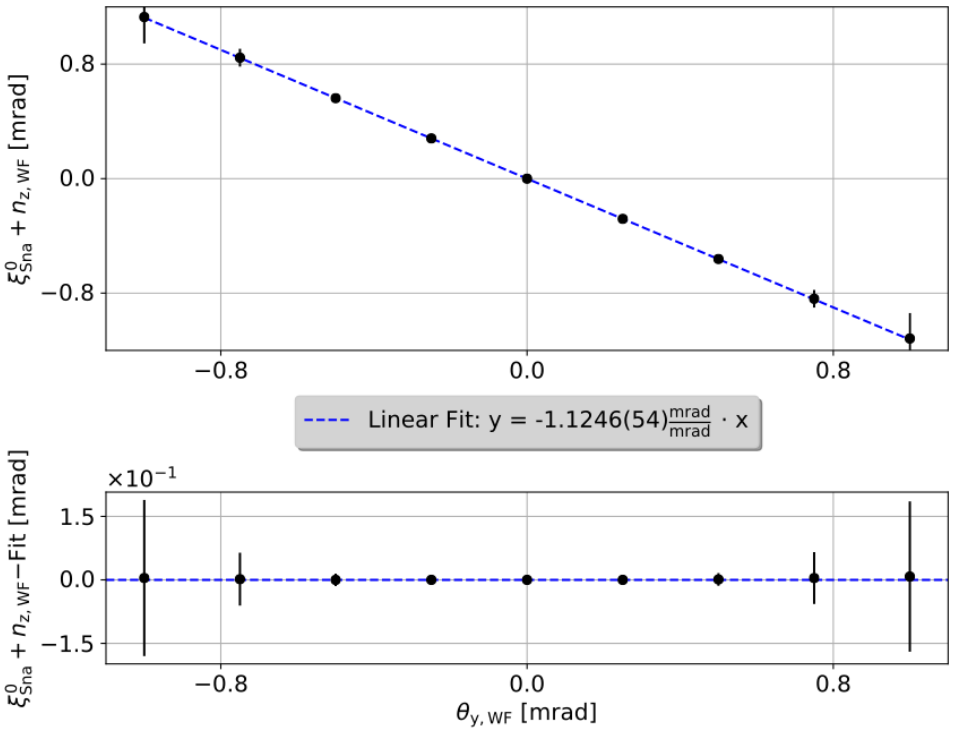

Figure 7.17: Difference between the longitudinal map minimum and the longitudinal ISA tilt at the RF Wien filter position as a function of the vertical pitch angle of an idealized RF Wien filter. In the top panel the simulated data points and their errors are shown in black. The errors of the simulated data points are derived from the fitting errors of the EDM resonance map. A straight line fit to the simulated data points is shown as a blue line and its main fitting parameters are given in the legend. The residuals of the fit are shown in the bottom panel.

Therefore, the vertical orientation of the RF Wien filter in relation to the beam path must be taken into account when comparing experimentally determined map minima with estimates of the ISA tilt at the RF Wien filter position. A correction factor due to rotation of the RF Wien filter, which has not been discussed so far, is the tilt of the RF Wien filter around the beam. As this rotation is also used to determine the radial map minimum, it can be directly related to an additional offset in the radial ISA tilt.

In addition to the pitch angle of the RF Wien filter, the angle at which the particle beam passes through the RF Wien filter must also be known in order to determine a correction factor for this. This beam angle is given by the relative horizontal $P_{\mathrm{x,WF}} = \frac{p_{\mathrm{x,WF}}}{p_0}$ and vertical $P_{\mathrm{y,WF}} = \frac{p_{\mathrm{x,WF}}}{p_0}$ momentum at the RF Wien filter position. In order to be able

to set these momenta in the simulation specifically for the RF Wien filter position, 4 additional steers are added to the COSY lattice in the horizontal phase space and 4 additional steers in the vertical phase space. Their task is to generate a local orbit bump at the RF Wien filter position, while the closed orbit still lies on the design orbit in the rest of the lattice. To do this, two steerers per phase space are installed around the BPM51 before the RF Wien filter and two steerers per phase space are installed around the BPM52 after the RF Wien filter.

Analogous to the previous approach, the difference between the minima ϕ^0_{WF} and ξ^0_{Sna} determined by the EDM resonance map and the ISA tilt angle at the RF Wien filter $n_{\mathrm{x,WF}}$ and $n_{\mathrm{z,WF}}$ determined by the TAO program can then be plotted against the relative momentum at the RF Wien filter position. The results of this procedure using an idealized COSY lattice with an EDM signal of $\eta_{\mathrm{EDM}} = 10^{-4}$ are shown in the figures (7.18), (9.19), (9.20) and (9.21). The top panel shows the aforementioned difference between the horizontal and vertical relative momenta at the RF Wien filter location. A linear fit, shown in blue, was applied to the simulated data points, shown in black. The errors on the simulated data points come directly from fitting the map minima. The bottom panel shows the results of the linear fit, with the slope of the fit shown in the legend. As the offset of the fit is zero within its errors for all different figures, it is not shown here.

In summary there is a dependence of this difference observable when there is relative vertical momentum present, shown by Figure (7.18). There is only negligibly small dependency on the relative horizontal momentum at RF Wien filter present. By changing the particle's reference momentum p_0, which also changes γ_0, it can be shown that the correction factor for the longitudinal map minimum is given by $\gamma - 1$. By combining the results for having a pitched RF Wien filter and a relative beam momentum at RF Wien filter, one derives Equation (7.19).

$$\begin{aligned} n_{\mathrm{x,WF}} &= -\phi^0_{\mathrm{WF}} \\ n_{\mathrm{z,WF}} &= -\xi^0_{\mathrm{Sna}} + (\gamma - 1) \cdot P_{\mathrm{y,WF}} - \gamma \cdot \theta_{\mathrm{y,WF}} \end{aligned} \tag{7.19}$$

Provided that the RF Wien filter is aligned with the beam trajectory in such a way that it causes minimal beam interference, a pure dependence of the correction factor on the vertical momentum is possible. However, it is difficult to estimate how accurate this alignment can be during an experiment such as Precursor Run 2.

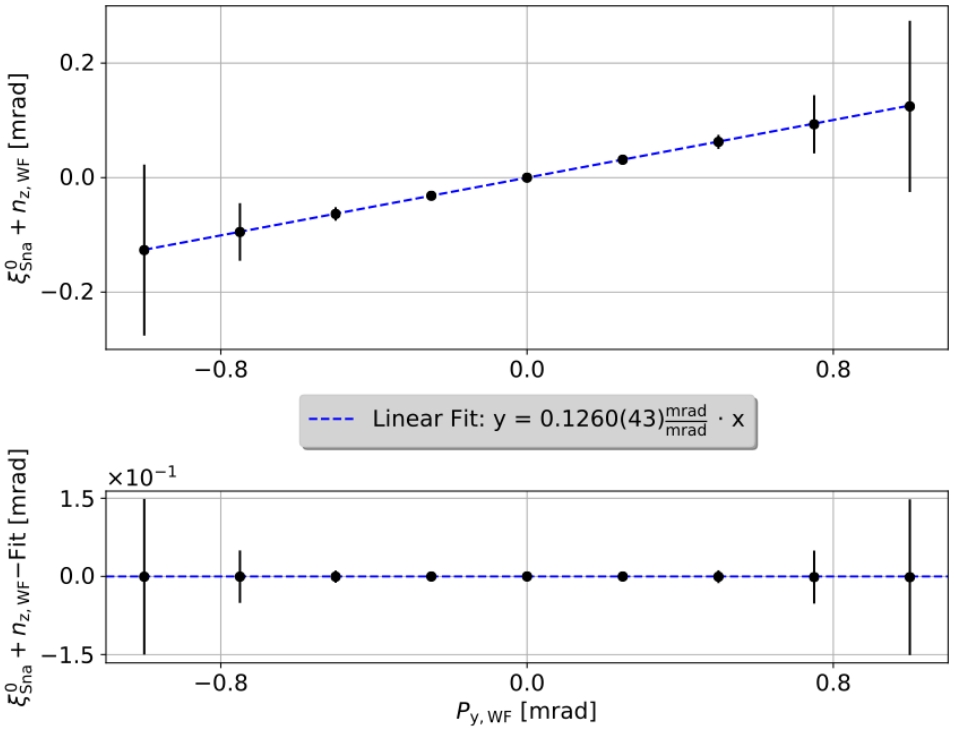

Figure 7.18: Difference between the longitudinal map minimum and the longitudinal ISA tilt at the RF Wien filter position as a function of the vertical momentum at an idealized RF Wien filter. In the top panel the simulated data points and their errors are shown in black. The errors of the simulated data points are derived from the fitting errors of the EDM resonance map. A straight line fit to the simulated data points is shown as a blue line and its main fitting parameters are given in the legend. The residuals of the fit are shown in the bottom panel.

7.3.4 Correction Factors using simulated RF Wien Filter Fields

As only an idealized RF Wien filter has been discussed so far, it is important to discuss the differences that occur when more realistic RF Wien filter fields with a fringe region are used. For this purpose, the simulated RF Wien filter fields from Section (6.2.7) are implemented in the simulation model. Then, analogous to Section (7.3.3), the dependence of the minima of the EDM resonance map on the relative beam momentum at the RF Wien filter and the tilt angle of the RF Wien filter is analyzed. The most important dependencies are shown in Figure (7.19) and Figure (7.20), all others are shown in figures (9.22), (9.23), (9.24), (9.25), (9.26) and (9.27). All figures are designed in the same way as their counterparts in the previous section. It is noticeable, that in contrast to the idealized RF Wien filter the dependencies on relative vertical beam momentum and vertical RF Wien filter pitch angle are scaling with $2\gamma_0$ instead of γ_0. By changing the reference momentum, it is possible to benchmark that the scaling factor is also in fact proportional to γ_0. It can also be seen that the implementation of the simulated RF Wien filter fields results in a small constant error in the determination of the radial ISA tilt

angle given by the offset of $\phi_{\mathrm{WF}}^{\mathrm{Off}} \approx 0.0054\,\mathrm{mrad}$. A summary of the results relating to the simulated RF Wien filter field can be found below:

$$\begin{aligned} n_{\mathrm{x,WF}} &= -\phi_{\mathrm{WF}}^{0} + \phi_{\mathrm{WF}}^{\mathrm{Off}} \\ n_{\mathrm{z,WF}} &= -\xi_{\mathrm{Sna}}^{0} + (2\gamma_0 - 1) \cdot P_{\mathrm{y,WF}} - 2\gamma_0 \cdot \theta_{\mathrm{y,WF}}. \end{aligned} \tag{7.20}$$

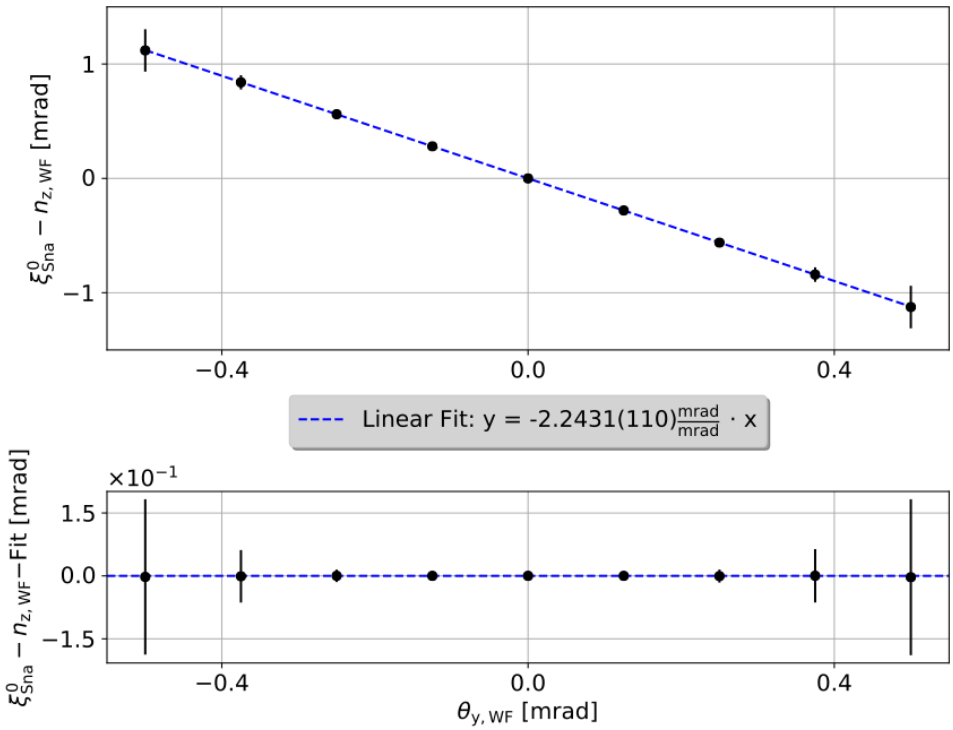

Figure 7.19: Difference between the longitudinal map minimum and the longitudinal ISA tilt at the RF Wien filter position as a function of the vertical pitch angle of an realistic RF Wien filter. In the top panel the simulated data points and their errors are shown in black. The errors of the simulated data points are derived from the fitting errors of the EDM resonance map. A straight line fit to the simulated data points is shown as a blue line and its main fitting parameters are given in the legend. The residuals of the fit are shown in the bottom panel.

7.4 Summary on ISA Determination and Correction Factors

As shown in this chapter, there are many factors to consider when determining the ISA tilt angle, starting with the choice of tracking algorithm in a simulation. Two tracking algorithms are available for the existing BMAD simulation model of COSY. While the BS tracking algorithm has a very short computation time, the PTC tracking algorithm provides more accurate results, but at the cost of significantly longer simulation times. It can be shown that the difference between the two tracking algorithms depends on the size

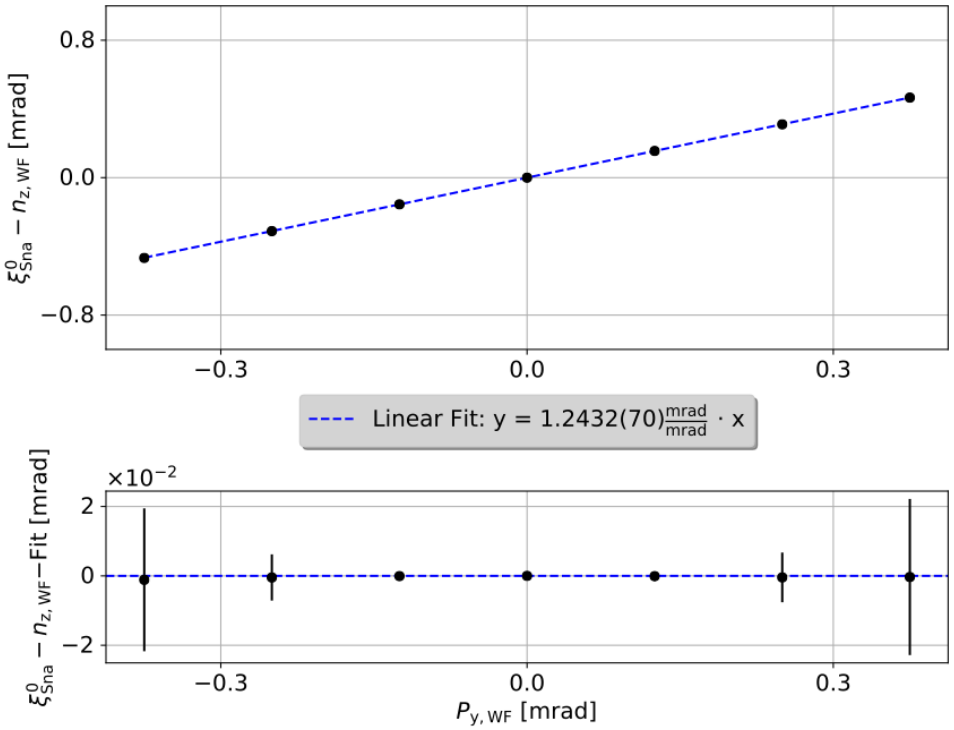

Figure 7.20: Difference between the longitudinal map minimum and the longitudinal ISA tilt at the RF Wien filter position as a function of the vertical momentum at an realistic RF Wien filter. In the top panel the simulated data points and their errors are shown in black. The errors of the simulated data points are derived from the fitting errors of the EDM resonance map. A straight line fit to the simulated data points is shown as a blue line and its main fitting parameters are given in the legend. The residuals of the fit are shown in the bottom panel.

of the closed orbit. For a closed orbit of a few millimeters there are only differences of a few μm and μrad between the two different tracking algorithms. For this reason, the BS tracking algorithm is preferable due to its speed. It is therefore used throughout this thesis.

While the ISA tilt angle can be determined directly in a simulation, it is more difficult to do so in an experiment in COSY. Two different methods are available. On the one hand, the two static solenoids of COSY, the 2 MeV Solenoid and the Snake Solenoid, can be used to determine the tilt of the longitudinal ISA at their position via their influence on the spin tune. If the beam trajectory is at an angle relative to a solenoid magnet, a correction must be applied to the fit parameters to match the ISA tilt angle. This correction depends on the relative vertical momentum of the beam at the magnet position and hence its vertical angle relative to the magnet. As the tilt angle of the solenoid magnets relative to the beam path itself has only a negligible effect compared to the tilt angle of the beam path the behavior can be summarized by:

$$\begin{aligned} n_{\mathrm{z,Sol}} &= c_{\mathrm{Sol}} - P_{\mathrm{y,Sol}}, \\ n_{\mathrm{z,Sna}} &= c_{\mathrm{Sna}} - P_{\mathrm{y,Sna}}. \end{aligned} \tag{7.21}$$

When the RF Wien filter and Snake Solenoid are used in combination, the radial and longitudinal ISA tilt can be determined in parallel at the RF Wien filter position. This is done by determining the macroscopic build-up of vertical polarization as a function of RF Wien filter rotation and Snake Solenoid field. A correction factor must also be taken into account if the beam path is pitched vertically relative to the RF Wien filter. In addition, the vertical pitch angle of the RF Wien filter plays a role, but not its horizontal pitch angle. These results are summarized by:

$$\begin{aligned} n_{\mathrm{x,WF}} &= -\phi^{0}_{\mathrm{WF}}, \\ n_{\mathrm{z,WF}} &= -\xi^{0}_{\mathrm{Sna}} + (\gamma_0 - 1) \cdot P_{\mathrm{y,WF}} - \gamma_0 \cdot \theta_{\mathrm{y,WF}}. \end{aligned} \tag{7.22}$$

If more realistic RF Wien filter fields from a separate simulation are used instead of the idealized RF Wien filter fields, there are further correction factors that need to be taken into account. These are given below, where in particular, the radial map minimum offset of $\phi^{\mathrm{Off}}_{\mathrm{WF}} \approx 0.0054\,\mathrm{mrad}$ must be considered:

$$\begin{aligned} n_{\mathrm{x,WF}} &= -\phi^{0}_{\mathrm{WF}} + \phi^{\mathrm{Off}}_{\mathrm{WF}}, \\ n_{\mathrm{z,WF}} &= -\xi^{0}_{\mathrm{Sna}} + (2\gamma_0 - 1) \cdot P_{\mathrm{y,WF}} - 2\gamma_0 \cdot \theta_{\mathrm{y,WF}}. \end{aligned} \tag{7.23}$$

Now that the determination of the ISA tilt angles and the factors to be taken into account in the presence of perturbations have been analyzed and understood, the next chapter will examine what ISA tilt angles can be expected for the closed orbits present during Precursor Run 2.

CHAPTER 8

Study of Ring Systematics in the Context of the Precursor Runs

While the last chapter showed how to determine the ISA tilt angle for a fixed closed orbit and which correction factors and uncertainties have to be taken into account, this chapter deals with the beam orbit and the systematics in the COSY storage ring during Precursor Run 2. A proper description of the orbit and the systematic effects is necessary since the ISA tilt angle in COSY is determined by both. Therefore, the BMAD simulation model of the COSY storage ring should represent them accurately. For a proper implementation of the systematics, it must be first controlled if the BMAD simulation model of COSY without systematics is able to represent the optical setup of COSY during Precursor Run 2.

8.1 The idealized BMAD Simulation Model and its Optics

To show this, the dipole fields from Table (6.2) and the quadrupole settings from Table (6.4) are used in the simulation model. This setup should result in a twofold optical symmetry with minimized dispersion in the straight sections, capable of holding deuterons at a momentum of $p_0 = 970\,\mathrm{MeV/c}$ on the design orbit of COSY. In order to create an idealized version of the COSY storage ring, all sources of perturbations of the beam orbit due to systematic effects are first neglected. Since no systematic effects are taken into account, there is no need to switch on the steerer magnets, since no additional orbit control is required. Figure (8.1) shows the simulated β-function and dispersion using the setup described above. By plotting the distance from the injection point on the x-axis, Figure (8.1) shows that the horizontal and vertical β functions are twofold symmetric. The horizontal dispersion is also twofold symmetric and is minimized in the straight sections of COSY. On the basis of the β-functions the betatron tunes of the idealized BMAD simulation model of COSY are determined to be $Q_{\mathrm{x}}^{\mathrm{Sim}} = 3.632$ and $Q_{\mathrm{y}}^{\mathrm{Sim}} = 3.708$. These

simulated betatron tunes differ from the measured betatron tunes during Precursor Run 2, which were determined to be $Q_{\mathrm{x}}^{\mathrm{PR2}} \approx 3.531$ and $Q_{\mathrm{y}}^{\mathrm{PR2}} \approx 3.592$. The simulated betatron tunes for an idealized BMAD simulation model of COSY are therefore both too large and off by $\Delta Q_i \approx 0.1$. This is a typical behavior when predicting the betatron tunes by calculation or via a simulation and can also be observed in other simulation models of the COSY storage ring. The reason for this difference are two systematic effects, as the betatron tunes for example depend on the quadrupole field description, the beam trajectory as well as on the magnetic multipole components of all magnets inside the storage ring. These systematic effects however are not implemented in the idealized BMAD simulation model of COSY. It can therefore be concluded that this initial description of the simulated COSY optics is sufficient for an idealized lattice. Furthermore, deuterons with a momentum of $p_0 = 970\,\mathrm{MeV/c}$ move perfectly on the design axis of COSY of the BMAD simulation model as intended. As this idealized BMAD simulation model of COSY has all the expected features implemented, it is taken as the starting point for the implementation and investigation of systematic effects. The following sections will discuss the systematic effects expected in COSY and their impact on the orbit. However, the impact of systematic effects on the betatron tune is neglected. The reason for this is that the betatron tune is already roughly described by the BMAD simulation model and it can be shown in Section (8.3) that primarily the closed orbit plays a crucial role for the ISA tilt.

8.2 Ring Systematics of COSY

8.2.1 Quadrupole systematics and Beam Based Alignment

In the BMAD simulation model of COSY, the quadrupole magnets are only characterized by their effective field length $L_{\mathrm{Eff}}^{\mathrm{Qua}}$ and their focusing strength k_1. These quantities are determined by moving a Hall probe across the fields of the COSY magnets. The accuracy of this measurement is quite good, as long as the Hall probe behaves linearly in the measurement regime and is accurately positioned within the measurement setup [18, 97]. In the BMAD simulation model, both of these quantities are assumed to be error-free, which is not the case in reality. In addition, the shortening of the effective length of the quadrupole magnet due to nearby magnetic material must be considered as a systematic effect. With respect to the closed orbit, these effects act as additional effective dipole kicks in the horizontal and vertical phase space at the location of the quadrupole. This is identical to an effect caused by a misalignment of a quadrupole. This can be illustrated as follows. Due to the field linearity of a quadrupole, a misalignment can be represented by an ideally placed quadrupole with the beam passing through its center and a small effective dipole kick at the position of the quadrupole. The effective dipole kick will be in the direction of the misalignment. Therefore, a purely horizontally misaligned quadrupole will mainly affect the horizontal orbit, while a purely vertically misaligned quadrupole

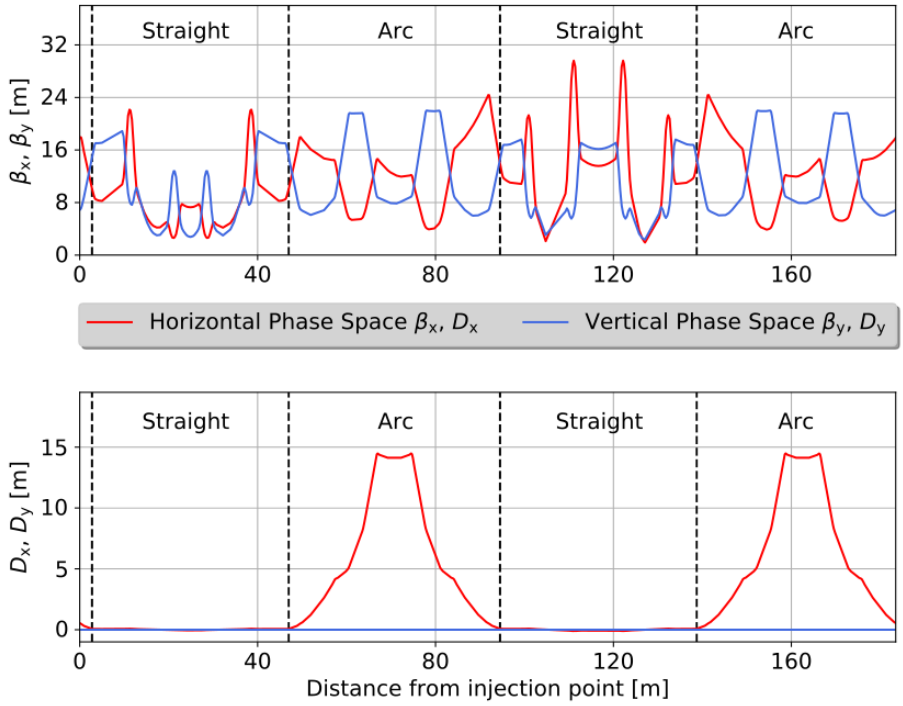

Figure 8.1: BMAD simulation of the COSY optics during Precurser Run 2 assuming an idealized lattice. The top panel shows the horizontal in vertical β-function, while the bottom panel shows the horizontal and vertical dispersion as a function of the distance from the injection point inside the COSY storage ring. For better orientation, the black dashed lines mark the straight sections and the arc regions of COSY.

will mainly affect the vertical orbit, assuming vanishing coupling between the transverse phase spaces. Figure (8.2) sketches this. As the modulation of effective field length and a shortening of it act similarly as a misalignment, it is not possible to distinguish between them when considering the closed orbit isolated and neglecting the optics. For simplicity these systematic effects will therefore be later included in the misalignments.

The misalignments of the COSY quadrupoles were determined by the company Stollenwerk&Burghof by laser-based measurement and an attempt was made to align them as precisely as physically possible. Along the beam axis, the quadrupole offset z_{off} may still deviate by a few millimeters from the intended position, since other elements block the movement of the quadrupole magnets along the COSY design axis in this direction. In the horizontal and vertical phase space, the alignment of the quadrupoles is much better and misalignments are in the order of less than one millimeter. In general, the company Stollenwerk&Burghof states that they are able to align magnets with an accuracy of about $\pm 200\,\mu$m using their laser based system [59, 95]. Unfortunately, the accuracy of this measurement depends on the measurement marks on the top of the quadrupole magnets, which can be loose in some cases. In addition, there is no guarantee that the laser-based reference system used by Stollenwerk&Burghof in their measurement matches the COSY

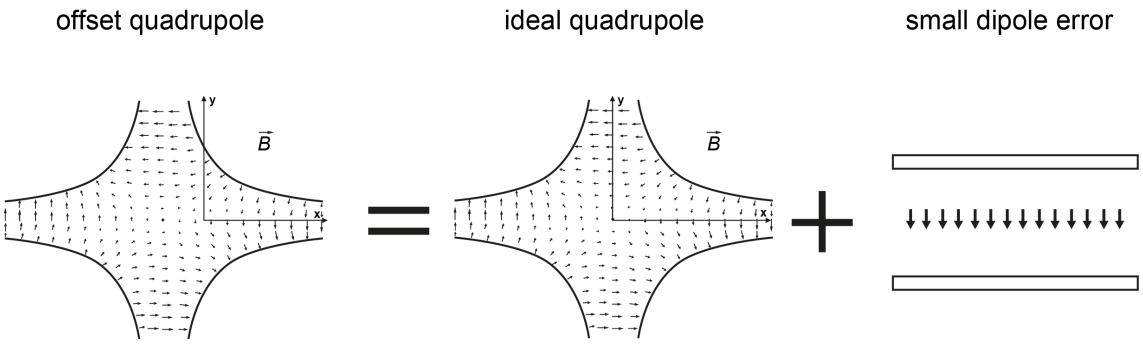

Figure 8.2: Simplified representation of quadrupole misalignment as an ideally positioned quadrupole and an effective dipole kick at the position of the quadrupole.

reference system used in a simulation. Therefore, the laser-based measurement of the magnetic misalignments should only be used to estimate the magnitude of the magnetic displacements and should also be taken into account in this form in the BMAD simulation.

This becomes even clearer when considering an alternative approach to determining the misalignment of the quadrupoles. This approach is to calibrate the BPMs. Such a calibration is necessary for a precision experiment such as Precursor Run 2, since a BPM that is not aligned with the beam axis can lead to an incorrect orbit measurement. T. Wagner performed a BPM calibration at COSY in 2020 [59] using the BBA (**B**eam-**B**ased **A**lignment) method. By creating subsystems in form of groups of nearby BPMs and quadrupole magnets, the BBA uses the magnetic center of the quadrupoles as a reference point to calibrate the BPMs in COSY. In addition, the optimal beam position within the quadrupoles is determined, which corresponds to a misalignment of a quadrupole in this direction. The Figure (8.3) shows the results of T. Wagner regarding the optimal beam position within the quadrupoles of COSY.

Compared to the misalignments determined by Stollenwerk&Burghof, the misalignments determined by BBA tend to be larger, especially in the horizontal phase space. Unfortunately, it cannot be excluded that the interpretation of the optimal position of the particle beam in a quadrupole as a misalignment of the quadrupole is prone to error. To discuss this aspect, a distinction must be made between the calibration of the BPMs via BBA in the straight sections and the calibration of the BPMs in the arcs. The COSY structure is responsible for this. In its straight sections, four quadrupoles in close proximity always form an optical triplet, usually with a BPM positioned somewhere between these quadrupoles. In COSY arcs, the individual quadrupoles are evenly distributed over the entire length of the arc. In most cases a BPM is positioned close to each quadrupole.

Due to this constructional difference, the magnetic center of all four quadrupoles in an optical triplet in the COSY straights can be used to calibrate the one BPM located in the triplet. With this BPM as a common reference point, it can be assumed that all elements

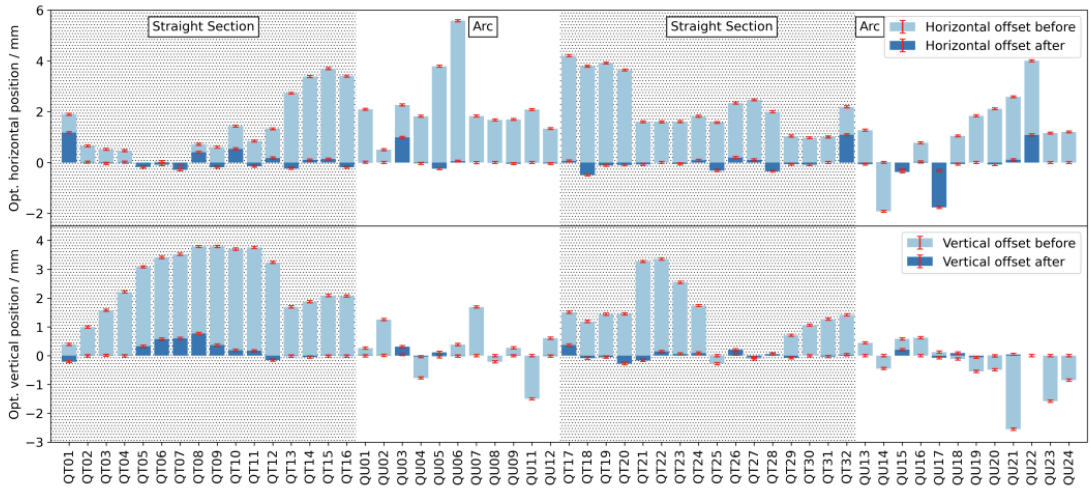

Figure 8.3: Optimal beam position inside the COSY quadrupoles as determined by the BBA before and after calibration of the COSY BPMs. The upper panel shows the horizontal position, while the lower panel shows the vertical position. The data before BPM calibration are shown in light blue and the data after BPM calibration are shown in dark blue. Taken from [59].

in this subsystem of COSY have exactly the relative position to each other as determined by the BBA with an uncertainty of σ_{BBA}=40 μm of the BBA method, indicated in Figure (8.3) as the red error bar. However, the BBA does not provide any information about the position of this subsystem in reference system of COSY. The position of this subsystem can only be estimated on the basis of the laser based measurement by Stollenwerk&Burghof and should be aligned by roughly 200 μm. In the COSY arcs, only one BPM and one quadrupole form a subsystem in which the relative magnetic misalignments determined by the BBA are valid. The errors within this subsystem are σ_{BBA}=40 μm, while the position of the whole subsystem can only be determined by roughly 200 μm. As in some cases even a dipole is positioned in between BPM and the quadrupole magnet the uncertainties on the optimal position in the quadrupole magnet or on the calibration value of the BPM may be even larger. Due to these uncertainties in determining the misalignments of the magnets and since other systematic effects also act as effective orbit kick, the quadrupole misalignments are used as fitting parameters in the further course of this work. It makes sense to limit the size of the possible misalignments. For the sake of simplicity, the rotation of the quadrupoles is neglected in the BMAD simulation model of COSY. Also neglected will be the impact of quadrupole fringe field and magnetic multipoles.

8.2.2 Dipole Systematics

In contrast to the quadrupole magnet, the dipole magnet implemented in the BMAD simulation model is characterized not only by its deflection angle and its bending radius, but also by its fringe field and the shortening of its effective length. Although the latter was estimated by J. Stein on the basis of the distance to nearby magnetic elements, an

independent determination of the dipole shortening is not possible in the COSY storage ring. One reason for this is that the dipoles in the COSY storage ring do not build up their magnetic field synchronously with the particle energy, but with a certain degree of uncertainty. Even when injected into COSY, the field in the dipole magnet and the expected beam momentum, which should ideally always be synchronized, do not match. A smaller dipole current than expected is required, because only then a beam can be injected into COSY. This discrepancy between momentum and dipole current remains during beam acceleration and is caused by non-linearities and remanence effects in the dipole magnet. To represent this effect, a base correction of the dipole field is required, which should generally be the same for all dipoles and is of the order of about 1.0 % of the dipole field [97]. In addition to the base correction of the dipole field, the misalignment of a dipole magnet influences the determination of the shortening of the effective field lengths of dipole magnets. Since all these effects in the horizontal orbit act like an effective kick in the dipole, they cannot be distinguished from each other. Therefore, in the BMAD simulation model, the dipole shortening is used later as a fitting parameter to represent the influence of these systematic effects on the horizontal orbit.

A dipole magnet also acts in the vertical phase space via its misalignment. If the dipole is not rotated and therefore the horizontal phase space is not coupled to the vertical phase space, the misalignment of a dipole can be represented by its fringe field through a purely vertical misalignment. If both phase spaces couple, for example if the dipole is tilted around the beam axis, the shortening of the effective dipole length also affects the vertical phase space. For simplification, however, it is assumed that the influence of the dipole on the vertical phase space is only given by its vertical offset. It will be shown later in the work that this assumption is absolutely sufficient, as this offset is also used here to represent the effective kick of a dipole through systematic effects in the vertical phase space.

Since only the effect on the orbit is to be considered the multipole moments located in the dipole are only represented via the dipole shortening and the vertical dipole offset. Now that all essential systemic effects have been discussed, it will be shown in the next section that the representation of these via effective kicks at their points of action is sufficient to describe the inclination of the ISA.

8.3 Impact on systematics on the ISA Tilt

To investigate the influence of the systematic effects on the ISA tilt, closed orbits perturbated by these have to be created for the BMAD simulation model of COSY. Therefore, starting with an idealized BMAD simulation model of COSY, all quadrupoles are randomly misaligned in both transverse phase space directions based on a normal distribution. This way, effective kicks at the quadrupole positions mimic systematics effects that influence the closed orbit and tilt the initially purely vertical ISA direction. The expectation value

of the normal distribution is zero, indicating that there is no average misalignment of the quadrupole center away from the design axis of COSY. The standard deviation of the normal distribution is gradually increased by an algorithm to produce increasingly larger closed orbits. To compare this perturbed lattice with a version where the orbit correction is applied in COSY and the closed orbits are optimized by the steerer magnets using the ORM method. The goal of the implemented ORM algorithm is to correct the closed orbits at the BPM positions back to the design axis.

Figure (8.4) shows the results of these two algorithms by simulating a thousand different closed orbits and plotting the average[1] radial $\overline{n}_{\mathrm{x}}$ and longitudinal $\overline{n}_{\mathrm{z}}$ ISA tilt as a function of the vertical $y^{\mathrm{Clo}}_{\mathrm{RMS}}$ closed orbit RMS. This form of presentation is chosen because the vertical closed orbit is much more important for ISA tilt than the horizontal closed orbit. The closed orbit RMS values are obtained at the BPM positions in the COSY storage ring and are used instead of the RMS values at all elements within COSY, so that the real storage ring and the BMAD simulation have a common reference value. However, the average ISA tilt is calculated for all elements over the whole COSY ring circumference to account for different relative momenta and longitudinal fields from elements passing off-center or at a relative angle.

There are two interesting observations in Figure (8.4). The first one is that the spread of the average ISA tilt is increasing with an increasing vertical orbit RMS. This is reasonable as in a lattice with larger orbit RMS stronger kicks tilt the ISA away from the ideally purely vertical orientation. Although the spread of the ISA tilt angles increases with increasing RMS values of the vertical orbit, the distribution of average ISA tilts remains centered around a purely vertical ISA position in both the radial and longitudinal directions. This can be explained by the random quadrupole misalignments, which are on average on the design axis and preferring no direction for their misalignment. The second observation in Figure (8.4) is that there is only a small difference visible in between the ISA tilt angle with or without orbit correction applied. One explanation for this is that the orbit correction optimizes only the BPM positions in the simulation model of COSY and does not care about any other position. Another issue is that the steerer magnets are not placed directly next to the quadrupoles. In result the orbit kicks induced by the quadrupoles cannot be corrected at the position of their origin. The small deviation in between the results before and after the orbit correction can therefore be explained by the fact that due to the optimization process more kicks in the vertical phase space are in general present. This does in particular influence the longitudinal ISA tilt, which will be demonstrated in the following.

The RMS value of the ISA tilt angles over the entire circumference of the storage ring can

[1] This means $\overline{n}_{\mathrm{j}} = \frac{1}{N}\sum_{i=1}^{N} n_{j,i}$.

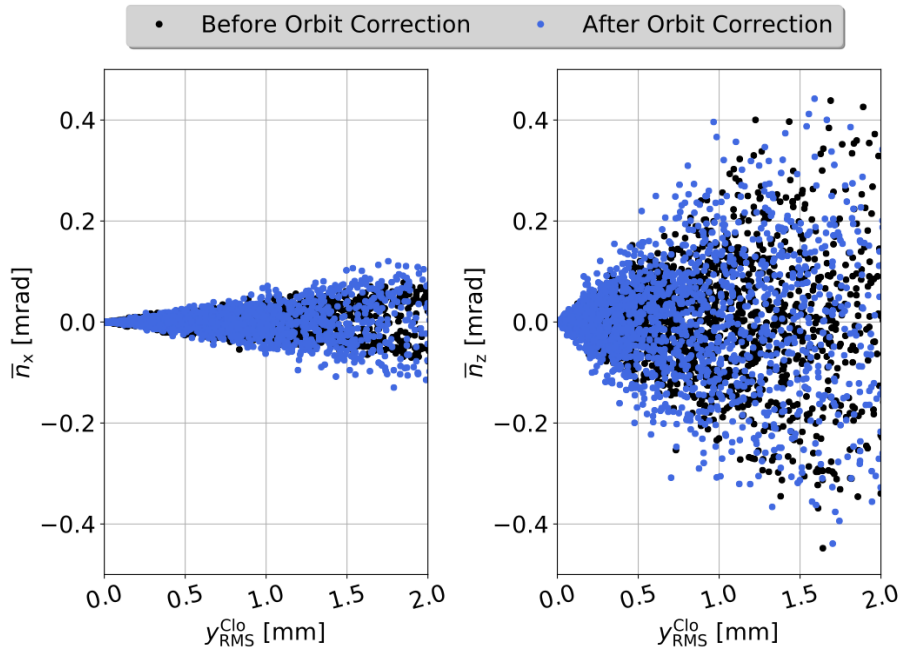

Figure 8.4: Average radial (left panel) and longitudinal (right panel) ISA tilt angles in the COSY storage ring as a function of the vertical orbit RMS value as recorded by the BPMs. In black a situation is shown where the vertical orbit is caused by randomly misaligned quadrupole magnets, while in blue an orbit correction is applied using the steerer magnets after the random quadrupole misalignment is applied.

be used to explain the difference between the scenario with and without orbit correction, and to further illustrate the different effects of the horizontal and vertical phase space on the ISA tilt angle. The reason for this is that the RMS value of the ISA tilt angle carries information about the magnitudes of the ISA tilt angles to be expected for a fixed closed orbit RMS. To show the individual dependencies, the correlation between the horizontal phase space with the RMS values for the closed orbit $x^{\mathrm{Clo}}_{\mathrm{RMS}}$ and for the relative momentum $p^{\mathrm{Clo}}_{\mathrm{x,RMS}}$ is shown, the vertical phase space with its RMS values for the closed orbit $y^{\mathrm{Clo}}_{\mathrm{RMS}}$ and the relative momentum $p^{\mathrm{Clo}}_{\mathrm{y,RMS}}$ and the RMS values for the radial $n_{x,\mathrm{RMS}}$ and longitudinal $n_{z,\mathrm{RMS}}$ ISA tilt must be determined. It is usefull to do this calculation for optimized orbit, as this mimics the situation in the real COSY storage ring. Therefore the correlations, after applying an orbit correction, based on the simulations already discussed for Figure (8.4) are shown in the Figure (8.5).

Figure (8.5) indicates via a color code, how strong the individual quantities are correlated. As all quantities show same sort of moderate positive correlation with each other, indicated by correlation values around 0.5 and no negative correlation is observed the color code is chosen in to range from 0.5 to 1.0. The correlations visible in Figure (8.5) need to be further explained and put into context. For example, by simply steering the horizontal closed orbit away from the design axis and leaving the vertical closed orbit on the design

Figure 8.5: Correlations of the horizontal and vertical RMS values of the closed orbit with the RMS values of the ISA tilt angles. The RMS values are obtained by perturbing the COSY lattice with random quadrupole displacements and then applying an orbit correction by the steerer magnets. The color code, ranging from white at a value of 0.5 to dark blue at a value of 1.0, indicates how strongly the quantities are correlated.

axis, it can be shown that the ISA is not tilted at all. However, if the vertical orbit is steered away from the design axis, there is also a very small horizontal orbit distortion, as there is more transverse coupling in that direction via the bending magnets. The explanation for this phenomenon is that as the vertical trajectories increase, the paths in the dipole magnets become longer, causing a kick in the horizontal phase space. The more the vertical trajectory is distorted, the more the horizontal trajectory reacts. At the same time, the ISA tilt angles also increase as they depend on the vertical orbit. It can therefore be concluded that the horizontal orbit generally has no effect on the ISA tilt angle. It should also be noted that, according to Liouville, the vertical orbit and the relative vertical momentum are directly dependent on each other. Their difference also results from this small coupling of the transverse phase spaces. In principle, however, it can be learned from these correlation coefficients that the tilt of the ISA can be in general deduced from the vertical orbit y^{Clo} at every position in the ring.

Independent of the orbit, the longitudinal fields in the COSY storage play a crucial role for the ISA tilt angles. To demonstrate this, the 2 MeV Solenoid magnet is switched on in the BMAD simulation model of the COSY storage ring and the horizontal and vertical closed orbits are again perturbed by quadrupole misalignments, while an orbit correction is applied by the steerer magnets. The effects of three different longitudinal field strengths on the average ISA tilt angles $\overline{n}_x$ and $\overline{n}_z$ are compared as shown in the Figure (8.6). Their magnitude is chosen so that average longitudinal ISA tilt angles are observed in the milliradian range.

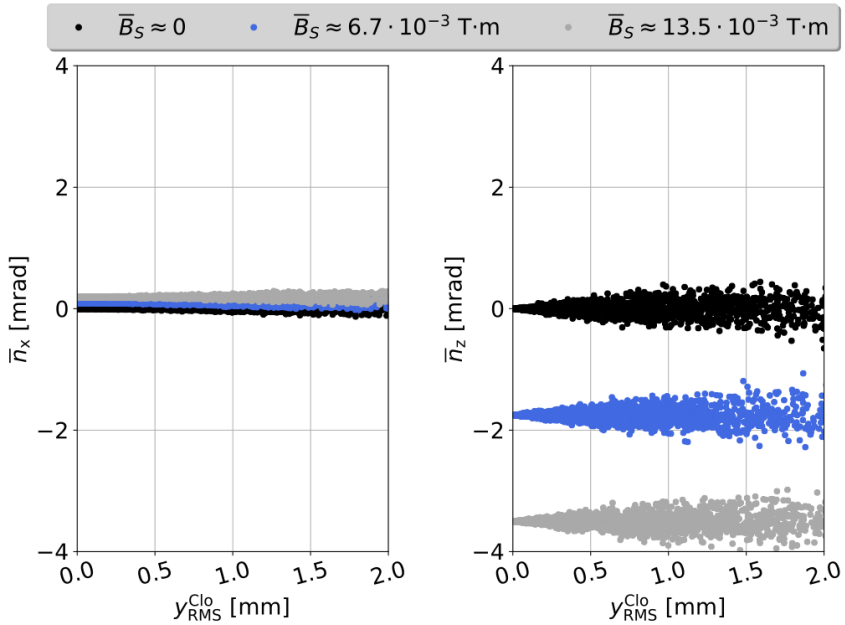

Figure 8.6: Effect of longitudinal fields on the average ISA tilt angle. The average radial (left panel) and longitudinal (right panel) ISA tilt angles in the BMAD simulation model of COSY are shown as a function of the RMS value of the vertical closed orbit. Three different fields from the 2 MeV Solenoid magnet influence the ISA tilt angles in addition to the perturbed orbit and are shown in grey, blue and black respectively.

As shown in Figure (8.6), longitudinal fields in the COSY storage tilt the ISA in addition to the vertical closed orbit. Although Figure (8.6) suggests that longitudinal fields have little effect on the radial ISA tilt angle, it can be shown mathematically using Equation (4.43) that the effect is only observed because the radial ISA tilts in both positive and negative radial directions equally when a longitudinal field is present at one position inside the storage ring. In absolute terms, however, the radial tilt angle of the ISA is about a factor of 4 smaller than the longitudinal tilt angle, which permanently tilted in one direction. In general unknown longitudinal fields could be present everywhere in the COSY storage ring. Ultimately, however, it is only necessary to know or estimate the sum of all longitudinal fields present in COSY to know how much the ISA is tilted in addition to the tilt due to the vertical orbit.

In addition to the influence of the longitudinal fields on the ISA tilt, the influence of a potential EDM signal on the ISA tilt will also be shown. For this purpose, the orbit is again perturbed by quadrupole misalignments and corrected by steerer magnets at the BPM positions. Three different EDM signals are implemented as parameters in the BMAD simulation to investigate their influence on the ISA tilt angles $\overline{n}_{\mathrm{x}}$ and $\overline{n}_{\mathrm{z}}$ as a function of the vertical RMS of the closed orbit. The magnitude of the EDM signals is chosen so as to expect milliradian tilt angles of the radial ISA. Figure (8.7) summarizes the results of this investigation and shows that, as expected, the implementation of an EDM signal only affects the radial ISA. The influence is in the form of a permanent tilt around the entire ring circumference. The longitudinal ISA remains completely unaffected by an EDM signal.

Based on this research, it can be shown that the radial and longitudinal ISA inclination is determined by the vertical closed orbit y_{Clo}, existing longitudinal fields B_{z} and an existing EDM signal η_{EDM}. Equation (8.1) summarizes these influencing factors in simplified form using the functions F_{i} and G_{i}. For example, a longitudinal magnetic field can also influence the vertical orbit. Other storage ring parameters, such as the betatron tunes, are included in the orbit description.

$$\begin{aligned} n_{\mathrm{x}}(s) = &\quad F_1(y_{\mathrm{Clo}}) + \quad F_2(B_{\mathrm{z}}) + F_3(\eta_{\mathrm{EDM}}) \\ n_{\mathrm{z}}(s) = &\quad G_1(y_{\mathrm{Clo}}) + \quad G_2(B_{\mathrm{z}}) \end{aligned} \tag{8.1}$$

The work presented so far in this chapter has ensured that the main systematic effects in the COSY storage ring, which influence the beam orbit, can be represented in a simplified way by effective dipole kicks in the quadrupole position and in the dipole positions. The ISA tilt, assuming a vanishing EDM, is defined by the beam orbit, with additional longitudinal fields to be taken into account. The following section will therefore answer the question of what ISA tilt angles can be expected for the orbit measured in Precursor Run 2.

8.4 Simulation of Precursor Run 2

As outlined in the previous section, a correct orbit description is crucial for a correct description of the ISA tilt angles. Therefore, the simulated orbit in the BMAD simulation model of COSY has to be fitted to the measured orbit during Precursor Run 2. The optimization algorithm of the TAO program is used as a fitting tool for this purpose. Unknown systematic effects in the simulation model, which influence the orbit and therefore have to be fitted, can be represented by effective kicks in the horizontal and vertical phase space at the quadrupole and dipole locations. To ensure that their effects do not become unphysically large, constraints must be placed on the optimization parameters. Due to

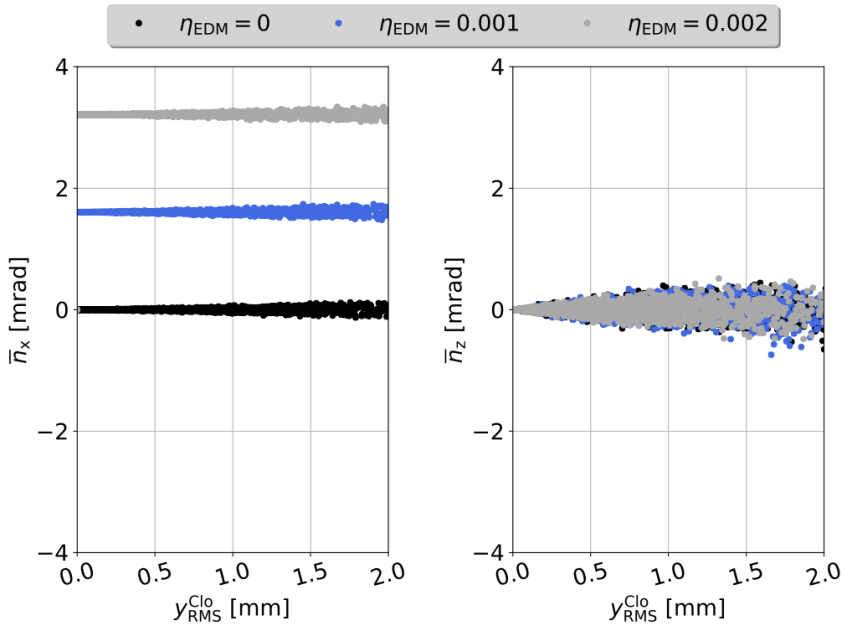

Figure 8.7: Effect of a potential EDM signal on the average ISA tilt angle. The average radial (left panel) and longitudinal (right panel) ISA tilt angles in the BMAD simulation model of COSY are shown as a function of the RMS value of the vertical closed orbit. Three different EDM signals influence the ISA tilt angles in addition to the perturbed orbit and are shown in grey, blue and black respectively.

the number of optimization variables, it should also be avoided that only one potential solution of the closed orbit is considered. To do this, the different optimization variables must be varied before the optimization process is started. Their range of variation should also be physically justified. Since not only the systematic influence of the quadrupoles and the dipole magnet is unknown, but also the position of the BPMs with respect to the design orbit, this property must also be taken into account in the optimization process. In the following, it is explained how all these effects have been considered during the orbit optimization by TAO.

On the one hand, the company Stollenwerk&Burghof has aligned the COSY magnets in several campaigns. They give an accuracy for their laser-based alignment process of $x^{Abs}_{Sto} = 0.2\,mm$ and $y^{Abs}_{Sto} = 0.2\,mm$. However, Stollenwerk&Burghof has found some magnet displacements that exceed the specified accuracy. In addition, T. Wagner's BBA showed that individual magnets may have a different misalignment than measured by Stollenwerk&Burghof due to loose fiducials on the COSY magnets. The difference between the two measurements can be up to 1 mm. Nevertheless, the measurement by Stollenwerk&Burghof gives a good first approximation of the absolute misalignment x^{Abs}_{Off} and y^{Abs}_{Off} of a single magnet with respect to the design axis of COSY.

As there is no further information on the vertical offset of the dipole magnets, the ac-

curacy given by Stollenwerk&Burghof of $y_{\mathrm{Sto}}^{\mathrm{Abs}} = 0.2\,\mathrm{mm}$ is chosen as the initial range of variation for the vertical dipole offset prior to the optimization process. To account for loose fiducials on the dipole magnets, an upper and lower bound of $y_{\mathrm{Lim}}^{\mathrm{Abs}} = 0.8\,\mathrm{mm}$ is set for this optimization variable.

In horizontal phase space, the dipole shortening effect is used to describe all systematic effects on the orbit. Since the dipole shortening effect $B_{\mathrm{Err}}^{\mathrm{Dip}}$ cannot be disentangled from other systematic effects, the optimization variable does not necessarily have to be positive. An initial range of variation is chosen to be $B_{\mathrm{Err,Set}}^{\mathrm{Dip}} = 0.5\,\%$, as this reflects the natural correction of the dipole field needed to inject particles. Shortening effects up to $B_{\mathrm{Err,Lim}}^{\mathrm{Dip}} = 3.0\,\%$ of the absolute dipole field are allowed for the optimizer, as this reflects the maximum shortening effect estimated by J. Stein.

In the case of the quadrupole magnets, in addition to the Stollenwerk&Burghof measurement, T. Wagner's BBA measurement has to be taken into account. In the straight sections of COSY, the BBA forms subsystems from a quadrupole triplet and the BPM in its center. Within a subsystem, the individual quadrupole magnets and the BPM are assumed to be initially misaligned by up to $x_{\mathrm{BBA}}^{\mathrm{Rel}} = 0.04\,\mathrm{mm}$ and $y_{\mathrm{BBA}}^{\mathrm{Rel}} = 0.04\,\mathrm{mm}$, since this corresponds to the precision of the BBA during T. Wagner's work. The position of the subsystem as a whole is used as an optimization variable and shifted before the optimization process based on the precision of the Stollenwerk&Burghof measurement, which corresponds to $x_{\mathrm{Sto}}^{\mathrm{Abs}} = 0.2\,\mathrm{mm}$ and $y_{\mathrm{Sto}}^{\mathrm{Abs}} = 0.2\,\mathrm{mm}$. The reason for these two separate steps is that the BBA is only a relative measurement of the magnet position within the subsystem, whereas the Stollenwerk&Burghof measurement refers to the assumed absolute COSY reference system, which is prone to error due to loose fiducials. Another advantage of this method is that the BPMs move based on the misalignment of the subsystem and therefore record an orbit depending on the misalignment. An upper and lower bound of $x_{\mathrm{Lim}}^{\mathrm{Abs}} = 0.8\,\mathrm{mm}$ and $y_{\mathrm{Lim}}^{\mathrm{Abs}} = 0.8\,\mathrm{mm}$ is chosen for the position of the whole subsystem during the optimization process.

In addition, each straight section of COSY has three BPMs that are not within a quadrupole triplet, but exactly between them. Their calibration during BBA is therefore assumed to be less than ideal, since the more distant quadrupoles of a triplet have to be used for this purpose. Since the position of the triplet subsystem in the global system of COSY can only be determined with a precision given by Stollenwerk&Burghof, these BPMs are misaligned by $x_{\mathrm{Sto}}^{\mathrm{Abs}} = 0.2\,\mathrm{mm}$ and $y_{\mathrm{Sto}}^{\mathrm{Abs}} = 0.2\,\mathrm{mm}$ before the start of the optimization process. Unlike the BPMs within a quadrupole triplet, the position of these BPMs is not changed during the optimization process as they are not coupled to any subsystem within COSY.

The BBA also forms subsystems in the COSY arcs. In contrast to the subsystems in

the COSY straight sections, the subsystems in the COSY arcs consist of a quadrupole and a BPM located directly next to each other. Similar to the subsystems in the COSY straight line, it is assumed that the individual elements within the arc subsystem are aligned relative to each other with an accuracy of $x^{\mathrm{Rel}}_{\mathrm{BBA}} = 0.04\,\mathrm{mm}$ and $y^{\mathrm{Rel}}_{\mathrm{BBA}} = 0.04\,\mathrm{mm}$. The subsystem as a whole is used as an optimization variable and is therefore varied in the range $x^{\mathrm{Abs}}_{\mathrm{Sto}} = 0.2\,\mathrm{mm}$ and $y^{\mathrm{Abs}}_{\mathrm{Sto}} = 0.2\,\mathrm{mm}$ before starting the optimization process. Again an upper and lower bound of $x^{\mathrm{Abs}}_{\mathrm{Lim}} = 0.8\,\mathrm{mm}$ and $y^{\mathrm{Abs}}_{\mathrm{Lim}} = 0.8\,\mathrm{mm}$ is chosen for the optimization variable of the subsystem during the optimization process.

In the COSY arcs it also happens that there is no BPM next to quadrupoles or vice versa. In such cases, it is questionable how well the calibration of the BPMs via the nearest quadrupole center has worked. In some cases, there are dipole magnets between the quadrupole and the BPM, which should make it difficult to determine the quadrupole offset or the BPMs position relative to the quadrupole. In these special cases, the quadrupoles are therefore shifted in the range $x^{\mathrm{Abs}}_{\mathrm{Sto}} = 0.2\,\mathrm{mm}$ and $y^{\mathrm{Abs}}_{\mathrm{Sto}} = 0.2\,\mathrm{mm}$ before the start of the optimization, and then used as independent optimization variables during the optimization process. The optimization variable is again limited to the range around $x^{\mathrm{Abs}}_{\mathrm{Lim}} = 0.8\,\mathrm{mm}$ and $y^{\mathrm{Abs}}_{\mathrm{Lim}} = 0.8\,\mathrm{mm}$. The BPMs are also shifted within $x^{\mathrm{Abs}}_{\mathrm{Sto}} = 0.2\,\mathrm{mm}$ and $y^{\mathrm{Abs}}_{\mathrm{Sto}} = 0.2\,\mathrm{mm}$ relative to the design orbit, but are not moved any further during the optimization process.

Figure (8.8) shows all the elements involved in the optimization process for better visualization. For the optimization of the orbit, the steerer kick values from Precursor Run 2 were loaded into the BMAD simulation model of COSY. Based on the variables described above, 1000 different similar scenarios were generated using magnet and BPM misalignments, as well as the dipole shortenings. The TAO optimization algorithm was designed to correct the horizontal and vertical closed orbit via the optimization parameters in such a way that the orbit measured at the BPMs is corrected to zero for all 1000 scenarios. This reflects the process during the real COSY beam time. The result for the orbit as perceived by the BPMs in the simulation is shown in Figure (8.9).

Figure (8.9) compares the average closed orbit after the TAO optimization process with the orbit measured during Precursor Run 2. Since it is only possible to measure the orbit in the COSY storage ring at its BPMs, the orbit at the position of the BPMs is also analyzed in the BMAD simulation. To mimic the way a real BPM works, the BPM simulation does not calculate the difference between the design orbit and the closed orbit, but the difference between the BPM center and the closed orbit. This is referred to as *BPM orbit*. This behavior is present in the BPMs installed in COSY and therefore has to be taken into account in Precursor Run 2.

Before starting a detailed discussion of Figure (8.9), it should be noted that the optimization algorithm has no information about the measured orbit. The goal of the optimization

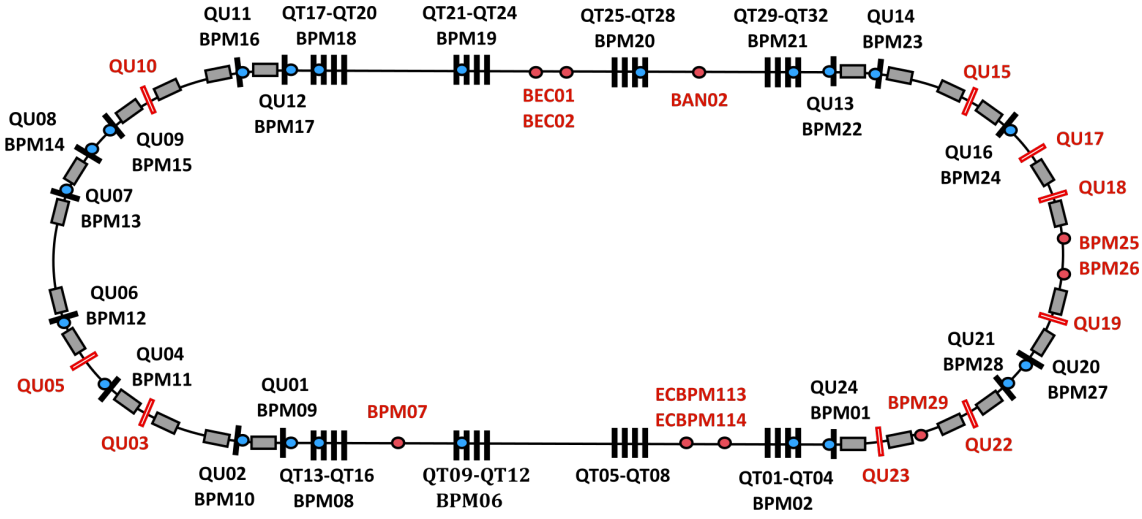

Figure 8.8: Floor plan of the COSY storage ring showing all dipoles, quadrupoles and BPMs. A BPM is marked as a blue circle if a quadrupole magnet is nearby and can be used via BBA to calibrate the BPM offset. The quadrupoles used for this purpose are indicated by a black rectangle. If the calibration is doubtful because the partners are too far apart or there is a dipole between them, the BPM or quadrupole is marked in red. Dipole magnets are indicated by a grey rectangle.

algorithm is to vary systematic effects in such a way that the BPM orbit is as close to zero as possible at all BPM positions in COSY. It is decided not to adapt the BPM orbit to the orbit measured in Precursor Run 2, since the transverse position of the BPM center in the reference system of the real COSY storage is only known to a limited extent. Therefore, problems arise when the optimization algorithm adjusts the BPM orbit to incorrectly measured orbits, since a correct description of correctly measured orbits is not always possible. This is due to the fact that a mathematically closed solution is required for the closed orbit description. However, this method can be used to estimate which BPMs may be inadequately calibrated. In addition, this method can be used to estimate the magnitude of all systematic effects present in the real COSY storage ring. This is due to the fact that two classes of effects act on the orbit in the simulation model. These are the steerer magnets and the systematic effects. While the influence of the steering magnets on the closed orbit is relatively well known from various measurements, the influence of the systematic effects is only roughly known. Therefore, the optimization algorithm searches for the correct combination of systematic effects so that the BPM orbit in the simulation matches the BPM orbit during Precursor Run 2.

In its upper panel, Figure (8.9) compares the average horizontal orbit of the simulation after applying the optimization algorithm and the horizontal orbit from Precurser Run 2. The error bars[2] in blue graph describe different results of the 1000 iterations in simulation

[2]One is talking here about $\sigma_x^2 = \frac{1}{N}\sum_{i=1}^{N}(x_i + \overline{x})$, at every BPM position, with N being the number of iterations.

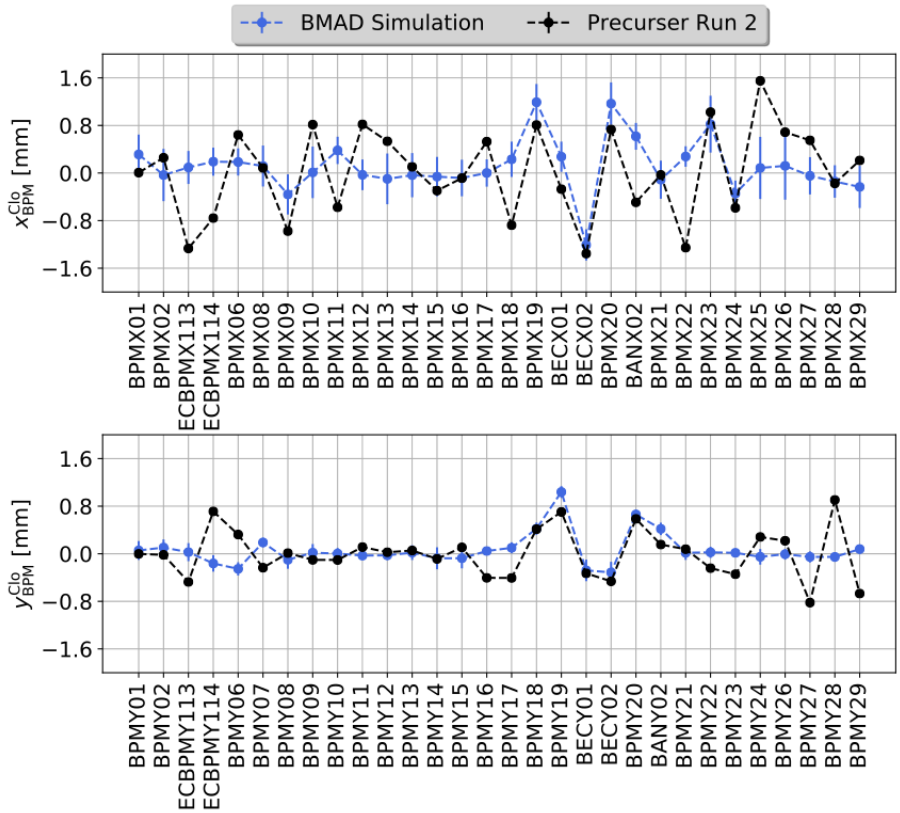

Figure 8.9: Optimized horizontal and vertical closed orbit as observed by the BPMs of COSY. The horizontal and vertical beam position at BPM location is shown in dependency of the individual BPM. In blue the average result of the 1000 scenarios after optimization is displayed, while the orbit during Precursor Run 2 as recorded by the COSY BPMs is shown in black.

with various initial conditions. The measured orbit shown in black also has error bars, based on the static fluctuation of the BPM results during Precursor Run 2. These are negligible in the scope presented. From the blue graph describing the simulation results one is able to observe that the adjustment of the BPM orbit to the value zero is generally very successful. However, there are exceptions. These exceptions are in the range from *BPMX18* to *BPMX23*. Interestingly, the BPM orbits for some of these exceptions agree very well with the measured orbits from Precursor Run 2. This agreement can be explained by the exceptionally strong horizontal steerer kick at the position of the electron cooler between *BECX01* and *BECX02*, which significantly determines the horizontal orbit at this point. In the remaining course, however, the simulated orbit and the measured orbit are in much worse agreement. An explanation for this difference becomes clear when looking at the fitting parameters and will be taken up again later. Since the horizontal orbit is generally only of minor importance for the ISA tilt angle, this orbit description is sufficient.

In the lower panel, Figure (8.9) shows the results for the vertical orbit from BMAD simulation and Precursor Run 2. Similar to the horizontal orbit the optimization algorithm is

in general successful in its flattening of the BPM orbit. It is also noticeable that the simulation results around *BECY*, which is the vertical counterpart to *BECX*, agree relatively well with the measurement results without any adjustment of the simulation to Precursor Run 2. The reason for this agreement is coming from the steerer magnet kicks around the electron cooler which dominate the orbit. In general, the simulated vertical orbit and the measured vertical orbit agree much better than is the case in the horizontal phase space. However, there are also deviations here. These will be discussed in more detail below.

It is not surprising that the BPM orbit results between simulation and measurement for *BPMY113* and *BPMY114* are so different. Both BPMs were not calibrated during the Precursor Run 2 beam time and have a strong noise, so their orbit measurement is doubtful. Close to these two BPMs are *BPMY06* and *BPMY07*, where simulation and measurement are also different. Since a quadrupole triplet can be used to calibrate *BPMY06*, the BPM orbit measured in Precureser Run 2 should be correct, as should the BPM orbit at *BPMY07*. A look at the relative vertical quadrupole misalignments determined by the BBA shows that the quadrupole triplet located between *ECBPMY113* and *BPMY07* is misaligned on average by about 0.5 mm in the vertical direction. However, the average misalignment is not taken into account in the BMAD simulation. It can therefore be concluded that the differences after optimization between the BMAD simulation and Precursor Run 2 are due to an incorrect orbit measurement and inadequate modelling in parallel. This problem illustrates perfectly the challenge one faces when evaluating why the BMAD simulation does not describe Precursor Run 2. Still not all deviations between simulation and measurement can be explained in exactly this same way. For example, it has not yet been possible to explain why there is such a difference between simulation and measurement for *BPMY16* and *BPMY17*.

On the other hand, the differences between simulation and measurement in the BPM orbit for the BPMs from *BPMY22* to *BPMY29* can be explained by the fact that in the second arc of COSY the beam is also injected and extracted. Therefore, in the second arc of COSY it is not clear whether the BPM calibration was successful or how well the quadrupoles were aligned, as shown in Figure (8.8). This suspicion is confirmed by similar observations made by M. Hartmann [93] using an orbit optimizer for the horizontal orbit. In general, however, it can be assumed that the vertical orbit adjustment is successful with the reliable information provided. Therefore, the optimization parameters will now be discussed.

Figure (8.10) and Figure (8.11) show the results of the quadrupole position optimization. In the straight sections of COSY, the quadrupole triplet position is optimized, while in the arcs each quadrupole is adjusted individually. In both figures the initial variation of the fitting parameters is shown as a blue area, while the limits of the fitting parameters are shown as a dashed blue line. To obtain an estimate of the magnitude of the mis-

alignments required to optimize the BPM orbit, the RMS value of the mean quadrupole misalignment is calculated for each phase space and shown in the legend. It is interesting to note that the resulting RMS of the mean quadrupole misalignment is identical for the arc and telescope quadrupoles and also for the horizontal and vertical phase space. One also obtains a similar RMS value for the transverse quadrupole misalignments when using the Stollenwerk&Burghof measurements from 2020. It can therefore be concluded that the magnitude of these misalignments is reasonable.

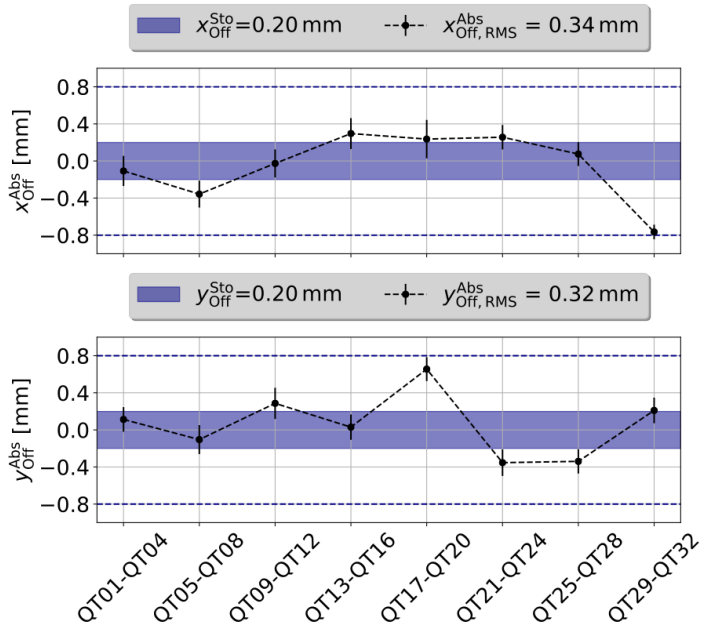

Figure 8.10: Quadrupole triplet optimization variables. The top/bottom panel shows the average horizontal/vertical misalignment of the quadrupole triplets in black. A blue area marks the range of initial variation before optimization, while a blue dashed line indicates the optimization limits. The legend displays the initial range of variation and the RMS of the optimization variable.

Another interesting observation is that the horizontal quadrupole misalignment associated with the quadrupole triplet *QT29-QT32* reaches the optimization limit. This particular quadrupole triplet is located at the end of the second straight section of COSY after the 100 keV electron cooler. It is located at a position with large horizontal momenta due to the strong steerer kicks from the 100 keV electron cooler steerer. Therefore, the optimizer tries to compensate for these large horizontal momenta by shifting this quadrupole group as much as possible in the horizontal phase space in order to smoothly enter the COSY arc. This problem becomes even more obvious when looking at the optimization parameter associated with the dipole, as shown in Figure (8.12).

This figure sketches the optimized dipole field error in its top panel. The largest kicks resulting from this optimization process are at the dipoles *BE13* and *BE14*, which are

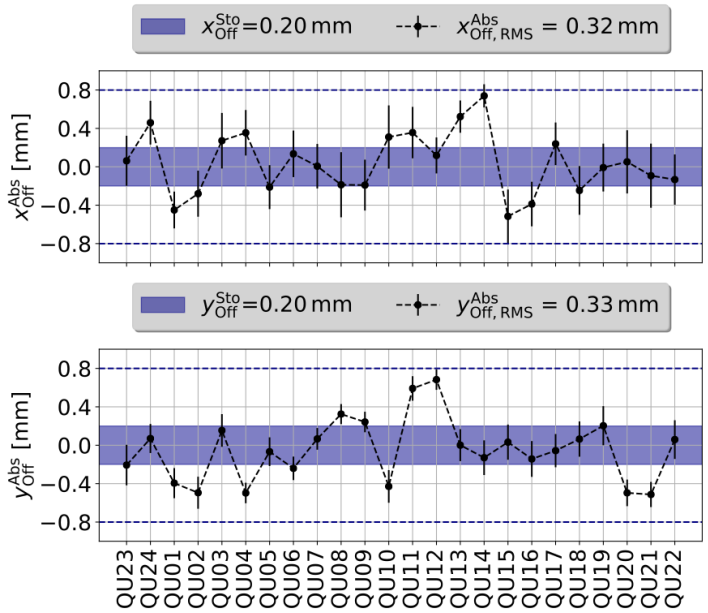

Figure 8.11: Arc quadrupole optimization variables. The top/bottom panel shows the average horizontal/vertical misalignment of the individual arc quadrupole in black. A blue area marks the range of initial variation before optimization, while a blue dashed line indicates the optimization limits. The legend displays the initial range of variation and the RMS of the optimization variable.

located right after the quadrupole triplet *QT29-QT32*. This demonstrates that strong horizontal kicks are necessary at positions after the 100 keV electron cooler to enter the second COSY arcs. However this figure also demonstrates why the horizontal simulated BPM orbit and the measured BPM orbit during Precursor Run 2 differ. The dipole field errors are way too small to describe the effective dipole field shortening effect in the real COSY ring. As the horizontal orbit is not important for the ISA tilt description this difference is in that context not relevant. However regarding a proper and precise orbit description it is. Figure (8.12) also shows the vertical misalignment of the dipoles after optimization. These values show no systematic deviation, although Stollenwerk&Burghof measured systematic deviations of up to 0.5 mm. Overall, it must be summarized that the use of the dipoles as an optimization variable did not bring any added value. There is still potential for improvement here. In principle, it can even be shown that the entire fitting process also works without the vertical dipole offsets. Despite the problems described, the optimization of the vertical orbit is successful and the quadrupole misalignments, which are important in the Straight sections, are in the correct order of magnitude. Therefore, the ISA tilt angle during Precursor Run 2 can now be discussed.

8.4.1 Discussion of Simulation Results and Experimental Results

In order to analyze the ISA tilt angles resulting from the optimization of the BPM orbit, the reference system has to be changed from the BPM orbit to the horizontal x^{Clo}_{Abs} and ver-

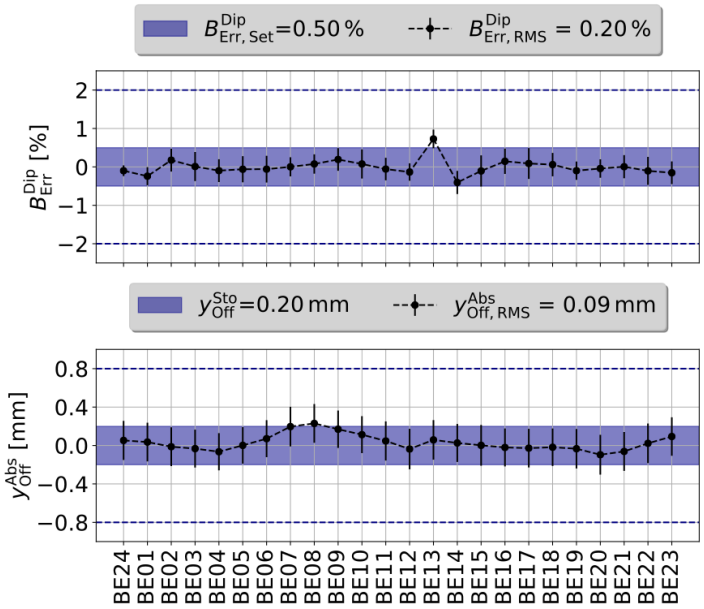

Figure 8.12: Dipole magnet optimization variables. The top panel shows the average dipole field error while the bottom panel displays the average vertical dipole misalignment. The blue area marks the range of initial variation before optimization, while a blue dashed line indicates the optimization limits. The legend displays the initial range of variation and the RMS of the optimization variable.

tical y^{Clo}_{Abs} orbit in the COSY reference system, which results from the difference between the design orbit and the closed orbit. As shown at the beginning of this chapter, the radial n_x and longitudinal n_z ISA tilt angle depends on the vertical orbit in the COSY reference system. To get a better idea of the expected orbits in the COSY reference system, Figure (8.13) shows the first 100 iterations of the optimization algorithm after optimization. In addition, Figure (8.14) shows the corresponding ISA tilt angles.

As shown in Figure (8.13) and Figure (8.14), both the orbit and the ISA tilt angle in the COSY reference system converge towards a mean solution. Overall, based on the vertical orbit in the BMAD simulation, radial ISA tilt angles of up to $\pm 80\,\mu$rad and longitudinal ISA tilt angles of up to $\pm 600\,\mu$rad are expected to occur during Precursor Run 2. For the comparison of the results from Precursor Run 2 with the BMAD simulation the ISA tilt angle has to be determined at particular locations in COSY. These are the position of the snake magnet, which is located at a distance of $s_{Sna} = 126.128\,$m from the injection point, the position of the 2 MeV Solenoid, which is located at a distance of $s_{Sol} = 16.272\,$m from the injection point, and at the RF Wien filter, whose distance from the injection point is given by $s_{WF} = 24.890\,$m. Since correction factors based on the relative vertical momentum at the measurement position are required in the case of a vertically perturbed orbit, the relative vertical momenta are also determined at all three locations in the BMAD simulation. Unfortunately an experimental determination of the relative vertical momentum

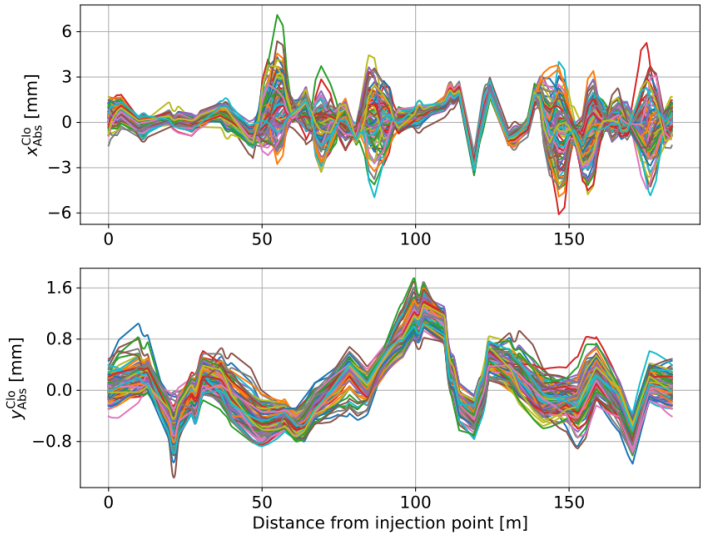

Figure 8.13: Simulated horizontal and vertical closed orbits in the reference system of the COSY storage ring after optimization of the BPM orbit. Both closed orbits are shown as a function of the distance from the injection point. Each color corresponds to one iteration of the optimization algorithm. A total of 100 different solutions with different initial conditions are shown.

is prone to error due to the limited number of BPMs in the COSY storage ring. The figures (8.15), (8.16) and (8.17) show the distribution of the ISA tilt angles and the vertical momentum at the position of the snake solenoid, the 2 MeV Solenoid and the RF Wien filter. For the determination of the mean of each distribution a Gaussian function is fitted to the simulated data points.

Using the means and standard deviations obtained in this way, the measurement results of Precursor Run 2 can be compared with their simulated counterparts. This is done in Table (8.1). In the simulation, a distinction is made between the results of an idealized RF Wien filter and the results of a RF Wien filter with simulated fields, which referred to as a realistic RF Wien filter. It was also assumed that the both simulated RF Wien filter fields have no vertical tilt angle relative to the design axis.

Element	**BMAD/TAO Simulation**	**Precursor Run 2** [98]
2 Mev Solenoid	$c_{\mathrm{Sol}} = +0.043(34)$ mrad	$c_{\mathrm{Sol}} = -0.0705(9)$ mrad
Snake Solenoid	$c_{\mathrm{Sna}} = +0.052(27)$ mrad	$c_{\mathrm{Sna}} = -0.057(1)$ mrad
Idealized RF Wien Filter	$\phi^0_{\mathrm{WF}} = -0.0201(92)$ mrad $\xi^0_{\mathrm{WF}} = -0.008(32)$ mrad	/ /
Realistic RF Wien Filter	$\phi^0_{\mathrm{WF}} = -0.0147(92)$ mrad $\xi^0_{\mathrm{WF}} = -0.084(46)$ mrad	$\phi^0_{\mathrm{WF}} = -2.1(1)$ mrad $\xi^0_{\mathrm{WF}} = +3.9(6)$ mrad

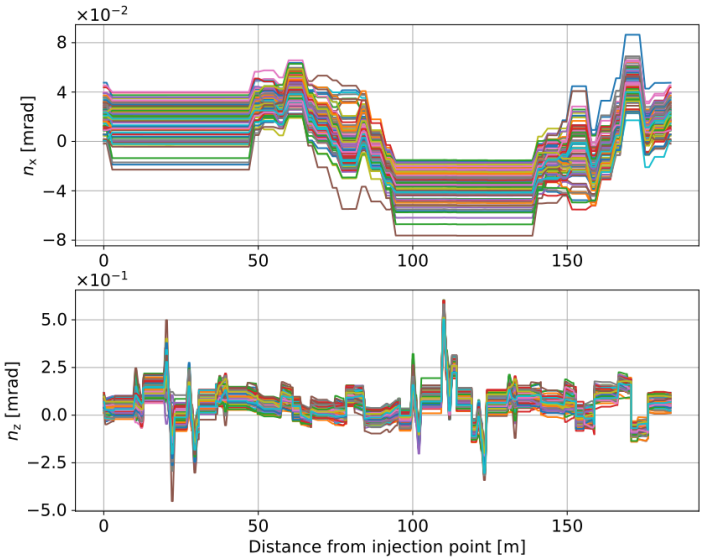

Figure 8.14: Resulting radial and longitudinal ISA tilt angles for the closed orbits shown in the Figure (8.13) as a function of distance from the injection point. Each color corresponds to an iteration of the optimization algorithm.

Table 8.1: Comparison of the ISA tilt results obtained in the BMAD/TAO simulation by optimizing the BPM orbit and in Precursor Run 2 at COSY's static solenoids and the RF Wien filter. The BMAD/TAO simulation assumes no RF Wien filter tilt angle and no EDM signal.

As it can be seen in the Table (8.1), the BMAD simulation results at the 2 MeV Solenoid and the Snake Solenoid are in the same order of magnitude and show a 4σ deviation. On the one hand, this can be explained by the relatively large errors in the simulation. On the other hand, the magnitudes of the ISA tilt angles are correctly described by the BMAD simulation. In this sense, the BPM orbit optimization can be seen as a significant success. Unfortunately, there is no agreement between the BMAD simulation and the Precursor Run 2 measurement for the ISA tilt angles at the RF Wien filter. The measurement during Precursor Run 2 shows significantly larger ISA tilt angles at the RF Wien filter than expected from the simulation.

This difference needs to be explained and contextualized. As outlined in the previous sections, there are three things in particular that contribute significantly to the ISA tilt angle. These three contributions are the vertical orbit, any longitudinal field and an EDM signal. What the BMAD simulation investigates by optimizing the BPM orbit is how much the orbit observable at the COSY BPMs contributes to the total ISA tilt angle. The other two effects are neglected in the BMAD simulation on purpose. On the basis of this investigation it can be said that the visible vertical orbit contributes in the order of 10^2 microradians to the ISA tilt. This is sufficient to explain the ISA tilt angle observed at the 2 MeV Solenoid and the Snake Solenoid. Since larger ISA tilt angles are observed at the RF Wien filter, they could be explained due to the abundance of an EDM signal and

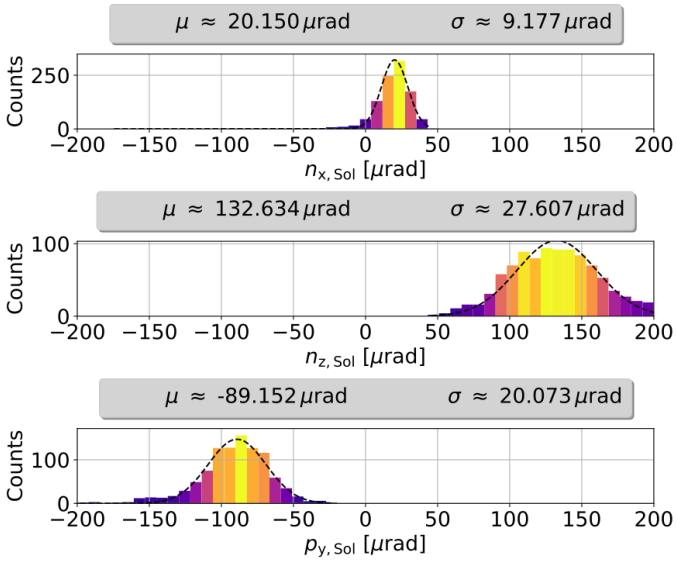

Figure 8.15: Distribution of radial and longitudinal ISA tilt and relative vertical momentum at the position of the **2 MeV Solenoid** after the optimization process. The simulated data points are represented by a histogram fitted with a Gaussian function. The corresponding fit parameters are given in the legend above the plots.

unknown longitudinal fields in COSY. However, this scenario is very unlikely. The reasons for this are explained in the following.

The RF Wien filter and the 2 MeV Solenoid are about 8 m apart and are located in the same straight section. The only optical element between them is a quadrupole triplet. Only a longitudinal magnetic field or the relative vertical momentum can affect the longitudinal ISA tilt angle at these two elements. According to the BPM orbit optimization performed, only vertical beam momenta below milliradians are expected at these elements in this section of COSY. Therefore, an ISA tilt angle in the milliradian range due to the vertical orbit can be generally excluded. The only possibility to generate such a large ISA tilt angle due to the vertical orbit would be an orbit bump, which is completely localized at the RF Wien filter and therefore not observed by the COSY BPMs. The size of the orbit bump must be larger than 10 mm. In response to this large orbit bump, the RF Wien filter must also be pitched, as otherwise a turned on RF Wien filter would significantly perturb the orbit in the rest of COSY, which is not observed in Precursor Run 2. In addition, the tilt angle of the RF Wien filter must also be in the order of milliradians. Since an unrecognized large localized vertical orbit bump and a large RF Wien filter tilt angle are very unlikely, this scenario is ruled out.

Another explanation for the large longitudinal ISA tilt angles at the RF Wien filter can be found by considering unknown longitudinal fields in COSY. However, there are two arguments against this explanation. On the one hand, longitudinal magnetic fields of the

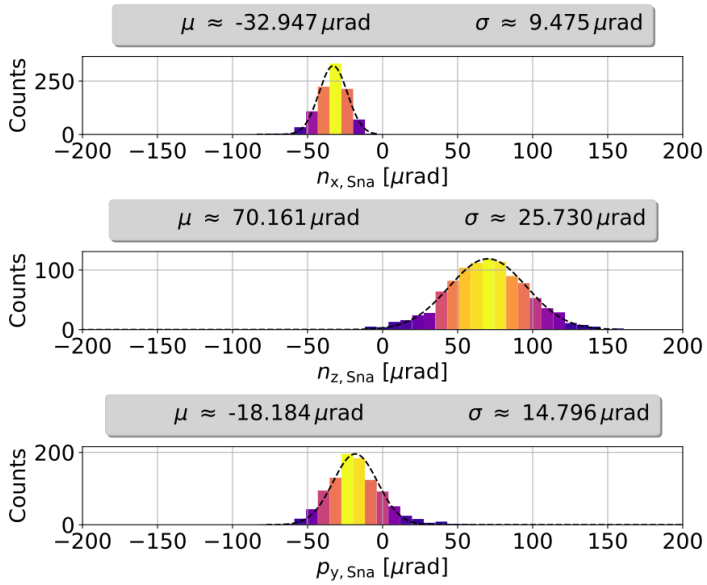

Figure 8.16: Distribution of radial and longitudinal ISA tilt angle and relative vertical momentum at the position of the **Snake Solenoid** after the optimization process. The simulated data points are represented by a histogram fitted with a Gaussian function. The corresponding fit parameters are given in the legend above the plots.

order of 10^{-3} T·m are required to produce ISA tilt angles in the milliradian range. Such large longitudinal field components have a significant effect on the beam orbit if the beam does not pass through them on axis. However, an unexplained orbit bump has not yet been observed, measured or expected. There is also no physical explanation for a longitudinal field of this size in COSY. It is therefore unlikely that this scenario is possible. On the other hand would such a large longitudinal field also affect the longitudinal ISA at the 2 MeV Solenoid, since both elements are located in the same straight section of COSY. It is impossible for a longitudinal field to affect the ISA at the RF Wien filter while leaving the ISA at the 2 MeV Solenoid unaffected. Discussing longitudinal fields, which are unknown in COSY or not implemented in the BMAD simulation model of COSY one has to mention the longitudinal fields arising from the crosstalk of dipole magnets and nearby magnetic material. Their magnitude can be expected to be in the range of 10^{-5} T·m. This effect is not included in the BMAD simulation model. This is because important information about the direction of their field and the number of times they occur has not yet been resolved. In J. Bökers' simulations, longitudinal fields from cross-talk can be observed when a dipole magnet and a vertical steerer magnet are in close proximity. As only this particular scenario has been simulated, it is unclear whether the same effect can occur for a horizontal steerer magnet and how it might differ. As these longitudinal fields tend to have less effect on the ISA tilt angle than the vertical orbit, they are neglected in the BMAD simulation so far.

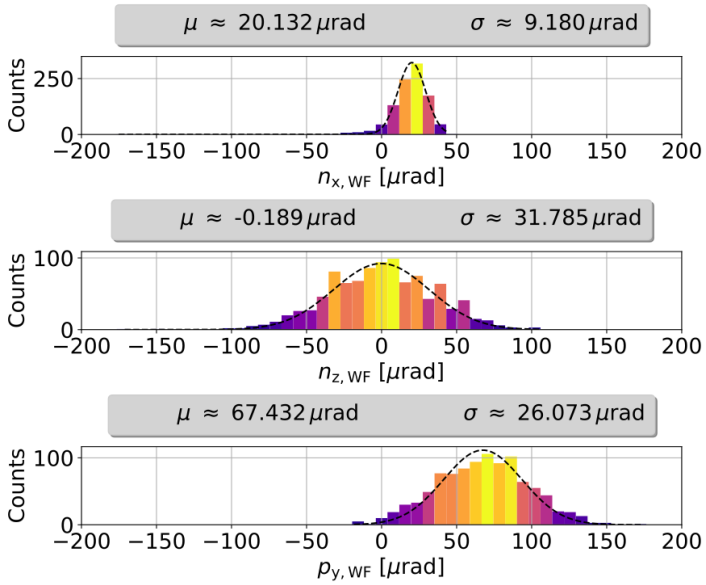

Figure 8.17: Distribution of radial and longitudinal ISA tilt angle and relative vertical momentum at the position of the **RF Wien filter** after the optimization process. The simulated data points are represented by a histogram fitted with a Gaussian function. The corresponding fit parameters are given in the legend above the plots.

With the arguments discussed above, it is clear that a measurement of the longitudinal ISA tilt angle of the order of milliradians at the RF Wien filter location is unlikely. Unfortunately, a radial ISA tilt angle at the RF Wien filter in the milliradian range must also be ruled out as a consequence. Since tilt angles due to the vertical orbit and the longitudinal fields cannot cause such large ISA tilt angles, the only explanation left for the radial ISA tilt angle is a possible EDM signal. A possible EDM signal is always an option as it can dominate the ISA tilt angle due to systematic effects without perturbing the orbit. However, an EDM signal exceeding all previous limits for other particles would be required to produce such a large ISA tilt angle. This is very unlikely. In addition, a consistent explanation for the large longitudinal ISA tilt angle at the RF Wien filter is needed to claim that this large radial ISA tilt angle comes from an EDM signal. Since the radial and longitudinal ISA tilt angles are very large and no explanation could be found for the difference in the longitudinal ISA tilt angles at the 2 MeV Solenoid and RF Wien filter, the natural conclusion is, that the constructed and operated RF Wien filter device is not completely understood at the moment.

8.5 Summary on potential ISA tilt angles in COSY

This chapter discusses which systematic effects present in the COSY storage ring play a role for the closed orbit and the ISA tilt angle, and how these can be implemented in the BMAD simulation model of COSY. It is shown that the systematic effects due to dipoles

and quadrupoles have to be simplified by effective dipole kicks at the location of these elements. The reason for this simplification is that only the order of magnitude of each individual systematic effect is approximately known. This simplification can be justified as the ISA tilt angle is determined by three main influencing factors. These are given by the vertical orbit y_{Clo}, existing magnetic fields B_{z} in the direction of the beam momentum and a potential EDM signal. Equation (8.2) summarizes these once again.

$$\begin{aligned} n_{\mathrm{x}}(s) = &\quad F_1(y_{\mathrm{Clo}}) + \quad F_2(B_{\mathrm{z}}) + F_3(\eta_{\mathrm{EDM}}) \\ n_{\mathrm{z}}(s) = &\quad G_1(y_{\mathrm{Clo}}) + \quad G_2(B_{\mathrm{z}}) \end{aligned} \tag{8.2}$$

Therefore, to a good approximation, a fixed closed orbit will always converge to the identical ISA tilt angle. Since the exact magnitude of the individual systematic effects affecting the beam path is unknown, the simulated beam path must be matched as closely as possible to the measured beam path. This is done by varying the effective kicks at the dipole and quadrupole magnets to determine the potential ISA tilt angle in the COSY storage ring coming from the closed orbit. In order not to arrive at unphysical solutions for the systematic effects, reasonable constraints have to be set by estimating the magnitudes of systematic effects. In addition, measurement uncertainties of the BPM position in COSY have to be taken into account. Due to the large number of variables to be considered and the uncertainty of the BPM position, the orbit matching algorithm provides a distribution of potential orbits and ISA tilt angles in result. After optimization, the measured vertical orbit and the simulated orbit match well, with a few exceptions. This result shows that the orbit matching algorithm is far from final, nor are the systematic effects fully understood and interpreted. There are various effects that can still be added to the simulation model and their implementation can still be improved. However, the included systematic effects give correct information about the ISA inclination angle due to orbit effects.

The resulting ISA tilt angle in the BMAD simulation present results well below 0.1 mrad over the whole ring circumference. Consistent results can be found when comparing the ISA tilt angle from the BMAD simulation and Precursor Run 2 at COSY's static solenoids. When comparing the ISA tilt angle results at the RF Wien filter however, the large measured ISA tilt angles of order of milliradians cannot be explained by the BMAD simulation. In addition, also a consistent explanation of these measured ISA tilt angles due to unknown longitudinal fields or a potential EDM signal is problematic. Based on the current BMAD simulation model one can therefore summarize that signal measured at the RF Wien filter during Precursor Run 2 is not the ISA tilt angle in COSY, which is present, when the RF Wien filter is not operated. Research is ongoing, what exactly causes this issue.

CHAPTER 9

Conclusion

The electric dipole moment of elementary particles is a property of great interest in particle physics, as it may answer the unsolved matter-antimatter asymmetry in the Universe. The EDM violates $\mathcal{P}$ and $\mathcal{T}$ in the standard model of particle physics and is predicted to be very small, since it occurs only as a higher-order loop effect. So far, no finite experimental signature of an EDM has been measured, although several scientists and collaborations are working on this topic to improve the statistical and systematic sensitivities.

This thesis discusses the simulations related to the first direct measurements of the deuteron EDM by the JEDI collaboration at Jülich in November 2018 and March 2021, in the Precursor Runs 1 and 2. In a storage ring, the EDM causes a tilt angle of the invariant spin axis in the radial direction. Therefore, a measurement of the ISA orientation leads to a first direct measurement of the deuteron electric dipole moment. This can be done with a static solenoid as well as with a radio frequency Wien filter operated at the spin precession frequency. Unfortunately, naturally occurring systematic effects in the storage can also tilt the ISA in the radial and longitudinal directions. Since the expected effect of the EDM on the ISA is very tiny, particle and spin tracking simulations have to been performed to separate systematic effects from a potential EDM signal. This has been done in the course of this thesis using the software library BMAD.

This way the systematic effects and uncertainties, which effect the ISA tilt angle in the storage ring COSY, were investigated. Although the existing BMAD simulation model of COSY has so far been successful in identifying correction factors in various ISA measurements and in performing a rough orbit fitting that can predict the magnitude of the ISA tilt angles at static solenoids, it fails to properly predict the magnitude of the expected systematic effects. In addition, the simulation model cannot explain the large ISA tilt angles

observed in the Precursor experiments at the RF Wien filter. The reason for this difference can be found in the BMAD simulation model as well as in the EDM experiment itself.

Based on the investigations performed for this thesis and other theoretical considerations, it can be concluded that an ISA tilt angle of the order of milliradians in COSY at the given beam orbit during Precursor Run 2 cannot reasonably be attributed to systematic effects or a potential EDM signal. Not only would a radial ISA tilt angle coming solely from an EDM correspond to an EDM of magnitude 10^{-17} e·cm, which is much larger than all upper limits measured so far for other particles, it would still not explain the longitudinal ISA tilt in the milliradian range. For this reason, another explanation for the observed ISA tilt angels during Precursor Run 2 have to be found. For this reason, research about the magnetic field axis of the RF Wien filter is ongoing to explain the observations at the RF Wien filter [98].

In addition, the BMAD simulation indicates, that only the orbit, longitudinal fields, and the EDM of a particle can affect the ISA tilt angle. Since systematic effects determine the orbit and the longitudinal fields in COSY, more information about each systematic variable is needed, as well as information about the measured orbit including its uncertainties. This can be achieved by using more BPMs than already present in COSY and having more information about the BPM alignment with respect to the magnets and the design orbit. This issue will also be critical for any future EDM experiment in a storage ring. In view of this precise control of the beam trajectory and the knowledge of the systematic effects, it seems essential to build a dedicated storage ring to study the ISA tilt angles and thus to measure a potential EDM signal.

Such an experiment is foreseen for the future, as the construction of an all-electric storage ring dedicated to proton EDM measurements is planned. As an intermediate step, a smaller ring, called the Proton Prototype EDM Ring, is proposed [99]. In contrast to the all-electric ring, the proton prototype EDM ring will have a low-cost ring design and operate in different modes, one with all-electric bending elements and one with combined electric and magnetic bending elements. This approach should provide a proof of concept for the frozen spin method as well as experience in handling high electric fields in a storage ring. In addition, features such as the control of two counterclockwise rotating polarized proton beams can be tested. In the final all-electric ring, the frozen-spin condition can be achieved using only electric fields by accelerating protons to the magic momentum. Again, two counter-rotating proton beams circulate simultaneously in the storage ring [100].

In conclusion, this thesis highly supports the demand for the construction of the Proton Prototype EDM ring under the constraint that all the knowledge available so far in taken into account when getting the final design for it. As this thesis outlines, systematic effects must be understood or measured to get an accurate simulation model. In addition,

the vertical orbit must also be accurately measured to see if all systematic effects affecting the orbit are accounted for.

Appendix

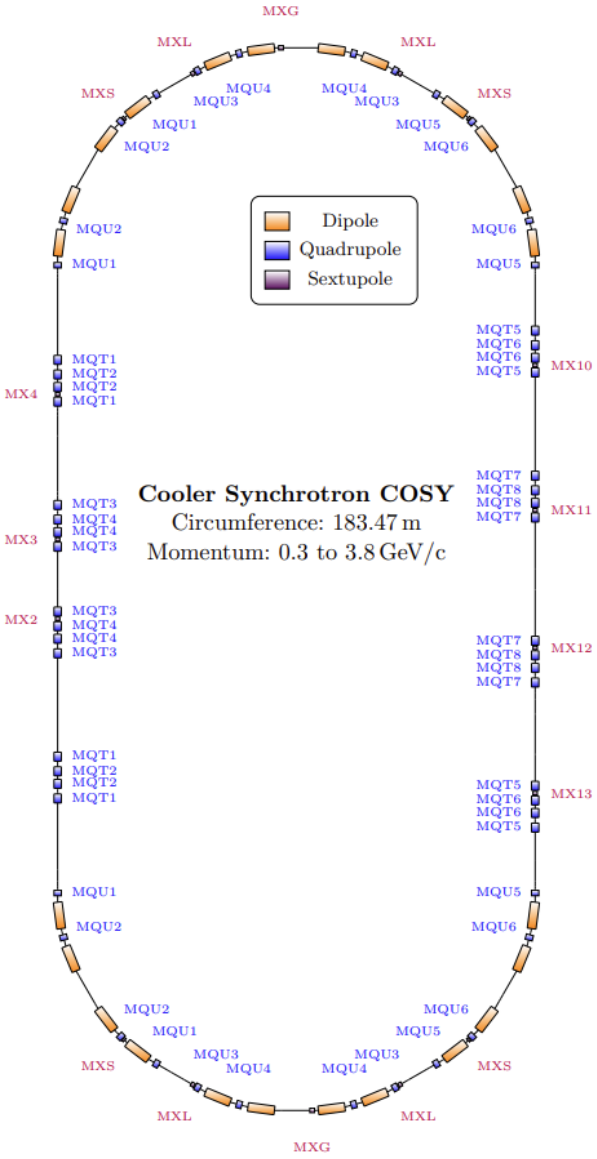

Figure 9.1: Floor plan of the quadrupole and sextupole magnets in COSY, which form a family with the corresponding family name. Taken from [101].

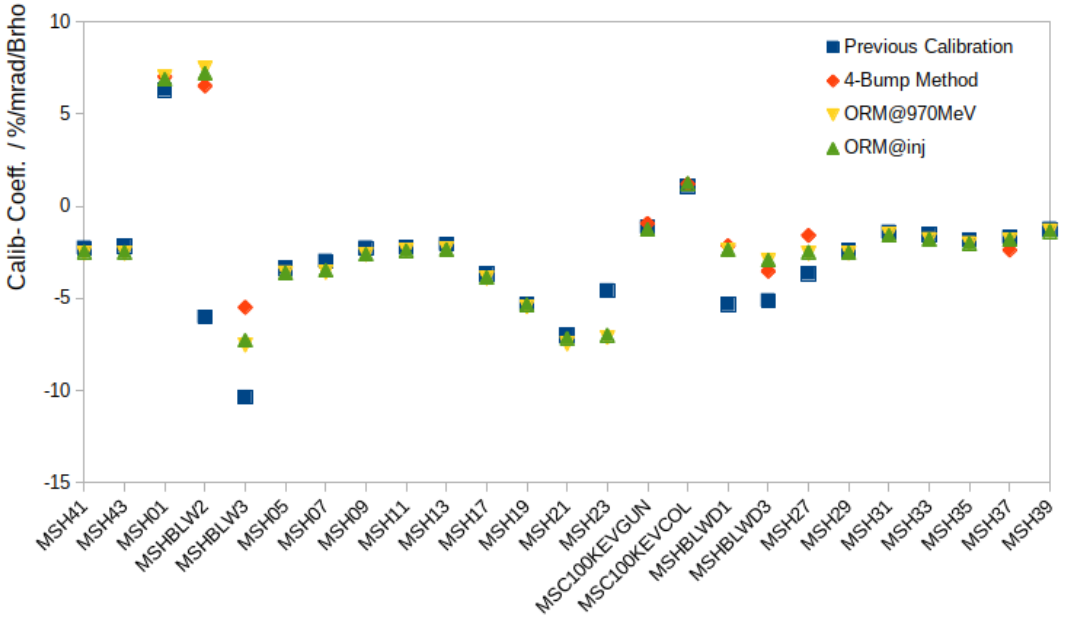

Figure 9.2: Calibration factors for the horizontal steerers magnets determined by the 4-bump and ORM method at two different beam energies. The recalibration campaign from summer 2020 is compared with the previously determined calibration factors. Taken from [94].

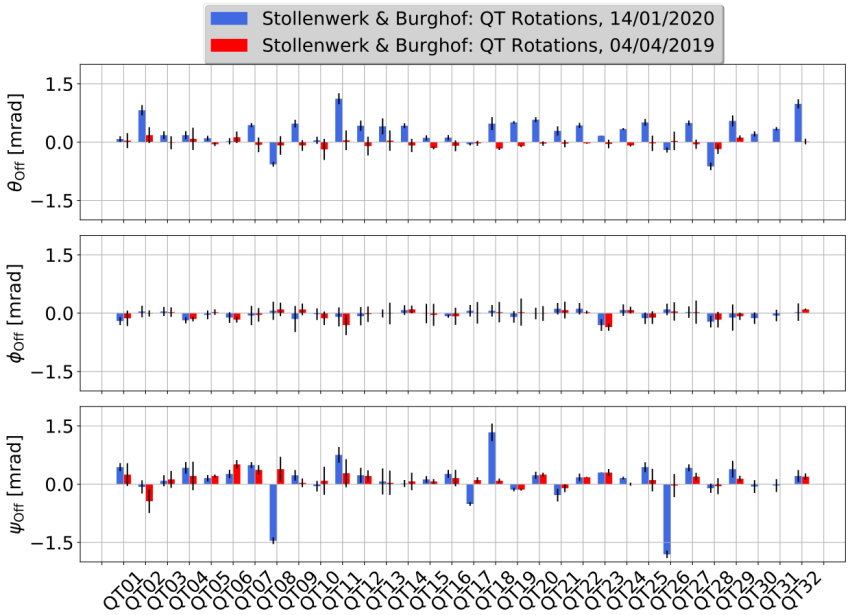

Figure 9.3: Measured rotations of the quadrupole magnets in the **straight** sections of COSY by the company Stollenwerk&Burghof in April 2019 and January 2020. The blue and red colored bars show the measured magnitude of the rotation, while a measurement error given by the company is shown as a black error bar.

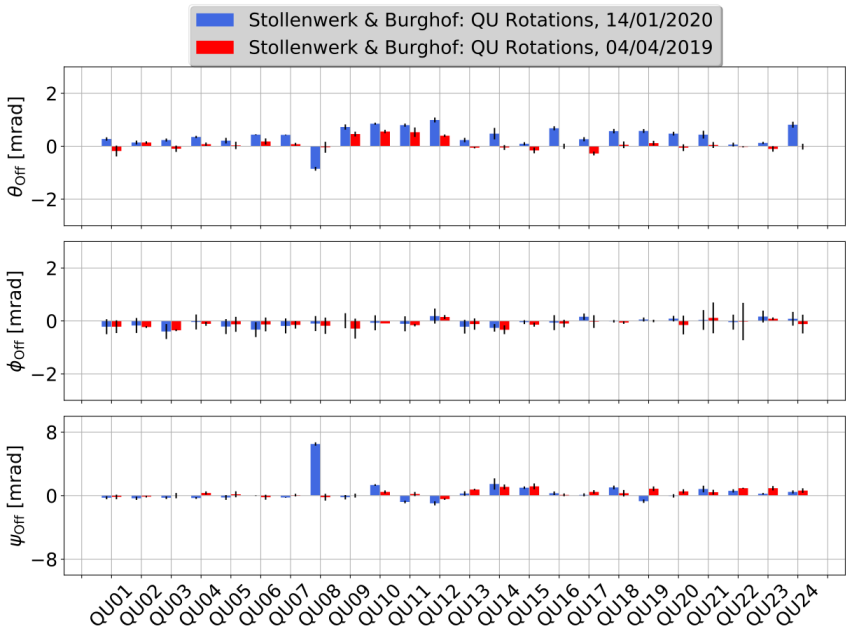

Figure 9.4: Measured rotations of the quadrupole magnets in the **arc** sections of COSY by the company Stollenwerk&Burghof in April 2019 and January 2020. The blue and red coloured bars show the measured magnitude of the rotation, while a measurement error given by the company is shown as a black error bar.

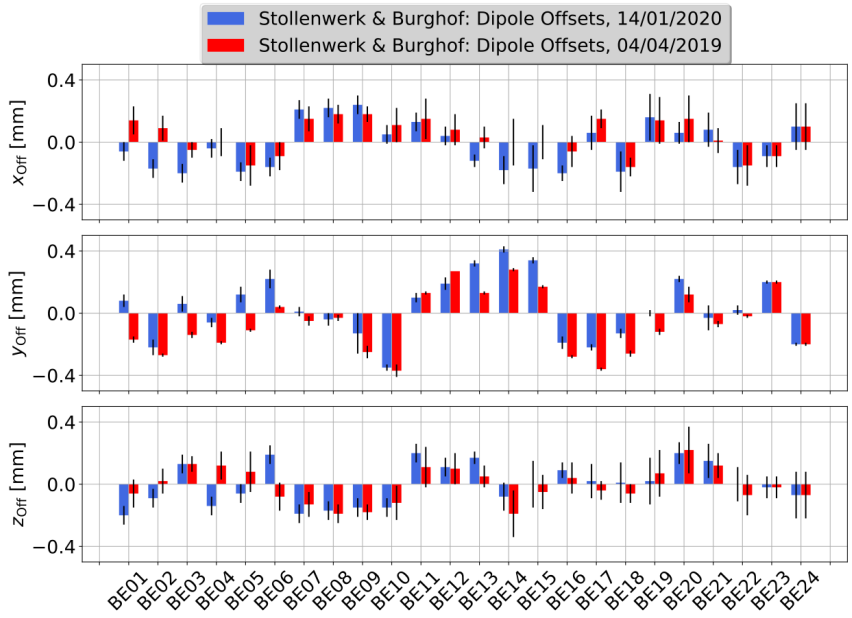

Figure 9.5: Measured offsets of the COSY dipole magnets by the company Stollenwerk&Burghof in April 2019 and January 2020. The blue and red bars show the measured magnitude of the misalignment, while a measurement error given by the company is shown as a black error bar.

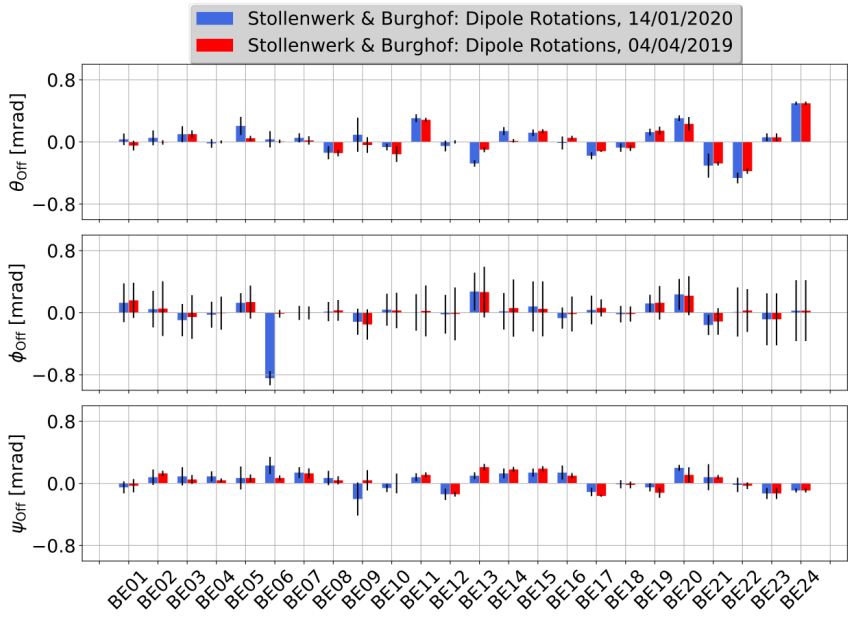

Figure 9.6: Measured rotations of the COSY dipole magnets by the company Stollenwerk&Burghof in April 2019 and January 2020. The blue and red bars show the measured magnitude of the misalignment, while a measurement error given by the company is shown as a black error bar.

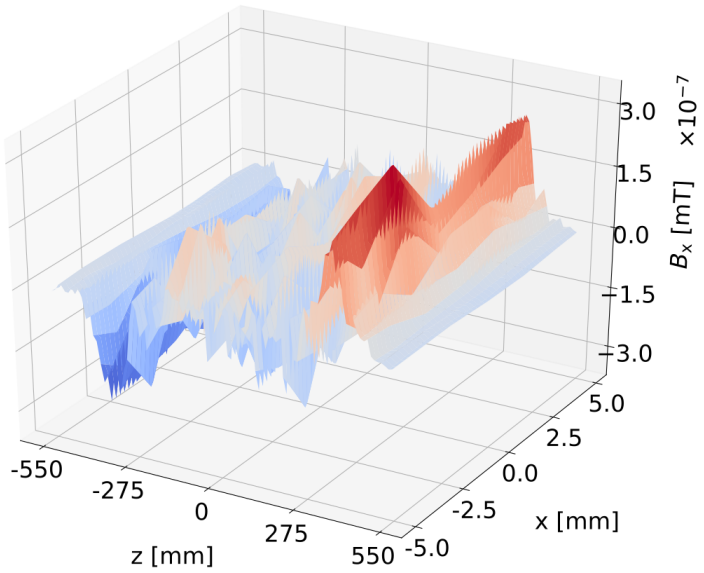

Figure 9.7: Simulated field map of the radial magnetic field component of a realistic RF Wien filter in the plane $y = 0\,\text{mm}$. The field map consists of a total of 10^4, with 10^2 points in each direction. A position of $x = 0\,\text{mm}$ and $z = 0\,\text{mm}$ indicates the target position *TP1* and the center of the RF Wien filter [47].

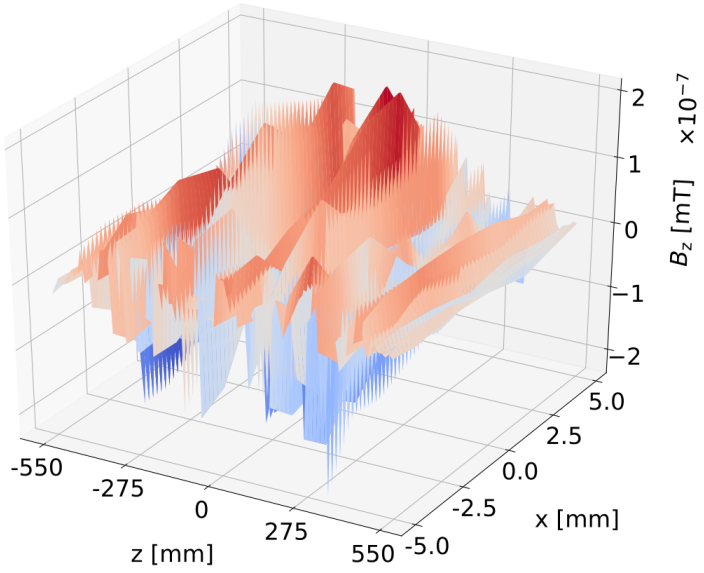

Figure 9.8: Simulated field map of the longitudinal magnetic field component of a realistic RF Wien filter in the plane $y = 0\,\text{mm}$. The field map consists of a total of 10^4, with 10^2 points in each direction. A position of $x = 0\,\text{mm}$ and $z = 0\,\text{mm}$ indicates the target position *TP1* and the center of the RF Wien filter [47].

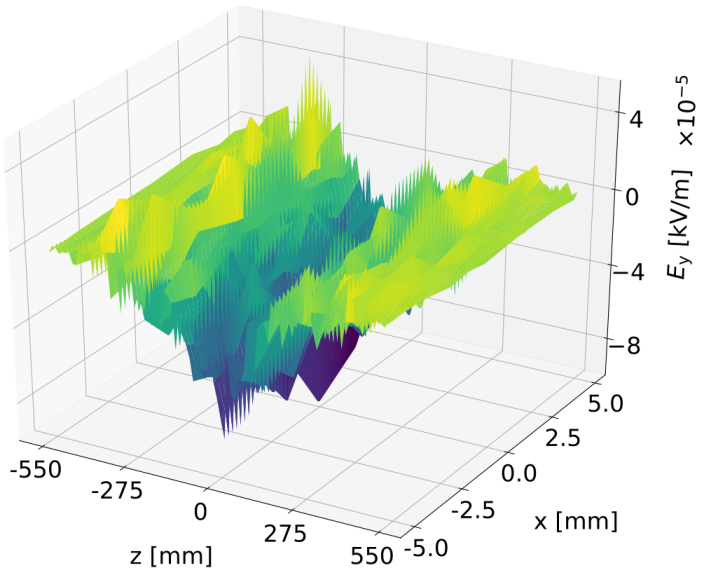

Figure 9.9: Simulated field map of the vertical electric field component of a realistic RF Wien filter in the plane $y = 0\,\text{mm}$. The field map consists of a total of 10^4, with 10^2 points in each direction. A position of $x = 0\,\text{mm}$ and $z = 0\,\text{mm}$ indicates the target position *TP1* and the center of the RF Wien filter [47].

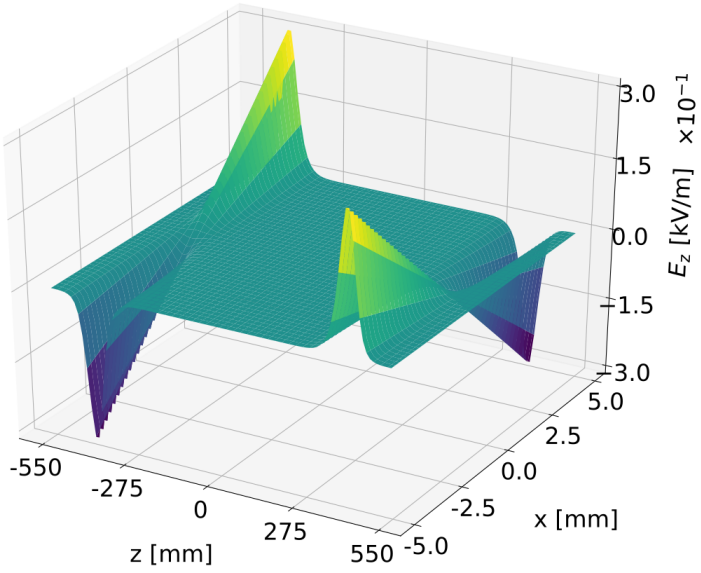

Figure 9.10: Simulated field map of the longitudinal electric field component of a realistic RF Wien filter in the plane $y = 0\,\text{mm}$. The field map consists of a total of 10^4, with 10^2 points in each direction. A position of $x = 0\,\text{mm}$ and $z = 0\,\text{mm}$ indicates the target position *TP1* and the center of the RF Wien filter [47].

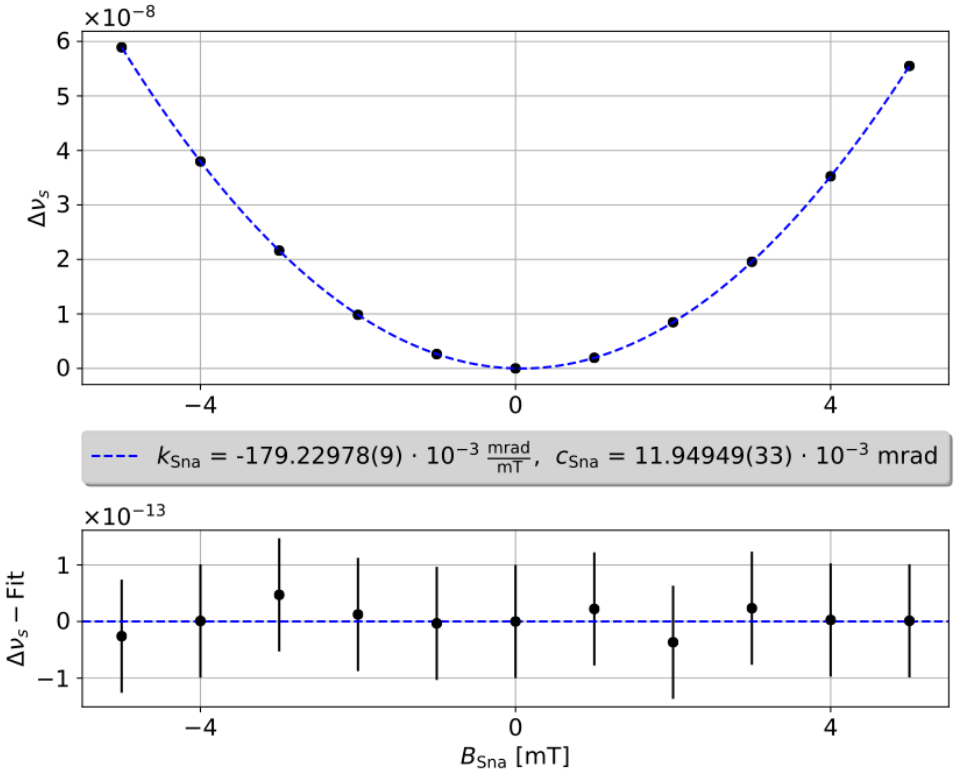

Figure 9.11: Calibration of the Snake solenoid after applying the measured steerer kicks and measured magnet displacements to an idealized COSY lattice. In the top panel, the black dots indicate the simulated data points, while the blue line shows the result of fitting the Equation (7.5) to the data points. The bottom panel shows the residuals from the top panel.

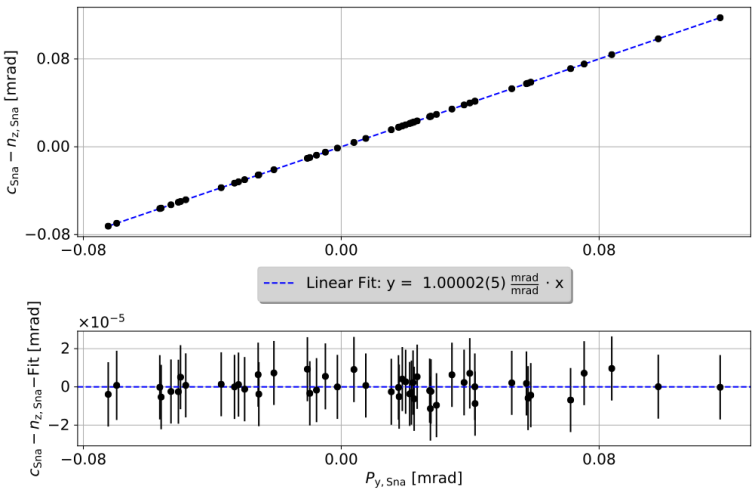

Figure 9.12: Determination of a correction factor for the Snake solenoid after perturbation of the closed orbit by random steerer kicks. The top panel shows the difference between the projection of the longitudinal ISA and the actual longitudinal ISA tilt at the solenoid position as a function of the relative vertical momentum of the beam at the solenoid position. The simulated differences are shown as black dots, while a linear fit with the fit parameter given in the legend is shown in blue. The bottom panel shows the residuals of the linear fit.

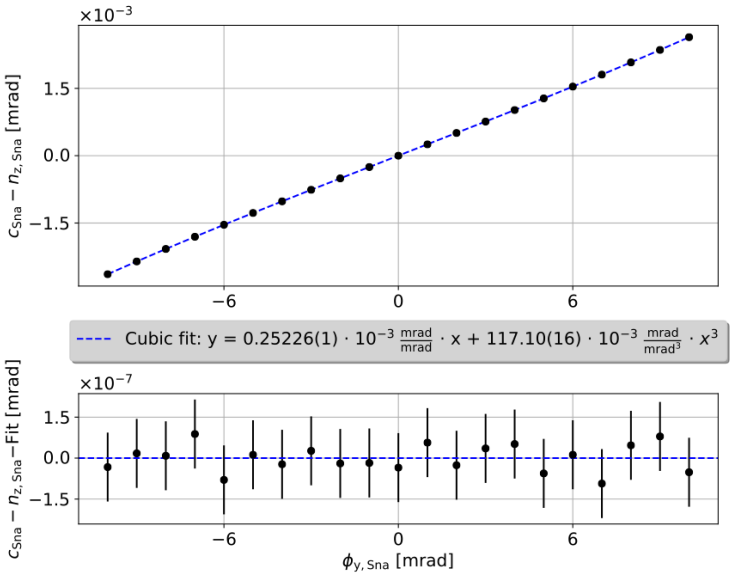

Figure 9.13: Determination of a correction factor for the snake solenoid after pitching the solenoid in the vertical direction. The top panel shows the difference between the projection of the longitudinal ISA and the ISA tilt at the solenoid position as a function of the vertical pitch angle. The differences are shown as black dots, while a cubic fit with the fit parameter given in the legend and the residuals shown in the bottom panel is shown in blue.

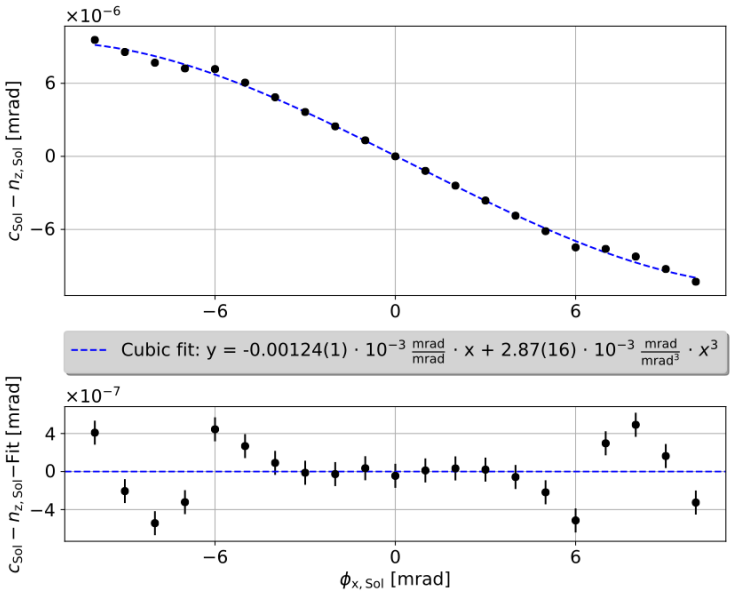

Figure 9.14: Determination of a correction factor for the 2MeV solenoid after pitching the solenoid in the horizontal direction. The top panel shows the difference between the projection of the longitudinal ISA and the ISA tilt at the solenoid position as a function of the horizontal pitch angle. The differences are shown as black dots, while a cubic fit with the fit parameter given in the legend and the residuals shown in the bottom panel is shown in blue.

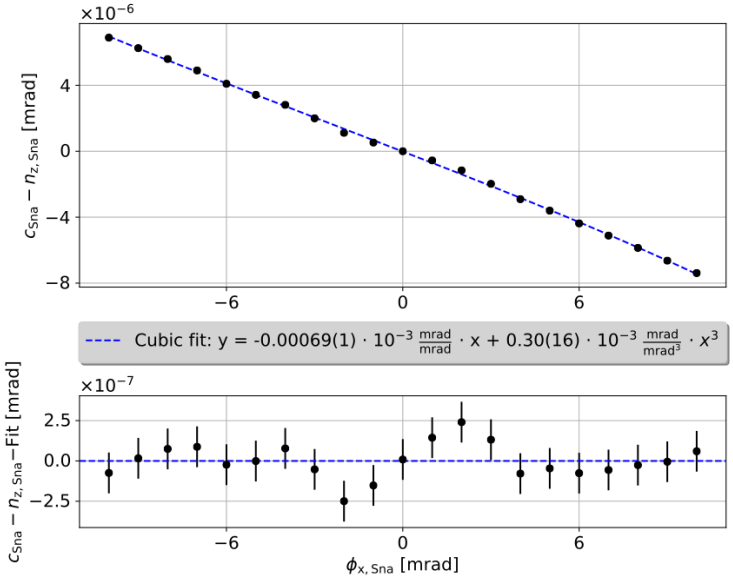

Figure 9.15: Determination of a correction factor for the Snake solenoid after pitching the solenoid in the horizontal direction. The top panel shows the difference between the projection of the longitudinal ISA and the ISA tilt at the solenoid position as a function of the horizontal pitch angle. The differences are shown as black dots, while a cubic fit with the fit parameter given in the legend and the residuals shown in the bottom panel is shown in blue.

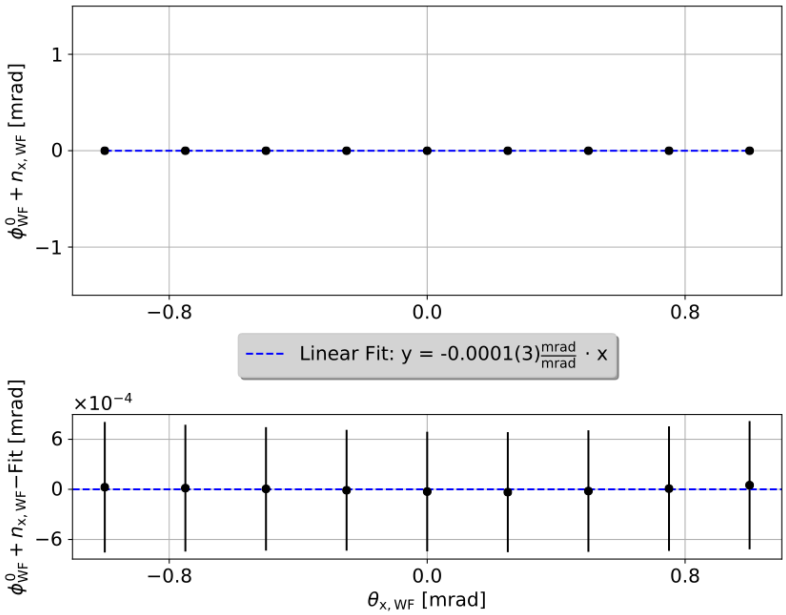

Figure 9.16: Difference between the radial map minimum and the radial ISA tilt at the RF Wien filter position as a function of the horizontal pitch angle of an idealized RF Wien filter. In the top panel the simulated data points and their errors are shown in black. A straight line fit to the simulated data points is shown as a blue line and its main fitting parameters are given in the legend. The residuals of the fit are shown in the bottom panel.

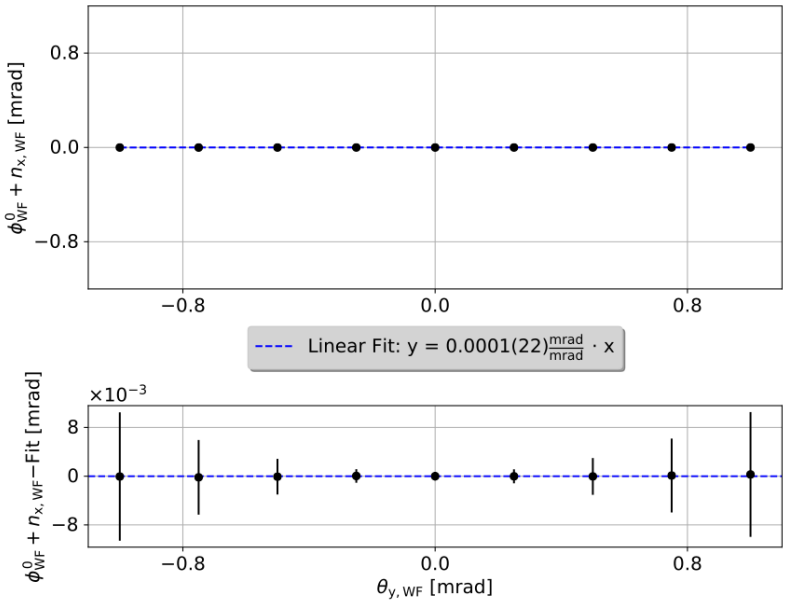

Figure 9.17: Difference between the radial map minimum and the radial ISA tilt at the RF Wien filter position as a function of the vertical pitch angle of an idealized RF Wien filter. In the top panel the simulated data points and their errors are shown in black. A straight line fit to the simulated data points is shown as a blue line and its main fitting parameters are given in the legend. The residuals of the fit are shown in the bottom panel.

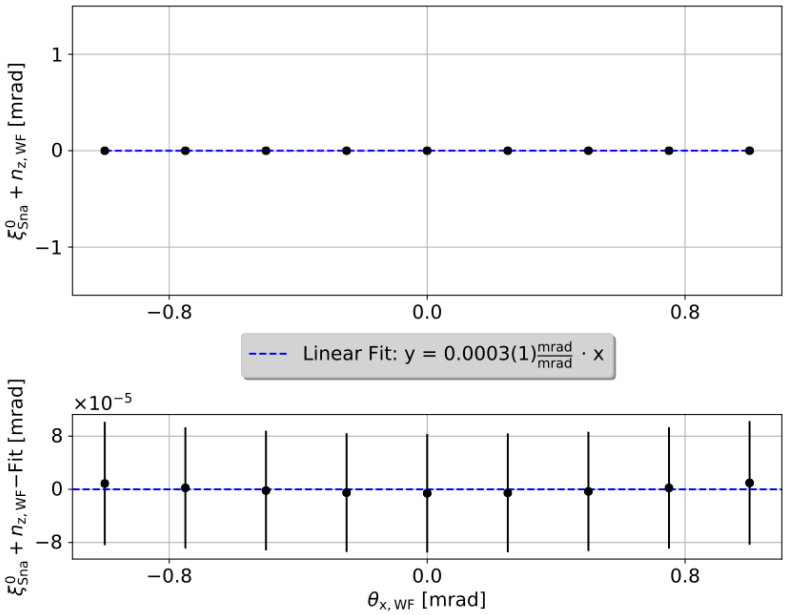

Figure 9.18: Difference between the longitudinal map minimum and the longitudinal ISA tilt at the RF Wien filter position as a function of the horizontal pitch angle of an idealized RF Wien filter. In the top panel the simulated data points and their errors are shown in black. A straight line fit to the simulated data points is shown as a blue line and its main fitting parameters are given in the legend. The residuals of the fit are shown in the bottom panel.

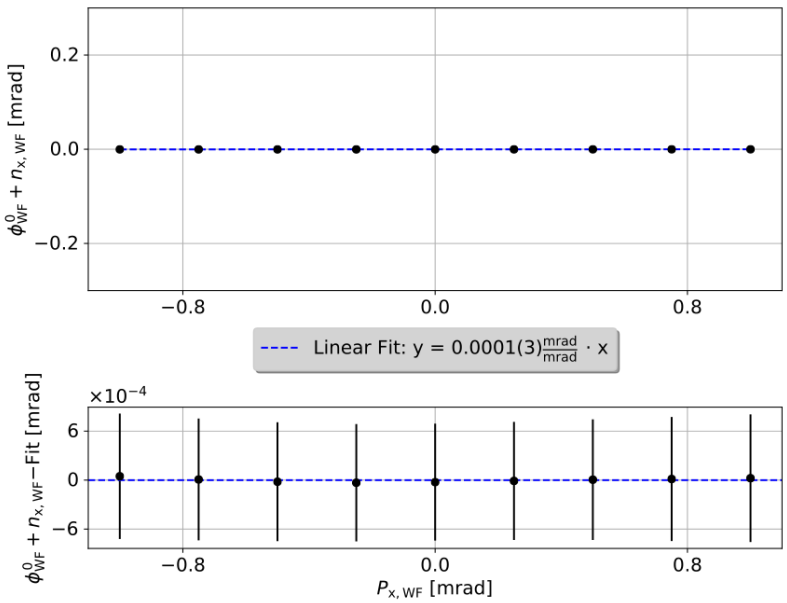

Figure 9.19: Difference between the radial map minimum and the radial ISA tilt at the RF Wien filter position as a function of the horizontal momentum at an idealized RF Wien filter. In the top panel the simulated data points and their errors are shown in black. A straight line fit to the simulated data points is shown as a blue line and its main fitting parameters are given in the legend. The residuals of the fit are shown in the bottom panel.

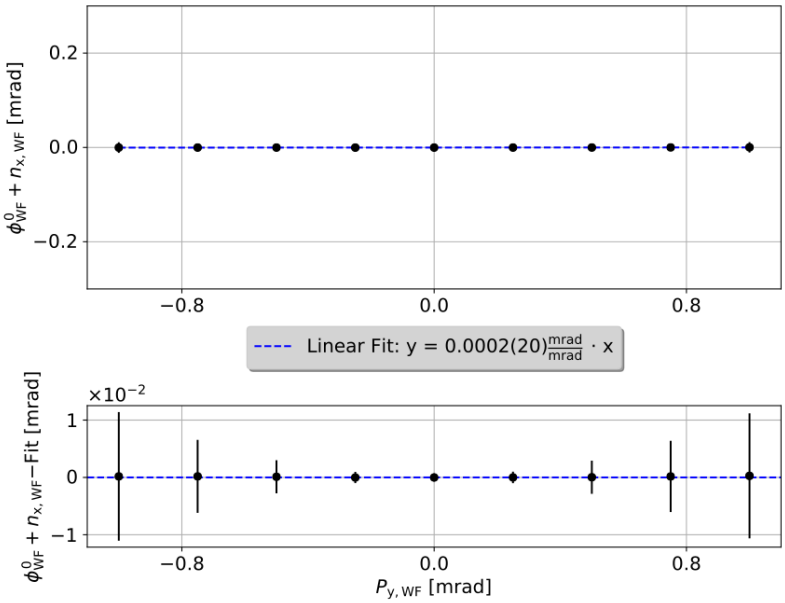

Figure 9.20: Difference between the radial map minimum and the radial ISA tilt at the RF Wien filter position as a function of the vertical momentum at an idealized RF Wien filter. In the top panel the simulated data points and their errors are shown in black. A straight line fit to the simulated data points is shown as a blue line and its main fitting parameters are given in the legend. The residuals of the fit are shown in the bottom panel.

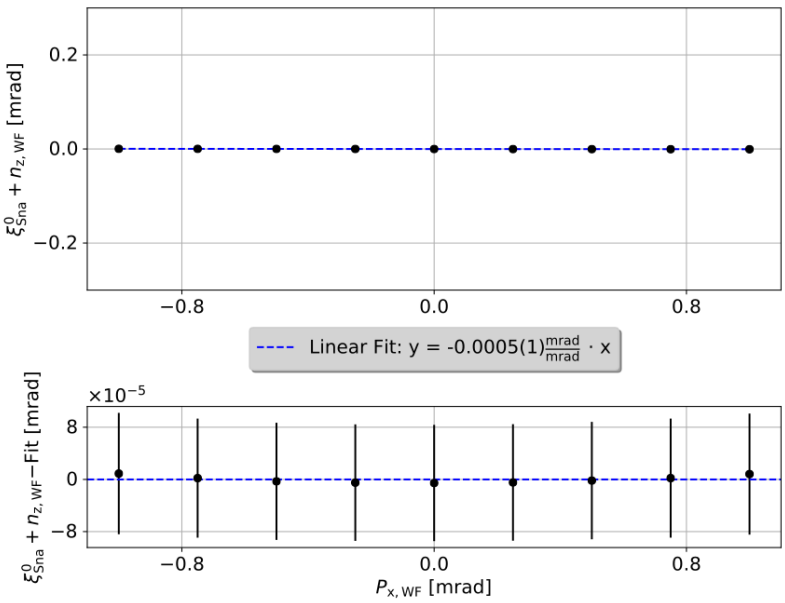

Figure 9.21: Difference between the longitudinal map minimum and the longitudinal ISA tilt at the RF Wien filter position as a function of the horizontal momentum at an idealized RF Wien filter. In the top panel the simulated data points and their errors are shown in black. A straight line fit to the simulated data points is shown as a blue line and its main fitting parameters are given in the legend. The residuals of the fit are shown in the bottom panel.

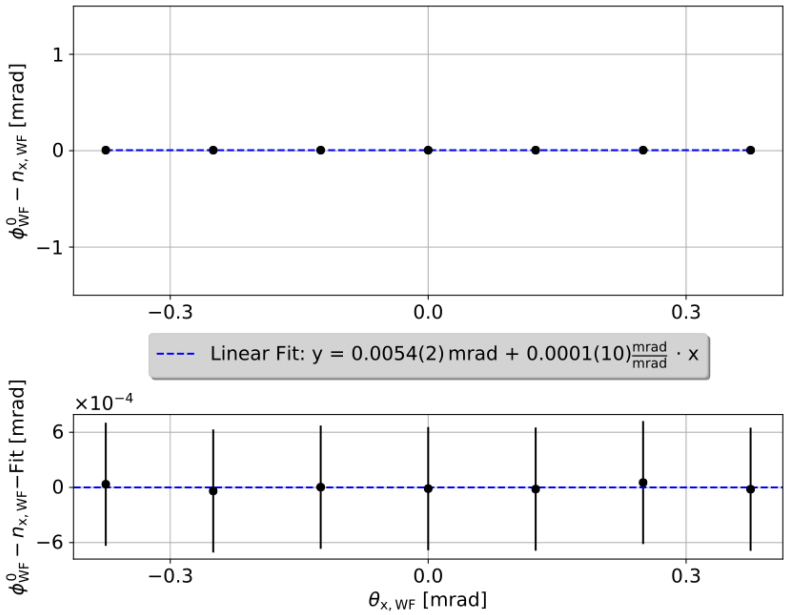

Figure 9.22: Difference between the radial map minimum and the radial ISA tilt at the RF Wien filter position as a function of the horizontal pitch angle of an realistic RF Wien filter. In the top panel the simulated data points and their errors are shown in black. A straight line fit to the simulated data points is shown as a blue line and its main fitting parameters are given in the legend. The residuals of the fit are shown in the bottom panel.

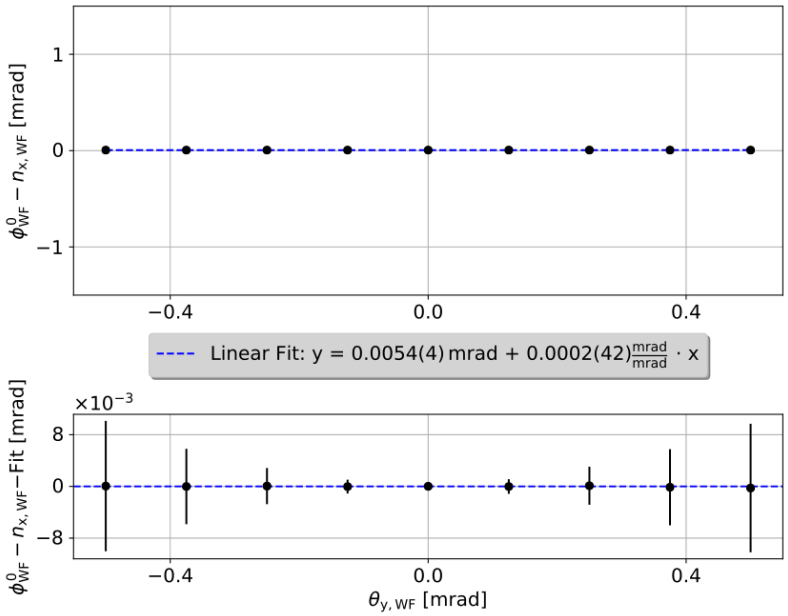

Figure 9.23: Difference between the radial map minimum and the radial ISA tilt at the RF Wien filter position as a function of the vertical pitch angle of an realistic RF Wien filter. In the top panel the simulated data points and their errors are shown in black. A straight line fit to the simulated data points is shown as a blue line and its main fitting parameters are given in the legend. The residuals of the fit are shown in the bottom panel.

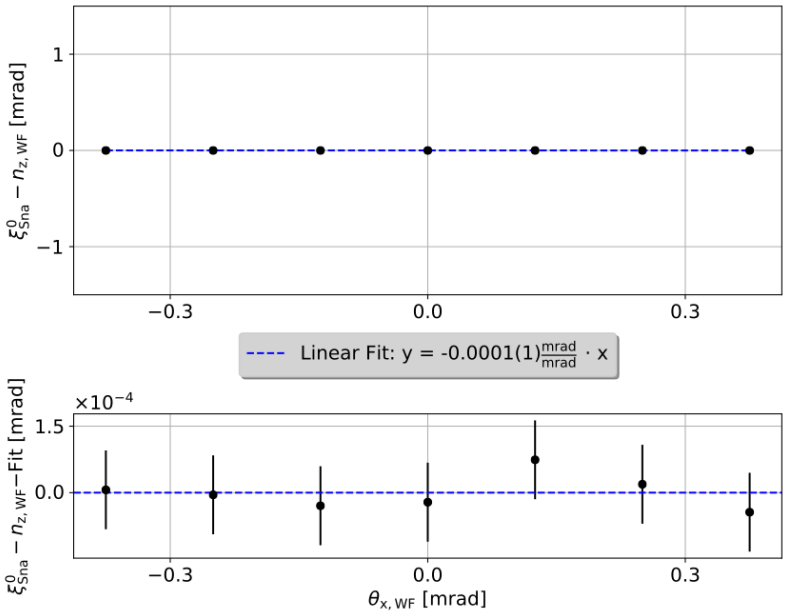

Figure 9.24: Difference between the longitudinal map minimum and the longitudinal ISA tilt at the RF Wien filter position as a function of the horizontal pitch angle of an realistic RF Wien filter. In the top panel the simulated data points and their errors are shown in black. A straight line fit to the simulated data points is shown as a blue line and its main fitting parameters are given in the legend. The residuals of the fit are shown in the bottom panel.

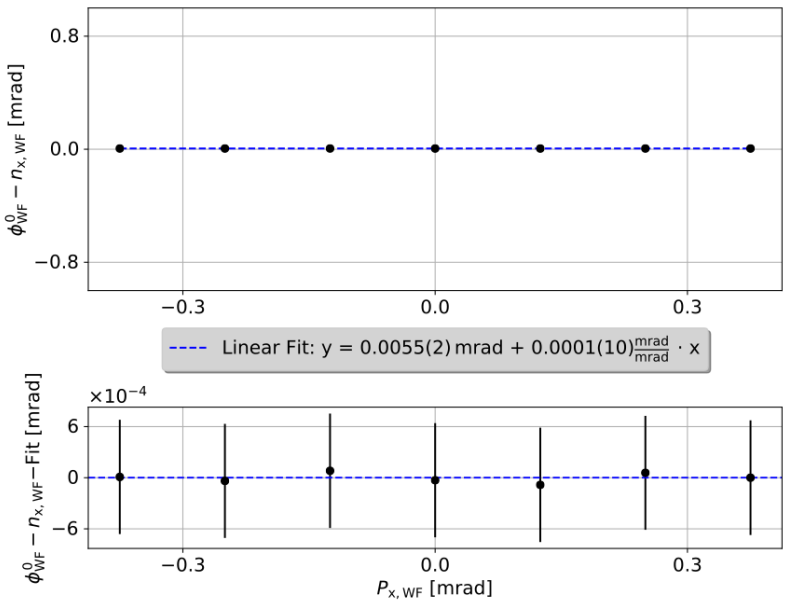

Figure 9.25: Difference between the radial map minimum and the radial ISA tilt at the RF Wien filter position as a function of the horizontal momentum at an realistic RF Wien filter. In the top panel the simulated data points and their errors are shown in black. A straight line fit to the simulated data points is shown as a blue line and its main fitting parameters are given in the legend. The residuals of the fit are shown in the bottom panel.

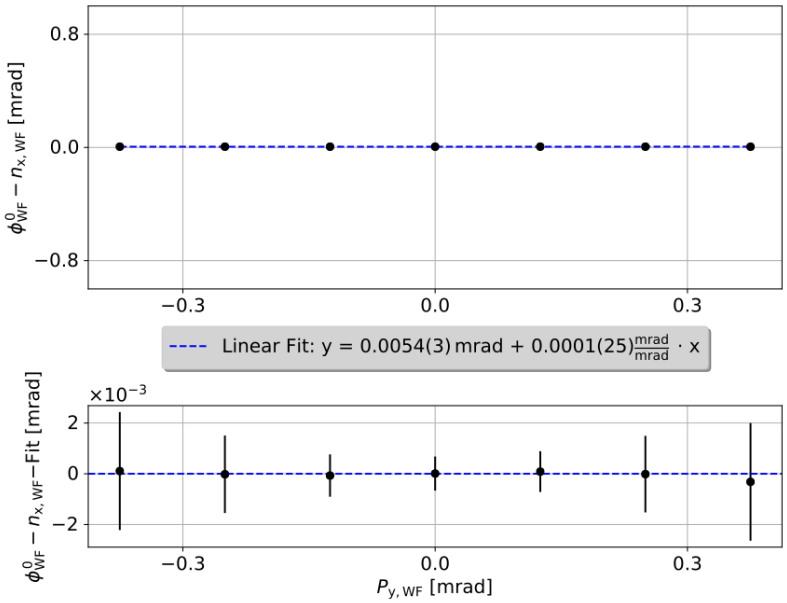

Figure 9.26: Difference between the radial map minimum and the radial ISA tilt at the RF Wien filter position as a function of the vertical momentum at an realistic RF Wien filter. In the top panel the simulated data points and their errors are shown in black. A straight line fit to the simulated data points is shown as a blue line and its main fitting parameters are given in the legend. The residuals of the fit are shown in the bottom panel.

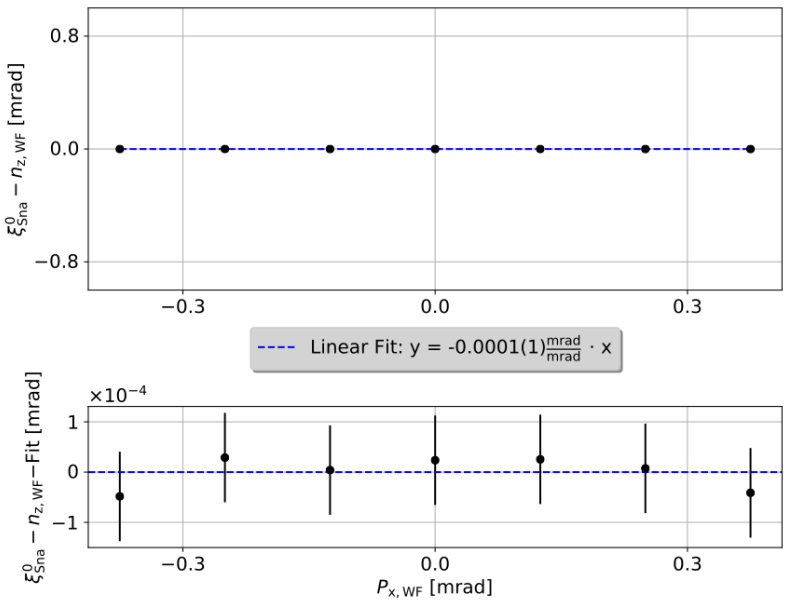

Figure 9.27: Difference between the longitudinal map minimum and the longitudinal ISA tilt at the RF Wien filter position as a function of the horizontal momentum at an realistic RF Wien filter. In the top panel the simulated data points and their errors are shown in black. A straight line fit to the simulated data points is shown as a blue line and its main fitting parameters are given in the legend. The residuals of the fit are shown in the bottom panel.

Subsystems Straights		Subsystems Arcs	
Quadrupole Name	**BPM Name**	**Quadrupole Name**	**BPM Name**
QT01	BPM02	QU01	BPM09
QT02	BPM02	QU02	BPM10
QT03	BPM02	QU04	BPM11
QT04	BPM02	QU06	BPM12
QT05	/	QU07	BPM13
QT06	/	QU08	BPM14
QT07	/	QU09	BPM15
QT08	/	QU11	BPM16
QT09	BPM06	QU12	BPM17
QT10	BPM06	QU13	BPM22
QT11	BPM06	QU14	BPM23
QT12	BPM06	QU16	BPM24
QT13	BPM08	QU16	BPM24
QT14	BPM08	QU20	BPM27
QT15	BPM08	QU21	BPM28
QT16	BPM08	QU24	BPM01
QT17	BPM18		
QT18	BPM18		
QT19	BPM18		
QT20	BPM18		
QT21	BPM19		
QT22	BPM19		
QT23	BPM19		
QT24	BPM19		
QT25	BPM20		
QT26	BPM20		
QT27	BPM20		
QT28	BPM20		
QT29	BPM21		
QT30	BPM21		
QT31	BPM21		
QT32	BPM21		

Table 9.1: BPMs with a quadrupole for calibration via BBA in their vicinity. If the quadrupole and the BPM are too far apart, or if a dipole magnet is placed between them, no direct partner is listed. Figure (8.8) shows the situation in the form of a floor plane of the COSY storage ring.

List of Figures

List of Tables

List of Acronyms

BAU	**B**aryon **A**symmetry in the **U**niverse
BBA	**B**eam **B**ased **A**lignment
BBN	**B**ig-**B**ang-**N**ucleosynthesis
BMAD	**B**aby **M**ethodical **A**ccelerator **D**esign
BMT	**B**argmann-**M**ichel-**T**elegdi
BPM	**B**eam **P**osition **M**onitor
BS	**B**mad_**S**tandard
CBS	**C**olliding **B**eam **S**ource
CMB	**C**osmic **M**icrowave **B**ackground
COSY	**CO**oler **SY**nchrotron
EDM	**E**lectric **D**ipole **M**oment
FAME	**F**orces and **MA**tter **E**xperiments
FORTRAN	**FOR**mula **TRAN**slation
ISA	**I**nvariant **S**pin **A**xis
JARA	**J**ülich **A**achen **R**esearch **A**lliance
JEDI	**J**ülich **E**lectric Dipole moment Investigations
JULIC	**JU**elich **L**ight **I**on **C**yclotron
MDM	**M**agnetic **D**ipole **M**oment
ORM	**O**rbit **R**esponse **M**atrix
PTC	**P**olymorphic **T**racking **C**ode
RF	**R**adio **F**requency
RK	**R**unge_**K**utta
RWTH	**R**heinisch-**W**estfälische **T**echnische **H**ochschule
SM	**S**tandard **M**odel
SVD	**S**ingular **V**alue **D**ecomposition
TAO	**T**ool for **A**ccelerator **O**ptics

Bibliography

[1] JARA – Jülich Aachen Research Alliance. Homepage.
https://www.jara.org/de/jara

[2] Forschungszentrum Jülich GmbH. Homepage.
https://www.fz-juelich.de/de

[3] RWTH Aachen University. Homepage.
https://www.rwth-aachen.de/go/id/a/?lidx=1

[4] JEDI Collaboration - Jülich Electric Dipole moment Investigations. Homepage.
https://collaborations.fz-juelich.de/ikp/jedi/index.shtml

[5] I. B. Khriplovich and S. K. Lamoreaux, *CP Violation Without Strangeness: Electric Dipole Moments of Particles, Atoms, and Molecules*, Edition 1, Springer-Verlag Berlin, 2012
https://doi.org/10.1007/978-3-642-60838-4

[6] L. Canetti, M. Drewes, and M. Shaposhnikov, *Matter and antimatter in the universe*, New Journal of Physics, Volume 14, pp. 095012, 2012
https://doi.org/10.1088/1367-2630/14/9/095012

[7] B. D. Fields, P. Molaro, and S. Sarkar, *Big-Bang Nucleosynthesis*, Chin. Phys. C38, pp. 339-344, 2014
https://doi.org/10.48550/arXiv.1412.1408

[8] C. L. Bennett et al., *Nine-Year Wilkinson Microwave Anisotropy Probe (WMAP) Observations: Final Maps and Results*The Astrophysical Journal Supplement Series, Volume 208, 2013
http://dx.doi.org/10.1088/0067-0049/208/2/20

[9] W. Bernreuther, *CP violation and baryogenesis*, Lect.Notes Phys. 591, pp. 237-293, 2002.
https://doi.org/10.48550/arXiv.hep-ph/0205279

[10] A. Wirzba, *Electric dipole moments of the nucleon and light nuclei*, Nuclear Physics A, Volume 928, pp. 116–127, 2014
http://dx.doi.org/10.1016/j.nuclphysa.2014.04.003

[11] A. D. Sakharov, *Violation of CP Invariance, C asymmetry, and baryon asymmetry of the universe*, Soviet Physics Uspekhi, Volume 34, Number 5, 1991, Originally in: Pisma Zh. Eksp. Teor. Fiz., 5 , pp. 32-35, 1967
https://doi.org/10.1070/PU1991v034n05ABEH002497

[12] M. S. Sozzi, *Discrete symmetries and CP violation: from experiment to theory*, Oxford University Press, 2007
https://doi.org/10.1093/acprof:oso/9780199296668.001.0001

[13] C. S. Wu et al, *Experimental Test of Parity Conservation in Beta Decay*, Physical Review, Volume 105, Issue 4, pp. 1413-1415, 1957
https://doi.org/10.1103/PhysRev.105.1413

[14] A. Angelopoulos and A. Apostolakis and E. Aslanides et al, *First direct observation of time-reversal non-invariance in the neutral-kaon system*, Physics Letters B, Volume 444, Number 1, pp. 43-51, 1998
https://doi.org/10.1016/S0370-2693(98)01356-2

[15] J. H. Christenson et al., *Evidence for the 2π Decay of the K_2^0 Meson*, Phys. Rev. Lett. 13, Volume 13, Issue 4, pp. 138-140, 1964
https://doi.org/10.1103/PhysRevLett.13.138

[16] M. Kobayashi and T. Maskawa, *CP-Violation in the Renormalizable Theory of Weak Interaction*, Progress of Theoretical Physics, Volume 49, Issue 2, pp. 652–657, 1973
https://doi.org/10.1143/PTP.49.652

[17] Julian Schwinger, *The Theory of Quantized Fields. I*, Phys. Rev., Volume 82, Issue 6, pp. 914-927, 1951
https://doi.org/10.1103/PhysRev.82.914

[18] V. Poncza, *Extensive optimization of a simulation model for the electric dipole moment measurement at the Cooler Synchrotron COSY*, PhD thesis, RWTH Aachen University, 2021
https://doi.org/10.18154/RWTH-2021-04834

[19] F. Guo and U. Meißner, *Baryon electric dipole moments from strong CP violation*, J. High Energ. Phys., Volume 2012, 97, 2012
https://doi.org/10.1007/JHEP12(2012)097

[20] J. M. Pendlebury et al., *Revised experimental upper limit on the electric dipole moment of the neutron*, Phys. Rev., Volume 92, Issue 9, pp. 092003, 2015
https://doi.org/10.1103/PhysRevD.92.092003

[21] W. Dekens and J. de Vries, *Renormalization Group Running of Dimension-Six Sources of Parity and Time-Reversal Violation*, Journal of High Energy Physics, Number 149, 2013.
https://doi.org/10.1007/JHEP05(2013)149

[22] C. Abel et al., *Measurement of the Permanent Electric Dipole Moment of the Neutron*, Phys. Rev. Lett. , Volumne 124, Issue 8, pp. 081803, 2020.
https://doi.org/10.1103/PhysRevLett.124.081803

[23] W. C. Griffith, M. D. Swallows and T. H. Loftus et al., *Improved Limit on the Permanent Electric Dipole Moment of* ^{199}*Hg,* Physical Review Letters 102, 101601, 2009.
https://arxiv.org/pdf/0901.2328.pdf

[24] T. S. Roussy et al., *An improved bound on the electron's electric dipole moment*, American Association for the Advancement of Science (AAAS), Science, Volume 381, Number 6653, 2023.
https://doi.org/10.48550/arXiv.2212.11841

[25] A. Andres et al., *First electric dipole moment measurement of the deuteron with the waveguide RF Wien Filter - Proposal for the* 2^{nd} *run*
https://collaborations.fz-juelich.de/ikp/jedi/public_files/proposals/JEDI-2nd-Precursor-run_proposal_08.09.2020-cover.pdf

[26] H. Wiedemann, *Particle Accelerator Physics*, Fourth Edition, Springer Cham, 2015.
https://doi.org/10.1007/978-3-319-18317-6

[27] K. Wille, *Physik der Teilchenbeschleuniger und Synchrotronstrahlungsquellen*, Erste Auflage, Vieweg+Teubner Verlag, 1992.
https://doi.org/10.1007/978-3-663-11850-3

[28] E.D Courant and H.S Snyder, *Theory of the alternating-gradient synchrotron*, Annals of Physics, Volume 3, Issue 1, pp. 1-48, 1958.
https://doi.org/10.1016/0003-4916(58)90012-5

[29] F. Hinterberger, *Physik der Teilchenbeschleuniger und Ionenoptik*, Second Edition, Springer Berlin, 2008.
https://doi.org/10.1007/978-3-540-75282-0

[30] A. J. Dragt, *Exact numerical calculations of chromaticity in small rings*, Particle Accelerators, Volume 12, pp. 205-218, 1982.
https://doi.org/10.1109/TNS.1981.4331779

[31] O. Kovalenko et al, *Orbit Response Matrix Analysis for FAIR Storage Rings*, Proceedings of IPAC2016, 7th International Particle Accelerator Conference, THPMB003, 2016.
https://doi.org/10.18429/JACoW-IPAC2016-THPMB003

[32] J. Safranek, *Experimental determination of storage ring optics using orbit response measurements*, Nuclear Instruments and Methods in Physics Research Section A: Accelerators, Spectrometers, Detectors and Associated Equipment, Volumne A 388, Issues 1-2, pp. 27-36, 1997.
https://doi.org/10.1016/S0168-9002(97)00309-4

[33] H. Yanai , K. Takeuchi , Y. Takane, *Projection Matrices, Generalized Inverse Matrices, and Singular Value Decomposition*, Springer New York, 2011.
https://doi.org/10.1007/978-1-4419-9887-3

[34] S. Y. Lee, *Spin Dynamics and Snakes in Synchrotrons*, Edition 1, World Scientific, 1997
https://doi.org/10.1142/3233

[35] F. Müller, *Polarimeter development for electric dipole moment measurements in storage rings*, PhD thesis, RWTH Aachen University, 2020
https://doi.org/10.18154/RWTH-2019-11439

[36] G. G. Ohlsen, *Polarization transfer and spin correlation experiments in nuclear physics*, Rep. Prog. Phys., Volume 35, Number 2, pp. 717, 1972
https://doi.org/10.1088/0034-4885/35/2/305

[37] L. H. Thomas, *I. The kinematics of an electron with an axis*, The London, Edinburgh, and Dublin Philosophical Magazine and Journal of Science, Volume 3, Issue 13, pp. 1-22, 1927.
https://doi.org/10.1080/14786440108564170

[38] V. Bargmann, Louis Michel, and V. L. Telegdi, *Precession of the Polarization of Particles Moving in a Homogeneous Electromagnetic Field*, Phys. Rev. Lett., Volume 2, Issue 10, pp. 435-436, 1959.
https://doi.org/10.1103/PhysRevLett.2.435

[39] T. Fukuyama and A. J. Silenko, *Derivation of Generalized Thomas-Bargmann-Michel-Telegdi Equation for a Particle with Electric Dipole Moment*, International Journal of Modern Physics A, Volume 28, pp. 1350147, 2013.
https://doi.org/10.1142/S0217751X13501479

[40] C. Carli and M. Haj Tahar, *Geometric phase effect study in electric dipole moment rings*, Phys. Rev. Accel. Beams, Vol. 25, pp. 064001, 2022.
https://doi.org/10.1103/PhysRevAccelBeams.25.064001

[41] J. Pretz, *Measurement of permanent electric dipole moments of charged hadrons in storage rings*, Hyperfine Interact, Volume 214, pp. 111-117, 2013.
https://doi.org/10.1007/s10751-013-0799-4 [14.06.2024]

[42] A. A. Skawran, *Comparison of Frozen and Quasi Frozen Spin Concepts for a Deuteron Electrical Dipole Moment Storage Ring*, Master Thesis, RWTH Aachen University, 2016.
https://juser.fz-juelich.de/record/845357

[43] A. Lehrach, *Erarbeitung und Umsetzung eines Konzepts zur Beschleunigung polarisierter Protonen im Kühlersynchrotron COSY*, PhD thesis, Universität Bonn, 1998.
http://hdl.handle.net/2128/4455

[44] G. H. Hoffstaetter, *High Energy Polarized Proton Beams* Edition 1, Springer-Verlag New York, 2006.
https://doi.org/10.1007/978-0-387-34754-7

[45] R. Maier et al., *Cooler synchrotron COSY — Performance and perspectives*, Nuclear Instruments and Methods in Physics Research, Volume A 390, Issues 1-2 , pp. 1-8, 1997.
https://doi.org/10.1016/S0168-9002(97)00324-0

[46] R. Gebel, R. Brings, O. Felden, R. Maier, S. Mey, D. Prasuhn, *20 YEARS OF JULIC OPERATION AS COSY'S INJECTOR CYCLOTRON*, Proceedings of Cyclotrons 2013, MOPPT003, 2013
https://accelconf.web.cern.ch/CYCLOTRONS2013/papers/moppt003.pdf

[47] J. Slim, *A novel waveguide RF Wien filter for electric dipole moment measurements of deuterons and protons at the COoler SYnchrotron (COSY)/Jülich*, PhD thesis, RWTH Aachen University, 2018
https://doi.org/10.18154/RWTH-2018-229484

[48] W. Haeberli, *Proposal for direct conversion of a polarized atomic beam to polarized negative ions*, Nuclear Instruments and Methods, Volume 62, Issues 3 , pp. 355-357, 1968.
https://doi.org/10.1016/0029-554X(68)90395-9

[49] R. Weidemann et al., *The polarized ion source for COSY*, Review on Scientific Instruments, Volume 67, Issues 3 , pp. 1357–1358, 1996.
https://doi.org/10.1063/1.1146665

[50] W. Bräutigam et al., *Status and perspectives of the cyclotron JULIC as COSY injector*, Review on Scientific Instruments, Volume 67, Issues 3 , pp. 1357–1358, 1996.
https://doi.org/10.1063/1.1146665

[51] S. Barsov, U. Bechstedt, W. Bothe, et al., *ANKE, a new facility for medium energy hadron physics at COSY-Jülich*, Nuclear Instruments and Methods in Physics Research, Volume 462, Issues 3, pp. 364-381, 2001.
https://doi.org/10.1016/S0168-9002(00)01147-5

[52] J. Bisplinghoff et al., *Position sensitivity by light splitting in scintillator arrays*, Nuclear Instruments and Methods in Physics Research Section A: Accelerators, Spectrometers, Detectors and Associated Equipment, Volume 329, Issues 1-2, pp. 151-162, 1993
https://doi.org/10.1016/0168-9002(93)90930-G

[53] B. Hoistad, J. Ritman, et al., *Proposal for the Wide Angle Shower Apparatus (WASA) at COSY-Jülich "WASA at COSY"*, 2004.
https://doi.org/10.48550/arXiv.nucl-ex/0411038

[54] D. Prasuhn et al., *Electron and stochastic cooling at COSY*, Nuclear Instruments and Methods in Physics Research, Volume 441, Issues 1-2, pp. 167-174, 2000.
https://doi.org/10.1016/S0168-9002(99)01128-6

[55] V. Reva et al., *COSY 2 MeV Cooler: Design, Diagnostic and Commissioning*, Proceedings of IPAC2014, 5th Int. Particle Acc. Conf., MOPRI075, 2014.
https://doi.org/10.18429/JACoW-IPAC2014-MOPRI075

[56] C. Weidemann, *Preparations for the spin-filtering experiments at COSY/Jülich*, PhD thesis, Universität zu Köln, 2011.

[57] R. Maier et al., *Non-beam disturbing diagnostics at COSY-Julich* , European particle accelerator conference, EPAC-2, pp. 800-802, 1990.
https://accelconf.web.cern.ch/e90/PDF/EPAC1990_0800.PDF

[58] J. Biri, M. Blasovszky, J. Gigler, et al., *Beam position monitor electronics at the cooler synchrotron COSY Julich*, IEEE Transactions on Nuclear Science, Vol. 41, No. 1, pp. 221-224, 1994.
https://doi.org/10.1109/23.281493

[59] T. Wagner, *Beam-based alignment at the cooler synchrotron COSY for an electric dipole moment measurement of charged particles*, PhD thesis, RWTH Aachen University, 2021
https://doi.org/10.18154/RWTH-2021-08453

[60] Matjaž Žnidarčič, *Libera Hadron: Hadron Beam Position Processor, Specifications*, v1.02. Instrumentation Technologies. Velika Pot 22, SI-5250 Solkan, Slovenia, Feb. 2018.

[61] I. Bekman et al., *BPM SYSTEM UPGRADE AT COSY*, Proc. 7th International Beam Instrumentation Conference, TUPC04, 2018.
https://doi.org/10.18429/JACoW-IBIC2018-TUPC04

[62] F. Abusaif, *Development of compact highly sensitive beam position monitors for storage rings*, Hyperfine Interact 240, 4, 2019.
https://doi.org/10.1007/s10751-018-1543-x

[63] F. Rathmann and N. Nikolaev, *Electric dipole moment searches using storage rings*, Proceedings of 23rd International Spin Physics Symposium, SPIN2018, p. 004, 2019
https://doi.org/10.22323/1.346.0004

[64] I. Bekman et al., *PROGRESS OF THE MACHINE CONTROL UPGRADE AT COSY/JÜLICH*, Proceedings of IPAC2019, 10th Int. Particle Acc. Conf., 2019
https://accelconf.web.cern.ch/ipac2019/papers/wepgw007.pdf

[65] A. Lehrach and R. Maier, *SIBERIAN SNAKE FOR THE COOLER SYNCHROTRON COSY*, Proceedings of the 2001 Particle Accelerator Conference, PACS 2001, WPPH052 ,Volume 4, pp. 2566–2568, 2001
https://doi.org/10.1109/PAC.1999.792665

[66] P. Benati et al., *Synchrotron oscillation effects on an rf-solenoid spin resonance*, Phys. Rev. ST Accel. Beams, Volume 15, Issue 12, pp. 124202, 2012
https://doi.org/10.1103/PhysRevSTAB.15.124202

[67] V. S. Morozov et al, *Spin manipulation of* 1.94 GeV/c *polarized protons stored in the COSY cooler synchrotron*, Phys. Rev. ST Accel. Beams, Vol. 7, pp. 024002, 2004
https://doi.org/10.1103/PhysRevSTAB.7.024002

[68] W. MacKay et al, *COMMISSIONING AND FUTURE PLANS FOR POLARIZED PROTONS IN RHIC*, Proceedings of the 2001 Particle Accelerator Conference, PACS 2001, MOPA004, Volume 1, pp. 24-26, 2001
https://doi.org/10.1109/PAC.2001.987421

[69] X. D. Yang et al, *Commissioning of electron cooling in CSRm*, Proceedings of COOL 2007, TUM1I02, 2007
https://accelconf.web.cern.ch/cl07/PAPERS/TUM1I02.PDF

[70] J. Dietrich et al, *Commissioning of electron cooling in CSRm*, Proceedings of COOL 2009, FRM1MCIO03, 2009
https://accelconf.web.cern.ch/COOL2009/papers/frm1mcio03.pdf

[71] F. Rathmann and N. Nikolaev, *Precursor experiments to search for permanent electric dipole moments of protons and deuterons at COSY*, Proceedings of 8th International Conference on Nuclear Physics at Storage Rings, MOPA004, Volume 150, p. 029, 2012
https://doi.org/10.22323/1.150.0029

[72] W. M. Morse, Y. F. Orlov and Y. K. Semertzidis, *rf Wien filter in an electric dipole moment storage ring: The "partially frozen spin" effect*, Phys. Rev. ST Accel. Beams, Vol. 16, pp. 114001, 2013
https://doi.org/10.1103/PhysRevSTAB.16.114001

[73] J. Slim et al., *First detection of collective oscillations of a stored deuteron beam with an amplitude close to the quantum limit*, Phys. Rev. Accel. Beams, Vol. 24, Issue 12, pp. 124601, 2021
https://doi.org/10.1103/PhysRevAccelBeams.24.124601

[74] Hans Grote, Frank Schmidt, Laurent Deniau, Ghislain Roy (editor), *The MAD-X Program*, Version 5.02.08, 2016
https://mad.web.cern.ch/mad/releases/5.02.08/madxuguide.pdf

[75] M. Berz, *Differential Algebraic Description of Beam Dynamics to Very High Orders*, Particle Accelerator Vol. 24, pp. 109-124, 1989
https://www.bmtdynamics.org/pub/papers/pada/pada.pdf

[76] W. Press, B. Flannery, S. Teukolsky, W. Wetterling, *Numerical Recipes in Fortran 77 - The Art of Scientific Computing, Second Edition*, Cambridge University Press, 1992
https://websites.pmc.ucsc.edu/~fnimmo/eart290c_17/NumericalRecipesinF77.pdf

[77] D. Sagan, *Bmad: A relativistic charged particle simulation library*, Nuclear Instruments and Methods in Physics Research A, Volume 558, Issue 1, pp. 356-359, 2006
https://doi.org/10.1016/j.nima.2005.11.001

[78] D. Sagan, *The Tao Manual*, Revision: December 20, 2023
https://www.classe.cornell.edu/bmad/tao.html

[79] D. Sagan, *The Bmad Reference Manual*, Revision: December 20, 2023
https://www.classe.cornell.edu/bmad/manual.html

[80] W. Romberg, *Vereinfachte numerische Integration*, Det Kongelige Norske Videnskabers Selskab Forhandlinger, Bind 28, Nr. 7, pp. 30–36, 1955

[81] Y. Dutheil, *Bmad Model of COSY, Status and Progress*, Proceedings of IPAC2016, 2016
http://jacow.org/ipac2016/papers/thpmr021.pdf

[82] I. Bekman, J. Hetzel, *COSY Model-Machine Optimization*, Proceedings of IPAC2021, 12th Int. Particle Acc. Conf., 2021
https://accelconf.web.cern.ch/ipac2021/papers/wepab302.pdf, doi:10.18429/JACoW-IPAC2021-WEPAB302

[83] U. Bechstedt, W. Bergs, G. Decker, G. Dolfus, W. Ermer, A. Hardt, G. Krol, Ch. Lippert, Th. Pawlat, J. Rook, M. Rook, D. Rosin, Th. Sagefka , *Field Measurement of the Magnets for COSY - Jülich*, European particle accelerator conference, EPAC-3, pp. 1379-1381, 1992
https://accelconf.web.cern.ch/e92/PDF/EPAC1992_1379.PDF

[84] U. Bechstedt, N. Bongers, W. Briell, A. Hardt, W. Xlein, U. Schwarz, E. Veiders, *Magnets and Power Supplies for COSY*, European particle accelerator conference, EPAC-1, pp. 1132-1134, 1988
https://accelconf.web.cern.ch/e88/PDF/EPAC1988_1132.PDF

[85] R. Hipple and M. Berz, *A Comparison of Storage Ring Modeling with COSY INFINITY, ZGOUBI, and MAD8*, Microscopy and Microanalysis, Volume 21, Issue S4, pp. 2–7, 2015
https://doi.org/10.1017/S1431927615013045

[86] B. Hartmann, M. Berz, H. Wollnik, *The computation of aberrations of fringing fields of magnetic multipoles and sector magnets using differential algebra*, Nuclear Instruments and Methods in Physics Research Section A: Accelerators, Spectrometers, Detectors and Associated Equipment, Volume 297, Issue 3, pp. 343-353, 1990
https://doi.org/10.1016/0168-9002(90)91317-5

[87] Martin Berz, Kyoko Makino, *Optics and nonlinear effects in repetitive systems*, Nuclear Instruments and Methods in Physics Research Section A: Accelerators, Spectrometers, Detectors and Associated Equipment, Volume 645, Issue 1, pp. 175-181, 2011
https://doi.org/10.1016/j.nima.2010.12.205

[88] K. Hwang and S. Y. Lee, *Dipole fringe field thin map for compact synchrotrons*, Physical Review Special Topics - Accelerator and Beams 18, 122401, 2015
https://doi.org/10.1103/PhysRevSTAB.18.122401

[89] Harald A. Enge, *Effect of Extended Fringing Fields on Ion-Focusing Properties of Deflecting Magnets*, Review of Scientific Instruments, Volume 35, Issue 3, 278–287, 1964
https://doi.org/10.1063/1.1718806

[90] J. Stein, J. Böker, Private communication. 2021/2022

[91] J. Hetzel, J. Stein, M. Hartmann, I. Bekmann, Private communication. Feb./Mar. 2021

[92] L.H.A. Leunissen, *Non-linear transverse dynamics at the Cooler Synchrotron COSY*, PhD thesis, Technische Universiteit Eindhoven, 1997
https://doi.org/10.6100/IR502906

[93] M. Hartmann, Private communication. 2023/2024

[94] I. Bekman, J. Hetzel, *Calibration of COSY Steerers for Advanced Orbit Feedback*, Annual Report 2020, Volume 4427, Berichte des Forschungszentrums Jülich, Forschungszentrum Jülich GmbH Zentralbibliothek, pp. 101-102, 2020
http://hdl.handle.net/2128/28809

[95] Vermessungsbüro Dipl.-Ing. H. J. Stollenwerk. Bahnstraße 8, 50126 Bergheim.

[96] A. Saleev et al., *Spin tune mapping as a novel tool to probe the spin dynamics in storage rings*, Phys. Rev. Accel. Beams, Vol. 20, Issue. 7, p. 072801, 2017 https://doi.org/10.1103/PhysRevAccelBeams.20.072801

[97] J. Stein, Private communication. 2024

[98] A. Andres, *The first direct measurement of the deuteron electric dipole moment at the Cooler Synchrotron COSY*, PhD thesis, RWTH Aachen University, 2024, unpublished

[99] A. Lehrach, S. Martin, R. Talman, *Design of a Prototype EDM Storage Ring*, Proceedings of 23rd International Spin Physics Symposium, SPIN2018, p. 114, 2019 https://doi.org/10.22323/1.346.0144

[100] CPEDM Collaboration, *Storage ring to search for electric dipole moments of charged particles: Feasibility study*, CERN Yellow Reports: Monographs, Vol. 3, 2021 https://doi.org/10.23731/CYRM-2021-003

[101] M. Rosenthal, *Experimental benchmarking of spin tracking algorithms for electric dipole moment searches at the cooler synchrotron COSY*, PhD thesis, RWTH Aachen University, 2016 https://publications.rwth-aachen.de/record/671012/files/671012.pdf

Eidesstattliche Erklärung

Ich, Maximilian Vitz

erkläre hiermit, dass diese Dissertation und die darin dargelegten Inhalte die eigenen sind und selbstständig, als Ergebnis der eigenen originären Forschung, generiert wurden.

Hiermit erkläre ich an Eides statt

1. Diese Arbeit wurde vollständig oder größtenteils in der Phase als Doktorand dieser Fakultät und Universität angefertigt;

2. Sofern irgendein Bestandteil dieser Dissertation zuvor für einen akademischen Abschluss oder eine andere Qualifikation an dieser oder einer anderen Institution verwendet wurde, wurde dies klar angezeigt;

3. Wenn immer andere eigene- oder Veröffentlichungen Dritter herangezogen wurden, wurden diese klar benannt;

4. Wenn aus anderen eigenen- oder Veröffentlichungen Dritter zitiert wurde, wurde stets die Quelle hierfür angegeben. Diese Dissertation ist vollständig meine eigene Arbeit, mit der Ausnahme solcher Zitate;

5. Alle wesentlichen Quellen von Unterstützung wurden benannt;

6. Wenn immer ein Teil dieser Dissertation auf der Zusammenarbeit mit anderen basiert, wurde von mir klar gekennzeichnet, was von anderen und was von mir selbst erarbeitet wurde;

7. Ein Teil oder Teile dieser Arbeit wurden zuvor veröffentlicht und zwar in:

- S. Karanth et al. (JEDI Collaboration), *First Search for Axionlike Particles in a Storage Ring Using a Polarized Deuteron Beam*, Phys. Rev. X 13, 031004, 2023
  https://doi.org/10.1103/PhysRevX.13.031004

- M. Vitz, A. Lehrach and J. Pretz, *Determination of the Invariant Spin Axis in a COSY model using Bmad*, Journal of Physics: Conference Series, Vol. 2687, pp. 052024, 2024
  https://dx.doi.org/10.1088/1742-6596/2687/5/052024

- M. Vitz, A. Lehrach and J. Pretz, *Determination of the Invariant Spin Axis in a COSY model using Bmad*, Proceedings of IPAC2023, 14th International Particle Accelerator Conference, TUPM076, 2023
  https://doi.org/10.18429/JACoW-IPAC2023-TUPM076

- M. Vitz, *Spin-Tracking Simulations in a COSY Model Using Bmad*, Proceedings of IPAC2022, 13th International Particle Accelerator Conference, WEPOTK040, 2022
  https://doi.org/10.18429/JACoW-IPAC2022-WEPOTK040

- M. Vitz, J. Pretz and A. Lehrach, *Spin-Tracking Simulations in an idealized COSY Model using Bmad*, Proceedings 24th International Spin Symposium (SPIN2021), JPS Conf. Proc. Vol. 37, pp. 021106, 2022
  https://doi.org/10.7566/JPSCP.37.021106

- M. Vitz, *Determination of ISA correction factors*, In: Annual Report 2023, Berichte des Forschungszentrums Jülich, p. 68, 2023
  https://doi.org/10.34734/FZJ-2024-01973

- M. Vitz, *SCT optimization and determination of the Invariant Spin Axis in a COSY model using Bmad*, In: IKP Annual Report 2022, Berichte des Forschungszentrums Jülich, p. 101, 2022
  https://doi.org/10.34734/FZJ-2024-01948

- M. Vitz, *Spin-Tracking simulations in an idealized COSY model using Bmad*, In: Annual Report 2021, Berichte des Forschungszentrums Jülich, p. 80, 2021
  https://juser.fz-juelich.de/record/1005535

Ort, Datum — Maximilian Vitz